UNIVERSIDAD DE CHILE
FACULTAD DE CIENCIAS FÍSICAS Y MATEMÁTICAS
DEPARTAMENTO DE ASTRONOMÍA

A COMPREHENSIVE PHOTOMETRIC STUDY OF THE MILKY WAY'S OUTER HALO SATELLITES

TESIS PARA OPTAR AL GRADO DE
DOCTOR EN CIENCIAS, MENCIÓN ASTRONOMÍA

SEBASTIÁN ANDRÉS MARCHI LASCH

PROFESOR GUÍA:
RICARDO MUÑOZ VIDAL

MIEMBROS DE LA COMISIÓN:
JULIO CHANAMÉ DOMÍNGUEZ
JAMES JENKINS
PAULINA LIRA TEILLERY

Este trabajo ha sido parcialmente financiado por CONICYT, DAS

SANTIAGO DE CHILE
2020

RESUMEN DE LA MEMORIA PARA OPTAR
AL TÍTULO DE DOCTOR EN CIENCIAS, MENCIÓN ASTRONOMÍA
POR: SEBASTIÁN ANDRÉS MARCHI LASCH
FECHA: 2020
PROF. GUÍA: RICARDO MUÑOZ VIDAL

UN ESTUDIO FOTOMÉTRICO EXHAUSTIVO DE LOS OBJETOS SATÉLITES DEL HALO EXTERNO DE LA VÍA LÁCTEA.

Una de las interrogantes más importantes en la astronomía Galáctica es entender los procesos responsables de la formación y evolución de la Vía Láctea. La mayor parte de la información para estudiar las etapas tempranas de formación Galáctica está contenida en el halo y sus subestructuras, dominadas por poblaciones estelares antiguas.

En esta tesis, realizo un estudio fotométrico completo de los satélites del halo externo de la Vía Láctea. Ellos se agrupan en cúmulos globulares, galaxias enanas esferoidales y galaxias enanas ultra-débiles. Para esto, usé un set de datos que al mismo tiempo es profundo, de campo amplio y altamente homogéneo, a diferencia de los existentes en la literatura.

En la primera parte de esta tesis, presento evidencia de una correlación entre el índice de Sérsic y el radio efectivo, seguida por una gran fracción de los satélites. Muestro que esta correlación puede ser enteramente reproducida al ajustar relaciones lineales al plano del brillo superficial central versus magnitud absoluta y al plano del índice de Sérsic versus magnitud absoluta, asumiendo la existencia de dos tipos de cúmulos globulares en el halo externo: un grupo caracterizado por presentar alto brillo superficial, con propiedades similares a los cúmulos del halo interno, y otro grupo caracterizado por bajo brillo superficial y que comparte características con las galaxias enanas esferoidales y ultra-débiles. Dadas estas similitudes, discuto la posibilidad de que los cúmulos globulares del halo externo se hayan formado dentro de halos de materia oscura y que las fuerzas de marea de galaxias madres diferentes sean las responsables de las diferencias en las propiedades observadas para ambos grupos de cúmulos.

En la segunda parte, llevo a cabo un estudio morfológico de los satélites, con el objetivo de determinar homogéneamente cuáles satélites están sufriendo desmembramiento de marea debido al potencial gravitatorio de la Vía Láctea. Para esto, uso la técnica *matched-filter* para calcular la densidad estelar en función de la distancia radial desde el centro del satélite. Muestro que la mayoría de las galaxias ultra-débiles presentan irregularidades en su morfología, consistente con algún grado de perturbación por fuerzas de marea, mientras que un pequeño número de ellas muestran fuertes signos de esta perturbación. Los cúmulos globulares y las galaxias enanas esferoidales muestran mayoritariamente una morfología regular. También muestro que una correlación observada entre la razón masa-luminosidad total y el $g_{\rm ratio}$ (definido como la razón entre la aceleración de marea provocada por la Vía Láctea en el satélite y la gravedad estelar interna del satélite) puede ser explicada si se asume que la influencia de marea de la Vía Láctea remueve masa estelar de las partes externas del satélite, mientras la dispersión de velocidad central no se ve afectada.

Los resultados de esta tesis apoyan la idea de que las propiedades observadas en los satétiles del halo externo de la Vía Láctea son moldeadas simultáneamente por procesos físicos internos de éstos y por la influencia del potencial gravitacional de la Vía Láctea sobre ellos.

Abstract

A COMPREHENSIVE PHOTOMETRIC STUDY OF THE MILKY WAY'S OUTER HALO SATELLITES

One of the main questions of Galactic astronomy is to understand the natural processes responsible for the formation and evolution of the Milky Way (MW). Most of the information needed to study the early stages of Galactic formation is contained in the halo and its substructures, because they are dominated by old stellar populations.

In this thesis, I carry out a comprehensive photometric study of the substructures of the MW's outer halo. They are grouped in Globular Clusters (GCs), dwarf-spheroidal (dSph) and ultra-faint dwarf (UFD) galaxies. To carry out this study, I use a dataset that is at the same time deep, wide-field and highly homogeneous, unlike any other in the current literature.

In the first part of this thesis, I present evidence of a correlation in the Sérsic index versus the effective radius plane followed by a large fraction of outer halo GCs and satellite dwarf galaxies. I show that this correlation can be entirely reproduced by fitting empirical linear relations in the central surface brightness versus absolute magnitude and Sérsic index versus absolute magnitude parameter spaces, and by assuming the existence of two types of outer halo GCs: one of high surface brightness (HSB group), with properties similar to inner halo clusters; and another of low surface brightness (LSB group), which share characteristics with dwarf spheroidal and UFD galaxies. Given the similarities of LSB clusters with dwarf spheroidal and UFD galaxies, I discuss the possibility that outer halo clusters also originated inside dark matter halos and that tidal forces from different host galaxy potentials are responsible for the different properties between HSB and LSB clusters.

In the second part, I perform a morphological study of the satellites in the sample, aiming at homogeneously determining which satellites are suffering from tidal disruption from the MW. To do this, I use a matched-filter technique to calculate the stellar density at each radius from the center of the satellite. With this, I determine the isodensity contours to characterize its morphology. I show that most of the UFDs have irregularities in their shapes consistent with some degree of tidal disturbance, with few of them having strong signs of tidal disruption, whereas GCs and dSphs show mostly a regular morphology. I also show that an observed correlation between the total mass-to-light ratio and the $g_{\rm ratio}$ (defined as the ratio between the tidal acceleration of the MW over the satellite and the internal stellar gravity of the satellite) can be explained if one assumes that the MW tidal influence removes stellar mass from the satellite while leaving the central velocity dispersion mostly unchanged.

The results of this thesis support the notion that the photometric and structural properties observed on the MW's outer halo satellites are shaped both by intrinsic processes of the satellite and the influence of the MW's gravitational potential over it.

Para mí...

Agradecimientos

En primer lugar, agradezco a mi familia, quienes me acompañaron de principio a fin en el proceso de convertirme en astrónomo profesional y me han apoyado en todas las decisiones que he tomado en mi vida profesional y personal.

Agradezco profundamente a mi profesor guía, Ricardo Muñoz, quien no solo me enseñó a hacer ciencia rigurosa y significativa, sino también me apoyó en los momentos de dificultad personal por los que pasé durante mis estudios doctorales y celebró conmigo las victorias.

Quiero agradecer también a los profesores de Calán, especialmente a los que trabajaron conmigo en proyectos de investigación y al comité de tesis, quienes me ayudaron con su conocimiento y comentarios a generar y concretar una tesis de la cual me puedo sentir orgulloso.

Dedico los mayores agradecimientos a mis amigos y compañeros de Calán, con los que compartí las alegrías y frustraciones de ser estudiante de postgrado. En especial, agradezco a Julián y Ángel, por ser las personas con los que comencé este proceso y que se mantienen hasta el día de hoy como grandes amigos; a Felipe (gracias weiiii!) y Thomas, por las largas y divertidamente tensas discusiones en la oficina; a Pepe, Juanpi, Mati, Juan, Jorge y Grecco por hacer de Calán mucho más que sólo el lugar de trabajo y por estar ahí en los momentos más emocionalmente duros. Cada uno de ustedes me acompañó en las buenas y en las malas. Estoy feliz de haberlos conocido y la amistad de ustedes es lo más preciado que Calán me pudo dar.

Agradezco a los funcionarios de Calán, que constantemente realizan un excelente trabajo. En particular, agradezco a Señora Nelly, Señora María, Jorge Molina y don Luis, cuya calidad humana es irremplazable; a Gissela, Ale, José, Vale, Sonia y don Ricardo, por las conversaciones en los almuerzos donde se hablaba de cualquier cosa menos de astronomía; a Marta, por su tremendo trabajo y buena disposición para que los asuntos administrativos no sean un obstáculo para que los estudiantes hagan investigación.

Finalmente, agradezco a Franco Giraudo por más de 27 años de amistad incondicional y por estar presente en esta, una de las etapas más importantes de mi vida.

Contents

List of Tables

List of Figures

Chapter 1

Introduction

In this thesis, I present the research I conducted during my Ph.D. studies at the Astronomy Department of the Universidad de Chile. This work consists of a comprehensive study of photometric and structural properties of the Milky Way's (MW) outer halo satellite objects, which are grouped in dwarf galaxies and globular clusters. In particular, in the first part of this thesis, I perform a comparison of the structural and photometric properties of dwarf spheroidal galaxies and globular clusters, while in the second part I analyze their morphological characteristics. Both investigations aim to contribute with new information to answer the question of how the Milky Way formed and evolved and to understand how the influence of our Galaxy shapes the properties of its satellite objects.

Since the discovery that the Galaxy is one of many others in the Universe, the question of how it formed and evolved into the structure that we observe today has caught the interest of Galactic astronomers because our vantage point inside the Galaxy allows us to understand in great detail its different structures and components, something that is not possible for other galaxies. Thus, the knowledge we can obtain from studying the Milky Way is essential to shedding light on the processes that govern other galaxies farther out.

The first model that tried to explain the formation of the Milky Way was that of Eggen, Lynden-Bell, & Sandage (1962). They measured the velocities of 221 dwarf stars to determine the eccentricities and angular momenta of their galactic orbits. They found that stars of low metallicity (located in the halo) show eccentric orbits, in contrast with their high metallicity counterparts (located in the disk), which have circular orbits. The proposed model to explain these observations is a top-down galactic formation model, that says that the Galaxy formed from the very rapid collapse of a giant gas cloud, during which the stars in the halo formed in early stages, while stars in the disk formed later when the gas was already in dynamic equilibrium.

Later, Searle & Zinn (1978) measured the metal abundances of stars in 19 globular clusters located farther than 8 kpc from the galactic center. They found that the distribution of the abundance of halo globular clusters is independent of the galactocentric distance and that the morphology of the clusters' color-magnitude diagrams shows no correlation with the metal abundance. These observations are inconsistent with a purely top-down formation model, so

they proposed that the halo of the Milky Way formed mainly from the accretion of smaller galaxies that contributed their globular cluster and stars to the halo population. In this picture, the properties of globular clusters reflect the properties of the smaller galaxy during the time of its accretion. This model is known as the bottom-up or hierarchical accretion model and is the one that better explains galactic formation.

In the context of hierarchical growth processes, the halo of MW contains important information about the ancient history of our Galaxy, especially because dynamical scales are long enough to retain information of past Galactic events (e.g., Johnston et al., 1996; Mayer et al., 2002). A significant fraction of this information is contained in the structural, dynamical, and chemical properties of satellite stellar structures of the MW, which dominate the outer halo stellar distribution (see Majewski, 2004; Willman, 2010; Ivezić et al., 2012, for reviews on this topic). Thus, by studying these substructures, it is, in principle, possible to peer into our galaxy's past and learn about the processes that governed its formation and evolution.

The stellar structures that surround the Galaxy have been usually classified as either globular clusters (GCs) or dwarf galaxies. Specifically, most of the dwarf galaxies are of the dwarf spheroidal type (dSph), which is devoid of gas and shows no current stellar formation. Both types of stellar structures are dominated by an old, metal-poor stellar population. Currently, it is accepted that dwarf galaxies formed their dark matter (DM) halos at small scales and were accreted later by the MW, as described by hierarchical growth models (Searle & Zinn, 1978; Bullock & Johnston, 2005). In the case of GCs, a fraction of them formed together with our galaxy during a phase of rapid collapse as proposed by Eggen et al. (1962), whereas others are thought to have been of external origin, i.e. they formed in galaxies that were later accreted by the MW, which stripped off their GCs and incorporated them to its satellite population (Zinn, 1993, 1996; Mackey & Gilmore, 2004a; Mackey & van den Bergh, 2005; Leaman et al., 2013; Zaritsky et al., 2016).

To understand better the role of these structures in the formation and evolution of the MW, current research efforts have focused on the detection of satellite objects to obtain a reliable census of them orbiting our Galaxy. The results have significantly changed the way we understand our Galaxy surroundings. Before 2005, only nine Galactic dSphs were known (now referred to as classical dSphs), with luminosities in the range $-12 \lesssim M_{\rm V} \lesssim -8$ and with half-light radii on the order of 100 pc. Regarding GCs, almost all of them were compact objects, with half-light radii of less than 10 pc and, in general, less luminous than classical dSphs. Over the last decade and a half, and thanks to large-area surveys like the Sloan Digital Sky Survey (SDSS; York et al., 2000), PanSTARRS1 (Chambers & Pan-STARRS Team, 2016) and the Dark Energy Survey (DES; Dark Energy Survey Collaboration et al., 2016), the population of satellite systems has increased significantly, more than doubling the total number (Willman et al., 2005a; Belokurov et al., 2006a, 2007, 2008, 2009, 2010, 2014; Zucker et al., 2006a,b; Walsh et al., 2007; Muñoz et al., 2012b; Bechtol et al., 2015; Kim & Jerjen, 2015; Koposov et al., 2015; Laevens et al., 2015a,b; Martin et al., 2015; Torrealba et al., 2016a,b; Homma et al., 2018). The new objects include low-luminosity dSphs ($M_{\rm V} > -8$), named ultra-faint dwarf galaxies (UFDs), some of them as small as some GCs; and halo GCs, some of them of a size comparable to these UFDs. In this new scenario, the size gap that seemed to separate GCs from dSphs in the size versus luminosity plot has started to become populated, casting doubts on the true different origins for extended GCs and UFDs (e.g.,

Drlica-Wagner et al., 2015; Torrealba et al., 2016b). For example, it is not clear whether the large half-light radii of extended GCs is an intrinsic property of a different class of objects or a result of interactions with the MW (e.g., van den Bergh & Mackey, 2004; Ripepi et al., 2007; Hwang et al., 2011).

Given the variety of characteristics across the whole range of satellite objects, an important question has become relevant: whether the properties we observe in satellite objects are intrinsic to them, or are the result of the MW's gravitational influence on them over a long period. This is known as the "Nature versus Nurture" problem.

To give answers to this question, it is necessary to have a set of observations that are deep, wide and homogenous, which allows for a comparison between GCs and dwarf galaxies. Despite the importance of such a set of data, until recently it did not exist. For GCs, the most complete dataset is that of Harris (1996), which is extremely heterogeneous due to the different cameras, filters and photometric methods used in its creation. For dSphs, Irwin & Hatzidimitriou (1995) carried out a successful study of structural parameters of eight classical dSphs using photographic plates, but its depth only reaches $r \sim 22$, which is three or four magnitudes lees deep than can be achieved with current technologies on ground telescopes. Finally, for UFDs the majority of photometric and structural parameters come from shallow images from the SDSS or follow-up programs of low spatial coverage or made up of few objects. In this work, I use a novel dataset (Muñoz et al., 2018a) characterized by deep and wide observations, which ensures an excellent analysis of photometric and structural parameters. At the same time, it is homogeneous and made up of 58 satellite objects, allowing for statistically meaningful comparisons.

In this thesis, I use this state-of-the-art dataset to analyze and compare the properties of satellite GCs and dSphs, to asses the contribution of "Nature" and "Nurture" in shaping the properties of the satellite objects in the formation and evolution of the MW. In what follows, I present a brief review of the properties of MW's outer halo satellite objects and our current understanding of their role in the formation and evolution of our Galaxy.

1.1 The MW's satellite population

As was previously mentioned, the outer halo of the MW is dominated by stellar structures that can be detected as overdensities of stars, in contrast with the more uniform distribution of the background members. These satellite objects are classified into two groups: dwarf galaxies and GCs. As I present in the following sections, these objects show many differences and similarities, and understanding them can help us elucidate the processes of formation and evolution that shaped our Galaxy. Luckily, these objects are close enough to us that we can use ground and space telescopes to resolve their stellar populations and characterize their color-magnitude diagrams (CMD). This diagram represents the most important tool to obtain the photometric and structural information needed to study the satellite population of the MW.

In what follows, I present the characteristics of both dwarf galaxies and GCs and introduce the scientific context that makes them excellent objects of study to better understand our Galaxy.

1.1.1 Dwarf galaxies

Dwarf galaxies can be defined as galaxies with small intrinsic size, small absolute luminosity, and low surface brightness, in comparison with more "normal" galaxies like the MW (Hodge, 1971). This is a consequence of their relatively low number of member stars, ranging from 100 million up to few billions of stars. This is much less than the number of MW's stars, which lies between the 200 – 400 billion. As a population, dwarf galaxies are the most numerous galaxies in the present-day Universe (Marzke & da Costa, 1997), and there is strong evidence that they were more numerous in the past (Ellis, 1997). Current observations show that this is also true in the Local Group (LG). An important characteristic of these galaxies is that they are not uniformly distributed across the LG volume. Instead, they concentrate around more massive galaxies like the Andromeda galaxy (M31) and the MW (Gurzadyan et al., 1993; Karachentsev, 1996), making them a relevant component of the satellite population of galaxies.

Dwarf galaxies are classified into three different types: dwarf elliptical (dE), Irregular (Irr) and dwarf Irregular (dIrr), and dwarf Spheroidal (dSph). There is another type, the ultra-faint dwarf (UFD), which in some cases are considered as extreme cases of dSphs. In this work, we consider them as part of the dSph type, although we dedicate a part of this introduction to talk about UFDs in more detail.

dEs are characterized by having no ordered rotation, giving them their elliptical appearance. Instead, they are pressure supported ($V_{\rm rot}/\sigma_v \sim 0.1$). They are dominated by intermediate and old populations of stars and show negligible amounts of gas and dust. Therefore, they are not forming new stars. In the LG there are four known dEs: M32, M110, NGC 185, and NGC 147. Interestingly, all of them are satellites of M31, so no dEs are present in the MW satellite population. Their absolute magnitudes lie on the range -13 to -19, they can have a total mass between $10^7 M_\odot$ and $10^9 M_\odot$, and their sizes go from 1 to 10 kpc.

Irr and dIrr are more numerous than dEs in the LG. They are characterized by having a large gas fraction and ongoing star formation. In consequence, they are populated by bright, young and blue stars, and HII regions. The scattered areas of star formation give them their irregular appearance, although it is thought that interactions between galaxies could also be responsible for their shape (such as the interactions between the Magellanic clouds and the MW). Additionally, these galaxies show evidence of being rotationally supported ($V_{\rm rot}/\sigma_v \sim 1-6$) and metallicities of less than 0.1 $Z_\odot$. The Magellanic Clouds are typical examples of Irr galaxies. Examples of dIrr also are Leo A, WLM, Sextans A, and the Sagittarius dIrr galaxy.

In the context of this work, dSphs are the most important type of dwarf galaxy. They dominate by number the total population of dwarf galaxies, as seen in the LG. This is also evident in the MW's satellite population, where almost all of the known satellite galaxies and the later discoveries are of this type. dSphs have the lowest surface brightness values of all dwarf galaxy types. Regarding their properties, they can are considered the low-luminosity, low-surface brightness versions of the dE's. Their total luminosity can be similar to those of GCs, but because dSphs are much more extended than GCs (their core radii are on the order of 10^2 higher), their central surface brightnesses are approximately 10 magnitudes arcsec^{-2} fainter. The dSphs show absolutely no detection of hydrogen and no signs of current nor

recent star formation. Therefore, they are generally dominated by old stellar populations ($\sim$ 13 Gyr old), although some of them have younger populations ($1 - 10$ Gyr old). They show intermediate to low metallicities ([Fe/H] from ~ -2.8 to ~ -0.4). Also, they are pressure-supported ($V_{\rm rot}/\sigma_v \lesssim 0.1$).

Given the numerical prevalence of dSphs in the LG in general, and in the MW's satellite population in particular, I devote the following subsections to review in detail the properties and historical aspects of this type of dwarf galaxy.

1.1.2 The classical dwarf spheroidal galaxies

Classical dwarf spheroidal galaxies are the dSphs with the highest luminosities and larger sizes. Their absolute magnitudes go from -8 to -15, their sizes from 0.1 to 0.5 kpc, and their total masses lie between $10^7 M_\odot$ to $10^9 M_\odot$.

The first dSph was discovered well into the XX century, because of their characteristic low luminosity ($M_{\rm V} > -15$) and extended structure, which give them an extremely low surface brightness ($\Sigma_{\rm V} > 22$ mag arcsec^{-2}). In 1938, Harlow Shapley discovered the Sculptor galaxy on photographic plates of deep exposure and managed to map its extended stellar density distribution and obtain an estimation of its distance (Shapley, 1938, 1939). Later, Baade & Hubble (1939) used the 60-inch telescope at Boyden Observatory and the 100-inch telescope at Mt. Wilson and detected W Virginis and RR Lyrae stars, which were used to determine a precise distance modulus for the galaxy (19.62 mag, very similar to the current value of 19.68 ± 0.08 mag measured by Pietrzyński et al. (2008)). The distance and the low absolute luminosity obtained made it clear that Sculptor is a faint dwarf galaxy but, in the words of Shapley, "remarkably uniform [and with] no indications of a nucleus, of clusters, or of diffuse nebulosity, either luminous or dark". Additional work of Shapley (1939) led to the discovery of a second dSphs, named Fornax, which is much farther out than Sculptor. After these findings, it was a matter of time that the population of dSphs would increase. In the 1950s, the dwarf galaxies Leo I, Leo II (Harrington & Wilson, 1950) and Ursa Minor and Draco (Wilson, 1955) were discovered, and by the end of the XX century, only three more new dSphs were detected: Carina (Cannon et al., 1977), Sextans (Irwin et al., 1990), and Sagittarius (Ibata et al., 1994). All these systems correspond to satellites of the MW. The name "classical dSphs" is used to distinguish them from the fainter and newly discovered UFDs.

One of the most important aspects of classical dSphs is that their density profiles are quite different from that of known elliptical galaxies. Traditionally, elliptical and dE galaxies are described by the de Vaucouleurs profile (de Vaucouleurs, 1948), given by

$$\ln I(R) = \ln I_{\rm e} + 7.669[1 - (R/R_{\rm e})^{1/4}] \tag{1.1}$$

where $I(R)$ is the surface brightness at radius R from the center, $R_{\rm e}$ is the effective radius (also known as half-light radius, inside of which half of the total emitted light is contained), and $I_{\rm e}$ is the surface brightness at the effective radius.

Later morphological studies of the Sculptor and Fornax dSphs made by Hodge (1961a,b)

showed that this type of dwarf galaxy does not follow the De Vaucouleurs profile. Instead, the density profile of dSphs is better described by a King profile. This profile was empirically defined for GCs (King, 1962), so it is interesting that it also works for dSphs. The profile is described by the analytical form

$$f = k\left(\frac{1}{[1+(r/r_{\rm c})^2]^{1/2}} - \frac{1}{[1+(r_{\rm t}/r_{\rm c})^2]^{1/2}}\right)^2 \tag{1.2}$$

where the adjusting parameters are the core radius $r_{\rm c}$ (equivalent to the half-light radius) and the tidal radius $r_{\rm t}$, which marks the radius where the density of stars drops abruptly.

The most remarkable thing about the empirical King profile is that it can be reproduced from theoretical formulations. King (1966) demonstrated that in a system made of "gas" of stars of a single mass, which is tidally truncated, spherically symmetric, isotropic and self-gravitating, two-body relaxation of stars is short enough that the system is dynamically relaxed after a Hubble time. The profile of this simulated object resembles the empirical King profile. The short relaxation time is true for GCs (10^8 years in the center, and 10^9 at the core radius), but the low density of dSphs makes this time much larger for them (on the order of 10^{13} years), so there is no real physical motivation to apply the King profile to dSphs.

Keeping in mind that the King profile only fits empirically to dSphs and that there is no theoretical foundation to use this density model is important because it implies that the physical meaning attributed to free parameters of the King profile (i.e., core and tidal radius) may not be valid in the context of dSphs. In particular, for GCs the tidal radius represents the boundary where stars beyond that point are no longer gravitational bound to it. In some cases, a King profile can be fitted successfully to the inner (and most luminous) part of the dSph, while the outer (and least luminous) parts of the dwarf galaxy show an "excess" population of stars (i.e., a higher number density that predicted by the model) beyond the tidal radius, where the King model does not offer a good fit (Innanen & Papp, 1979; Eskridge, 1988; Irwin & Hatzidimitriou, 1995) (see Figure 1.1 for examples of King profiles fitted to classical dSphs with excess stars). Given the traditional physical meaning of the tidal radius, one interpretation is that these stars are extratidal, i.e they are gravitationally unbound to the dwarf galaxy. However, and paying attention to the fact that the tidal radius may not have the same interpretation as in a GC, another possibility is that these stars are bound to the system, but the King profile is not enough to completely describe the density profile. Ultimately, it remained unclear whether these stars were bound or unbound to the galaxy.

Better observations with more sensitive CCD photometry revealed that this "excess" population extends to much larger radii than previously seen (Kuhn et al., 1996; Palma et al., 2003; Westfall et al., 2006; Muñoz et al., 2005, 2006; Sohn et al., 2007). The higher quality of the data also allowed to define a better empirical density profile for dSphs. The excess population is well fitted by an exponentially decaying curve (a "break" population), while the inner parts follow a King profile.

Also, spectroscopic observation determined that the excess stars are associated with the dSph, although it was still not clear if they were bound or unbound (Majewski et al., 2005;

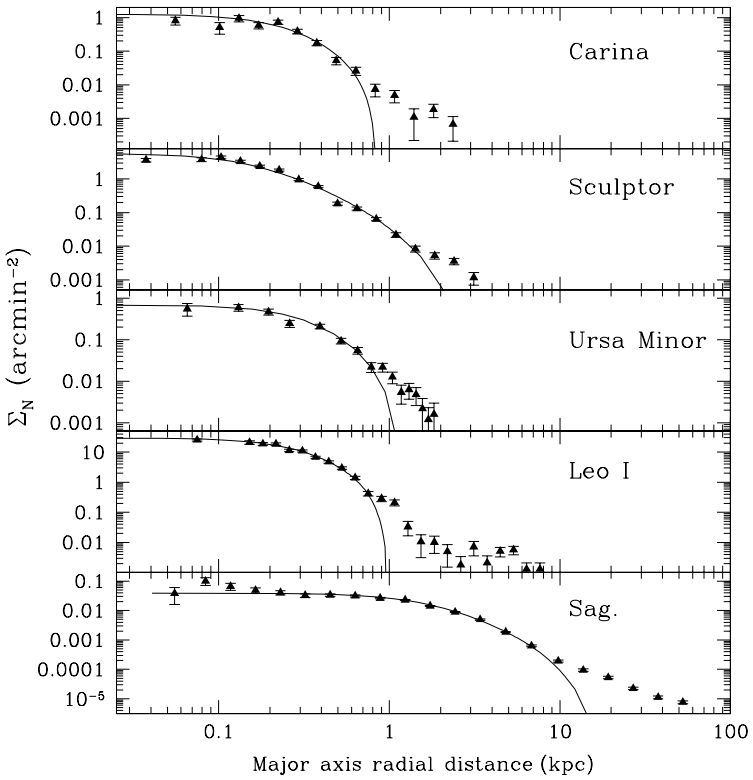

Figure 1.1: King profile (solid lines) fitted to the number density of stars (Σ_N) as a function of radial distance from the center of the dwarf galaxy (solid squares). The data come from the following references: Carina (Muñoz et al., 2006), Sculptor (Westfall et al., 2006), Ursa Minor (Palma et al., 2003), Leo I (Sohn et al., 2007), Sagittarius (Majewski et al., 2003) (Credit of the figure: Steven R. Majewski).

Muñoz et al., 2005, 2006; Sohn et al., 2007). There were two possible explanations for this scenario. The first possibility is that the excess stars are an extended, bound halo population (e.g. Hayashi et al., 2003; Mashchenko et al., 2005; McConnachie et al., 2007), which requires that there is a large quantity of DM avoiding the disruption of the galaxy, given the low quantity of luminous mass (e.g. Moore, 1996). The DM would also need to be extended well beyond the limit of the excess population of stars (e.g. Peñarrubia et al., 2008a,b; Walker et al., 2007). The second possibility is that the extended population (or part of it) is truly extratidal, as a consequence of mass loss due to tidal stripping. Some iconic satellites where this phenomenon is already seen are the Palomar 5 GC (Odenkirchen et al., 2001, 2002, 2003, 2009; Rockosi et al., 2002; Grillmair & Dionatos, 2006) and the Sagittarius dSph (Majewski et al., 2003; Majewski, 2004; Martínez-Delgado et al., 2007; Casetti-Dinescu et al., 2008).

1.1.3 The ultra-faint dwarf galaxies

Until 2005, the only known dSphs members of the MW's satellite population were the classical dSphs. However, thanks to more sensitive observations, the number of satellite dSphs increased dramatically. The first wave of discoveries came after the data release of the SDSS when extremely low luminosities dwarf galaxies ($M_{\rm V} > -8$) were detected as overdensities of stars in the MW's outer halo (Willman et al., 2005a; Zucker et al., 2006a; Belokurov

et al., 2006a, 2007; Irwin et al., 2007; Belokurov et al., 2008, 2010; Walsh et al., 2007; Grillmair, 2009; Watkins et al., 2009). Given the low luminosities of these new dwarf galaxies, they were named ultra-faint dwarf (UFD) galaxies. More recently, the DES and other surveys contributed with a new set of UFDs, this time reaching absolute magnitudes as low as $M_{\rm V} = 0$ (Koposov et al., 2015; Bechtol et al., 2015; Drlica-Wagner et al., 2015; Martin et al., 2015; Kim & Jerjen, 2015; Kim et al., 2015a, 2016; Laevens et al., 2015a,b; Luque et al., 2016; Torrealba et al., 2016a,b, 2018; Homma et al., 2018). It is clear why these galaxies were not discovered until recently: their absolute magnitudes go from less than ~ 0 to less than -8, and their sizes can be less than 100 pc, which correspond to extremely low surface brightnesses (~ 28 mag arcsec^{-2} for the central surface brightness).

Further studies have revealed that UFDs have old populations, similar to dSphs. They also show high velocity dispersion, which suggests an enormous fraction of DM content if the system is in equilibrium. However, they also show distorted morphologies, which points to possible tidal stripping. These properties are typical of classical dSphs, so UFDs are sometimes referred to as an extension to low luminosities of dSphs.

The discovery of UFDs has brought new challenges for the study of MW's satellite population. First, establishing their photometric and structural parameters is especially difficult, because it has been shown that the low number of member stars that compose these systems introduces uncertainty in the measurements, due to low number statistics (Martin et al., 2008; Muñoz et al., 2008). Therefore, the distorted morphologies may not be an intrinsic feature. Second, the extremely low luminosities and compact size of UFDs are similar to those of extended GCs, so in general, it is difficult to differentiate one from the other just by using photometric information. Because of this, many of the newly discovered satellites are still not classified as either GC or UFD.

1.1.4 Dark Matter content in dwarf spheroidal galaxies

As we mentioned before, one possible explanation for the existence of the "excess" star population in the outskirts of dSphs is that these galaxies are embedded in extended DM halos. To check this statement, one must quantify both the stellar and the total mass and compare them. If the total mass is larger than the stellar mass, then there is an unseen matter, which would correspond to DM. The mass-to-light ratio is the value used to quantify the proportion of both types of matter. By definition, the mass-to-light ratio is the total mass of a system expressed as a ratio to the mass it would have if all its luminosity were emitted by stars of a solar mass.

The only way to measure the total mass of a system like dwarf spheroidal galaxies is by dynamical information. Rood et al. (1972) derived a formula for estimating the central mass-to-light ratio of the Coma Cluster by fitting a density distribution to it, using only observed quantities. This approach assumes a spherical, isotropic, and constant mass-to-light ratio system. The resulting formula is

$$\frac{M_{\rm tot}}{L} = \eta \frac{9\sigma_{\rm p}^2(0)}{2\pi G I(0) r_{\rm c}} \tag{1.3}$$

where $M_{\rm tot}$ is the total mass of the system, L is the luminosity, $\sigma_{\rm p}(0)$ is central the velocity dispersion projected on the line-of-sight, $I(0)$ is the central surface brightness, $r_{\rm c}$ is the half-light radius, and η is a parameter that depends on the model used to fit the density distribution.

These assumptions for the dynamical system can also be applied to dwarf spheroidal galaxies, where the member stars are used to calculate the velocity dispersion and the density distribution. The first measurement for the mass-to-light ratio of a classical dSphs (the Draco dwarf galaxy) came from Aaronson (1983), who obtained a value of $M{\rm tot}/L \sim 31$, much larger than the typical value of $M_{\rm tot}/L \sim 1-5$ for dEs. Later studies for other classical dSphs (Armandroff & Da Costa, 1986; Mateo et al., 1991, 1993, 2008; Wilkinson et al., 2004; Walker et al., 2007, 2009a,c) showed that these galaxies have a high velocity dispersion, corresponding to high mass-to-light ratios ($M_{\rm tot}/L$ between 5 and 100; see Figure 1.2).

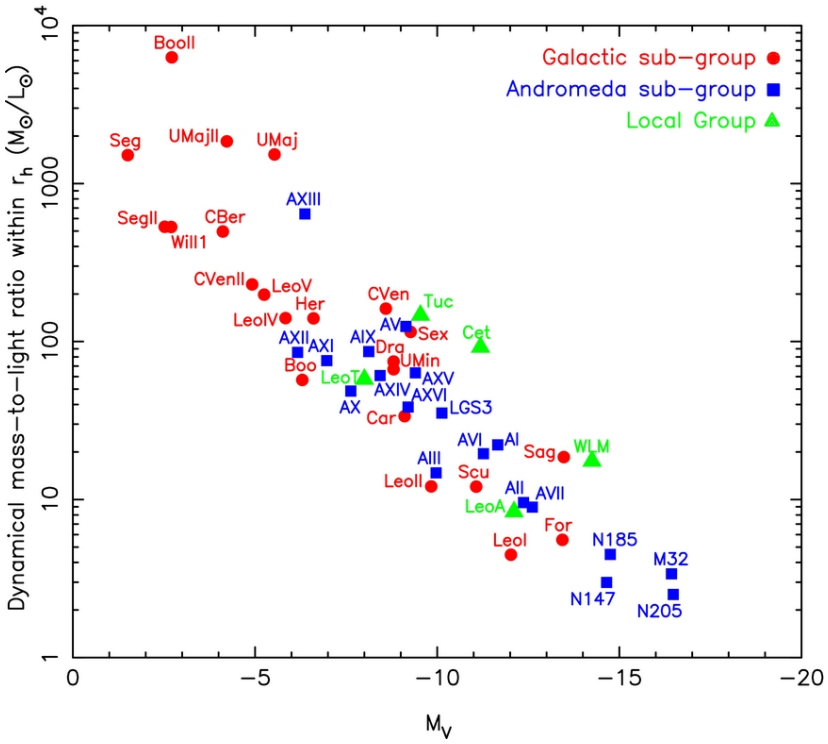

Figure 1.2: Dynamical mass-to-light ratio versus absolute magnitude for MW's dwarf galaxy satellites, Andromeda galaxy's satellites and other Local Group galaxies. Figure from McConnachie (2012).

One interesting aspect of classical dSphs is that DM content is not random: there is a strong correlation between the mass-to-light ratio and the absolute magnitude $M_{\rm V}$, where fainter galaxies have a higher mass-to-light ratio (e.g. Vogt et al., 1995; Mateo, 1998). The studies of DM on UFDs have confirmed that this trend extends to the faint end of dSphs galaxies. Simon & Geha (2007) presented spectroscopic data of stars in eight UFDs and calculated their mass-to-light ratio. They showed that it extends to the order 10^3 for the faintest UFD that was known at the time (see Figure 1.10 of Simon & Geha (2007)). More recent studies, including recently discovered UFDs (Geha et al., 2009; Simon et al., 2011; McConnachie, 2012; Simon et al., 2015; Kirby et al., 2015b; Kim et al., 2016), have confirmed

that these faint dwarf galaxies are the most DM dominated objects in the Universe. Figure 1.2, taken from McConnachie (2012), shows this trend. Their high fraction of DM has made them targets for the direct detection of the annihilation of DM particles (e.g. Albert et al., 2017; Archambault et al., 2017).

The fact that dSph galaxies are embedded in DM halos has had consequences for current models of galactic hierarchical accretion. In a Cold Dark Matter (CDM) scenario, simulations of galactic formation predict that large DM halos (such as that where the MW is embedded) should be populated by smaller DM subhalos, that are essentially a miniature replication of their larger DM host (Kauffmann et al., 1993; Klypin et al., 1999a). In this context, dSphs satellites are the observable evidence of those DM subhalos that formed stars and were accreted by the MW. However, soon a problem arose: simulations showed that there were thousands of subhalos capable (in principle) of forming stars surrounding the MW's DM halo, but observations revealed just a few classical dSph galaxies at that time (Klypin et al., 1999b; Moore et al., 1999). The discovery of UFDs helped to alleviate the problem by matching some of the simulated subhalos with low-luminosity, low-mass dSphs, but hundreds of the simulated subhalos remained without an observable counterpart (Simon & Geha, 2007). This incongruence was named "the missing satellite problem".

Some explanations have been proposed to solve this problem. First, considering that only a portion of the sky has been scanned looking for satellite galaxies, future surveys may increase the number of known satellites to the hundreds (Tollerud et al., 2008). Currently, the number of known dwarf galaxy satellites is around 50 (Drlica-Wagner et al., 2015). Second, it has been shown that reionization from UV radiation coming from distant galaxies and supernova feedback can suppress gas accretion for DM halos of mass below $10^9\,M_\odot$ (e.g. Efstathiou, 1992; Bullock et al., 2000; Kravtsov & Yepes, 2000; Benson et al., 2002; Bovill & Ricotti, 2009; Sawala et al., 2016), and that atomic cooling does not occur on subhalos with masses below $10^8\,M_\odot$ (e.g. Rees & Ostriker, 1977). Both masses are in the regime of UFD galaxies ($M_{\rm tot} \lesssim 10^9\,M_\odot$). These processes suggest that there is a population of satellite DM subhalos that never produced any star. With this in mind, it is now accepted that simulations are consistent with observations and that the missing satellite problem is solved.

Models of very extended DM halos in dSph galaxies can explain their velocity dispersion radial profiles, characterized by flat or rising curves at large radii. This produces rising mass-to-light ratios with radius and a large total mass for the dwarf galaxy (e.g. Walker et al., 2007; Kleyna et al., 2002; Łokas et al., 2005; Mashchenko et al., 2005; Koch et al., 2007). However, the one caveat is that all formulas to calculate the total dynamical mass assume that the system is in dynamical equilibrium. As an alternative, models of tidally disrupting galaxies can also explain those flat or rising velocity dispersion profiles, because stars that are being tidally stripped inflate the velocity dispersion (e.g. Piatek & Pryor, 1995; Kroupa, 1997; Kleyna et al., 1999; Mayer et al., 2001; Sohn et al., 2007; Muñoz et al., 2008). Therefore, it is necessary to assess to what extent classical dSph and UFD galaxies are being affected by a tidal disruption, to correctly determine if the high velocity dispersions observed in them are due to a large, massive DM halo, or a consequence of escaping stars due to the tidal pull of the MW.

To answer this question, Sohn et al. (2007) and Muñoz et al. (2008) modeled the evo-

lution of two dSphs (Leo I and Carina, respectively) assuming both DM content and tidal disruption, as the dwarf galaxies orbit around the MW. It was known that Carina and Leo I suffered from considerable tidal disruption. In the simulations, they used a large coverage of parameter spaces (masses, size, densities and orbital eccentricities). They found that assuming a mass-follow-light model for each galaxy (i.e., baryonic and DM follow each other's distribution), a combination of DM content and tidal disruption could simultaneously match the observed density laws, velocity profiles, velocity dispersion profiles, the large central mass-to-light ratios, and the signature of tidal disruption for each galaxy (tidal tails for Carina and asymmetric velocity distribution for Leo I). In conclusion, they showed that tidal disruption can be a viable alternative explanation to the extended DM halo model to explain the observed properties of at least some of the MW's satellite dSphs.

1.1.5 Globular clusters

The other important constituent of MW's satellite objects is GCs. These objects are typically characterized by having old stellar populations ($\sim 10^{10}$ years old), which makes them relics of the formation of the MW. They are composed of hundreds of thousands of stars and are very compact (half-light radius of ~ 10 pc), so they can be detected and their stellar population resolved up to large distances (more than 100 kpc from the galactic center). Thus, we can obtain detailed information about their properties (distances, abundances, and ages) and, in consequence, about the history of the MW.

There are notable examples of the usefulness of studying GCs to understand the formation and evolution of the MW. Shapley (1918) considered the distribution of the majority of GCs in a halo around the galactic center to measure the position of the Sun relative to that point and showed that the MW was much larger than previously thought. Many decades later, Searle & Zinn (1978) showed that there was no correlation between the metallicity and the Galactocentric distance ($R_{\rm gc}$) for GCs in the halo beyond $R_{\rm gc} = 8$ kpc, proposing that a model of hierarchical growth for the MW, where the outer halo formed from the stellar contributions of many protogalaxies, was consistent with this observation.

Currently, approximately 150 known GCs are orbiting around the MW. Different studies have shown that GCs are a heterogeneous group. One of the most important aspects discovered by these works is that GCs could be divided in a metal-rich group ([Fe/H] > -0.8), located in the bulge and disk of the Galaxy and characterized by a red photometric color; and a metal-poor group ([Fe/H] < -0.8), found in the MW's halo and having a blue photometric color (Zinn, 1985; Armandroff, 1989). Later, Lee et al. (1994) showed that inner halo GCs follow a tight relationship between [Fe/H] and the Horizontal Branch (HB) index (a measure of how "red" or "blue" is the HB of the cluster), with blue (red) HB corresponding to low (high) metallicities. However, they found that for outer halo GCs and a given metallicity, a fixed HB index would indicate a much redder color than the corresponding for that metallicity. The authors interpreted this as the age of the cluster is the "second parameter" driving its HB morphology. In this scheme, for a fixed metallicity, a blue HB index corresponds to an older cluster than one with a redder HB index.

Using the previous information, Zinn (1993) showed that the GC population can be cleanly divided into three groups, using the [Fe/H] and HB index parameter space: the Bulge/Disk

(BD) group, where clusters show a red HB and [Fe/H] > -0.8 and are located in the disk and bulge of the MW; the Old Halo (OH) group, made up by GCs in the halo with [Fe/H] < -0.8 and with blue HB index for a given metallicity; and the Young Halo (YH) group, constituted by halo GCs with [Fe/H] < -0.8 and red HB index for a given metallicity. The differences between OH and YH clusters are that the firsts are older than the former (as the group names suggest) and the kinematics of the OH clusters show some rotation and small line-of-sight velocity dispersion, while the YH clusters show almost no rotation and a relatively high line-of-sight dispersion.

Perhaps the most important part of the Zinn (1993) paper is the conclusion about the origin of the GCs in each group. He concluded that the observed properties of BD and the majority of OH clusters are consistent with GCs being formed in-situ during the collapse of the primordial cloud that formed the bulge and disk of the MW, in a similar process described by Eggen et al. (1962). In contrast, the YH and a small part of OH clusters seem to form in external dwarf galaxies that were later accreted by the MW, whose tidal force took these GCs from their original hosts and captured them in the MW's potential. This is a consequence of the hierarchical growth mechanism of the MW described by Searle & Zinn (1978).

One way to test the idea that YH clusters formed externally, is to compare their properties to GCs that belong or belonged to satellite dwarf galaxies. Mackey & Gilmore (2004b) made uniform measurements of HB indexes, metallicity and structural parameters for GCs in the Large Magellanic Cloud (LMC), the Small Magellanic Cloud (SMC), the Fornax and the Sagittarius dSph galaxies. With these data, they showed that several GCs in the MW have similar properties than external clusters. First, they put the external clusters in a metallicity versus HB index plot (like the one used by Zinn (1993) to create the BD/OH/YH classification) and found that they are essentially indistinguishable from the YH clusters, although $20 - 30$ percent of OH clusters also have characteristics of external GCs. Second, they used the clusters' core radii to show that BD and OH groups are dominated by compact clusters, while the YH group is mainly composed of extended ones. When comparing the YH halo core radii distribution with the one for the external clusters, it is revealed that both distributions closely match. Third, they propose that the OH group is made up of a mix of BD-like and YH-like clusters, with $\sim 83 - 85$ percent of the objects having BD properties, while the $\sim 15 - 17$ percent is more similar to YH clusters. All this evidence supports the hypothesis that the YH clusters and a small fraction of the OH clusters come from external dwarf galaxies that were accreted by the MW.

Apart from their origin, several properties can be used to distinguish YH clusters from BD and OH ones. It has been shown that YH-type clusters typically reside at much larger Galactocentric distances than do BD and OH clusters, although the YH group also extends to the central part of the galaxy (Zinn, 1993; van den Bergh, 1993; Mackey & Gilmore, 2004b). Additionally, Mackey & van den Bergh (2005) show that the BD and OH groups have fewer extended clusters, fewer low luminosity clusters, and fewer low surface brightness clusters than the YH group. They attribute this to the fact that YH clusters have been affected by weaker tidal forces and have not suffered from disk and bulge shocks, which has allowed for the survival of extended, low luminosity, low surface brightness clusters in this group. Another interesting aspect is the ellipticity of clusters in different groups. Mackey

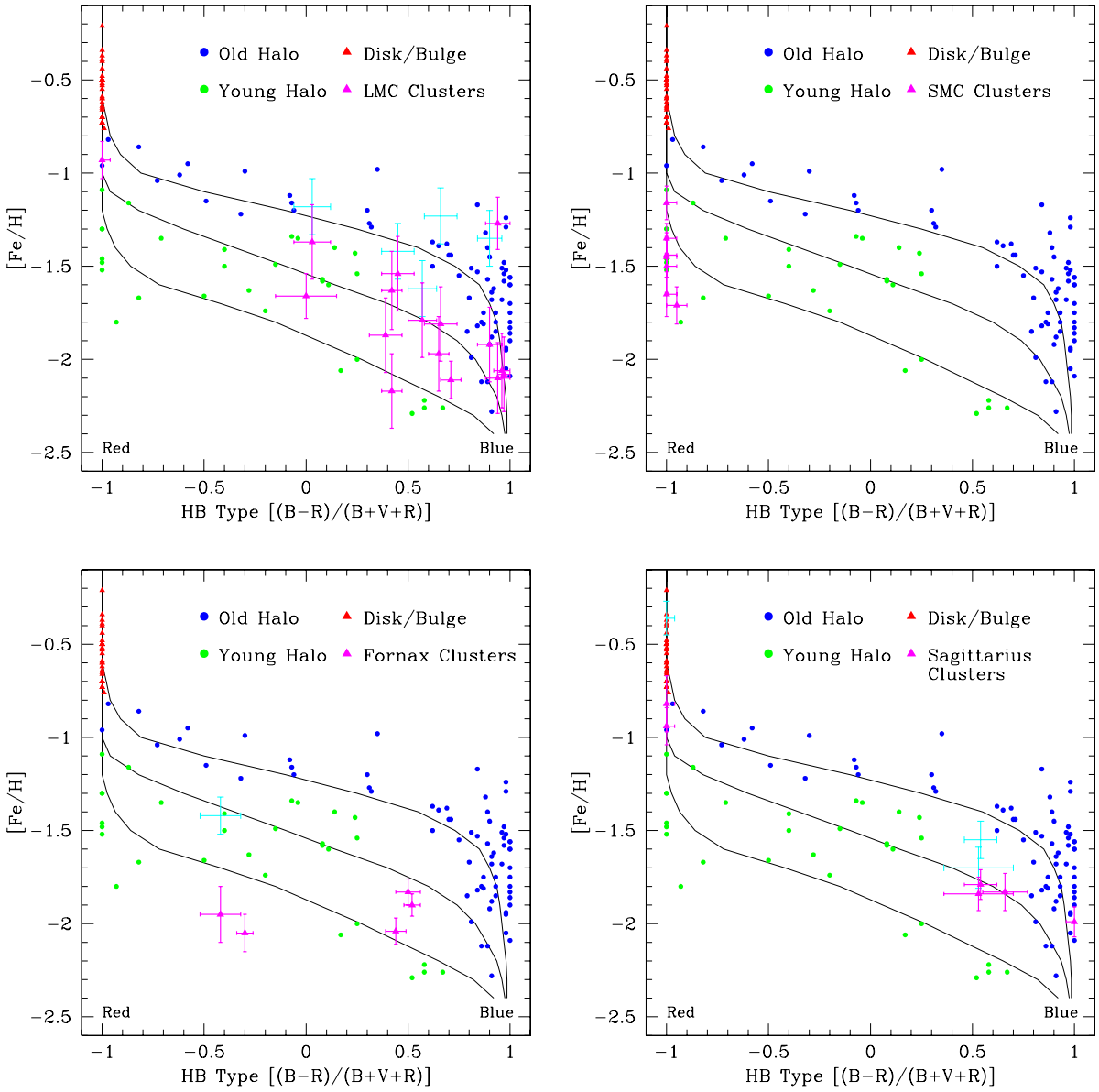

Figure 1.3: Metallicity ([Fe/H]) versus HB type for Galactic and external GCs. For Galactic clusters, the different classifications are distinguished according to the colors in the legend. In each panel, the external clusters of a dwarf galaxy (LMC, SMC, Fornax, and Sagittarius) are plotted. Each cyan point represents an alternative measurement of higher metallicity for an external cluster, with respect to the magenta point directly beneath it. Figure form Mackey & Gilmore (2004b).

& van den Bergh (2005) found that YH clusters have somewhat lower ellipticities than BD and OH objects. This is in contrast to the proposition that clusters in strong tidal fields (like BD and OH objects) should have lower ellipticities than objects present in the outer halo (typical of YH clusters) because strong tidal fields are more effective in reducing the triaxiality (Goodwin, 1997). The discovery of very low surface brightness GCs with a high ellipticity (e.g. Willman et al., 2005b) is also at odds with the results of Mackey & van den Bergh (2005). Overall, the fact that outer halo GCs have higher ellipticities than inner GCs

remains unclear.

It is clear that the MW's GC population is a heterogeneous group. In particular, evidence shows that GCs of the MW's outer halo played (and are still playing) and important role in the formation and evolution of the Galaxy. Therefore, it is of great importance to study them with as much detail as possible, in order to understand the processes that lead to the MW as we observe it today.

1.1.6 The classification of satellite objects

Satellite objects of the MW (dSphs, UFDs, and GCs) are an important source of information that is worth studying because, as we have seen, they are the relics of the process of hierarchical formation of our Galaxy. To fully understand these objects and have a scheme for classifying them, it is necessary to analyze their differences and similarities.

Traditionally, to know if an object was a GC or a dwarf galaxy, it was enough to see its properties in a luminosity versus size plot. The first to use one of these plots was Kormendy (1985) when he compared the properties of GCs, elliptical galaxies, dwarf elliptical galaxies, galactic bulges, and dwarf spheroidal plus irregular galaxies. He found that there was a clean separation between dwarf galaxies and GCs, with clusters being less luminous and much smaller than dwarf galaxies. However, the discovery of UFD galaxies altered this simple scheme of classification. McConnachie (2012) compiled all the parameters available for dSphs and newly discovered UFDs and, together with the GCs data of Harris (1996, 2010 edition), offered a new version of the luminosity versus size plot. This time, it was evident that the new UFD galaxies, less luminous and of smaller half-light radii than classical dSphs, started to close the gap between dwarf galaxies and GCs, adding confusion to the classification of an object that fell in that area. Figure 1.4 shows the most recent absolute magnitude versus half-light radius plot for Local Group galaxies and GCs.

Having a good classification scheme for satellite objects based on physical properties is of extreme importance because it determines how confident we are about the conclusions we make from studies that involve those objects. Motivated by this, Willman & Strader (2012) proposed a definition for "galaxy", which is free of assumptions from a physical model. From their paper:

A galaxy is a gravitationally bound collection of stars whose properties cannot be explained by a combination of baryons and Newton's laws of gravity.

At present, the most accepted model to explain the properties of a galaxy (based on the previous definition) is that they are dominated by a DM halo, in addition to the mass in the form of baryons.

With this definition of "galaxy", what remains is to develop the diagnostics that allow for the use of observational properties of objects to distinguish them between a galaxy and GC. These diagnostics were developed to assess the amount of DM present in the object to be classified, but they could be used to support any of the alternative models.

The first diagnostic used in literature is stellar kinematics. By measuring the individual

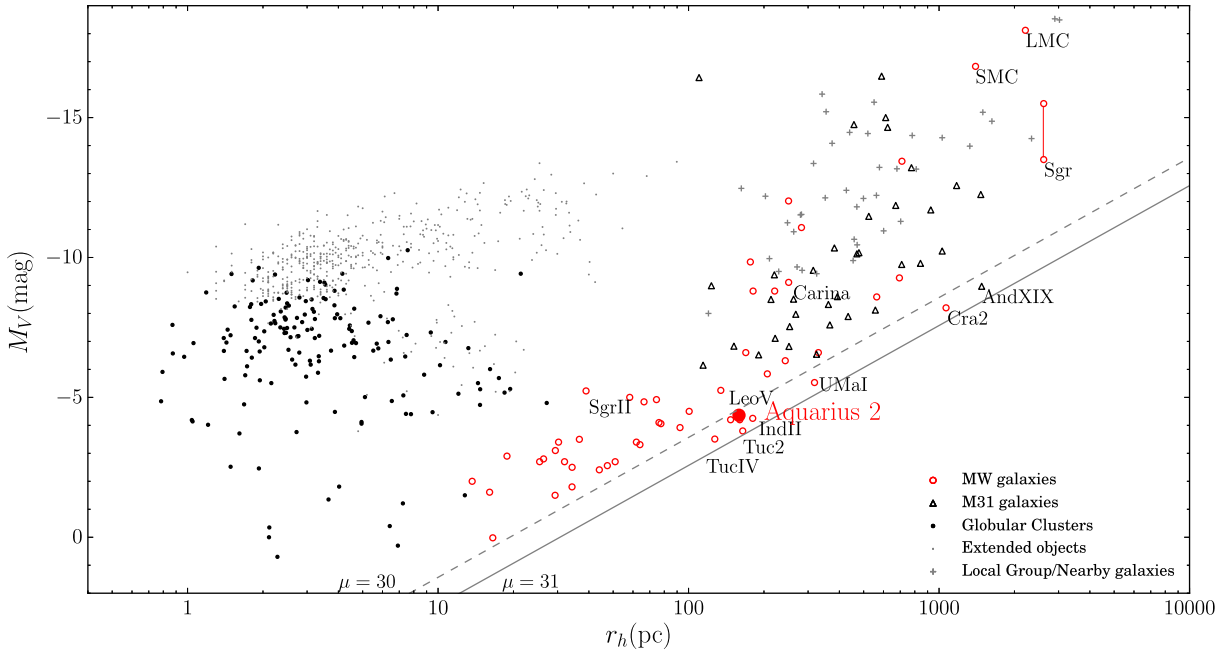

Figure 1.4: Absolute magnitude versus half-light radius plot from Torrealba et al. (2016b). It includes the most recent discoveries of GCs and UFD galaxies and shows that the traditional gap between clusters and dwarf galaxies is closing, mixing them and making it difficult to classify newly discovered objects using only photometric information. Some notable objects and recent discoveries are tagged by name. Dashed and solid lines are the constant surface brightness levels within a half-light radius of 30 and 31 mag arcsec^{-2}, respectively. These levels correspond to the detectability limits of resolved stellar systems in SDSS (Koposov et al., 2008).

stellar velocities, one can determine the line-of-sight velocity dispersion and use the Wolf et al. (2010) formula to determine the dynamical mass enclosed by the three-dimensional deprojected half-light radius on a dispersion-supported galaxy,

$$M_{\rm half} = 4{\rm G}^{-1}\langle\sigma^2_{\rm los}\rangle r_{\rm half} \tag{1.4}$$

where $M_{\rm half}$ is the total mass enclosed by the three-dimensional deprojected half-light radius, $\langle\sigma^2_{\rm los}\rangle$ is the luminosity-weighted square of the line-of-sight velocity dispersion, and $r_{\rm half}$ is the two-dimensional projected half-light radius. Using this method and this formula, it has been shown that for classical dSphs, the mass-to-light ratio within their half-light radii ranges from ~ 6 to ~ 100, and from ~ 100 to ~ 3000 for UFDs (see Figure 1.2), making the latter the most DM-dominated objects known in the universe. In the case of GCs, they have values consistent with no DM content, with typical values for the mass-to-light ratio of ~ 1 to ~ 4 (e.g., McLaughlin, 2000; Rejkuba et al., 2007; Baumgardt et al., 2009).

The second diagnostic is the metallicity spread, which allows constraining the potential well inside of which the object formed. This method is based on the idea that higher potentials can retain more metals. Supernovae of types II and Ia are known to produced iron, so a

higher [Fe/H] spread means that the object is embedded in a potential capable of retaining the supernova ejecta, so multiple star populations can be formed. This method has been used to support the galaxy classification of Segue 1 and Willman 1, which show a [Fe/H] spread of over 1 dex (Martin et al., 2007; Norris et al., 2010; Simon et al., 2011; Willman et al., 2011). Figure 1.5 shows the distribution of MW's dwarf galaxies and GCs in the [Fe/H] versus absolute magnitude space. It is evident that GCs occupy a different region than dwarf galaxies, and that those dwarf galaxies have a larger metallicity spread than GCs.

These two diagnostics have shown that the most important difference between GCs and dwarf galaxies is their DM content, which allows to classify them in each category. However, one of the downsides of these diagnostics is that they require spectroscopical observations, which can take a large amount of telescope time, especially in the case of low luminosity objects. Given that the evidence shows that DM is present in galaxies and not in GCs, it could be possible that DM leaves a photometric imprint that would allow developing a classification system that does not require spectroscopic data. In this thesis, I explore this possibility in Chapter 2.

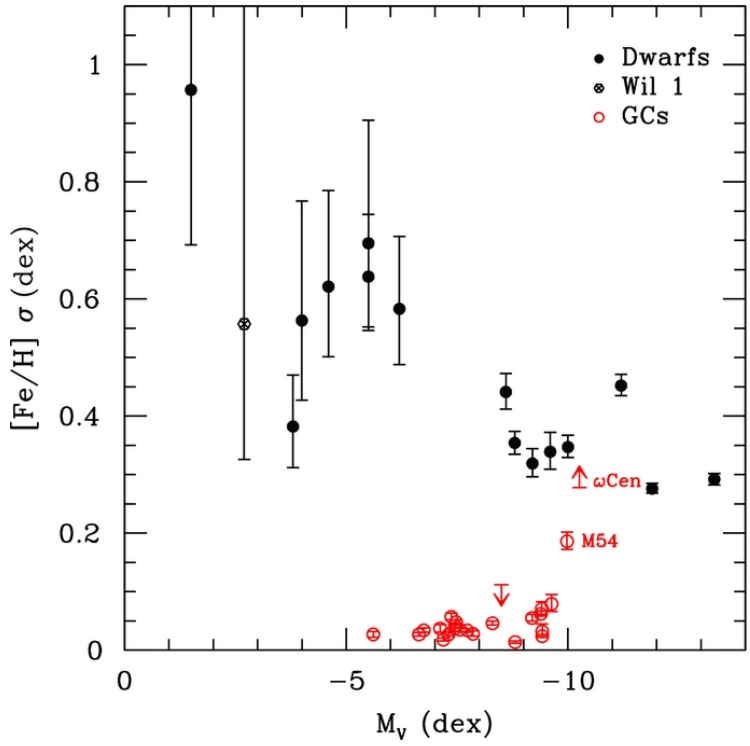

Figure 1.5: Dispersion in metallicity ([Fe/H] σ) versus absolute magnitude for MW's dwarf galaxies (black circles) and GCs (red circles). It shows that dwarf galaxies have a larger metallicity spread than GCs. Figure from Willman & Strader (2012).

1.1.7 Tidal effects on satellite objects

Outer halo satellite objects are subjected to the tidal effects of the MW's strong potential well. The gravitational pull from the MW's potential over individual stars of the satellite object can be strong enough to distort its morphology or kinematics, to the extent of removing stars from the objects' potential or even disrupting it completely. Simulations of hierarchical

galactic formation show that these phenomena are key ingredients during the formation process because they propose that stars stripped from outer halo satellites contributed to the outer halo stellar population. As we saw previously, the tidal pull from the MW is also responsible for the stripping of GCs from satellite dwarf galaxies and the later capture of them by the MW, contributing to the heterogeneity of the GC population (e.g. Mackey & Gilmore, 2004b; Marchi-Lasch et al., 2019).

Observations reveal that tidal stripping and disruption over satellite objects are processes that are still happening at present. The most important example of tidal disruption on satellite dwarf galaxies is the case of the Sagittarius dSph (Ibata et al., 1994), whose tidal disruption has left a long stream of orbits that goes around the MW in a polar orbit (e.g. Lynden-Bell & Lynden-Bell, 1995; Newberg et al., 2002; Majewski et al., 2003; Belokurov et al., 2006b). Also, the Canis Major dwarf galaxy is the progenitor of the Monoceros ring (e.g. Newberg et al., 2002; Momany et al., 2006). Several other satellite dwarf galaxies show an elongated and/or distorted shape, suggesting they are suffering from tidal disruption (e.g. Kuhn et al., 1996; Belokurov et al., 2006a; Martin et al., 2008; Sand et al., 2009). Regarding GCs, the most famous case of tidal disruption is that of Palomar 5, which is the progenitor of the Palomar 5 stream (e.g. Rockosi et al., 2002; Odenkirchen et al., 2003). In other words, Grillmair & Johnson (2006) discovered a stellar stream originating from the cluster NGC 5466 and Chen & Chen (2010) presented the shape and sizes of 116 Galactic GCs and showed that several of the halo GCs have an elongated shape. More recently, Carballo-Bello et al. (2018) gave evidence for tidal tails around some Galactic GCs. Additionally to the observations that confirm ongoing tidal effects over MW's satellites, there is evidence of stellar streams that do not have any known progenitor associated with them (Helmi et al., 1999; Duffau et al., 2006; Grillmair, 2009; Newberg et al., 2009, 2010; Vickers et al., 2016). These streams are thought to be the stripped stars of completely disrupted dwarf galaxies or GCs and their existence supports the idea that the accretion of stellar substructures played a major role in forming the Galactic halo.

Considering the evidence, knowing the full extent of tidal effects on MW's satellite objects is of extreme importance to completely understand the processes of hierarchical accretion that formed our Galaxy and, in particular, built its stellar halo. Also, tidal effects play a major role in the formation and evolution of satellite dwarf galaxies and GCs. For dSph and UFD galaxies, Muñoz et al. (2008) created a library of simulated dSphs evolving inside DM halos and subjected to tidal forces from the MW's potential. They showed that a combination of DM halos plus tidal forces can reproduce the properties of dSphs, offering an alternative to the extended DM halo scenario previously accepted. More recently, Hammer et al. (2018) showed that there is a strong direct correlation between the total-to-stellar mass ratio and the ratio of the MW to dSph gravitational acceleration, suggesting that the line-of-sight velocity dispersion is induced by the Galactic gravitational acceleration. For GCs, it has been shown that the tidal field intensity in which a cluster formed and evolved has an impact on the cluster properties (e.g. Renaud et al., 2017).

To better estimate how common and intense the tidal effects are on satellite objects, deep and wide observations are necessary. One of the results of Muñoz et al. (2008) is that in most cases the imprints of tidal effects on the morphology of an object are only detectable at large radii and deep observations. The data used in this thesis have such characteristics.

In Chapter 3 we analyze the morphology of satellite dSphs, UFDs and outer halo GCs, to detect signatures of tidal effects.

1.2 The data

The dataset used in this work is composed of observations of 57 satellite objects of the MW, which includes GCs, classical dSphs, UFDs, and several objects not yet classified (i.e., their structural properties neither allow for a clear differentiation nor are their DM content or metallicity spread known). The classification for each object is based on information in the literature.

Observations of 44 of these objects were carried out using the MegaCam imager on the Canada-France-Hawaii Telescope (CFHT) in the northern hemisphere and the MegaCam imager on the Magellan II–Clay Telescope at Las Campanas Observatory in the southern hemisphere. The data for the remaining 13 objects were obtained from different sources, most of them from public data from the DES Year Release 1 (see Muñoz et al., 2018a, for details).

Muñoz et al. (2018a) described the data reduction, astrometry, point-source photometry, and photometric calibration performed on the whole sample to obtain a homogeneous dataset. To select the targets, no constrains on morphology or classification were used because, as we discussed before, clear-cut classification of satellites, especially between UFDs and GCs, is not possible. The criterion for selecting targets is based on the Galactocentric distance $R_{\rm GC}$. All objects located farther than $R_{\rm GC} = 25$ kpc are selected. Muñoz et al. (2018a) adopted this value for the inner limit of the MW's outer halo because stars inside this radius have higher metallicities and different kinematics than the ones located in the outer parts (e.g. Carollo et al., 2007, 2010). The outer limit for the selection area is given by the farthest object that is considered a member of the MW satellite system (e.g. Mateo, 1998; McConnachie, 2012). The farthest members are the Leo T, Leo I and Leo II dwarf galaxies, which are located at $D_\odot \approx 417$, 200 and 233 kpc, respectively. This places the limit of the selection area near the virial radius of the MW, which is between 200 and 300 kpc (e.g. Klypin et al., 2002; Dehnen et al., 2006; Xue et al., 2008).

The selection criterion was used to target objects during the MegaCam survey and to include observations from other programs. The Triangulum II satellite was discovered using Pan-STARRS observations (Laevens et al., 2015a), while the Crater satellite object was independently detected by both Pan-STARRS (Laevens et al., 2014) and VST/ATLAS (Belokurov et al., 2014) observations. Additional discoveries came from SDSS images: Balbinot 1 (Balbinot et al., 2013) and Pegasus 3 (Kim et al., 2015a). The majority of the discoveries of satellites not known during the MegaCam survey were possible thanks to DECam (Flaugher et al., 2015) on the Blanco telescope at Cerro Tololo Observatory. Seven new stellar systems – Eridanus 3, Horologium I, Reticulum II, Eridanus II, Pictoris I, Tucana 2, and Phoenix 2 – appeared in searches made by Koposov et al. (2015) and the DES Collaboration (Drlica-Wagner et al., 2015), using public data from the Dark Energy Survey (DES Diehl & Dark Energy Survey Collaboration, 2014). An additional satellite (Grus I) was found in DES images by Koposov et al. (2015) and Indus 1 was discovered in DECam images from the *Stromlo Milky Way Satellite Survey* by Kim et al. (2015b). Finally, two more objects were found in

DECam images: Horologium II by Kim & Jerjen (2015) from DES Y1A1 public data, and Hydra II by Martin et al. (2015) from their DECam Survey of the MAgellanic Stellar History (SMASH).

The MegaCam survey was designed to obtain reliable, high-quality estimates for the photometric and structural parameters of satellite objects of the MW. One requirement for this is to have deep observations. The MegaCam imaging is ~ 2.2 mag deeper than SDSS observations and, on average, the MegaCam photometry reaches ~ 2 mag below the main-sequence turnoff in the program objects. Another advantage of the MegaCam survey is its wide coverage, given by the CFHT-MegaCam $0.96^\circ \times 0.94^\circ$ field of view and the Clay-MegaCam $0.4^\circ \times 0.4^\circ$ field of view. Finally, the MegaCam observations are characterized by having a smaller FWHM than SDSS, with typical values of $0.8''$ and $0.9''$ for CFHT-MegaCam and Clay-MegaCam, respectively, significantly better than the $1.4''$ value of SDSS.

The techniques used to measure the photometric and structural parameters are described in detail in Muñoz et al. (2018b). As a first step, some of the parameters were calculated by a maximum likelihood approach (Martin et al., 2008) that was applied to the observations of every object, assuming a Sérsic density profile (Sersic, 1968). The density profile to be fitted has the form,

$$\Sigma(r) = \Sigma_{0,\mathrm{S}} \exp\left[-b_n \left(\frac{r}{r_\mathrm{e}}\right)^{1/n}\right] + \Sigma_\mathrm{bkg} \tag{1.5}$$

where $\Sigma(r)$ is the stellar density for any given radius r, $\Sigma_{0,\mathrm{S}}$ is the Sérsic central stellar density, n is the Sérsic index, r_e is the effective radius (the radius at which the cumulative luminosity is half the total luminosity), b_n is approximated by $1.999n - 0.327$ (Capaccioli, 1989; Caon et al., 1990), and Σ_bkg is the background stellar density, which is composed by foreground Galactic stars and unresolved field galaxies.

The Sérsic profile has proven to be a good fit for the brightness profiles of different types of galaxies. Its flexibility lies in the parameter n, known as the Sérsic index, which controls the degree of curvature of the profile. For elliptical galaxies, $n = 4$ offers the best fit, and the Sérsic profile becomes the well known de Vaucouleurs profile; for spiral galaxies, the bulge is also well modeled by a $n = 4$ Sérsic profile, while its disc profile can be matched by an exponential profile ($n = 1$). It has also been shown that low-mass dSph-like galaxies, like the ones that populate the Galactic outer halo, can be well described by a Sérsic profile (e.g. Jerjen & Binggeli, 1997; Graham & Guzmán, 2003; Graham et al., 2003; Ferrarese et al., 2006; Côté et al., 2007). Another important feature of the sérsic profile is that the n parameter is a proxy for the central concentration of light, where high values of n indicate a higher central concentration of light than a lower n (Trujillo et al., 2001).

To better constrain the free parameters in Equation 1.5, Muñoz et al. (2012b) showed that it is not only necessary to have a large enough number of satellite stars, but also a large contrast between the density of stars in the central part of the satellite and the background density. Taking advantage that the sources on the images are completely resolved, even in crowded fields (except in the central parts of some GCs) Muñoz et al. (2018b) used

DAOPHOT morphological classification indices χ and *sharp* (Stetson, 1994) to classify point sources as stars or background galaxies. DAOPHOT allows for the calculation of the point-source function (PSF) of the image from a set of reference stars. This model PSF is then fitted to each source in the image to describe its brightness profile. χ describes how well the model PSF fits the source's brightness profile, while *sharp* indicates how sharp is the distribution. The range of values that correspond to stellar sources ($\chi < 3$ and $-0.5 <$ sharp < 0.5). To determine the satellite's member stars, for every object a Color-Magnitude Diagram was constructed and only stars close to the following regions were selected: the main sequence, the main sequence turn off, red giant branch, horizontal branch, and/or red clump. To calculate the total luminosity L, the individual fluxes from each star down to a specified magnitude threshold are summed. Then, a theoretical luminosity function is fitted to the data to obtain the fraction of stars over the magnitude threshold. After that, the theoretical luminosity function is integrated and this value is compared to the total flux of the stars above the threshold to correct for the flux from the stars below it. Finally, to calculated the central surface brightness, the parameters obtained from fitting equation 1.5 to the observed satellite's density profile are used in the following equation,

$$I_0 = L/[2\pi r_{\rm e}^2 n\Gamma(2n)(1-\varepsilon)] \tag{1.6}$$

where I_0 is the central surface brightness in physical units ($L_\odot\,{\rm pc}^{-2}$), ε is the satellite's ellipticity, and Γ is the gamma function. Then, the central surface brightness in units of mag arcsec^{-2}, μ_0, is calculated by

$$\mu_0 = M_\odot + 21.572 - 2.5\log I_0 \tag{1.7}$$

and the effective surface brightness $\mu_{\rm e}$ for the Sérsic profile is given by

$$\mu_{\rm e} = \mu_0 + 1.086 b_n \tag{1.8}$$

It is important to mention that, although our observations come from different instruments and full photometric homogeneity is not possible, as described in Muñoz et al. (2018a), care was taken to make the dataset as homogeneous as possible: the MegaCam imagers used to create the primary catalog are similar in structure and performance, the same bands were used for all 57 objects, the same reduction pipeline and techniques were used for all objects, and the spatial coverage for every object in our dataset is comparable (at least five effective radii), with only a few exceptions.

The photometric and structural parameters of all the satellite objects used in this work are presented in Table 1.1.

Table 1.1: Outer halo object parameters used in this work

Object	Type	M_V	$\mu_{V,0}$ (mag/$''^2$)	$\mu_{V,e}$ (mag/$''^2$)	R_e (pc)	n	ε
AM 1	Outer Halo GC	-5.02 ± 0.26	$23.19^{+0.39}_{-0.40}$	$25.18^{+0.39}_{-0.40}$	16.50 ± 1.08	1.08 ± 0.13	0.16 ± 0.06
AM 4	Outer Halo GC	-0.89 ± 0.81	$24.74^{+1.18}_{-1.25}$	$27.51^{+1.18}_{-1.25}$	7.34 ± 1.35	1.44 ± 0.33	0.29 ± 0.14
Balbinot 1	Outer Halo GC	-1.21 ± 0.89	$24.38^{+1.16}_{-1.20}$	$27.24^{+1.16}_{-1.20}$	7.79 ± 1.02	1.48 ± 0.23	0.35 ± 0.10
Bootes I	UFD	-6.00 ± 0.25	28.40 ± 0.31	29.43 ± 0.31	216.18 ± 5.18	0.64 ± 0.03	0.25 ± 0.02
Bootes II	UFD	-2.92 ± 0.74	$27.56^{+1.04}_{-1.08}$	$28.75^{+1.04}_{-1.08}$	37.26 ± 5.50	0.71 ± 0.43	0.24 ± 0.12
CVn I	UFD	-8.48 ± 0.13	27.10 ± 0.19	28.44 ± 0.19	486.38 ± 14.59	0.78 ± 0.04	0.46 ± 0.02
CVn II	UFD	-4.85 ± 0.36	$26.83^{+0.67}_{-0.72}$	$27.76^{+0.67}_{-0.72}$	70.28 ± 10.70	0.59 ± 0.49	0.46 ± 0.11
Carina	dSph	-9.42 ± 0.05	25.27 ± 0.07	26.74 ± 0.07	312.76 ± 3.36	0.84 ± 0.02	0.37 ± 0.01
ComBer	UFD	-4.36 ± 0.25	$26.99^{+0.36}_{-0.37}$	$28.66^{+0.36}_{-0.37}$	72.06 ± 3.84	0.93 ± 0.12	0.37 ± 0.05
Draco	dSph	-8.70 ± 0.05	25.01 ± 0.07	26.74 ± 0.07	207.15 ± 1.99	0.96 ± 0.02	0.30 ± 0.01
Eridanus	Outer Halo GC	-4.92 ± 0.26	23.24 ± 0.40	25.45 ± 0.40	16.77 ± 1.05	1.18 ± 0.14	0.09 ± 0.04
Eridanus II	UFD	-7.19 ± 0.09	$26.64^{+0.29}_{-0.31}$	$27.96^{+0.29}_{-0.31}$	200.07 ± 18.79	0.77 ± 0.19	0.37 ± 0.06
Eridanus III	Not classified	-7.19 ± 0.09	$18.01^{+1.36}_{-3.51}$	$21.22^{+1.36}_{-3.51}$	7.34 ± 5.82	1.64 ± 0.27	0.32 ± 0.13
Fornax	dSph	-13.45 ± 0.14	$23.60^{+0.16}_{-0.17}$	$24.79^{+0.16}_{-0.17}$	786.80 ± 8.55	0.71 ± 0.01	0.28 ± 0.01
Grus 1	UFD	-3.46 ± 0.59	$26.87^{+1.35}_{-1.76}$	$29.41^{+1.35}_{-1.76}$	72.61 ± 30.37	1.33 ± 0.31	0.54 ± 0.26
Hercules	UFD	-5.19 ± 0.45	$27.47^{+0.65}_{-0.67}$	$29.70^{+0.65}_{-0.67}$	230.00 ± 22.27	1.19 ± 0.17	0.69 ± 0.04
Horologium I	UFD	-3.53 ± 0.56	$26.29^{+0.99}_{-1.10}$	$28.07^{+0.99}_{-1.10}$	35.39 ± 7.81	0.98 ± 0.47	0.31 ± 0.16
Horologium II	UFD	-1.54 ± 1.02	$27.66^{+1.85}_{-2.37}$	$29.67^{+1.85}_{-2.37}$	64.21 ± 29.72	1.09 ± 0.37	0.86 ± 0.19
Hydra II	UFD	-4.58 ± 0.37	$26.15^{+0.79}_{-0.89}$	$28.40^{+0.79}_{-0.89}$	58.47 ± 12.47	1.20 ± 0.46	0.17 ± 0.13
Indus 1	Not classified	-3.31 ± 0.62	$24.39^{+1.53}_{-2.20}$	$26.69^{+1.53}_{-2.20}$	25.31 ± 13.09	1.22 ± 0.44	0.72 ± 0.29
Koposov 1	Outer Halo GC	-1.03 ± 0.69	$25.11^{+1.18}_{-1.32}$	$27.51^{+1.18}_{-1.32}$	10.12 ± 2.53	1.27 ± 0.56	0.55 ± 0.15
Koposov 2	Outer Halo GC	-0.91 ± 0.81	$23.40^{+1.22}_{-1.32}$	$25.98^{+1.22}_{-1.32}$	4.34 ± 0.91	1.35 ± 0.70	0.48 ± 0.12
Laevens 1	Outer Halo GC	-4.79 ± 0.33	$24.50^{+0.62}_{-0.67}$	$25.81^{+0.62}_{-0.67}$	20.67 ± 2.95	0.77 ± 0.36	0.11 ± 0.10
Laevens 2	UFD	-1.59 ± 0.76	$25.74^{+1.15}_{-1.24}$	$28.53^{+1.15}_{-1.24}$	17.45 ± 3.49	1.45 ± 0.45	0.39 ± 0.11
Leo I	dSph	-11.76 ± 0.28	22.62 ± 0.30	23.93 ± 0.30	243.82 ± 2.22	0.77 ± 0.02	0.30 ± 0.01
Leo II	dSph	-9.73 ± 0.04	24.25 ± 0.06	25.43 ± 0.06	168.09 ± 2.03	0.71 ± 0.02	0.07 ± 0.02
Leo IV	UFD	-4.98 ± 0.26	$27.82^{+0.51}_{-0.54}$	$29.33^{+0.51}_{-0.54}$	116.92 ± 13.89	0.86 ± 0.26	0.19 ± 0.09

Continued on next page

Table 1.1 – *Continued from previous page*

Object	Type	M_V	$\mu_{V,0}$ (mag/$''^2$)	$\mu_{V,e}$ (mag/$''^2$)	R_e (pc)	n	ε
Leo T	UFD	-7.59 ± 0.14	$25.43^{+0.37}_{-0.40}$	$27.31^{+0.37}_{-0.40}$	151.63 ± 16.98	1.03 ± 0.26	0.23 ± 0.09
Leo V	UFD	-4.39 ± 0.36	$24.90^{+0.79}_{-0.90}$	$28.24^{+0.79}_{-0.90}$	51.78 ± 11.39	1.70 ± 0.36	0.35 ± 0.07
Muñoz 1	Outer Halo GC	-0.48 ± 0.97	$26.34^{+1.34}_{-1.42}$	$30.08^{+1.34}_{-1.42}$	22.25 ± 4.19	1.89 ± 0.31	0.50 ± 0.05
NGC 2419	Outer Halo GC	-9.33 ± 0.03	18.83 ± 0.05	22.19 ± 0.05	25.71 ± 0.24	1.71 ± 0.02	0.05 ± 0.01
NGC 5694	Outer Halo GC	-7.93 ± 0.09	13.42 ± 0.14	20.01 ± 0.14	4.28 ± 0.10	3.20 ± 0.08	0.06 ± 0.02
NGC 5824	Outer Halo GC	-9.28 ± 0.04	11.15 ± 0.08	19.09 ± 0.08	4.95 ± 0.09	3.82 ± 0.05	0.04 ± 0.01
NGC 6229	Outer Halo GC	-8.03 ± 0.16	13.88 ± 0.22	19.21 ± 0.22	3.19 ± 0.09	2.62 ± 0.08	0.02 ± 0.01
NGC 7006	Outer Halo GC	-7.41 ± 0.08	15.99 ± 0.13	21.17 ± 0.13	6.11 ± 0.12	2.55 ± 0.07	0.07 ± 0.01
NGC 7492	Outer Halo GC	-6.10 ± 0.04	21.24 ± 0.06	23.05 ± 0.06	9.56 ± 0.08	1.00 ± 0.02	0.02 ± 0.02
Palomar 13	Outer Halo GC	-2.82 ± 0.55	$22.15^{+0.70}_{-0.71}$	$26.61^{+0.70}_{-0.71}$	9.53 ± 0.68	2.22 ± 0.19	0.10 ± 0.06
Palomar 14	Outer Halo GC	-5.39 ± 0.24	23.59 ± 0.33	26.47 ± 0.33	32.04 ± 1.34	1.49 ± 0.08	0.11 ± 0.04
Palomar 15	Outer Halo GC	-5.65 ± 0.19	23.07 ± 0.24	24.97 ± 0.24	19.02 ± 0.39	1.04 ± 0.06	0.05 ± 0.02
Palomar 2	Outer Halo GC	-9.05 ± 0.07	$16.57^{+0.11}_{-0.12}$	$19.88^{+0.11}_{-0.12}$	7.83 ± 0.16	1.69 ± 0.04	0.05 ± 0.02
Palomar 3	Outer Halo GC	-5.48 ± 0.21	$23.55^{+0.27}_{-0.28}$	$25.08^{+0.27}_{-0.28}$	19.37 ± 0.54	0.87 ± 0.05	0.07 ± 0.03
Palomar 4	Outer Halo GC	-6.01 ± 0.16	$22.74^{+0.22}_{-0.23}$	$24.81^{+0.22}_{-0.23}$	20.24 ± 0.63	1.12 ± 0.08	0.03 ± 0.02
Phoenix 2	Not classified	-3.28 ± 0.63	$25.85^{+0.97}_{-1.03}$	$27.97^{+0.97}_{-1.03}$	38.87 ± 6.52	1.14 ± 0.27	0.61 ± 0.15
Pictoris 1	Not classified	-3.44 ± 0.60	$24.51^{+1.46}_{-2.04}$	$27.43^{+1.46}_{-2.04}$	21.89 ± 10.61	1.51 ± 0.31	0.24 ± 0.19
Pisces II	UFD	-4.21 ± 0.38	$26.53^{+0.71}_{-0.77}$	$28.61^{+0.71}_{-0.77}$	64.59 ± 10.59	1.12 ± 0.34	0.40 ± 0.10
Pyxis	Outer Halo GC	-5.69 ± 0.19	$23.07^{+0.24}_{-0.25}$	$24.87^{+0.24}_{-0.25}$	18.57 ± 0.46	0.99 ± 0.05	0.04 ± 0.02
Reticulum II	UFD	-3.86 ± 0.38	26.79 ± 0.46	27.73 ± 0.46	48.78 ± 1.83	0.60 ± 0.05	0.56 ± 0.03
Sculptor	dSph	-10.81 ± 0.14	$23.41^{+0.36}_{-0.38}$	$24.66^{+0.36}_{-0.38}$	215.14 ± 22.51	0.74 ± 0.07	0.26 ± 0.01
Segue 1	UFD	-1.29 ± 0.73	$28.08^{+0.98}_{-1.01}$	$29.57^{+0.98}_{-1.01}$	26.43 ± 3.21	0.85 ± 0.28	0.34 ± 0.11
Segue 2	UFD	-1.85 ± 0.88	$28.49^{+1.05}_{-1.06}$	$29.92^{+1.05}_{-1.06}$	37.06 ± 2.95	0.82 ± 0.16	0.21 ± 0.07
Segue 3	Outer Halo GC	-0.85 ± 0.67	$23.86^{+1.02}_{-1.08}$	$26.32^{+1.02}_{-1.08}$	4.08 ± 0.71	1.30 ± 0.30	0.22 ± 0.09
Sextans	dSph	-8.71 ± 0.06	27.23 ± 0.08	28.18 ± 0.08	442.04 ± 4.25	0.60 ± 0.01	0.30 ± 0.01
UMa I	UFD	-5.12 ± 0.38	$29.12^{+0.47}_{-0.48}$	$29.78^{+0.47}_{-0.48}$	235.32 ± 9.59	0.47 ± 0.08	0.57 ± 0.03
UMa II	UFD	-4.23 ± 0.26	28.08 ± 0.33	29.66 ± 0.33	129.85 ± 4.28	0.89 ± 0.10	0.56 ± 0.03
UMi	dSph	-9.02 ± 0.05	25.77 ± 0.06	27.09 ± 0.06	367.21 ± 2.43	0.77 ± 0.01	0.55 ± 0.01

Continued on next page

Table 1.1 – *Continued from previous page*

Object	Type	$M_{\rm V}$	$\mu_{\rm V,0}$ (mag/$''^2$)	$\mu_{\rm V,e}$ (mag/$''^2$)	$R_{\rm e}$ (pc)	n	ε
Whiting 1	Outer Halo GC	-2.54 ± 0.44	$21.45^{+0.64}_{-0.66}$	$25.84^{+0.64}_{-0.66}$	6.39 ± 0.61	2.19 ± 0.26	0.24 ± 0.05
Willman I	UFD	-2.52 ± 0.74	$25.88^{+0.92}_{-0.94}$	$28.43^{+0.92}_{-0.94}$	27.97 ± 2.43	1.34 ± 0.20	0.47 ± 0.06

1.3 Aims

The main objective of this thesis is to perform a homogeneous characterization of the physical properties of outer halo satellites, including classical dSphs, UFDs and GCs.

The specific objectives are:

- Analyze the intrinsic photometric differences and similarities among GCs, dSphs, and UFDs.
- Perform a complete and detailed morphological analysis of outer halo satellites, using the matched-filter method, to identify which objects show signs of disturbance from MW tidal forces and analyze the effects of this disturbance on their dynamics and structural properties.
- Contribute to the understanding of the "Nature versus Nurture" problem. That is, understand the influence of their internal physical processes and of the MW's potential in shaping their observed physical properties.

Chapter 2

Scaling relations of Milky Way's satellites

The halo of the Milky Way (MW) contains important information about the ancient history of our Galaxy, especially because dynamical scales are long enough to retain information of past Galactic events (e.g., Johnston et al., 1996; Mayer et al., 2002). A significant fraction of this information is contained in the structural, dynamical, and chemical properties of satellite stellar structures of the MW, which dominate the outer halo stellar distribution (see Majewski, 2004; Willman, 2010; Ivezić et al., 2012, for reviews on this topic). Thus, by studying these substructures, it is, in principle, possible to peer into our galaxy's past and learn about the processes that governed its formation and evolution.

The stellar structures that surround the Galaxy have been usually classified as either globular clusters (GCs) or dwarf galaxies. Specifically, most of the dwarf galaxies are of the dwarf spheroidal type (dSph), which is devoid of gas and shows no current stellar formation. Both types of stellar structures are dominated by an old, metal-poor stellar population. Currently, it is accepted that dwarf galaxies formed their dark matter (DM) halos at small scales and were accreted later by the MW, as described by hierarchical growth models (Searle & Zinn, 1978; Bullock & Johnston, 2005). In the case of GCs, a fraction of them formed together with our galaxy during a phase of rapid collapse as proposed by Eggen et al. (1962), whereas others are thought to have an external origin, i.e. they formed in galaxies that were later accreted by the MW, which stripped off their GCs (Zinn, 1993, 1996; Mackey & Gilmore, 2004a; Mackey & van den Bergh, 2005; Leaman et al., 2013; Zaritsky et al., 2016).

To understand better the role of these structures in the formation and evolution of the MW, current research efforts have focused on the detection of satellites to obtain a reliable census of satellite objects orbiting our Galaxy. The results have significantly changed the way we understand our Galaxy surroundings. Before 2005, only nine Galactic dSphs were known (now referred to as classical dSphs), with luminosities in the range $-12 \lesssim M_{\rm V} \lesssim -8$ and with half-light radii on the order of 100 pc. Regarding GCs, almost all of them were compact objects, with half-light radii of less than 10 pc and, in general, less luminous than classical dSphs. Over the last decade and a half, and thanks to large-area surveys like the Sloan Digital Sky Survey (SDSS; York et al., 2000), PanSTARRS1 (Chambers & Pan-STARRS Team, 2016) and the Dark Energy Survey (DES; Dark Energy Survey Collaboration et al., 2016), the population of satellite systems has increased significantly, more than doubling the

total number (Willman et al., 2005a; Belokurov et al., 2006a, 2007, 2008, 2009, 2010, 2014; Zucker et al., 2006b; Walsh et al., 2007; Muñoz et al., 2012b; Bechtol et al., 2015; Kim & Jerjen, 2015; Koposov et al., 2015; Laevens et al., 2015a,b; Martin et al., 2015; Torrealba et al., 2016a,b; Homma et al., 2018). The new objects include low-luminosity dSphs ($M_{\rm V} > -8$), named ultra-faint dwarf galaxies (UFDs), some of them as small as some GCs; and halo GCs, some of them of size comparable to these UFDs. In this new scenario, the size gap that seemed to separate GCs from dSphs in the size versus luminosity plot has started to become populated, casting doubts on the true different origins for extended GCs and UFDs (e.g., Drlica-Wagner et al., 2015; Torrealba et al., 2016b). For example, it is not clear whether the large half-light radii of extended GCs is an intrinsic property of a different class of objects or a result of interactions with the MW (e.g., van den Bergh & Mackey, 2004; Ripepi et al., 2007; Hwang et al., 2011).

One widely accepted difference between dSphs and GCs is in their DM content. For classical dSphs, the mass-to-light ratio within their half-light radii ranges from ~ 6 to ~ 100, and from ~ 100 to ~ 3000 for UFDs (see Figure 11 of McConnachie (2012)), making the latter the most DM-dominated objects known in the universe. In the case of GCs, they have values consistent with no DM content, with typical values for the mass-to-light ratio of ~ 1 to ~ 4 (e.g., McLaughlin, 2000; Rejkuba et al., 2007; Baumgardt et al., 2009). This feature, together with the different metallicity spread between dSphs and GCs, has become the standard for classifying a halo stellar overdensity either as a dSph or a GC (Willman & Strader, 2012). In principle, it is reasonable to think that the presence of DM should leave a distinct imprint in the structural and photometric parameters of the baryonic matter of dSphs, in stark contrast with GCs. To explore this idea and to shed some light on the different processes that formed these two types of substructures, it is useful to have a complete characterization of their respective structural and photometric properties and to compare them homogeneously.

This part of the thesis is based on a catalog of structural parameters constructed from deep, wide, and homogeneous observations of 58 satellite objects located in the outer halo of the MW (Muñoz et al., 2018a,b). These parameters include the half-light radius, surface brightness, luminosity, ellipticity, and Sérsic index. In this research, we focus on the observed trend of the Sérsic index with the effective radius, which shows a strong correlation when all outer halo objects are considered.

2.1 Parameter distributions

Given the characteristics of our new dataset (wider, deeper and nearly homogeneous), in Côté, P. et al. (2019, in preparation) we explore in depth a wide range of correlations between different structural parameters to globally assess the similarities and differences between GCs and dSphs. Here, we briefly highlight some of those results.

Figure 2.1 shows the distribution of six structural parameters: absolute magnitude in the V band ($M_{\rm V}$), effective radius ($R_{\rm e}$), central surface brightness in the V band ($\mu_{\rm V,0}$), effective surface brightness in the V band ($\mu_{\rm V,e}$), Sérsic index (n), and ellipticity (ε), divided into dwarf galaxies and GC subgroups. In general, as a group, dwarf galaxies are larger, brighter, more diffuse, less concentrated, and more elongated than GCs, but all parameters show overlap between the two classes of objects, with no clear boundaries separating the two

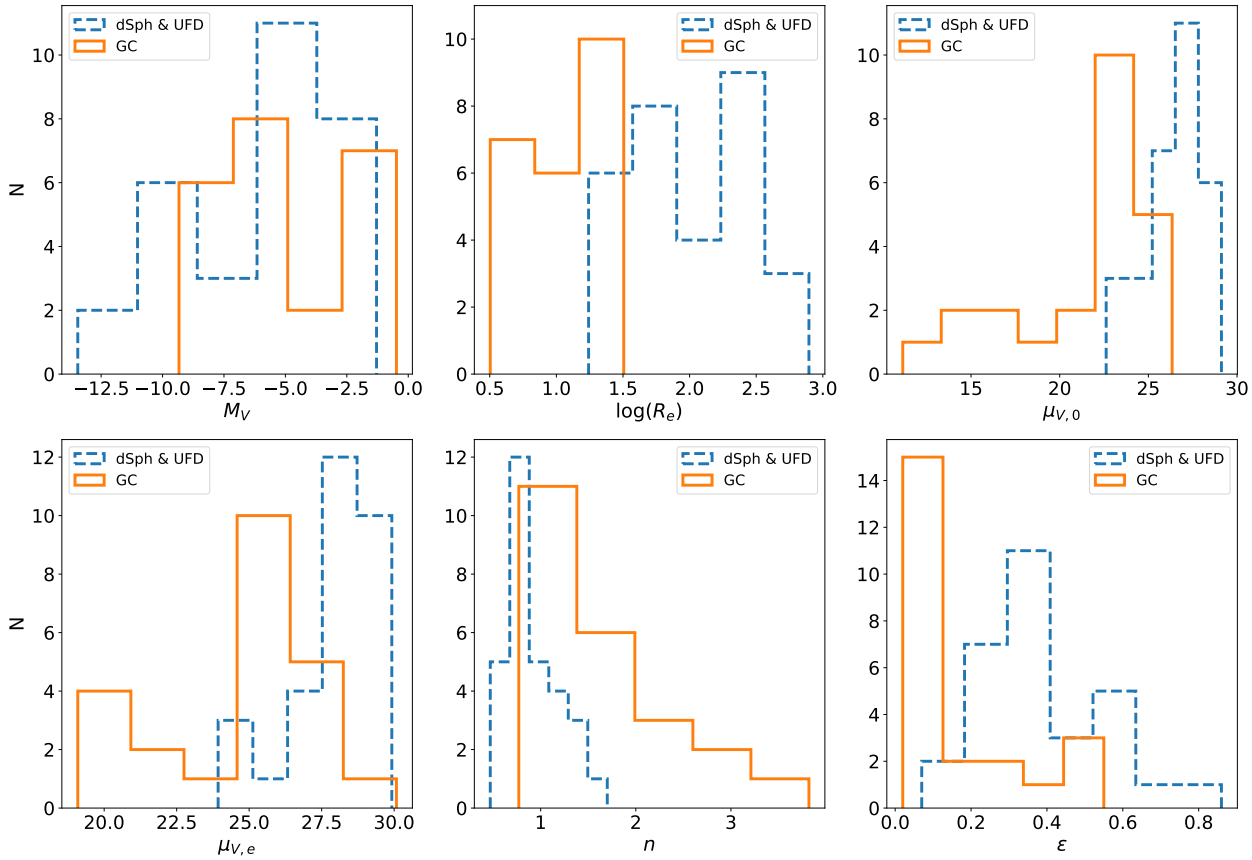

Figure 2.1: Comparison of the GC and dSph parameter distributions, for all the structural and photometric parameters analyzed in our study.

families.

One interesting result from Figure 2.1 is the ellipticity distribution (bottom right panel). The vast majority of GCs are significantly round, with their ellipticities concentrated around $\varepsilon < 0.15$. Dwarf galaxies, on the other hand, are distributed along the whole range, preferentially at $\varepsilon > 0.2$, except for Leo II, which shows little elongation. However, some GCs extend the distribution to significantly higher ellipticity values, overlapping with most of the dwarf galaxy distribution. In Figure 2.2 we show how the ellipticity behaves as a function of luminosity for all objects in our catalog. Most luminous GCs, up to $M_V \sim -6$, have ellipticities consistent with little or no elongation. This changes at lower luminosities, where GCs are characterized by progressively increasing ellipticities, up to ~ 0.7 for the faintest object.

2.1.1 Effect of low numbers of member stars on measured parameters.

Martin et al. (2008) showed that rounder objects can mistakenly seem elongated if their structural parameters are measured from samples with low numbers of stars. Similar studies have shown that the low number of stars detected in ultra-low-luminosity objects affect our ability to reliably measure their structural properties (e.g., Sand et al., 2010; Muñoz et al.,

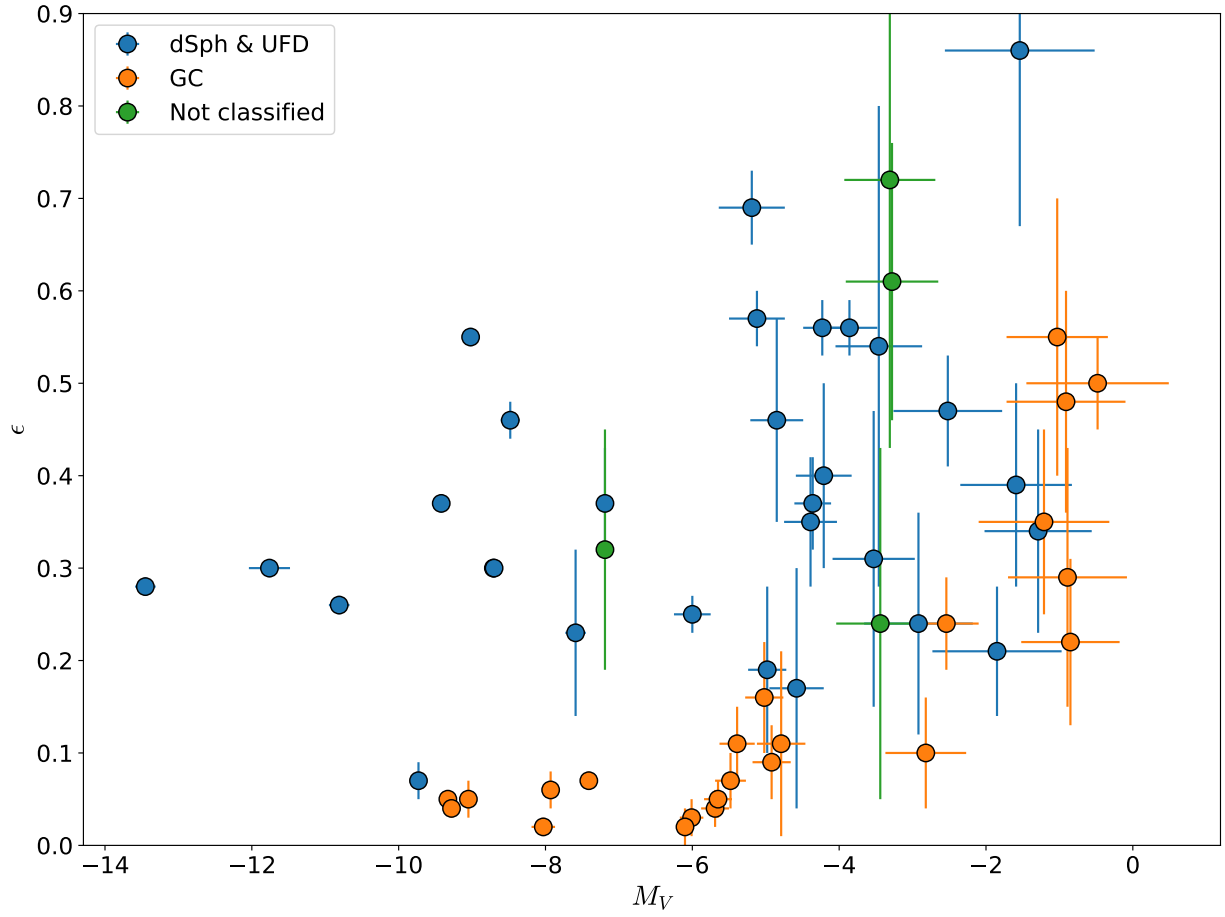

Figure 2.2: Evolution of ellipticity with luminosity for GCs, dSphs, and UFDs. GCs with luminosities higher than $M_V \sim -5$ are clearly more round than dwarf galaxies of comparable luminosity. At lower luminosities, clusters seem to increase their ellipticities to values similar to those of galaxies.

2012a).

To explore the effect of low numbers of member stars on the measured ellipticities, we fit a stellar density profile over a set of simulated stellar overdensities of different numbers of member stars. To simulate a stellar overdensity, we generate member stars randomly across a defined field of view using a Sérsic density profile as a probability distribution. Given that we want to test the potential departure from a round shape at low luminosities, we set the ellipticity of our simulated object equal to 0. We run two sets of simulations, where the effective radius is kept constant at $1.25'$ and we give two different values to the Sérsic index, 1 and 4, to see the effect of different concentrations. The field of view is given by a 30 arcmin × 30 arcmin area, and, for simplicity, we put the simulated object at the center. Finally, we add a particle background given by a constant stellar background density through the entire field of view. The value we adopt for this parameter is $0.5\,[1/\mathrm{arcmin}^2]$, which is the typical value derived by Muñoz et al. (2018b) for the objects in our dataset (see their Figure 4–14, right panels).

We generate samples of different numbers of member stars by taking random subsamples

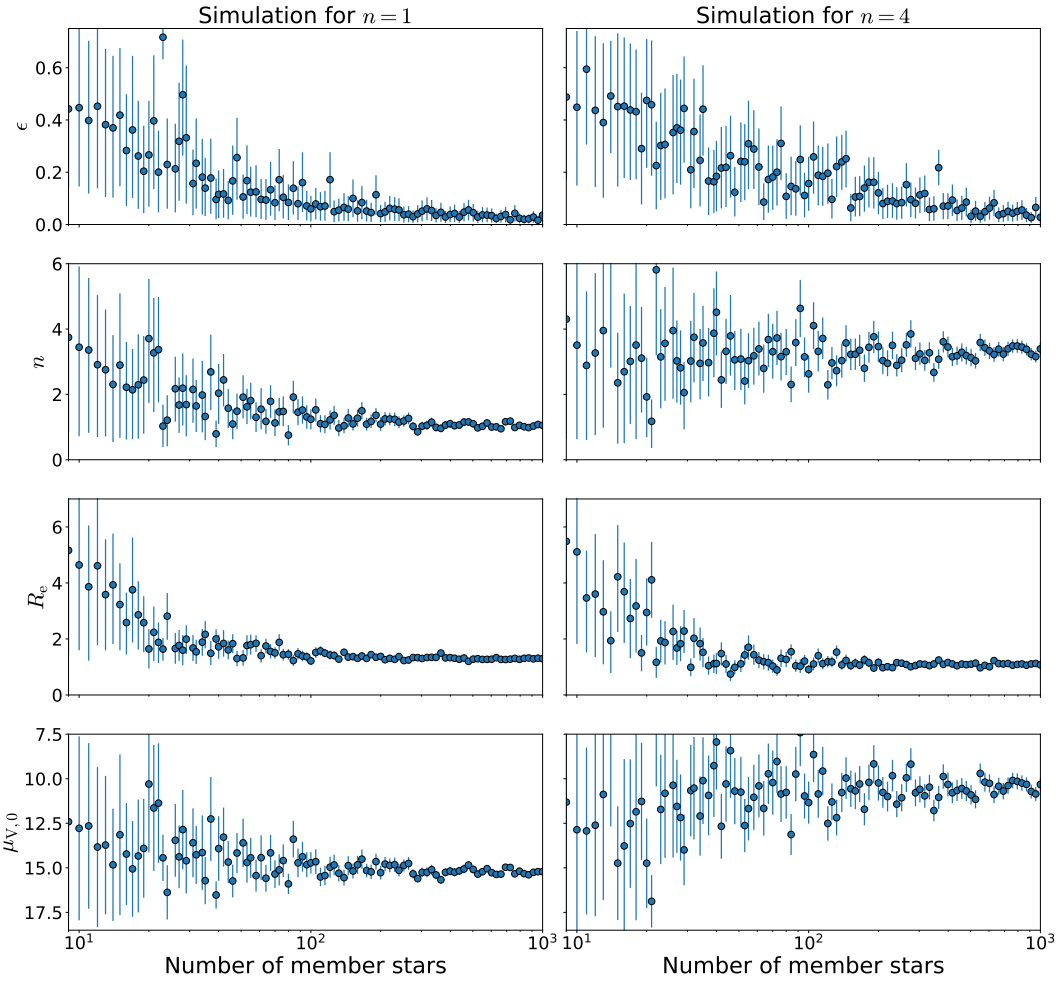

Figure 2.3: Ellipticity, Sérsic index, effective radius, and central surface brightness estimations for different subsamples of member stars from the simulated satellite object. The left panels are the results for $n = 1$, while the right panels are for $n = 4$. This plot shows that the increase in ellipticities observed in globular clusters in Figure 2.2 is likely due to a statistical effect of the low number of observed member stars. This effect is only seen at a much lower number of member stars for the rest of the parameters.

without replacement from the originally simulated object. The number of member stars for the subsamples ranges from 1 to 2000 stars in different steps given by a logarithmic scale. For every simulated subsample, we then fit a Sérsic profile with the effective radius, Sérsic index, central coordinate, and ellipticity as free parameters, while the background density is kept fixed. The fit is performed through a Bayesian MCMC approach, using the `emcee` Python package (Foreman-Mackey et al., 2013). The likelihood function is represented by the Sérsic density profile, and the priors for all the free parameters are defined to be uniform and positive. The density profile used is given by

$$\Sigma(r) = \Sigma_{0,\mathrm{S}} \exp\left[-b_n \left(\frac{r}{r_\mathrm{e}}\right)^{1/n}\right] + \Sigma_{\mathrm{bkg}} \tag{2.1}$$

where $\Sigma(r)$ is the stellar density for any given radius r, $\Sigma_{0,\mathrm{S}}$ is the Sérsic central stellar density, n is the Sérsic index, r_e is the effective radius, b_n is approximated by $1.999n - 0.327$ (Capaccioli, 1989), and Σ_{bkg} is the background stellar density.

The top panels of Figure 2.3 show the estimation of the ellipticity for every simulated subsample. It is evident that a low number of member stars increases the bias and the uncertainty of the estimation. This is consistent with the interpretation that the trend in ellipticity that we see in Figure 2.2 is possibly due to the low luminosity of the satellite objects and it is not a real effect.

In the same vein, likely, the ellipticity measurements of dSphs at low luminosities are also affected by low numbers of member stars. Therefore, for absolute magnitudes fainter than ~ -5 we cannot reliably use the ellipticity values, and thus we cannot clearly establish differences or similarities in ellipticities for GCs and dSphs.

In Figure 2.3, we also show the behavior of the Sérsic index, effective radius, and central surface brightness as a function of the number of stars. All of these parameters appear more robust to the shot noise introduced by the low number of stars, with significant deviations observed only in the more extreme cases of fewer than ~ 30 stars for the $n = 1$ case, and fewer than ~ 100 stars for $n = 4$. Although the measured parameters for objects with true Sérsic index equal to 4 are more sensitive to the number of member stars, we note that all our objects with high Sérsic index are dominated by a large number of member stars. We, therefore, regard trends involving R_e , n , and $\mu_{\mathrm{V},0}$ as more reliable, considering that the object with the lowest number of member stars in our sample has on the order of 100 stars.

It is important to mention that the values for $\mu_{\mathrm{V},0}$ in figure 2.3 were not obtained directly from the output of the simulation just described, but derived from the other parameters, as in Muñoz et al. (2018b). The relations used are

$$I_0 = L b_n^{2n} / [2\pi R_\mathrm{e}^2 n \Gamma(2n)(1-\varepsilon)]$$

$$\mu_0 = M_\odot + 21.572 - 2.5 \log I_0$$

where $b_n = 1.9992n - 0.3271$, I_0 is the central intensity, and L is the total luminosity of the object. Uncertainties were calculated by propagation of errors.

2.2 $n - R_\mathrm{e}$ correlation

An intriguing result regarding the overall properties of GCs and dwarf galaxies is a relation between the Sérsic index and effective radii that is followed by all outer halo objects in our

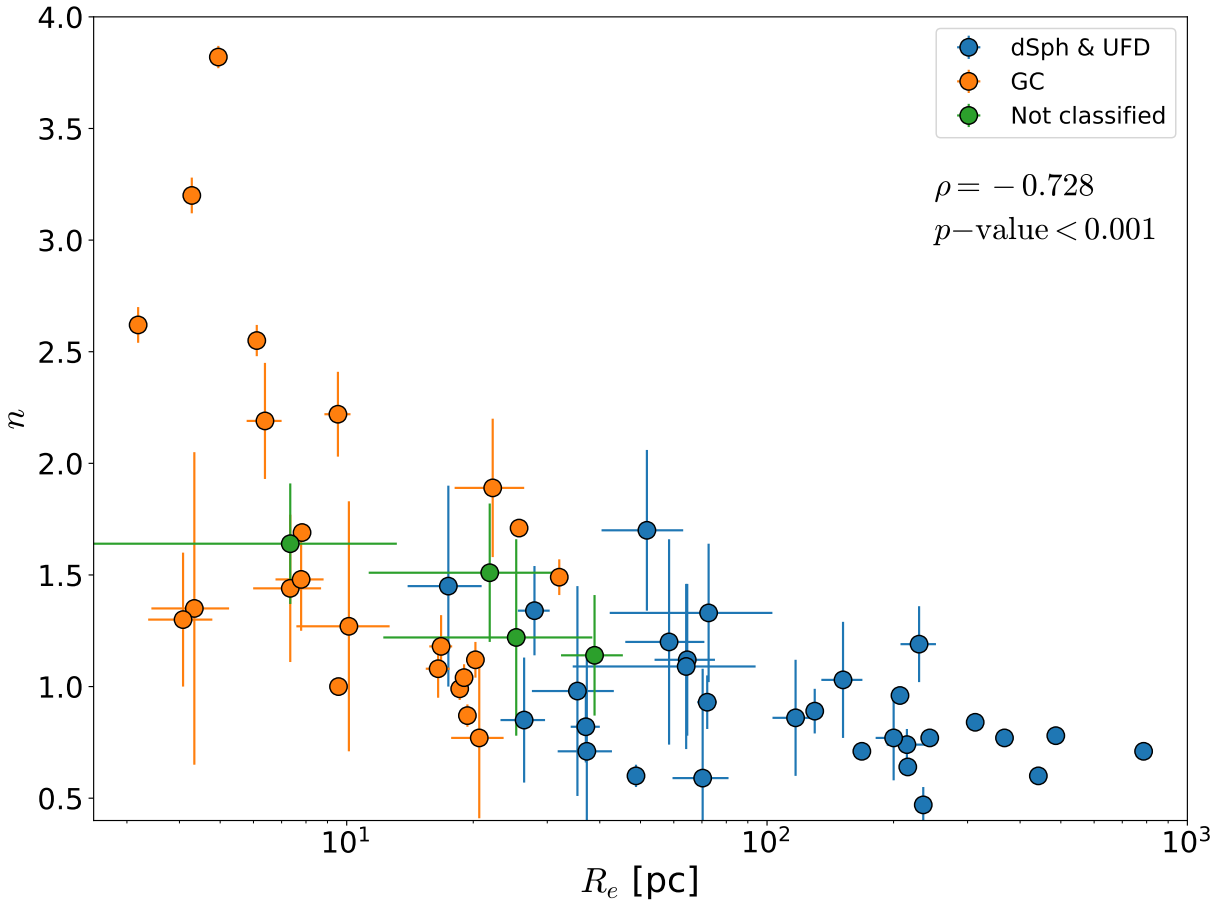

Figure 2.4: Correlation between the Sérsic index and the effective radius in parsecs for all the objects in our sample.

sample. In Figure 2.4, we present the relation between the Sérsic index and the effective radius for dwarf galaxies and GCs. The figure shows that the Sérsic index decreases linearly with increasing size in log space. This means that smaller satellite objects are more centrally concentrated than larger ones since the Sérsic index is a proxy for central concentration (Trujillo et al., 2001). The Spearman's correlation coefficient is -0.728, with a p-value less than 0.001, indicating that the correlation is significant at a high level. A similar trend, but in the opposite sense, has already been reported for dwarf and elliptical galaxies (Caon et al., 1993), where larger galaxies have a higher Sérsic index (i.e. are more concentrated).

The fact that both GCs and dwarf galaxies share the same locus, forming a continuous group, suggests a remarkable similarity between these two types of objects that is at first glance surprising, given that GCs and dwarf galaxies do not follow continuous trends in other structural parameter planes. We note that, even though our structural parameters come from fitting a Sérsic profile to the number density profiles, Trujillo et al. (2001) demonstrated that a relation between $R_{\rm e}$ and n cannot be produced by parameter coupling due to model fitting.

2.3 Discussion

2.3.1 Origin of the $n - R_{\rm e}$ relation

The observed $n - R_{\rm e}$ trend for GCs and dwarf galaxies does not have an obvious interpretation, especially if one takes into account that these objects have long been considered to be intrinsically different; GCs are believed to be DM-free while dwarf galaxies are heavily DM-dominated.

Graham (2011) showed that it is possible to understand the existence of a relationship between the effective radius and mean effective surface brightness for elliptical and dwarf elliptical galaxies by showing that it can naturally arise if $\mu_0 - M_{\rm V}$ and $\log(n) - M_V$ behave linearly when both types of galaxies follow a Sérsic density profile. In what follows, we consider a similar approach to understand the $n - R_{\rm e}$ trend and show an analytic procedure to reproduce the $n - R_{\rm e}$ relation by considering linear fittings to the $\mu_0 - M_{\rm V}$ and $n - M_{\rm V}$ plots.

Note that in Graham (2011), they aimed to explain a correlation in a different parameter space than $n - R_{\rm e}$ (the one we present in this paper). However, the analytical procedure is the same. Unlike the case of elliptical galaxies, we know beforehand that GCs and dwarf galaxies do not form a single relation in either $\mu_0 - M_{\rm V}$ and $n - M_{\rm V}$ spaces, and thus we follow Graham's (2011) procedure to investigate how the different behaviors in these parameter spaces can still result in the $n - R_{\rm e}$ trend we detected. Additionally, we use the form $n - M_{\rm V}$ instead of a $\log(n) - M_V$ relation. We do this because our range of n is small enough that transforming to log space would not produce any substantial improvement. Moreover, by using the $n - M_{\rm V}$ relation, we avoid introducing an extra $\log(n)$ term in equation 2.6.

The intensity profile at any given radius r is modeled by the Sérsic profile as

$$I(r) = I_{\rm e} \exp\left\{-b_n\left[\left(\frac{r}{r_{\rm e}}\right)^{1/n} - 1\right]\right\} \tag{2.2}$$

where $I_{\rm e}$ is the intensity at the effective radius $r_{\rm e}$, n is the Sérsic index, and b_n is a function that depends on n. As demonstrated by Graham & Driver (2005), from a Sérsic profile, it is possible to derive the following expression:

$$M_{\rm tot} = \mu_{\rm e} - 2.5\log[f(n)] - 2.5\log(2\pi R^2_{\rm e,kpc}) - 36.57 \tag{2.3}$$

where $M_{\rm tot}$ is the total absolute magnitude, $\mu_{\rm e}$ is the effective surface brightness, $R_{\rm e,kpc}$ is the effective radius in kiloparsecs, n is the Sérsic index, and

$$f(n) = \frac{n{\rm e}^b}{b^{2n}}\Gamma(2n)$$

with $b = 1.9992n - 0.3271$ for $0.5 < n < 10$ (Capaccioli, 1989) and Γ is the gamma function.

Finally, if we consider relationships of the form

$$\mu_0 = \mathrm{A}M_{\mathrm{tot}} + \mathrm{B} \tag{2.4}$$

$$n = \mathrm{C}M_{\mathrm{tot}} + \mathrm{D} \tag{2.5}$$

where μ_0 is the central surface brightness and the fact that $\mu_{\mathrm{e}} = \mu_0 + 1.086b$, one obtains an equation that relates the Sérsic index with the effective radius, of the form

$$\log(R_{\mathrm{e,kpc}}) = \mathrm{E}n + \mathrm{F}\log\left[f(n)\right] + \mathrm{G} \tag{2.6}$$

with $\mathrm{E} = \frac{\mathrm{A}-1}{5\mathrm{C}} + 0.434$, $\mathrm{F} = -0.5$, and $\mathrm{G} = \frac{\mathrm{B}}{5} - \frac{\mathrm{D}(\mathrm{A}-1)}{5\mathrm{C}} - 7.784$.

This procedure shows that, for a Sérsic density profile, linear relations in the $\mu_0 - M_{\mathrm{V}}$ and $n - M_{\mathrm{V}}$ spaces reproduce a relation in the $n - R_{\mathrm{e}}$ space. One can reproduce other relationships between pairs of structural parameters if other linear relationships exist.

2.3.2 Surface brightness versus absolute magnitude

Figure 2.5 shows the central and effective surface brightness versus absolute magnitude. In both plots, galaxies form a continuous group characterized by a luminosity versus surface brightness dependency that flattens at $M_{\mathrm{V}} \sim -6$, in the region dominated by UFDs. This flattening was already identified by McConnachie (2012), and it is possibly due to detection bias because the surface brightnesses of the least luminous UFDs are very near the detection limit of current surveys.

In the case of GCs, they show a higher central and effective surface brightness than galaxies at high luminosities (lower than $M_{\mathrm{V}} \sim -4$). At lower luminosities, GCs tend to concentrate at an almost constant surface brightness value, showing similar behavior to the UFDs.

Although GCs and dwarf galaxies come closer at low luminosities in the $\mu_0 - M_{\mathrm{V}}$ space, neither group mixes completely–GCs have a higher average surface brightness than UFDs. This is not easily explained as detection bias, because the surface brightness values at which GCs are concentrated are higher than the detection limits. A possible explanation for this different surface brightness floor is the fact that UFDs are believed to be currently embedded in a DM halo. For a given luminosity (or stellar mass), an object inside a DM halo is likely more robust to tidal disintegration than a DM-free one and thus could reach lower luminosities, allowing also for lower surface brightnesses.

2.3.3 Sérsic index versus Absolute magnitude

Figure 2.6 shows the relation between the Sérsic index and the absolute magnitude. Dwarf galaxies concentrate at relatively small values of the Sérsic index, between ~ 0.5 and ~ 1.5, following a trend where the Sérsic index increases slightly at lower luminosities. On the

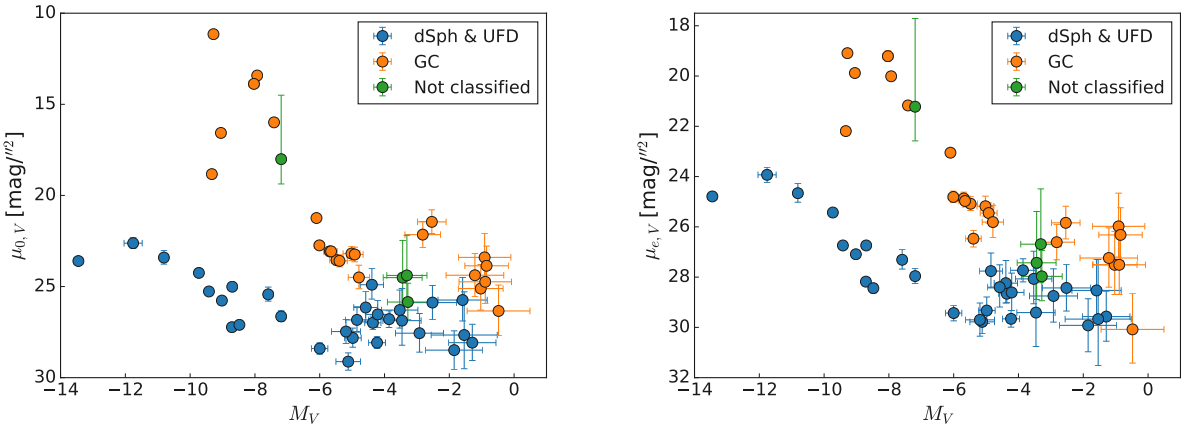

Figure 2.5: Comparison of surface brightness with absolute magnitude for the objects in our dataset. Left panel: central surface brightness versus absolute magnitude. Right panel: effective surface brightness versus absolute magnitude. Note that in both panels, it is evident that dwarf galaxies and globular clusters are well separated at high luminosities ($M_{\rm V} \lesssim -5$). At lower luminosities, both groups tend to mix, although on average globular clusters still show higher surface brightnesses.

other hand, GCs do not seem to follow a single trend. Overall, it appears that the Sérsic index increases with luminosity. However, the data allow a different interpretation: most low-luminosity GCs follow the trend delineated by dwarf galaxies, and only the six brighter clusters are off this trend and occupy a different region in the plot. In the surface brightness versus absolute magnitude relations (Figure 2.5), these clusters are also the ones with the highest surface brightnesses. In fact, from this Figure 2.5, it is also possible to infer that the low luminosity outer halo GCs and dwarf galaxies constitute a single group (although GCs have a higher mean central and effective surface brightnesses) with the high surface brightness GCs being outliers, which may be part of a different subgroup of clusters.

In the next subsections, we apply to our dataset the procedure from which the $n - R_{\rm e}$ relation originates, to see if it can be reproduced by linear fits obtained from the $\mu_0 - M_{\rm V}$ and $n - M_{\rm V}$ plots.

2.3.4 Linear fits to the $\mu_0 - M_{\rm V}$ and $n - M_{\rm V}$ relations

As a first approach, we fit linear relations to dwarf galaxies and GCs assuming that they constitute two separate groups, following the conventional classification for each object. The left panel of Figure 2.7 shows the linear fit to the central surface brightness versus absolute magnitude relation for GCs and galaxies. The fit for galaxies is given by

$$\mu_{\rm V,0} = (0.569 \pm 0.120) M_{\rm V} + (30.597 \pm 1.105) \tag{2.7}$$

while for GCs, the fit is given by

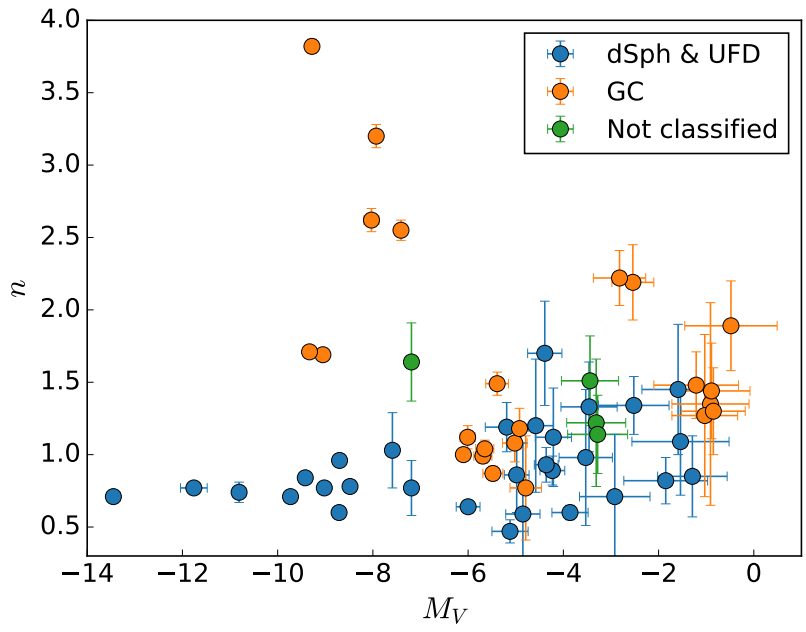

Figure 2.6: Sérsic index against absolute magnitude for all the objects in our dataset. Dwarf galaxies and globular clusters follow a nearly linear relationship that spans the whole range of luminosity, where low-luminosity objects have a slightly higher Sérsic index. There are six globular clusters located between $M_{\rm V} \sim -10$ and $M_{\rm V} \sim -8$ that do not follow this tendency, having high Sérsic indexes for their luminosities.

$$\mu_{\rm V,0} = (1.104 \pm 0.194) M_{\rm V} + (26.598 \pm 1.091) \tag{2.8}$$

Next, we analyze the relationship between the Sérsic index and absolute magnitude for dwarf galaxies, which is presented in the middle panel of Figure 2.7. The relations are characterized by

$$n = (0.036 \pm 0.015) M_{\rm V} + (1.124 \pm 0.101) \tag{2.9}$$

while for GCs, the fit is given by

$$n = (-0.100 \pm 0.053) M_{\rm V} + (1.184 \pm 0.300) \tag{2.10}$$

Finally, we obtain two relations similar to equation 2.6, one for dwarf galaxies and another for GCs. For galaxies, the relation is

$$\begin{aligned} \log_{10}(R_{\rm e,kpc}) = (-1.965 \pm 1.211) n + -0.500 \log_{10}(f(n)) \\ + (1.033 \pm 1.401) \end{aligned} \tag{2.11}$$

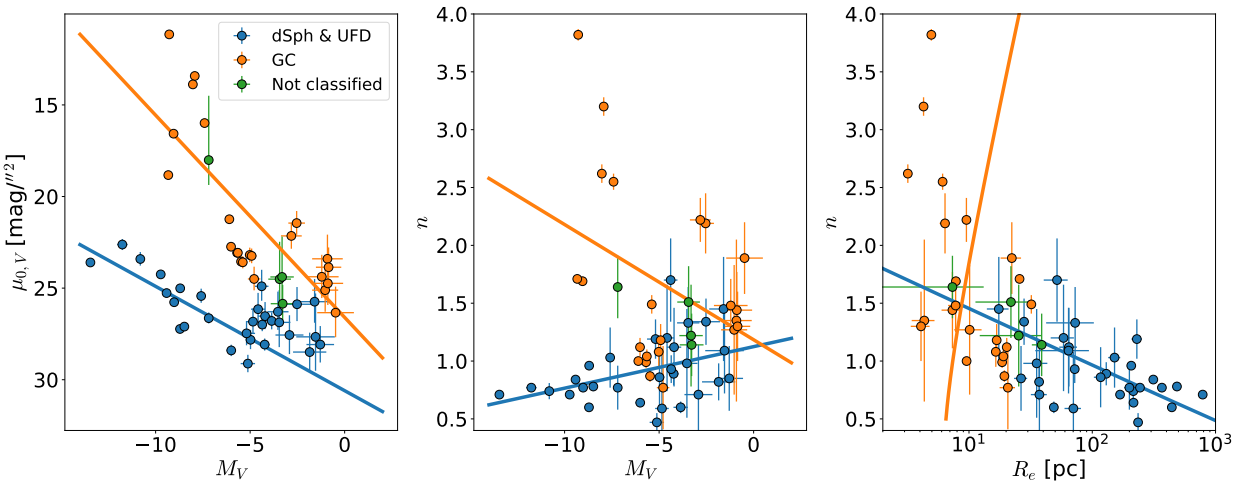

Figure 2.7: Linear relation fits for the $\mu_0 - M_V$ and $n - M_V$ plots and predicted relations for the $n - R_e$ correlation, for outer halo GCs and dSphs. Left and middle panels: linear relation fits for the $\mu_0 - M_V$ and $n - M_V$ plots, respectively. GCs are represented by orange circles, dSphs and UFDs are represented by blue circles, and green circles represent unclassified objects. The solid blue (orange) line represents the linear fit for dSphs (GCs). Right: solid lines represent the predicted relations for the $n - R_e$ correlation for GCs and for dwarf galaxies. Colors and symbols follow the same convention as the previous panels.

while for GCs the relation is

$$\log_{10}(R_{e,kpc}) = (0.226 \pm 0.406)n + -0.500 \log_{10}(f(n)) + (-2.218 \pm 0.531) \quad (2.12)$$

These derived relations are overplotted on our data in the right panel of Figure 2.7. Dwarf galaxies seem to follow the predicted relation, represented by a blue solid line. On the contrary, GCs do not follow their predicted relation, represented by an orange solid line. This shows that separating our data into two groups, one composed of GCs and the other of dSphs, and fitting linear relations in the $\mu_0 - M_V$ and $n - M_V$ parameter spaces do not explain completely the observed correlation observed in the $n - R_e$ parameter space. This is expected for GCs because it is clear that a linear fit in the $n - M_V$ for these objects is not a good model.

2.3.5 Two separate GC populations

Interestingly, some of the GCs seem to follow the extrapolation of the $n - R_e$ relation for dwarf galaxies. This prompts us to revisit the idea of two different GCs groups and consider the possibility that some outer halo GCs do not constitute a different group from UFDs.

To further explore the origin of the $n - R_e$ correlation, we add to our sample the inner GC data from Carballo-Bello et al. (2012), covering a range in galactocentric radius from 11 to 21 kpc. We estimated their Sérsic index, effective radius, and central surface density by fitting a Sérsic profile to radial density profiles through an MCMC fitting procedure (see thee Appendix section A.1 for further details on the MCMC algorithm). We used uniform,

Table 2.1: Parameters for inner halo GCs

Object	M_V	$\mu_{V,0}$ (mag/$''^2$)	R_e (pc)	n
Kim 1	0.74	25.22	5.36 ± 1.27	1.24 ± 0.55
NGC 1261	-7.80	17.73	4.75 ± 0.12	1.73 ± 0.05
NGC 1851	-8.33	14.25	1.85 ± 0.04	3.68 ± 0.09
NGC 1904	-7.86	16.02	3.17 ± 0.04	2.21 ± 0.03
NGC 2298	-6.31	18.90	3.02 ± 0.06	1.49 ± 0.04
NGC 4147	-6.17	17.38	2.94 ± 0.06	2.40 ± 0.07
NGC 4590	-7.37	18.81	5.46 ± 0.17	1.94 ± 0.08
NGC 5024	-8.71	17.38	7.63 ± 0.14	2.06 ± 0.05
NGC 5053	-6.76	22.03	11.08 ± 0.40	1.06 ± 0.08
NGC 5272	-8.88	16.64	3.92 ± 0.22	3.05 ± 0.15
NGC 5466	-6.98	21.61	6.91 ± 1.13	2.08 ± 0.31
NGC 5634	-7.69	17.20	5.08 ± 0.18	2.23 ± 0.12
NGC 6864	-8.57	15.52	2.70 ± 0.09	2.36 ± 0.09
NGC 7078	-9.19	14.21	3.40 ± 0.05	2.50 ± 0.05
Palomar 5	-5.17	24.64	21.86 ± 1.10	1.16 ± 0.15
Ruprecht 106	-6.35	21.82	12.98 ± 0.50	0.64 ± 0.07

positive priors for all the parameters. We also included a "nuisance parameter" among the free parameters that corrects for possible sub-estimations of the surface density errors in the data. This parameter is constrained by a uniform, positive prior. Also, given a degeneracy when estimating the Sérsic index and the background surface density, we fixed the latter by visually exploring the density profiles for each inner cluster and manually setting the background level for every density profile. We also obtained central surface brightness and absolute magnitude values from Harris (1996, 2010 edition). Additionally, we add parameters of the object Kim 1 from the DES dataset, which were calculated in Muñoz et al. (2018b). It is relevant to mention that adding the inner halo GCs to the datasets breaks its homogeneity. However, this only affects the high surface brightness clusters, keeping the homogeneity for the low surface brightness clusters and galaxies intact.

Table 2.1 shows the estimated parameters for inner GCs, and Figure 2.8 shows our Sérsic profile fit to the radial density profiles of inner halo GCs. Figure 2.9 shows the same plots as Figure 2.7, but this time including the inner GCs mentioned before. As can be seen in the central surface brightness versus absolute magnitude plot (left panel), most inner GCs are located in a high-luminosity, high central surface brightness area, in comparison to most outer halo clusters. There are four inner halo clusters (purple circles) separated from the main group of inner halo clusters, below the $\mu_{V,0} \sim 20$ line. Additionally, some outer halo clusters (orange stars) are mixed with the inner halo GCs and separated from the rest of the outer halo cluster population (orange circles), which is located close to the UFD group. The separation between the two GC groups seems to be also marked by the $\mu_{V,0} \sim 20$ line. We tentatively name the groups of clusters above this line the High Surface Brightness (HSB) group, while the group of clusters below this division line is the Low Surface Brightness (LSB) group.

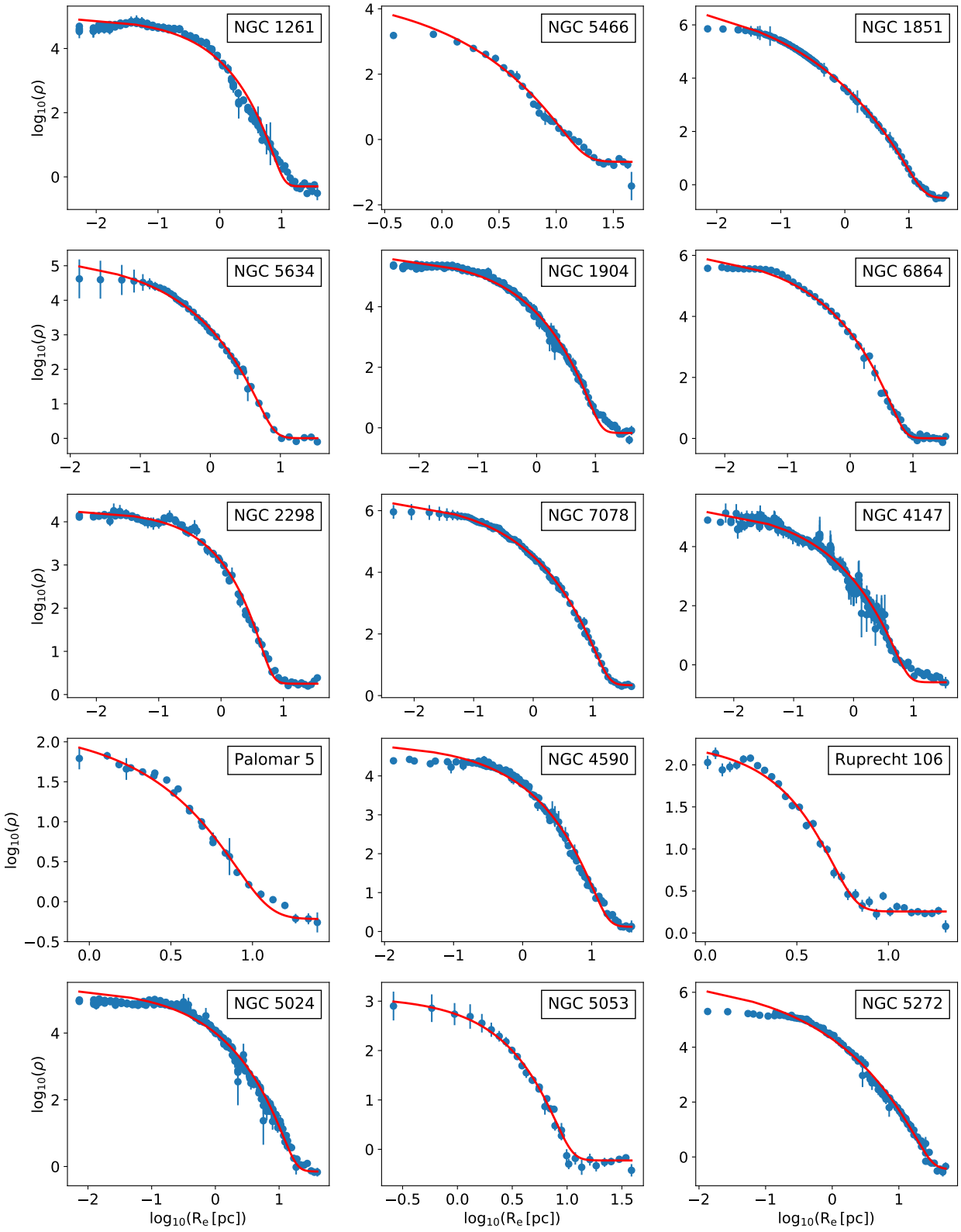

Figure 2.8: Radial density profiles (blue circles) and fitted Sérsic profile (red line) for each of the inner halo GCs from Carballo-Bello et al. (2012).

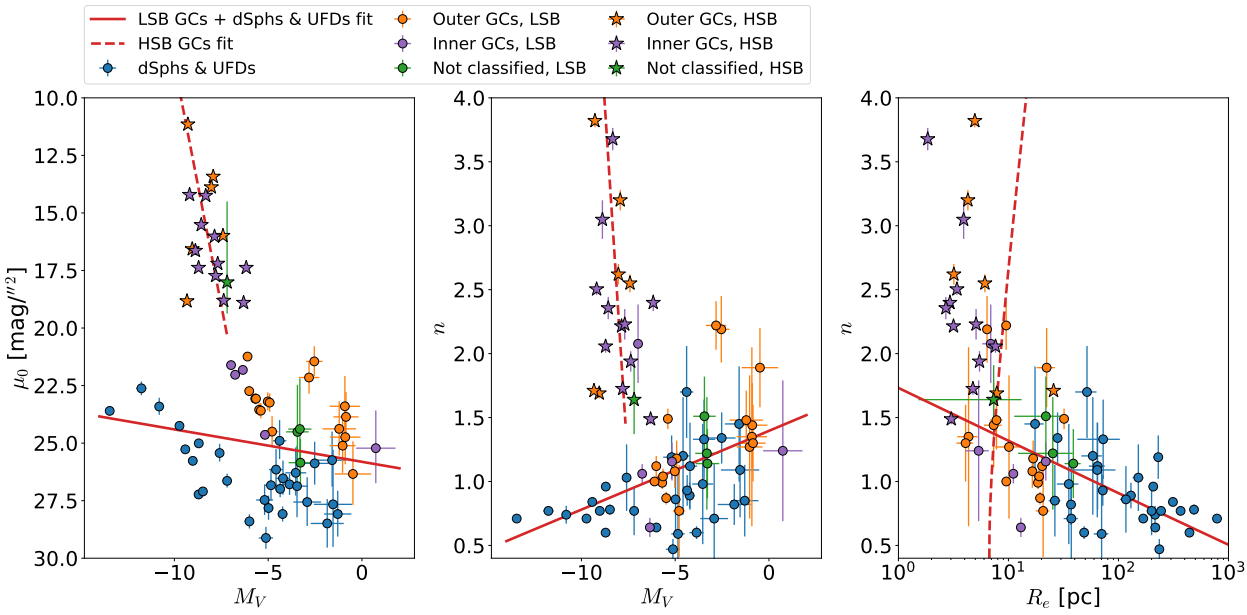

Figure 2.9: Linear relation fits for the $\mu_0 - M_{\rm V}$ and $n - M_{\rm V}$ plots and predicted relations for the $n - R_{\rm e}$ correlation, for outer and inner halo GCs and dSphs. Color coding is the same as Figure 2.7. Purple represents inner halo GCs. Stars represent satellite objects with $\mu_{\rm V,0} < 20$ (HSB clusters), while circles are objects with $\mu_{\rm V,0} \geq 20$ (LSB clusters plus dwarf galaxies). In the left and middle panels, the red solid line represents the empirical linear fit to the LSB clusters plus the dwarf galaxies group, while the red dashed line is the empirical linear fit to the HSB clusters. In the right panel, lines are the predicted relations based on the empirical linear fits of the left and right panels.

The middle panel of Figure 2.9, Sérsic index versus absolute magnitude, also shows the separation of the HSB and LSB groups. Although the HSB group is distributed between $-10 < M_{\rm V} < -5$ and $1 < n < 4$, the LSB group occupies the region $-4 < M_{\rm V}$ and $n \lesssim 2$ and mix with the low-luminosity part of the dwarf galaxy group.

Finally, in the $n - R_{\rm e}$ plot, the right panel in Figure 2.9, the HSB clusters are concentrated in the upper left region of the plot and deviate from the main correlation composed of LSB clusters and dwarf galaxies.

Adding the inner halo clusters to our outer halo sample reinforces the notion that there might be two subgroups of satellite objects: one composed of high-luminosity, high central surface brightness clusters from the MW's inner and outer halos, and another composed of dwarf galaxies and GCs of lower central surface brightness and in general lower luminosity, which share the same parameter space occupied by low-luminosity galaxies. With this in mind, we explore if fitting different linear relations to both groups defined above will reproduce the distribution in the Sérsic index versus the effective radius plot. To find the relation in the $n - R_{\rm e}$ parameter space for the LSB GC + dwarf galaxy and HSB GC groups, we repeat the same procedure as before. For the LSB GCs + dwarf galaxies, the equations of empirical linear fit are

$$\mu_{\mathrm{V},0} = (0.141 \pm 0.091) M_{\mathrm{V}} + (25.811 \pm 0.524) \tag{2.13}$$

$$n = (0.062 \pm 0.016) M_{\mathrm{V}} + (1.396 \pm 0.092) \tag{2.14}$$

and its $n - R_{\mathrm{e}}$ relation is

$$\begin{aligned} \log_{10}(R_{\mathrm{e,kpc}}) = (-2.356 \pm 0.783) n + -0.500 \log_{10}(f(n)) \\ + (1.273 \pm 1.128) \end{aligned} \tag{2.15}$$

For the HSB GC group, the empirical linear fit equations are

$$\mu_{\mathrm{V},0} = (4.190 \pm 1.985) M_{\mathrm{V}} + (50.439 \pm 25.170) \tag{2.16}$$

$$n = (-2.261 \pm 1.675) M_{\mathrm{V}} + (-15.848 \pm 11.878) \tag{2.17}$$

and its $n - R_{\mathrm{e}}$ relation is

$$\begin{aligned} \log_{10}(R_{\mathrm{e,kpc}}) = (0.152 \pm 0.273) n + -0.500 \log_{10}(f(n)) \\ + (-2.168 \pm 7.435) \end{aligned} \tag{2.18}$$

To fit the $\mu_0 - M_{\mathrm{V}}$ and $n - M_{\mathrm{V}}$ relations for HSB clusters, we in practice consider the $\mu_{\mathrm{V},0}$ and n parameters as independent variables and M_{V} as the dependent variable, because the distribution of clusters on those parameter spaces is strongly vertical when assuming M_{V} as the independent variable. Then, we invert the equations to obtain the coefficients when M_{V} acts as the independent variable.

The results of this last procedure are shown in Figure 2.9. The left and middle panels show the linear fits to the $\mu_0 - M_{\mathrm{V}}$ and $n - M_{\mathrm{V}}$ plots, respectively. In each parameter space, the red solid line is the best linear fit to the LSB GC + dwarf galaxy group, while the red dashed line is the best linear fit to the HSB GC group. The right panel shows the predicted relations for the two groups, according to equation 2.6. Objects in the LSB GC + dSph group follow the predicted relation (red solid line). On the other hand, clusters in the HSB group do not follow the relation predicted for them (red dashed line). This is surprising because the linear fits for the HSB group closely follow the objects' distributions. One possible explanation for this is that HSB clusters are not well described by a pure Sérsic profile and so equation 2.3 does not hold for the HSB clusters. Supporting this idea, Figure 2.8 shows that the Sérsic fit to the radial density profile in most cases is not ideal, especially in the central part, where the Sérsic profile is cuspy and the observed radial density follows a core profile. The same

is true for the outer halo GCs in the HSB group (Palomar 2, NGC 2419, NGC 5694, NGC 5824, NGC 6229, and NGC 7006; see from Figure 6 to 16 in Muñoz et al. (2018b)).

The fact that the $n - R_{\rm e}$ correlation can be reproduced by using the same empirical relations for the LSB GCs and the dSphs and that the HSB clusters move off this trend might hint at the existence of two different groups of MW outer halo GCs, one composed of GCs with structural and photometric properties similar to dwarf galaxies, and one composed of some outer halo GCs with properties more similar to inner halo GCs.

2.3.6 DM in GCs

The continuity between GCs and dwarf galaxies in the $n - R_{\rm e}$ plot, together with the overlap of the LSB cluster with ultra-faint galaxies in the $n - M_{\rm V}$ and $\mu_0 - M_{\rm V}$ plots, shows that the photometric properties of an important number of the MW's clusters, at least in this plane, seem indistinguishable from those of dwarf galaxies. This may point to a common formation process for these two types of objects. Because it is commonly accepted that dwarf galaxies are embedded in the DM halo in which they formed, it is perhaps tempting to assume that GCs are also contained and/or were formed inside DM minihalos.

This is not necessarily a controversial idea, because simulations of GCs forming and relaxing inside DM halos do exist, and they reproduce properties observed in real GCs (Mashchenko & Sills, 2005a). Other simulations show that the tidal effects of the host galaxy can remove a large amount of the original DM inside GCs (Mashchenko & Sills, 2005b). More recently, Peñarrubia et al. (2017) showed that stars ejected due to hard encounters in the central region of GCs embedded in a DM halo generate an envelope of gravitationally bounded stars. Supporting this model, so-called extratidal stars have been observed in many GCs of the MW (e.g. Carballo-Bello et al., 2012, 2018) and the Andromeda galaxy (Mackey et al., 2010). Additionally, Ibata et al. (2013) concluded that the presence of DM cannot be ruled out from the outer parts of the cluster NGC 2419.

2.3.7 Possible Origin of the HSB and LSB GC groups

In a scenario where all GCs formed through the same process, naively one could expect continuity in their photometric properties. The existence of the HSB and the LSB groups challenges that notion. Here, we postulate that a possible explanation for the existence of these two groups is the effect of different processes of secular evolution, due to different environments, something that is possible if some GCs formed and evolved inside the MW's potential, while others formed inside external satellite galaxies with weaker potentials and were later stripped from them during the MW's hierarchical accretion stage.

Zinn (1993) studied the Galactic clusters and found that they can be classified into three different groups, according to their metallicity and horizontal branch (HB) morphology. There is a metal-rich group ([Fe/H] > -0.8) located in the bulge and disk of the Galaxy (the bulge/disk group, or BD group), while a more metal-poor group ([Fe/H] < -0.8) is found in the Galactic halo. Zinn also found that the halo group contains clusters that can have a redder or bluer HB morphology for the same metallicity. This is the known second parameter effect and can be attributed to the age of the clusters, with redder clusters being

younger than bluer ones for the same metallicity. This led to the definition of the Old Halo (OH) and Young Halo (YH) groups, where the former formed in-situ during a dissipative collapse while the latter formed inside the potential of dwarf galaxies that were later accreted by the MW.

Later, Mackey & Gilmore (2004a) supported this view, showing that the metallicities and HB morphologies of GCs confirmed to be members of the Large Magellanic Cloud, Small Magellanic Cloud, and the Fornax and Sagittarius galaxies are consistent with the YH group values (see their Figure 13).

With this in mind, we can explore whether the classification of GCs into HSB and LSB is consistent with the existence of the BD, OH and YH groups. We use Table 1 of Mackey & van den Bergh (2005) to obtain the classification in the Zinn scheme for the clusters in our sample. Nine of them, all part of the LSB group, are not listed in the table. Moreover, these clusters do not show any HB in the color-magnitude plot in Muñoz et al. (2018b), so it is not possible to measure an HB index, which is necessary to classify them (Table 2.2 shows this classification for our clusters present in Mackey & van den Bergh (2005)). Of the remaining clusters, we count 17 GCs in the HSB group and 13 in the LSB group (in both cases including the inner halo GCs from Carballo-Bello et al. (2012)). According to the classification in Mackey & van den Bergh (2005), of the HSB group, nine clusters are OH, seven are YH, and one is an SG (part of the Sagittarius dwarf galaxy); in the LSB group, two are OH and 11 are YH. In other words, about half of the clusters in the HSB group are consistent with an in-situ origin and the other half are consistent with an external origin, while in the LSB group, the vast majority ($\sim 85\%$) are consistent with an external origin.

To explain the current properties of HSB and LSB clusters, tidal stripping processes must have affected GCs differently. In light of the idea that OH clusters formed in-situ and YH clusters did so in external galaxies, it is evident that HSB and LSB clusters must have been affected by different tidal forces during their secular evolution because they were located at a different galactic host environment. OH clusters formed in-situ, were subjected to a stronger tidal force, stripping stars from the high-luminosity clusters (this would give rise to OH clusters with HSB group characteristics) and completely disintegrating clusters of lower stellar mass (this would explain why there are almost no OH clusters with LSB group properties). YH clusters, on the other hand, formed in external galaxies with weaker potential, so they were affected by a weaker tidal force. Later, with the accretion of dwarf galaxies by the MW, they were incorporated into its GC system. Some of these clusters have already been disrupted by the MW's tidal force, leaving a stream of stars behind (e.g. Grillmair, 2009); others are in the process of disintegration, as evidenced by the tidal tails emerging from them (e.g. Palomar 5; Rockosi et al., 2002); and others still survive because they have not been affected by the MW's tidal force long enough or they do not live in destructive orbits. Among this last group, there are clusters of low luminosity and extended (the ones that constitute the LSB group) and others of higher luminosity and compact (characteristics of HSB GCs).

Hurley & Mackey (2010), through N-Body simulations, provided further insights into the formation of GCs in galactic gravitational potentials of different intensities. They showed that Large Magellanic Cloud-like galaxies of weak tidal fields can produce extended clusters of up to 30 pc from a standard process of formation and evolution. Furthermore, they showed that,

Table 2.2: HB classification for the clusters in our sample that have that information in Mackey & van den Bergh (2005).

Object	Surface Brightness Class	HB Class
NGC 1261	HSB	YH
NGC 1851	HSB	OH
NGC 1904	HSB	OH
NGC 2298	HSB	OH
NGC 2419	HSB	OH
NGC 4147	HSB	SG
NGC 4590	HSB	YH
NGC 5024	HSB	OH
NGC 5272	HSB	YH
NGC 5634	HSB	OH
NGC 5694	HSB	OH
NGC 5824	HSB	OH
NGC 6229	HSB	YH
NGC 6864	HSB	OH
NGC 7006	HSB	YH
NGC 7078	HSB	YH
Palomar 2	HSB	YH
AM 1	LSB	YH
Eridanus	LSB	YH
NGC 5053	LSB	YH
NGC 5466	LSB	YH
NGC 7492	LSB	OH
Palomar 13	LSB	YH
Palomar 14	LSB	YH
Palomar 15	LSB	OH
Palomar 3	LSB	YH
Palomar 4	LSB	YH
Palomar 5	LSB	YH
Pyxis	LSB	YH

Note: YH stands for young halo cluster, OH for old halo cluster, and SG for the Sagittarius cluster.

for GCs forming in MW-like tidal fields at 10 kpc from the galactic center, their maximum half-light radius is $\sim$ 10 pc. Finally, they pointed out that MW-like galaxies could form extended clusters at large galactocentric distances ($\sim$ 100 kpc) and any extended cluster present at the inner portions of the galaxy likely formed inside an accreted dwarf galaxy. These simulations support the idea that LSB clusters (typically extended) formed in accreted dwarf galaxies, while HSB clusters (usually more compact) formed inside the MW.

The notion that LSB GCs are of external origin while HSBs are a mix of clusters formed in-situ and externally could explain the differences presented in this work. To confirm or reject this idea, the best way is to know the orbit of each satellite object. However, this has proven to be a hard task, because to constrain their orbits, it is necessary to perform high-precision phase-space measurements, something that is difficult in objects with a low number of member and/or low-luminosity stars.

The *Gaia* mission promises high-precision kinematic information for many of the satellite objects. In fact, the second data release of this mission has already provided us with very accurate proper motions for some satellite dwarf galaxies (Fritz et al., 2018; Gaia Collaboration et al., 2018; Kallivayalil et al., 2018; Massari & Helmi, 2018; Pace & Li, 2019; Simon, 2018) and inner halo GCs (Gaia Collaboration et al., 2018; Vasiliev, 2019). This new information has allowed us to conclude that most of the UFDs inside a galactocentric radius of 100 kpc follow eccentric, high-velocity, and retrograde orbits and some of the galaxies are consistent with being in their first infall (Simon, 2018). In the case of GCs, Vasiliev (2019) showed that clusters in $R_{\rm G} \lesssim 10$ kpc rotate in prograde orbits and that the velocity dispersion is isotropic, while for clusters farther out the velocity distribution becomes radially anisotropic.

In light of these results, we predict that the LSB GCs should follow orbits similar to UFDs' and that they are on their first infall. This last point is consistent with the existence of such low-luminosity, LSB objects inside the strong tidal field of the MW. Also, they should exhibit a radially anisotropic velocity distribution. For the HSB group, given its mixed composition, we predict that GCs located in the inner halo should follow prograde orbits (consistent with clusters formed in-situ) with isotropic velocity dispersion, while the ones located near the frontier between the inner and outer halos should have kinematics similar to the LSB clusters.

Chapter 3

Morphology of Milky Way's outer halo satellites

Outer halo satellites are subjected to the tidal effects of the strong potential of the Milky Way (MW). The gravitational pull over individual stars of the satellite can be strong enough to distort its morphology or kinematics, to the extent of removing stars from the objects' potential or even disrupting it completely. Simulations of hierarchical galaxy formation show that these phenomena are key ingredients during the formation process, as it proposes that stars stripped from halo satellites contributed to the halo stellar population. As has been previously proposed by other studies, the tidal pull from the MW is also responsible for the stripping of Globular Clusters (GCs) from satellite dwarf galaxies and the later capture of them by the MW, contributing to the heterogeneity of the GC population (e.g. Mackey & Gilmore, 2004b; Marchi-Lasch et al., 2019).

Observations reveal that tidal stripping and disruption of satellite systems are processes that are still happening at present. The most important example of tidal disruption of a satellite dwarf galaxy is the case of the Sagittarius dSph (Ibata et al., 1994), whose tidal disruption has left a long stream that goes around the MW in an almost polar orbit (e.g. Lynden-Bell & Lynden-Bell, 1995; Newberg et al., 2002; Majewski et al., 2003; Belokurov et al., 2006b). Also, the Canis Major dwarf galaxy is the progenitor of the Monoceros ring (e.g. Newberg et al., 2002; Momany et al., 2006). Several other satellite dwarf galaxies show an elongated and/or distorted shape, suggesting they are suffering from tidal disruption (e.g. Kuhn et al., 1996; Belokurov et al., 2006a; Martin et al., 2008; Sand et al., 2009). Regarding GCs, the most famous case of tidal disruption is that of Palomar 5, which is the progenitor of the Palomar 5 stream (e.g. Rockosi et al., 2002; Odenkirchen et al., 2003). In other words, Grillmair & Johnson (2006) discovered a stellar stream originating from the cluster NGC 5466 and Chen & Chen (2010) presented the shape and sizes of 116 Galactic GCs and showed that several of the halo GCs have an elongated shape. More recently, Carballo-Bello et al. (2018) gave evidence for tidal tails around some Galactic GCs. In addition to the observations that confirm ongoing tidal effects over MW's satellites, there is evidence of stellar streams that do not have any known progenitor associated with them (Helmi et al., 1999; Duffau et al., 2006; Grillmair, 2009; Newberg et al., 2009, 2010; Vickers et al., 2016). These streams are thought to be the stripped stars of completely disrupted dwarf galaxies or GCs and their existence

supports the idea that the accretion of stellar substructures played a major role in forming the Galactic halo.

Knowing the full extent of tidal effects on MW's satellites is of thus of great importance to completely understand the processes if hierarchical accretion that formed our Galaxy and, in particular, built its stellar halo. Also, tidal effects play a major role in the formation and evolution of satellite dwarf galaxies and GCs. For dSph and UFD galaxies, Muñoz et al. (2008) created a library of simulated dSphs evolving inside DM halos and subjected to tidal forces from the MW's potential. They showed that a combination of DM halos plus tidal forces can reproduce the properties of dSphs, offering an alternative to the extended DM halo scenario previously accepted. More recently, Hammer et al. (2018) showed that there is a strong direct correlation between the total-to-stellar mass ratio and the ratio of the MW to dSph gravitational acceleration, suggesting that the line-of-sight velocity dispersion is induced by the Galactic gravitational acceleration. For GCs, it has been shown that the tidal field intensity in which a cluster formed and evolved has an impact on the cluster properties (e.g. Renaud et al., 2017).

One of the most important questions in the area of Galactic astronomy is whether the properties we see on satellites are mainly determined by their process of formation and secular evolution, or they are the result of the influence of the MW's gravitational potential over them. This is known as the "Nature vs Nurture" problem, and studying it aims to have a better picture of the role of the MW in shaping its satellite population and its history of formation and evolution.

A way to shed light on the "Nature vs Nurture" problem is to estimate how common and intense tidal effects are on satellite systems. To achieve this, deep and wide observations are necessary- One of the results of Muñoz et al. (2008) is that in most cases the imprints of tidal effects on the morphology of an object are only detectable at large radii and low surface brightness. The data used in this work have such characteristics. In what follows, we analyze the morphology of satellite dSphs, UFDs and outer halo GCs, to detect signatures of tidal effects.

In this part of the thesis, I use a matched-filter technique described by Rockosi et al. (2002) to determine the morphology of each satellite in our sample. This way, I show which objects are suffering from tidal disruption from the MW's gravitational pull and which show a regular morphology, devoid of clear signs of tidal effects. This information is important to better estimate the extent to which the presence of the MW is influencing the properties of satellite objects.

3.1 Determination of satellite's morphology

3.1.1 Matched-filter formulation

One common way of studying the morphology of a stellar cluster or nearby dwarf galaxy is to calculate the stellar density at different radii from the object's center to determine its isodensity contours. In this way, any departure from a regular morphology that appears as an overdensity of stars against the background would be reflected in these contours. To achieve

this task, we need a way to discriminate between the stars that belong to the object and the ones that are part of the background field.

We do this by using a matched-filter technique. The advantage of this technique versus other procedures is that it considers the number of background stars in the color-magnitude coordinates of a particular star to determine its probability of belonging to the object. For example, if a star is located in the main sequence of stellar population attributed to the object and in the same color-magnitude area there are a few background stars, then the star has a higher probability of being a member of the object compared to a star in the same color-magnitude position that is embedded in a large group of background stars. In other words, this technique uses the contrast between the object's stellar population and the background field to determine the membership of each star.

In this work, we use the matched-filter algorithm described in detail in Rockosi et al. (2002). Here, we briefly explain the theoretical basis of this technique. For a solid angle in the sky dΩ, the expected number density of stars in each bin of the CMD is given by

$$n_{\mathrm{tot,(i,j)}} = n_{\mathrm{obj,(i,j)}} + n_{\mathrm{bkg,(i,j)}} \tag{3.1}$$

where $n_{\mathrm{obj,(i,j)}}$ is the number density of stars that belong to the object (member stars) in each color-magnitude bin (i, j), and $n_{\mathrm{bkg,(i,j)}}$ is the number density of stars that are part of the background field in each color-magnitude bin (i, j). Note that the index i corresponds to the color coordinate in the CMD, while the index j, to the magnitude coordinate.

The quantity $n_{\mathrm{obj,(i,j)}}$ can be related to the number of member stars α inside dΩ by

$$n_{\mathrm{obj,(i,j)}} = \alpha f_{\mathrm{obj,(i,j)}} \tag{3.2}$$

where $f_{\mathrm{obj,(i,j)}}$ represents the probability density function of finding a member star in any color-magnitude bin (i, j).

Then, equation 3.1 becomes

$$n_{\mathrm{tot,(i,j)}} = \alpha f_{\mathrm{obj,(i,j)}} + n_{\mathrm{bkg,(i,j)}} \tag{3.3}$$

With this last expression, we can apply the following least-squares fit to estimate α, if we assume that the noise comes only from the background

$$\chi^2 = \sum_{\mathrm{i},j}^{(\mathrm{color,mag})} \frac{[n_{\mathrm{tot,(i,j)}} - (\alpha f_{\mathrm{obj,(i,j)}} + n_{\mathrm{bkg,(i,j)}})]^2}{n_{\mathrm{bkg,(i,j)}}} \tag{3.4}$$

By minimizing χ^2 with respect to α, the minimum least-square expression for α is

$$\alpha = \sum_{\mathrm{i},j}^{(\mathrm{color,mag})} \left(\frac{n_{\mathrm{tot,(i,j)}} f_{\mathrm{obj,(i,j)}}}{n_{\mathrm{bkg,(i,j)}}} - f_{\mathrm{obj,(i,j)}} \right) \Bigg/ \sum_{\mathrm{i},j}^{(\mathrm{color,mag})} \frac{f^2_{\mathrm{obj,(i,j)}}}{n_{\mathrm{bkg,(i,j)}}} \tag{3.5}$$

Finally, if we make the color-magnitude bin infinitesimally small, the binned distributions $f_{\mathrm{obj,(i,j)}}$ and $n_{\mathrm{bkg,(i,j)}}$ become the continuous distributions f_{cl}(color,mag) and n_{bkg}(color,mag), respectively, and the stars inside the dΩ solid angle become a collection of delta functions in the color-magnitude space δ_{stars}(color,mag). Then, Equation 3.5 has the form (see Kepner et al. (1999) for details on the mathematical derivation)

$$\begin{aligned} \alpha = \Bigg[\sum_{\mathrm{i},j}^{\mathrm{stars}} \frac{f_{\mathrm{cl}}(\mathrm{color,mag})}{n_{\mathrm{bkg}}(\mathrm{color,mag})} \delta_{\mathrm{stars}}(\mathrm{color,mag}) - \\ - \int f_{\mathrm{cl}} \mathrm{d(color,mag)} \Bigg] \Bigg/ \int \frac{f^2_{\mathrm{cl}}}{n_{\mathrm{bkg}}} \mathrm{d(color,mag)} \end{aligned} \tag{3.6}$$

In practice, what we do is create CMD bins small enough that only one star is inside each bin and solve the integrals in Equation 3.6 numerically, as a sum of discrete bins.

Equation 3.6 shows that it is possible to have an estimation of the number of member stars inside a specific solid angle dΩ if one has a good characterization of the stellar population of the object and of the background field near that object. By comparing this two diagrams, one weights each star when counting the number of member stars by the factor f_{cl}(color,mag)/n_{bkg}(color,mag).

The final result of the matched-filter technique is a quantification of how the number density of the satellite's member stars varies across the entire observed field.

3.1.2 Estimating the member star distributions

As we mentioned previously, $f_{\mathrm{obj,(i,j)}}$ represents the probability density function of finding a member star in a specific color-magnitude coordinate. In practice, one can build this distribution from a stellar population isochrone and initial mass function or an observed CMD of the object. In this work, we use the second approach.

The first step we do to estimate $f_{\mathrm{obj,(i,j)}}$ is selecting stars inside a defined radius from the center of the object. In general, we use a value near one object's half-light radius, except for extended objects where larger values are necessary to include more stars. We select stars from the center of the satellite because inside this area the contamination from background sources and foreground stars is minimum.

Second, we construct a CMD with bin sizes 0.1 for g magnitude and 0.01 for $g - r$ color.

In the third step, we apply a 2D convolution to the entire CMD, using a 2D Gaussian kernel. The idea behind this convolution is to smooth the granularity due to the bin size and

to recover large-scale patterns that better resemble the true distribution of member stars. It is important to mention that we do not apply a single kernel to the entire CMD. Instead, we divide the CMD into portions that contain several rows and all the columns and apply different Gaussian kernels to each portion. The kernel size for each CMD portion is defined by the magnitude and color errors. For each satellite, we determine the color error as a function of magnitude by fitting an exponential function to that parameter space, using all the stars in the sample (member and background stars). Then, for each portion of the CMD where we apply a convolution, we use the exponential function to determine the color errors for the central magnitude of the CMD portion. Finally, we build the 2D Gaussian kernel by setting its y-axis and x-axis dispersion equal to the color error, in units of bin numbers. The result of this is that the convolution accounts for the measurement errors in magnitude and color and does so differently for each magnitude portion in the CMD. Figure 3.1 shows the exponential function fitted to the color error as a function of magnitude for one of the satellites.

Finally, we interpolate the convolved CMD to obtain a more continuous $f_{\mathrm{obj,(i,j)}}$ estimation. In the interpolation process, we modify the bin size to 0.01 for magnitude and 0.001 for color.

As an example, the left panel of Figure 3.3 shows the estimated $f_{\mathrm{obj,(i,j)}}$ for the Palomar 14 GC.

3.1.3 Estimating the background distribution

To determine the background distribution in the CMD, we select stars from two rectangular areas far from the center of the satellite, to avoid the inclusion of the satellite stellar population. The areas are chosen by visually inspecting the plot of the celestial coordinates of the satellite.

We construct the initial $n_{\mathrm{bkg,(i,j)}}$ CMD using a bin size of 0.1 and 0.01 for the magnitude and color, respectively. Then, as for the case of $f_{\mathrm{obj,(i,j)}}$, we convolve the CMD using a 2D Gaussian kernel. However, in this case, we use the same kernel size for the entire CMD, without considering the magnitude range where the convolution is being applied. We do this because it is important that no $n_{\mathrm{bkg,(i,j)}}$ bin has a zero value, and we couldn't obtain satisfactory results by reproducing the convolution procedure previously explained. We found that testing different kernel sizes and using a unique 2D Gaussian kernel to the entire CMD produces better results. This is especially true for backgrounds with few stars, where a kernel of large size is necessary to smooth the CMD and achieve non-zero values in all bins.

Finally, as for $f_{\mathrm{obj,(i,j)}}$, we do a simple linear interpolation to have a bin size of 0.01 and 0.001 for magnitude and color, respectively.

As an example, the middle panel of Figure 3.3 shows the estimated $n_{\mathrm{bkg,(i,j)}}$ for the Palomar 14 GC.

3.1.4 Counting member stars

The goal is to determine the number density of member stars, α, across a defined area in the sky and use the values to generate isodensity contours. For this, we divide the field into

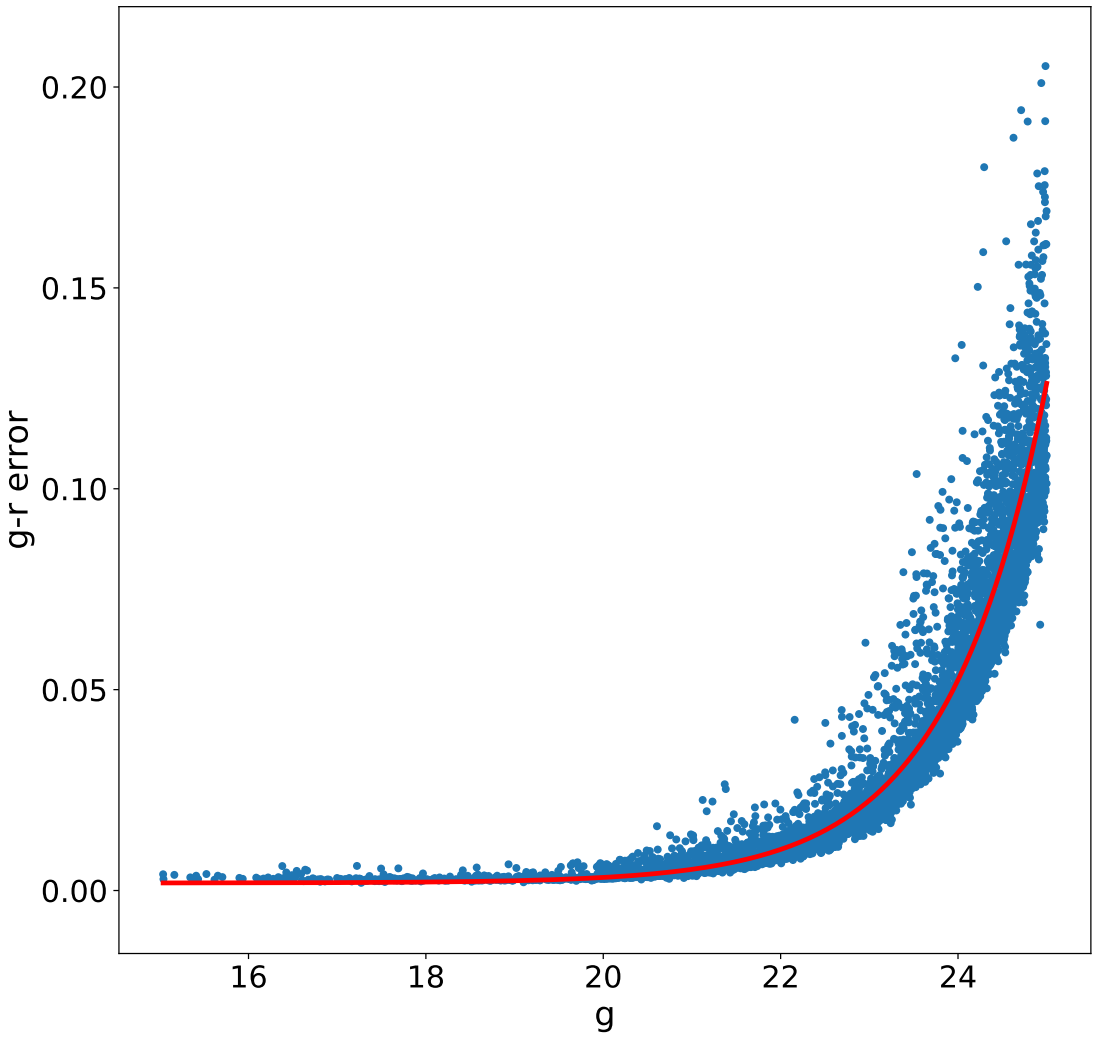

Figure 3.1: Exponential fit (red line) to the color error as a function of magnitude. Each blue circle corresponds to a star.

several solid angles dΩ of equal area and apply equation 3.6 in each of them. The size of dΩ is $0.08° \times 0.08°$, although in very few cases the bin size is slightly larger or smaller. The size of dΩ was determined so that we get enough resolution, but the computing time is not excessive. ^{oo} We have already build $f_{\mathrm{obj,(i,j)}}$ and $n_{\mathrm{bkg,(i,j)}}$ for a particular object. Now, for each solid angle dΩ we build $n_{\mathrm{tot,(i,j)}}$, which is the CMD of all the stars inside dΩ. Because we have to compare this CMD with $f_{\mathrm{obj,(i,j)}}$ and $n_{\mathrm{obj,(i,j)}}$, we use the same final bin size of 0.01 for magnitude and 0.001 for color. Also, this bin size empirically ensures that there is a maximum of one star per bin in $n_{\mathrm{tot,(i,j)}}$. This is a necessary condition for applying the weight $f_{\mathrm{obj,(i,j)}}/n_{\mathrm{bkg,(i,j)}}$ to a single star each time.

The final result of this process is a matrix of α values, each one for a particular $d\Omega$ of the entire field covered by the satellite. The last step is a smoothing of the α matrix by convolution with a 2D Gaussian kernel, to obtain large-scale density features. The kernel size is one pixel in both dimensions, and it translates to spatial dimensions according to the size of each solid angle $d\Omega$.

To build the isodensity contours, we define each level as c_n,

$$c_n = n\left(\frac{\alpha - \mu_{\alpha,\mathrm{bkg}}}{\sigma_{\alpha,\mathrm{bkg}}}\right) \tag{3.7}$$

where n is the level number, and $\mu_{\alpha,\mathrm{bkg}}$ and $\sigma_{\alpha,\mathrm{bkg}}$ are the mean and dispersion of the residual background, respectively. We define the residual background as the background density that was not removed during the matched-filter process. In theory, if there are no member stars in a particular $d\Omega$, then the background density should be zero. In practice, however, this might not be the case.

We model the distribution of the density of member stars and the density of the residual background as two Gaussians, where the residual component is represented by the Gaussian with the lowest mean and dispersion, and the member stars correspond to the Gaussian with the highest mean and dispersion. We extract each component by applying a Gaussian Mixture Model (GMM) to the count distribution of α. GMM uses Gaussians as basis distributions to detect subpopulations on the distribution of observed data. In our case, we force the total distribution to composed of two Gaussians. Figure 3.2 shows the result of applying the GMM algorithm to the Hercules UFD. As can be seen, the algorithm is capable of discriminating between the two subpopulations. Also, the background component is well described by a Gaussian, while the member star component follows a distribution different from the Gaussian. This last point is not relevant, however, because we use GMM to discriminate between the two subpopulations and we use the fitted Gaussian only in the case of the background density distribution.

With the GMM algorithm, we obtain $\mu_{\alpha,\mathrm{bkg}}$ and $\sigma_{\alpha,\mathrm{bkg}}$. In this way, using equation 3.7, the values in α are in units of dispersion of the residual background and we can plot the isodensity contours by specifying the level above $\sigma_{\alpha,\mathrm{bkg}}$ we want to show.

Note that the values for each isodensity contour (each one a factor of $\sigma_{\alpha,\mathrm{bkg}}$) do not necessarily represent probabilities in the traditional Gaussian sense. Therefore, to assess the significance of each contour, we perform bootstrap realizations for each object. We randomly draw RA and DEC coordinates values from uniform distributions spanning the whole observed area for each object, with replacement. We assign one of these coordinates to each star, keeping its magnitude and color values unaltered. In other words, we distribute the stars (member and background stars) uniformly across the observed area in the sky. We do this bootstrap nine times, an run our matched-filter algorithm on each of them. Because we did not change the magnitude and color values for each star, $f_{\mathrm{obj,(i,j)}}$ and $n_{\mathrm{bkg,(i,j)}}$ are the same as before the bootstrap, so we only need to calculate $n_{\mathrm{tot,(i,j)}}$ and α for each bootstrap instance. Finally, we measure $\mu_{\alpha,\mathrm{bkg}}$ and $\sigma_{\alpha,\mathrm{bkg}}$ for each bootstrap iteration to see how common each contour level is.

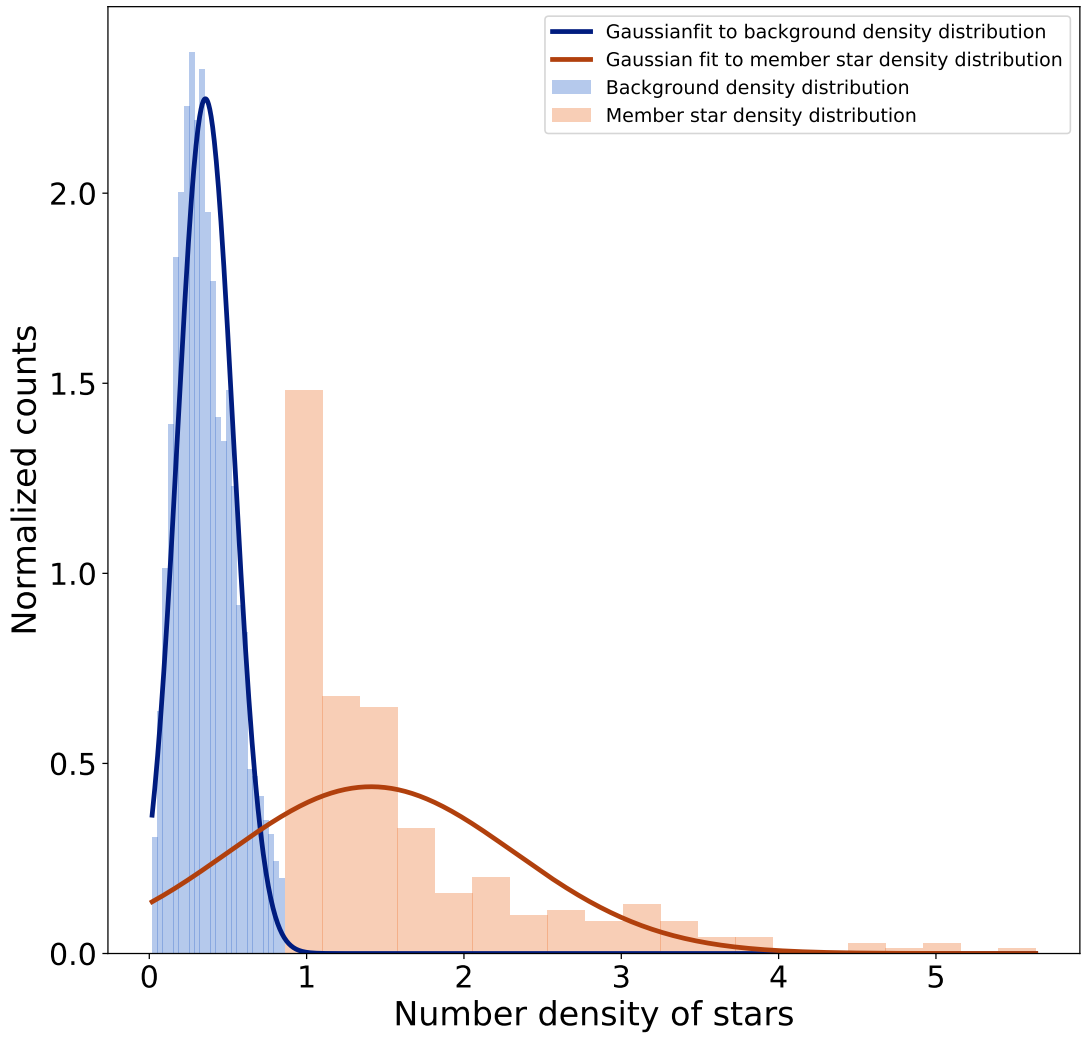

Figure 3.2: The residual background density distribution and the member star density distribution obtained by applying a GMM algorithm to the number density distribution of the Hercules UFD. The Gaussians used to discriminate between the two subpopulations are plotted as solid lines.

3.2 Results

We present our results in Figure 3.5 through Figure 3.31. We have divided the figures according to the type of satellite object they represent. Classical dSph galaxies are grouped from Figure 3.5 to Figure 3.8; UFD galaxies, from Figure 3.9 to Figure 3.18; GCs, from Figure 3.19 to Figure 3.28; and not classified objects, in Figures 3.30 and 3.31. In all cases, we plot the isodensity contours in the left panels, while the nine bootstrap iterations of the randomized positions of stars are shown in the right panels. For most objects, we plot

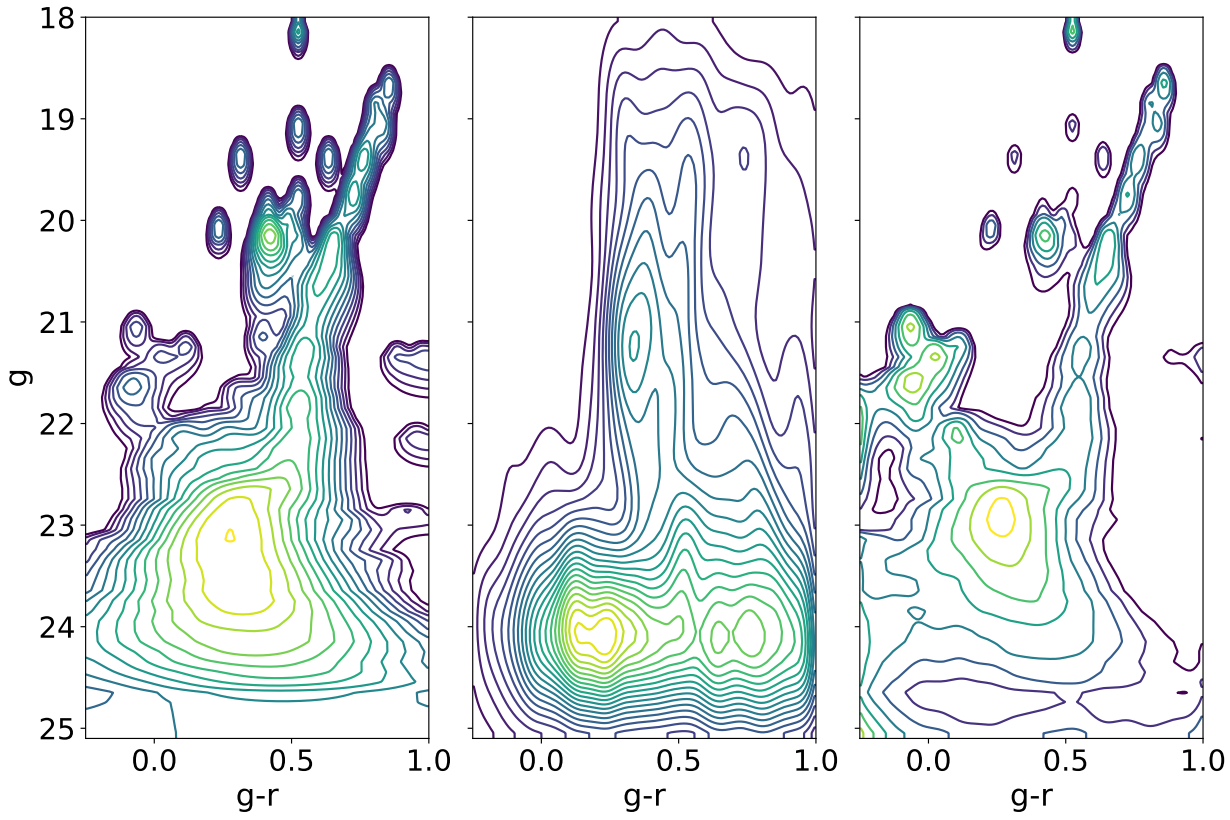

Figure 3.3: Estimated member star distribution (left panel), background star distribution (middle panel), and star weight distribution (right panel) for Palomar 14. The star weight in each color-magnitude bin is given by the factor $f_{\mathrm{obj,(i,j)}}/n_{\mathrm{bkg,(i,j)}}$. In all panels, yellow represents higher counts than purple.

contours from 3 to 20 $\sigma_{\alpha,\mathrm{bkg}}$, except for Leo I and Draco, where we plot from $1\sigma_{\alpha,\mathrm{bkg}}$ because the bootstrap iterations show that for these objects a $3\sigma_{\alpha,\mathrm{bkg}}$ was above the significant level. In the isodensity contours plot, we also include a red arrow that points to the center of the MW. The true origin of the arrow is the center of the satellite object, but we translate it to the upper part of the plot to avoid interference with the contours. The grey-scale image behind the contours is a 2D histogram of stellar densities, with black representing high stellar density and white, low stellar density.

3.2.1 Morphology of classical dSph galaxies

The isodensity contours of classical dSph galaxies reflect the fact that, as a family, these galaxies have a projected elliptical shape, except for Leo II, which has a more spherical morphology. Although an elliptical shape could be interpreted as suggestive of tidal stripping (interpreted as the departure from an inherent spherical shape), the truth is that by no means an elliptical shape is an indication of tidal effects. In fact, dwarf and giant elliptical galaxies have intrinsic elliptical shapes, even when found isolated. Sculptor, Carina, Sextans, Leo II, and Draco show regular morphological shapes with no obvious signs of tidal disruption, although the bulk of stars of Sextans is off-center, maybe due to some tidal interactions. Leo I shows some distorted external contours which may hint at some tidal effect. However, according to the bootstrap results, these contours are not significant, so no obvious signs of tidal effects are present in this galaxy either. The Ursa Minor galaxy (Figure 3.7) shows an elongated morphology, together with possible fragmentation of the inner parts, suggesting stronger tidal effects compared to the other classical dSph galaxies. Previous studies showed that member stars of this galaxy are well beyond the King tidal radius, which may be due to tidal stripping (Martínez-Delgado et al., 2001; Palma et al., 2003; Muñoz et al., 2005).

In summary, our results show that classical dSphs galaxies have regular morphologies, with no signs of evident tidal effects. This is in line with most previous studies of these satellites.

3.2.2 Morphology of UFD galaxies

In general, all UFD galaxies show some kind of irregular morphology, which might be interpreted as an indication of ongoing tidal disruption. However, it is important to keep in mind that the typically low number of member stars of these low-luminosity objects is an important source of noise (i.e., shot-noise due to statistics of low numbers) (e.g. Martin et al., 2008; Muñoz et al., 2012b) which can, in some cases, produce artificial features in the density contour maps.

From our maps, several UFD galaxies show morphological irregularities. Ursa Major II (Figure 3.9) shows an elongated and distorted shape, which seems to be partially in line with the direction to the center of the MW (given by the red arrow in the isodensity contours plot), consistent with the interpretation that its morphology is due to tidal effects. Also, the 10th level contour suggests the existence of two overdensities, which might have been produced by the splitting of the central parts. Ursa Major I (Figure 3.11) also shows a distorted and elongated shape with several overdensities in the central part, in agreement with previous findings (Okamoto et al., 2008), indicating strong tidal effects.

Another UFD galaxy that shows strong signs of tidal disruption is Hercules (Figure 3.15), given its elongated and distorted shape that is partially in line with the center of the MW. This dwarf galaxy is the one with the most evidence of tidal disruption, both photometric and spectroscopic (e.g. Coleman et al., 2007; Adén et al., 2009; Sand et al., 2009; Martin & Jin, 2010; Deason et al., 2012; Blaña et al., 2015; Garling et al., 2018). Segue 2 (Figure 3.9) and Willman 1 (Figure 3.11) also show irregular morphologies, suggesting some degree of tidal disruption. This is supported by previous studies (Kirby et al. (2013) and Willman et al. (2011), respectively).

There are interesting results for other UFD galaxies in our study. Segue 1 (Figure 3.10) shows a highly irregular morphology. However, Simon et al. (2011) concluded that Segue 1 is not suffering any tidal disruption. Boötes II (Figure 3.14) also reveals a distorted shape which, based on the bootstrap iterations, is significant from the 4th or 5th level. In contrast, Walsh et al. (2008) found no significant distortion in Boötes II's morphology. Some morphological distortion is present in Leo IV (Figure 3.12), but the bootstrap simulations show that the morphology is significant at high contour levels, which casts doubts about a true distortion. Both Boötes I and Reticulum II show an overall elliptical morphology, but they have more than one central overdensity, which may be splitting due to tidal effects. Finally, the Grus I and Tucana II UFD galaxies (both in Figure 3.17) show some hints of distortion. For both, the bootstrap simulation shows that the distortion is not significant. It is worth mentioning that both UFDs have a very low number of true member stars in their CMDs, so the inclusion of a few stars that belong to the field would affect the final morphology.

The rest of the UFD galaxies show no evident signs of disruption. Rather, they show a rounded or elliptical morphology with no distortions at the significant contour levels.

3.2.3 Morphology of outer halo GCs

Our results show that almost all of our outer halo GCs show regular morphology with no distortions attributable to tidal disruptions. There are, however, some cases that are worth discussing. Whiting 1 (Figure 3.19) shows some distortions in the outer parts, but it is known that it is embedded inside the debris of the Sagittarius dSph, making it difficult to assess its outer morphology. Koposov 2 (Figure 3.21) also has some degree of outer morphological irregularities. However, the bootstrap simulations show that they are not significant. This is expected because the low luminosity of this cluster makes it difficult to detect many member stars standing out from the background, even if the MegaCam photometry reaches a magnitude as deep as $g = 25$. Finally, Sohn et al. (2003) reported signs of tidal disruption for Palomar 4. However, our results do not show any evidence of that

Some clusters show different degrees of tidal disruption signs. Palomar 14 (Figure 3.26) shows significant evidence of tidal effects in its irregular external morphology. This is supported by previous studies (Jordi & Grebel, 2010; Sollima et al., 2011). Other interesting cases are Eridanus (Figure 3.20 and Palomar 15 (Figure 3.27). Myeong et al. (2017) reported tidal tails coming from these clusters, which are evident in their figures 1 and 2. In our results, we see some hint of tails in each cluster. However, our results do not reproduce the findings of Myeong et al. (2017).

An interesting fact of the morphology of outer halo GCs is that no object shows clear signs

of disruption. A possible explanation for this is that the MW tidal field has already completely disrupted the low-mass GCs and only the most massive ones have survived. Because GCs do not have any DM content that can resist the MW's tidal pull, low-mass GCs would be destroyed quickly, in comparison with UFDs that are currently being disrupted but that still exist due to the protection of their DM halo.

3.2.4 Morphology of not classified objects

Neither object shows clear signs of tidal disruption. One exception could be Phoenix II (Figure 3.31), which shows an elongated shape. However, the bootstrap simulations reveal that the significance of this distortion is very low because circular structures of high σ above the background were detected in every iteration. These structures represent member stars that are located in a CMD region where the background is not populated, giving those stars a high probability of being member stars. Because Phoenix II intrinsically has a low number of member stars, one single star that might not be a true member star, could be driving the elongated shape we see in the morphology figure. This is an example of how having a low number of member stars introduces high uncertainties on the derived parameters.

It is worth mentioning that all these objects are not populated by a large number of stars. Additionally, the observations come from the DES survey, which is not as deep as our MegaCam observations, reaching magnitudes of 24 in *g*. These limitations make difficult to obtain al well-populated, smooth distribution of members stars to be used in the matched-filter algorithm.

3.3 Discussion

Hammer et al. (2018) found a correlation between the total-to-stellar mass ratio of dSphs and UFDs and the ratio between the gravitational acceleration exerted by the MW over the satellite galaxy and its acceleration by internal gravity assuming the potential is created only by the stars. They interpret that correlation as an indication that the MW's *gravitational acceleration*, and not dark matter, drives the internal kinematics of the satellite. They also make the distinction between the effects of the MW's *gravitational acceleration* and those of the MW's *tidal acceleration*, showing that a correlation also exists for the latter, albeit not as strong (see their Figure 9).

In Hammer et al. (2019) the same authors argue that tidal shocks is the mechanism responsible for the observed kinematics in dSphs. In the context of that work, tidal shock occurs when a dwarf galaxy, which still has mass in the form of HI gas, enters the halo of the MW and interacts with its hot gas. By ram-pressure exerted by the MW's halo hot gas, the HI gas is rapidly stripped from the dwarf galaxy, creating a sudden decrease in self-gravity. This, in turn, allows for the stars to expand freely in all directions. Later, tidal forces from the MW would create an elongation along the direction of the MW gravitational force, which coincides with the line-of-sight. Thus, they propose that the observed velocity dispersion along the line-of-sight observed in dSphs is due to the effects of tidal shocks. The same shocks would prevent the dwarf galaxies from suffering mass loss, i.e., tidal stripping should be unimportant. Because our results explore the potential effects of tidal stripping on the satellites' morphology, we use our data to explore this last scenario.

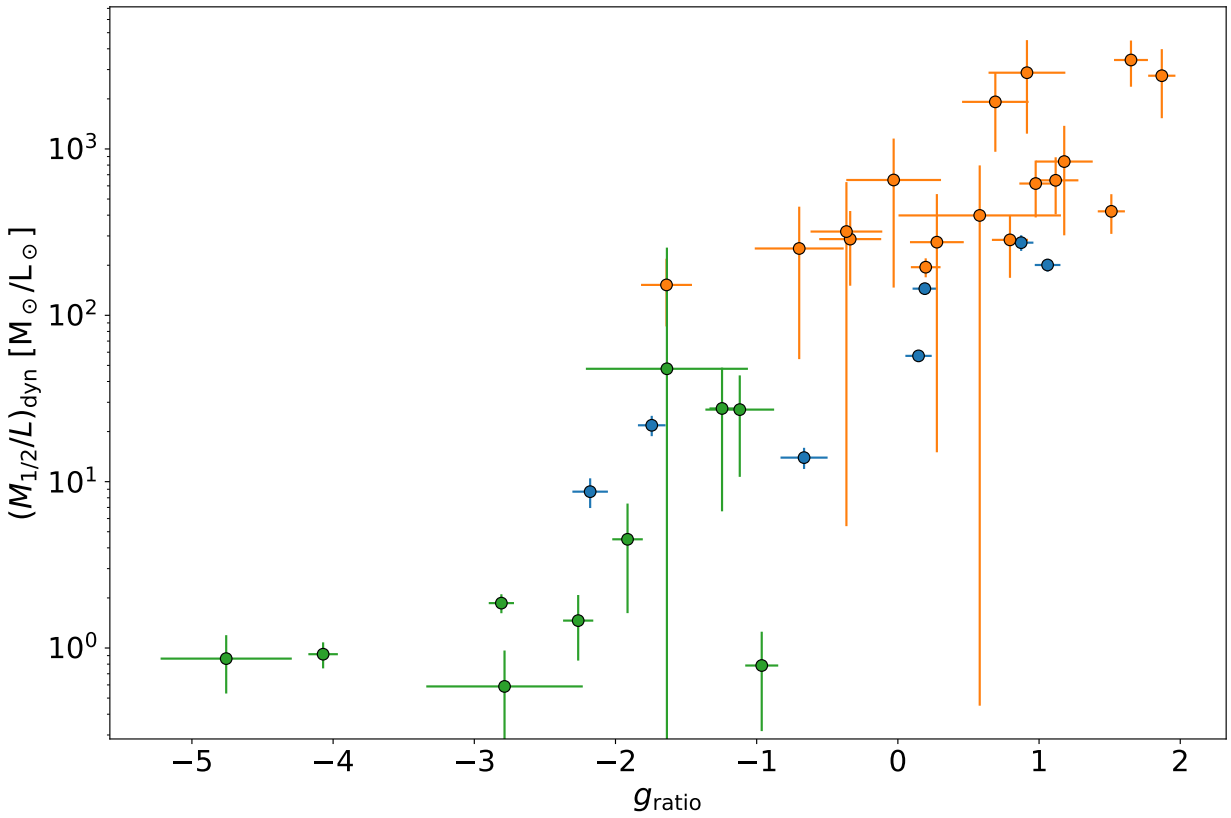

Figure 3.4: Dynamical mass-to-light ratio $(M_{1/2}/L_{1/2})_{\rm dyn}$ versus $g_{\rm ratio}$, a parameter that measures the ratio of tidal forces from the MW and internal gravity of the satellite object. A higher ratio indicates a higher influence of the MW tidal forces compared to the internal stellar gravity of the satellite object. Green circles are GCs, blue circles are classical dSphs and orange circles are UFDs.

Following the work of Hammer et al. (2018), we define $g_{\rm ratio}$, a parameter that measures the ratio of tidal forces of the MW to internal gravity of the satellite, as

$$g_{\rm ratio} \equiv \frac{g_{\rm MW,tides}}{g_{\rm sat,stars}} = \frac{2M_{\rm MW}(D_{\rm MW})}{M_{\rm stellar}} \left(\frac{r_{\rm half}}{D_{\rm MW}}\right)^3 \tag{3.8}$$

where $g_{\rm MW}$ is the tidal acceleration by the MW, $g_{\rm sat,stars}$ is the acceleration by the internal gravity of stars only in a satellite system, $D_{\rm MW}$ is the object's distance to the center of the MW, $M_{\rm MW}(D_{\rm MW})$ is the MW's mass inside radius $D_{\rm MW}$, $M_{\rm stellar}$ is the stellar mass of the satellite object, and $r_{\rm half}$ is the half-light radius of the satellite.

We note that by using only the stellar mass, Hammer et al. (2018) aimed at assessing how much of the velocity dispersion could come from tidal effects from the MW rather than from large amounts of DM. For $M_{\rm MW}$ we use the following expression (see Equation 17 from Sofue (2012)):

$$M_{\rm MW} = 4\pi\rho_0 h^3 \left(\log(X) - \frac{X}{1+X}\right) \tag{3.9}$$

where $\rho_0 = 1.06 \pm 0.14, M_\odot\,{\rm pc}^{-3}$, $h = 12.53 \pm 0.88\,{\rm kpc}$, and $X = D_{\rm MW}/h$. The remaining parameters to calculate $g_{\rm ratio}$ were obtained from Muñoz et al. (2018b).

To calculate the dynamical mass-to-light ratio, $(M_{1/2}/L_{1/2})_{\rm dyn}$ of each satellite, we first calculate the dynamical mass inside the 3D projected half-light radius using the Wolf et al. (2010) formula:

$$M_{1/2} = 4G^{-1}\sigma_{\rm p}^2 R_{\rm e} \tag{3.10}$$

where G is the gravitational constant, $\sigma_{\rm p}$ is the observed intrinsic velocity dispersion, and $R_{\rm e}$ is the 2D projected half-light radius. Finally, we divide this mass by half the total luminosity to obtain $(M_{1/2}/L_{1/2})_{\rm dyn}$. Velocity dispersions for each satellite are available in the literature but we choose to recalculate them to obtain kinematic data as homogeneous as possible. The radial velocities for each star are obtained from the references specified in Table 3.1 in the column "Kinematic data references". We calculate $\sigma_{\rm p}$ using the methodology of Walker et al. (2006), where the following logarithmic probability is maximized:

$$\ln(p) = -\frac{1}{2}\sum_{\rm i=1}^{N}\ln(\sigma_{\rm i}^2 + \sigma_p^2) - \frac{1}{2}\sum_{\rm i=1}^{N}\frac{(v_{\rm i} - \langle v_r\rangle)^2}{\sigma_{\rm i}^2 + \sigma_p^2} - \frac{N}{2}\ln(2\pi) \tag{3.11}$$

Here, $v_{\rm i}$ is the radial velocity of a single star, $\sigma_{\rm i}$ is the observed velocity dispersion of a single star, and N is the total number of stars. Note that the mean radial velocity $\langle v_r\rangle$ is also calculated, but it is not used in this work. To derive the confidence interval of $\sigma_{\rm p}$, we estimate 68% confidence intervals using the covariance matrix variances as described in Walker et al. (2006). The resulting values for all kinematical parameters as well as the $g_{\rm ratio}$ are listed in Table 3.1. Note that this table does not list all the satellites for which we have isodensity contours. This is because there is no kinematic information in the literature for all objects in our sample.

Figure 3.4 shows the relation between $g_{\rm ratio}$ and $(M_{1/2}/L_{1/2})_{\rm dyn}$, including Globular Clusters, which Hammer et al. (2018) did not include. A direct correlation between the two variables is clear. This is a high and significant correlation, having a Spearman's coefficient (ρ) of 0.87 and a $\rm p-value \sim 3.1\times10^{-11}$. If we only consider dSph and UFD dwarf galaxies, we get $\rho = 0.72$ and $\rm p-value \sim 6.3\times10^{-5}$, still a significant correlation but weaker than the one including GCs. We can also consider each group of satellites (GC, dSphs, and UFD) separately. UFDs and dSphs follow a clear correlation, with UFDs having in general higher values for both $g_{\rm ratio}$ and $(M_{1/2}/L_{1/2})_{\rm dyn}$ than dSphs. On the other hand, GCs do not follow any significant correlation ($\rho = 0.38$, p-value = 0.28). Perhaps the most important feature of GCs as a group is that they occupy an area different than dwarf galaxies. In general, GCs have at the same time lower values of $g_{\rm ratio}$ and $(M_{1/2}/L_{1/2})_{\rm dyn}$.

Following the reasoning of Hammer et al. (2018), the correlation of Figure 3.4 is consistent with the fact that the observed values for velocity dispersion might be due to tidal effects from the MW instead of a result of dynamical equilibrium inside a DM halo. In this interpretation, the derived total mass-to-light ratios might be overestimated, because they are calculated directly from the velocity dispersion values. One way to get some insight about this is to check whether the satellites that suffer the most from the MW's tidal pull (i.e., the ones with the highest $g_{\rm ratio}$) show any evidence of tidal effects in our isodensity plots. The idea behind this is to see at which values of $g_{\rm ratio}$ the tidal effects might become observable (in principle one could expect this to happen for $g_{\rm ratio} > 0$), and if the strongly affected satellites concentrate at the highest values of $g_{\rm ratio}$.

From the analysis in Section 3.2, we now that the UFDs that show morphologies potentially associated with tidal effects are Ursa Major II, Ursa Major I, Hercules, Segue 1, Boötes II, Boötes I, Reticulum II and Leo IV. All of these dwarf galaxies are located at the highest values of $\log g_{\rm ratio}$, starting from ~ 0.5. Regarding classical dSphs, there are two of them with values near $\log(g_{\rm ratio}) \sim 1$, Ursa Minor and Sextans. Consistent with our morphological maps, both dSphs show signs of potential disruption. The rest of the dSphs all have fairly regular morphologies and are located at relatively low or negative values of $\log(g_{\rm ratio})$. In the case of GCs, they are mostly located at low values of $\log(g_{\rm ratio})$. This is expected because from our results no GC shows clear signs of tidal effects.

Does the above necessarily imply that the observed mass-to-light ratios are driven by the MW tidal acceleration instead of a true high DM content? Several authors, (e.g., Muñoz et al. 2008) used $N-$body simulations to show that tidal disruption inflates the velocity dispersion of stars at large radii from the dSph center, while the central velocity dispersion is mostly unaffected and in agreement with the supposition of dynamical equilibrium almost until the moment the satellite becomes completely unbound. Several other studies (Law et al., 2005; Sohn et al., 2007; Klimentowski et al., 2007) have shown that classical dSphs can be embedded inside DM halos and, at the same, be suffering from tidal disruption. More recently, Iorio et al. (2019) used state-of-the-art photometric and spectroscopic observations of stars in the Sculptor dSph in order to adapt an $N-$body simulation of a Sculptor-like satellite dSph orbiting in a MW-like potential. They found that the stellar component of the galaxy was not affected by the MW's tidal tides, while $\approx 30-60\%$ of the DM halo is stripped. For UFDs, Fellhauer et al. (2008) performed $N-$body simulations of a Bootes I-like UFD, and concluded that tidal effects could not significantly inflate the central velocity dispersion of the satellite.

We propose here a different scenario that may explain the correlation of figure 3.4. A satellite that is being strongly tidally affected is expected to be losing both dark and luminous (stellar) matter. Therefore, the quantity $M_\star$ and the total DM should be lower than the original quantities that the satellite had before suffering tidal disruption. However, the quantity $M_{1/2}$ (i.e. the dynamical mass inside the 3D de-projected half-light radius) should be robust to tidal stripping and remain quite similar to the original value.

Now, note that the $g_{\rm ratio}$ has a $M_\star$ term in the denominator. Then, if two satellites had the same original stellar mass before entering the MW's potential, and having all the other parameters equal, the one that is being tidally disrupted the most should have a lower current

$M_\star$. In consequence, the $g_{\rm ratio}$ for the tidally-disrupted satellite should be artificially higher.

In the same vein, the $(M_{1/2}/L_{1/2})_{\rm dyn}$ term has a luminosity quantity in the denominator. The luminosity is directly proportional to the stellar mass. Now, remember that $M_{1/2}$ is robust to tidal effects, while L would decrease in the case of tidal disruption. Then, for two satellites with the same initial mass-to-light ratio, the one suffering from tidal disruption should have a higher current $(M_{1/2}/L_{1/2})_{\rm dyn}$, because its luminosity has decreased by losing stellar mass.

In this way, i.e., if tidal disruption is affecting a fraction of satellites (and to different degrees) it should be natural for a correlation like the one in Figure 3.4 to appear. The results presented above are remarkably in line with this explanation: satellites that have strong signs of tidal disruption show the highest $g_{\rm ratio}$ and the highest $(M_{1/2}/L_{1/2})_{\rm dyn}$.

Simulations of tidally disrupting satellites including both luminous and dark matter could be used to test if the correlation of Figure 3.4 can be reproduced. In particular, more simulations of satellites with UFD characteristics should be performed, because our results indicate that the strongest tidal effects are currently happening in this regime of MW's satellites. This would allow a high-contrast comparison with simulations of satellites that do not show strong tidal effects, like most of the dSph galaxies.

Table 3.1: Kinematic and derived parameters.

Name	Type	$D_{\rm MW}$[a] (kpc)	$\log M_\star$[a]	$\log L_\star$[a]	$\sigma_{\rm p}$ (km s^{-1})	$\log(M/L)_{\rm dyn}$	$\log g_{\rm ratio}$	Kinematic data references
Sculptor	dSph	86.1	6.60 ± 0.04	6.39 ± 0.04	9.25 ± 0.19	1.14 ± 0.06	-0.66 ± 0.17	1
Carina	dSph	106.7	6.07 ± 0.02	5.70 ± 0.02	7.01 ± 0.20	1.76 ± 0.03	0.15 ± 0.09	1,5
Leo I	dSph	256.0	7.15 ± 0.08	6.63 ± 0.08	9.05 ± 0.38	0.94 ± 0.09	-2.18 ± 0.13	11
Sextans	dSph	89.2	5.78 ± 0.02	5.40 ± 0.02	7.83 ± 0.29	2.30 ± 0.04	1.06 ± 0.09	1
Leo II	dSph	235.7	6.32 ± 0.01	5.79 ± 0.01	6.56 ± 0.45	1.34 ± 0.06	-1.74 ± 0.10	13
Ursa Minor	dSph	78.0	5.85 ± 0.01	5.54 ± 0.01	11.78 ± 0.62	2.44 ± 0.05	0.87 ± 0.09	19
Draco	dSph	76.0	5.81 ± 0.01	5.40 ± 0.01	9.71 ± 0.32	2.16 ± 0.03	0.19 ± 0.09	21
Segue 2	UFD	41.2	3.03 ± 0.16	2.66 ± 0.16	2.36 ± 0.61	2.92 ± 0.28	1.18 ± 0.20	2,3
Ursa Major II	UFD	38.5	4.00 ± 0.06	3.60 ± 0.06	6.74 ± 1.42	3.44 ± 0.19	1.87 ± 0.10	7
Leo T	UFD	422.1	5.43 ± 0.04	5.02 ± 0.04	7.52 ± 1.55	2.18 ± 0.19	-1.64 ± 0.18	7
Segue 1	UFD	28.1	2.79 ± 0.18	2.49 ± 0.18	4.25 ± 0.79	3.46 ± 0.25	0.91 ± 0.27	10
Ursa Major I	UFD	101.9	4.24 ± 0.06	3.86 ± 0.06	7.53 ± 1.03	3.53 ± 0.13	1.65 ± 0.12	7
Leo V	UFD	178.8	4.04 ± 0.09	3.68 ± 0.09	3.54 ± 1.28	2.40 ± 0.34	-0.70 ± 0.31	1
Leo IV	UFD	154.6	4.28 ± 0.06	3.94 ± 0.06	3.32 ± 1.54	2.44 ± 0.41	0.28 ± 0.19	7
Coma Berenices	UFD	45.2	4.05 ± 0.06	3.67 ± 0.06	4.65 ± 0.80	2.79 ± 0.16	0.98 ± 0.12	7
Canes Venatici II	UFD	160.7	4.19 ± 0.01	3.98 ± 0.01	4.58 ± 1.03	2.46 ± 0.21	-0.34 ± 0.22	7
Canes Venatici I	UFD	217.8	5.85 ± 0.02	5.43 ± 0.02	7.61 ± 0.45	2.29 ± 0.06	0.20 ± 0.11	7
Bootes II	UFD	39.8	3.54 ± 0.12	3.08 ± 0.12	5.77 ± 1.12	3.28 ± 0.22	0.69 ± 0.24	4,15
Bootes I	UFD	63.5	4.70 ± 0.04	4.34 ± 0.04	4.79 ± 0.60	2.62 ± 0.12	1.51 ± 0.10	16
Hercules	UFD	126.2	4.53 ± 0.04	4.24 ± 0.04	5.13 ± 0.90	2.81 ± 0.16	1.12 ± 0.16	7
Pisces II	UFD	181.1	3.98 ± 0.10	3.60 ± 0.10	3.25 ± 1.53	2.50 ± 0.43	-0.36 ± 0.25	23
Horologium I	UFD	79.3	3.69 ± 0.15	3.38 ± 0.15	4.87 ± 1.60	2.81 ± 0.34	-0.03 ± 0.34	25
Reticulum II	UFD	31.5	3.81 ± 0.10	3.52 ± 0.10	3.22 ± 0.54	2.45 ± 0.18	0.79 ± 0.13	21
NGC 2419	GC	90.4	5.93 ± 0.01	5.72 ± 0.01	4.52 ± 0.29	0.27 ± 0.06	-2.81 ± 0.09	6
Palomar 3	GC	96.0	4.61 ± 0.05	4.09 ± 0.05	1.24 ± 0.39	0.65 ± 0.28	-1.91 ± 0.11	9
Palomar 4	GC	111.5	4.87 ± 0.04	4.29 ± 0.04	0.87 ± 0.18	0.16 ± 0.18	-2.26 ± 0.11	14
NGC 5694	GC	29.1	5.45 ± 0.03	5.10 ± 0.03	3.81 ± 0.31	-0.04 ± 0.08	-4.07 ± 0.10	17

Continued on next page

Table 3.1 – *Continued from previous page*

Name	Type	$D_{\rm MW}$[a] (kpc)	$\log M_\star$[a]	$\log L_\star$[a]	$\sigma_{\rm p}$ (km s^{-1})	$\log(M/L)_{\rm dyn}$	$\log g_{\rm ratio}$	Kinematic data references
NGC 5824	GC	25.6	5.97 ± 0.01	5.68 ± 0.01	6.70 ± 1.28	-0.06 ± 0.17	-4.76 ± 0.46	18
Palomar 14	GC	71.3	4.59 ± 0.06	4.04 ± 0.06	0.38 ± 0.11	-0.11 ± 0.26	-0.96 ± 0.12	20
Segue 3	GC	25.5	2.57 ± 0.15	2.36 ± 0.15	1.20 ± 2.60	1.68 ± 1.89	-1.64 ± 0.57	22
Palomar 13	GC	27.1	3.42 ± 0.12	3.05 ± 0.12	1.31 ± 0.35	1.43 ± 0.26	-1.12 ± 0.24	24
NGC 7492	GC	25.4	4.80 ± 0.01	4.36 ± 0.01	0.87 ± 0.28	-0.23 ± 0.28	-2.79 ± 0.55	9

Sources for radial velocity and velocity dispersion for each star: (1) Walker et al. (2009b), (2) Kirby et al. (2013), (3) Belokurov et al. (2009), (4) Geha (unpublished), (5) Muñoz et al. (2006), (6) Ibata et al. (2011), (7) Simon & Geha (2007), (8) Palma et al. (2000), (9) Côt'e (unpublished), (10) Simon et al. (2011), (11) Mateo et al. (2008), (12) Willman et al. (2011), (13) Koch et al. (2007), (14) Frank et al. (2012), (15) Koch et al. (2009), (16) Koposov et al. (2011), (17) Bellazzini et al. (2015), (18) Da Costa et al. (2014), (19) Armandroff et al. (1995), (20) Jordi et al. (2009), (21) Walker et al. (2015), (22) Fadely et al. (2011), (23) Kirby et al. (2015a), (24) Bradford et al. (2011), (25) Koposov et al. (2015).

[a] Values taken from Muñoz et al. (2018b)

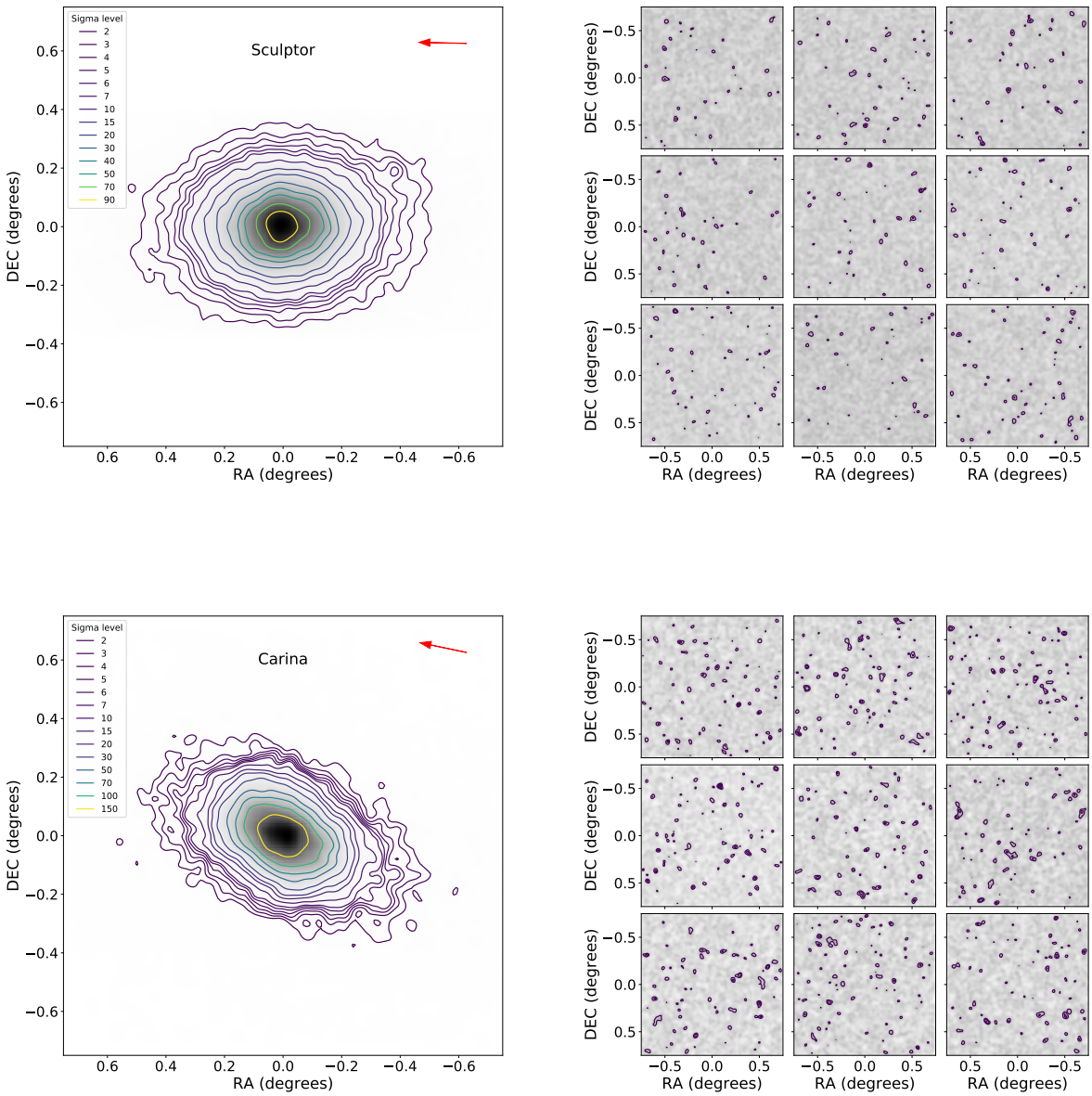

Figure 3.5: Matched-filter results for Sculptor and Carina dSphs. Left panels: isodensity contours for different levels of above the residual background noise. Right panels: Bootstrap iterations for the determination of isodensity contours, made by uniformly randomizing the position of stars across the field-of-view. The red arrow points to the center of the MW.

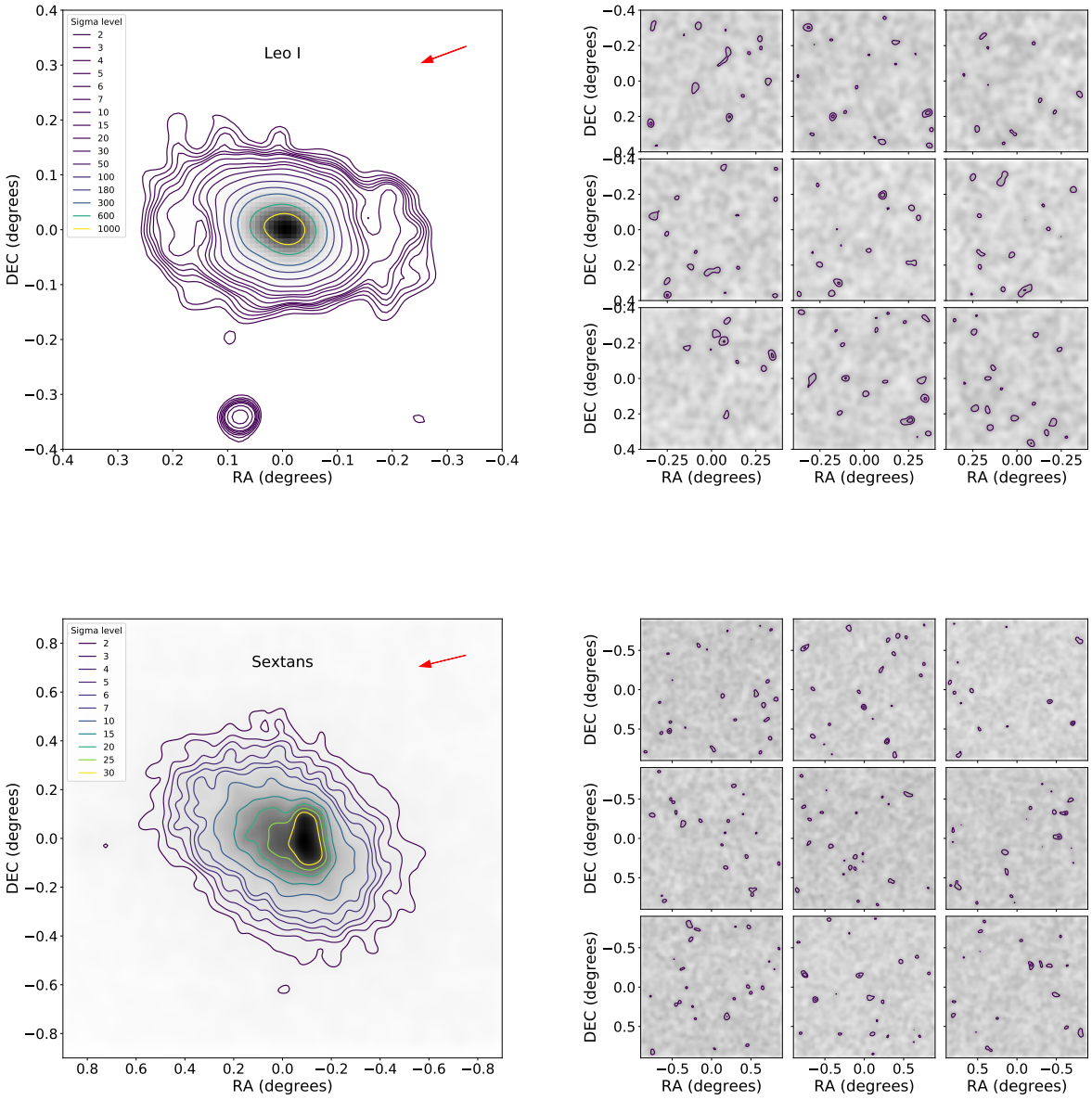

Figure 3.6: Same as Figure 3.5 but for Leo I and Sextans.

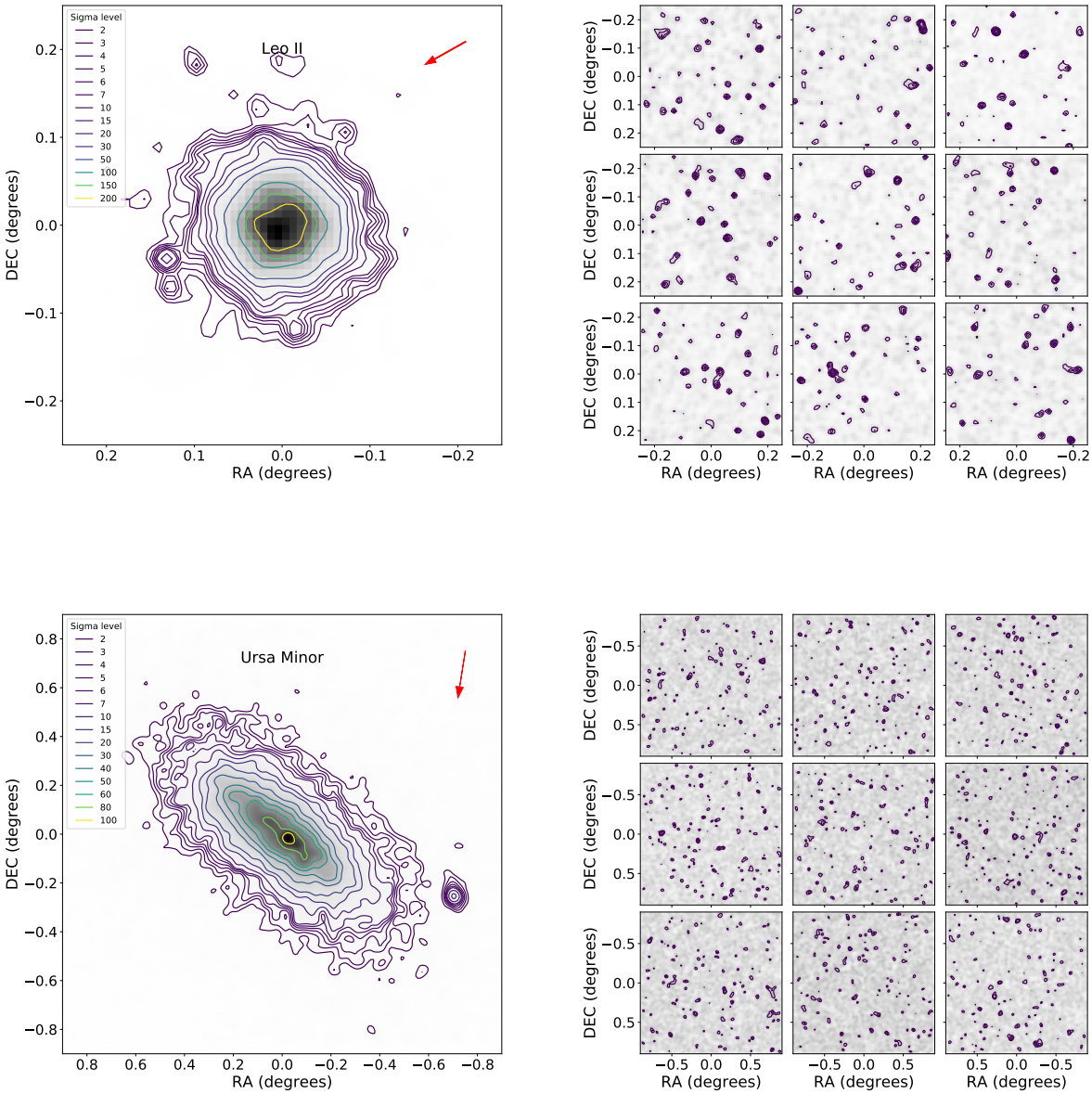

Figure 3.7: Same as Figure 3.5 but for Leo II and Ursa Minor I.

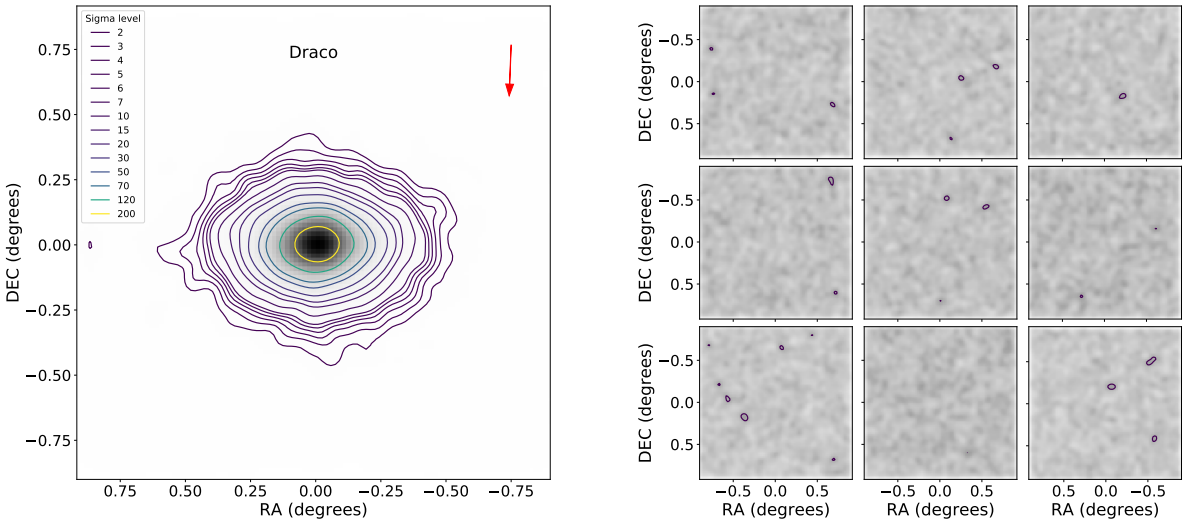

Figure 3.8: Same as Figure 3.5 but for Draco.

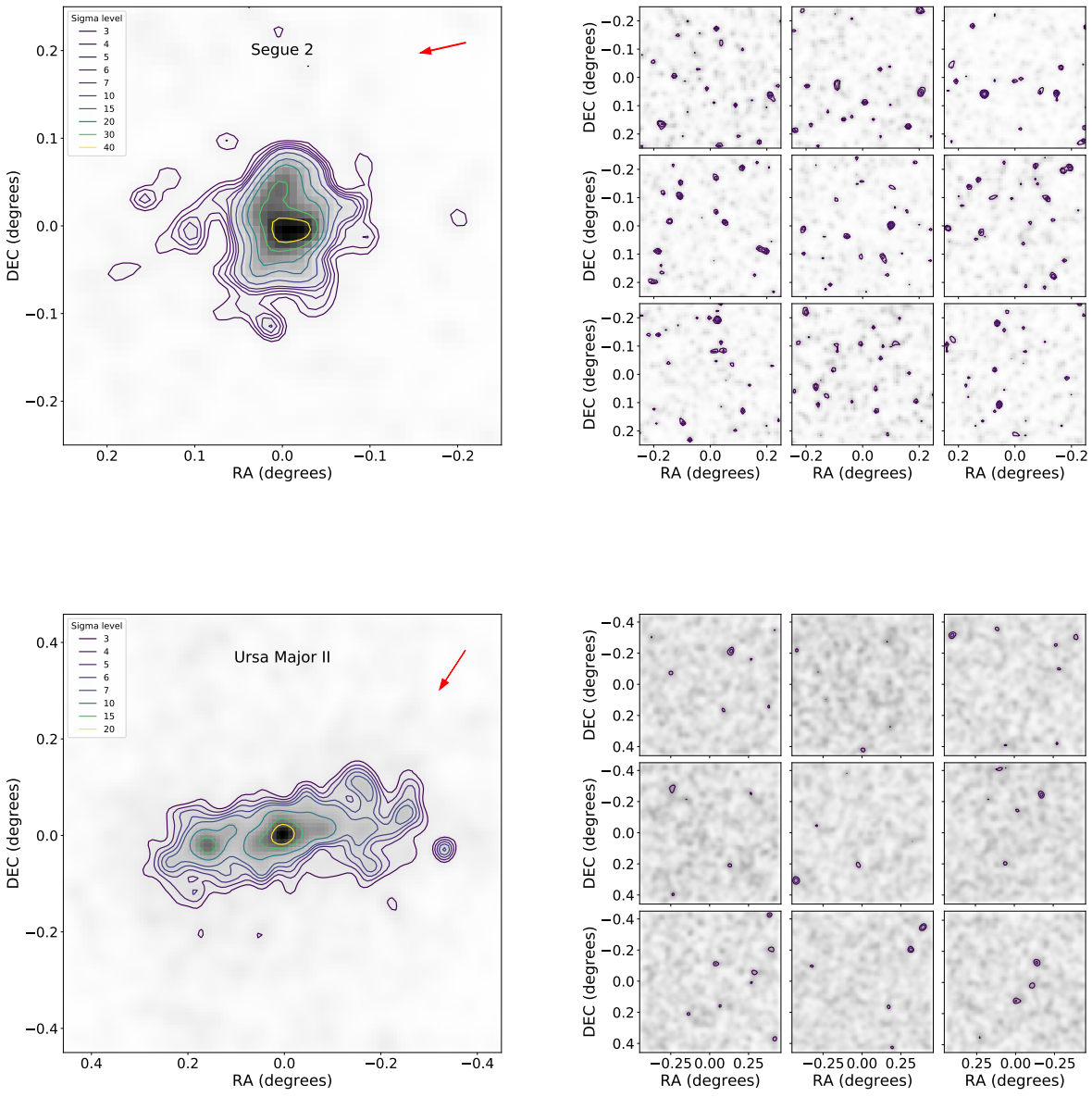

Figure 3.9: Matched-filter results for Segue 2 and Ursa Major II UFDs. Left panels: isodensity contours for different levels of above the residual background noise. Right panels: Bootstrap iterations for the determination of isodensity contours, made by uniformly randomizing the position of stars across the field-of-view. The red arrow points to the center of the MW.

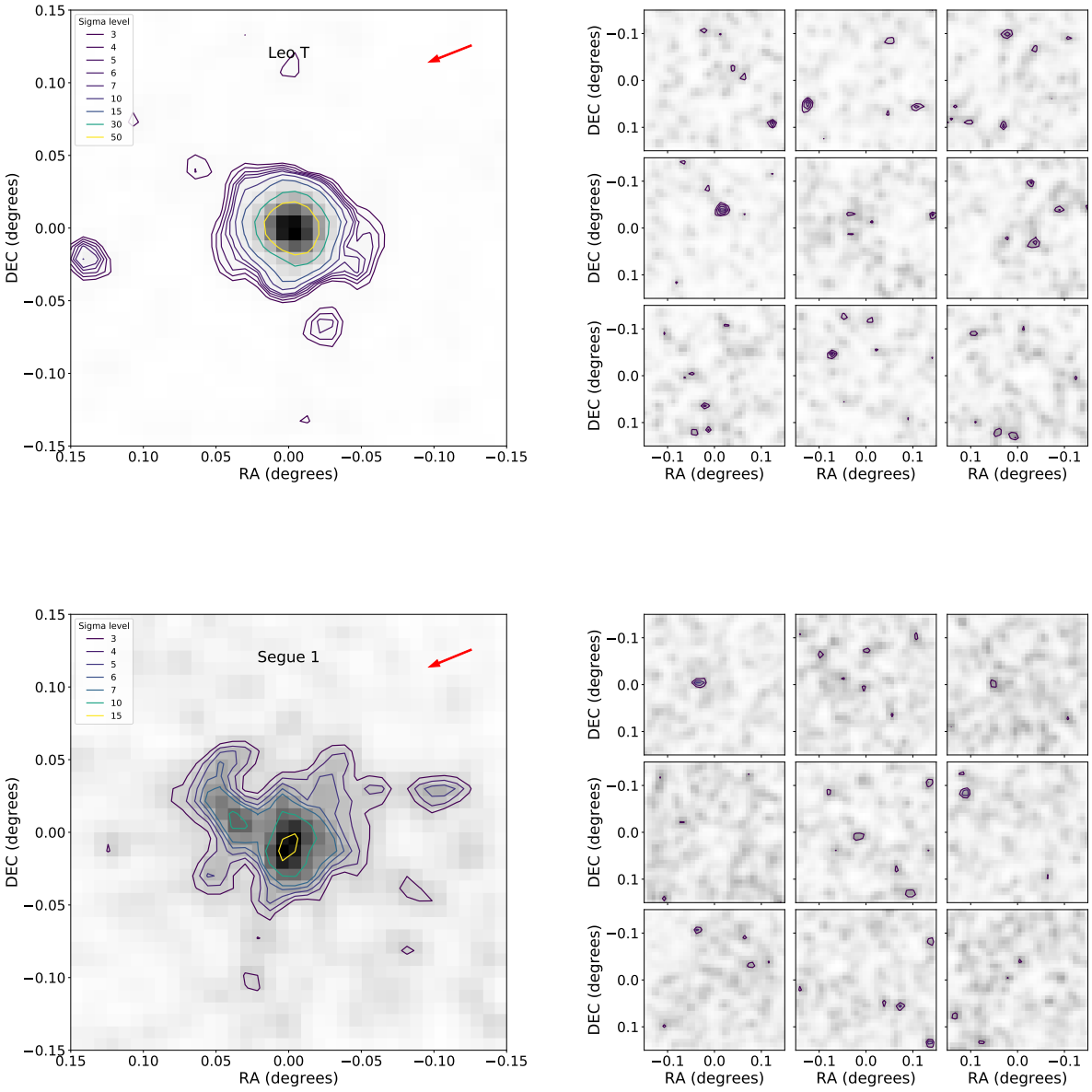

Figure 3.10: Same as Figure 3.9 but for Leo T and Segue 1 UFDs.

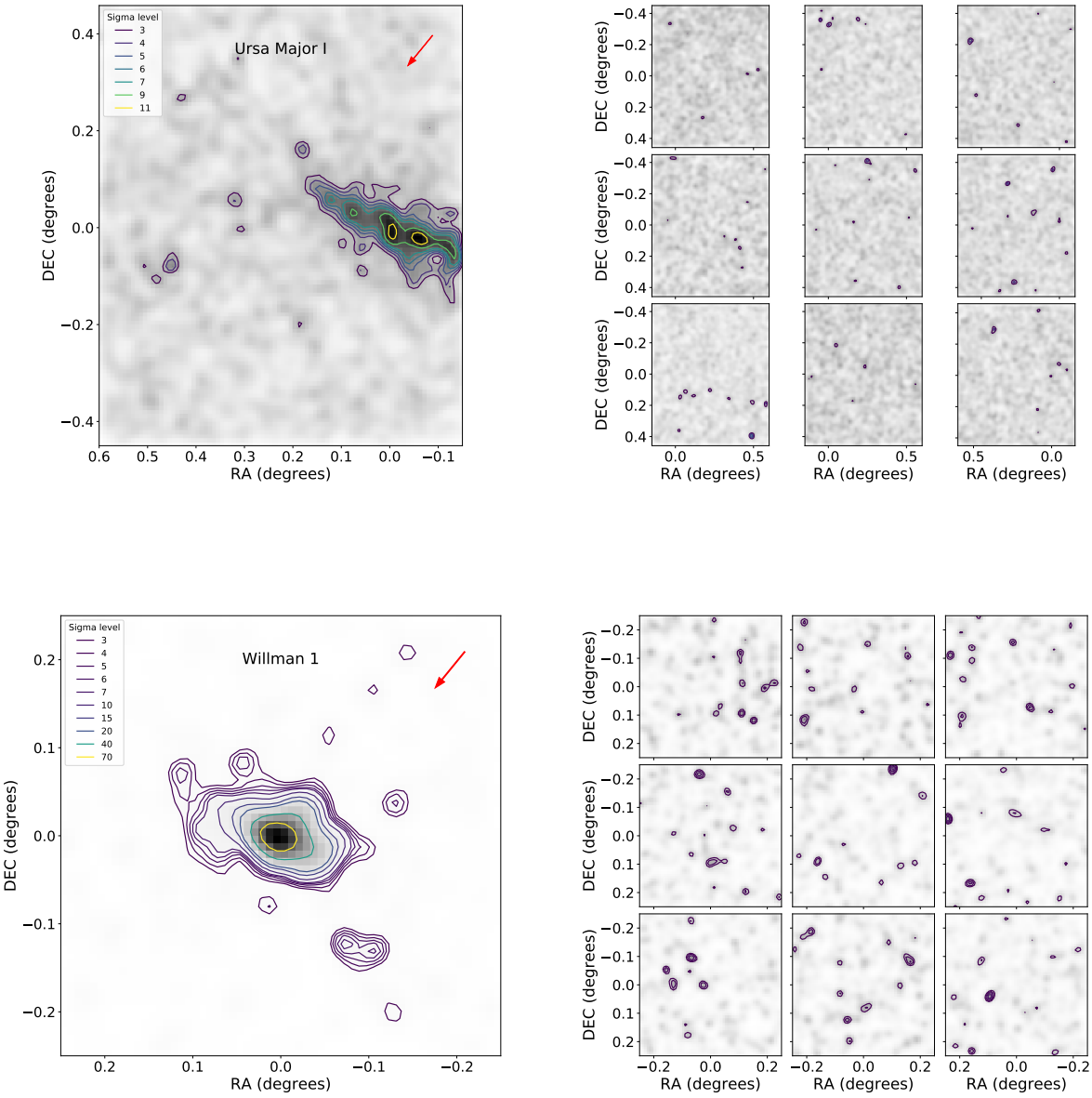

Figure 3.11: Same as Figure 3.9 but for Ursa Major I and Willman I UFDs.

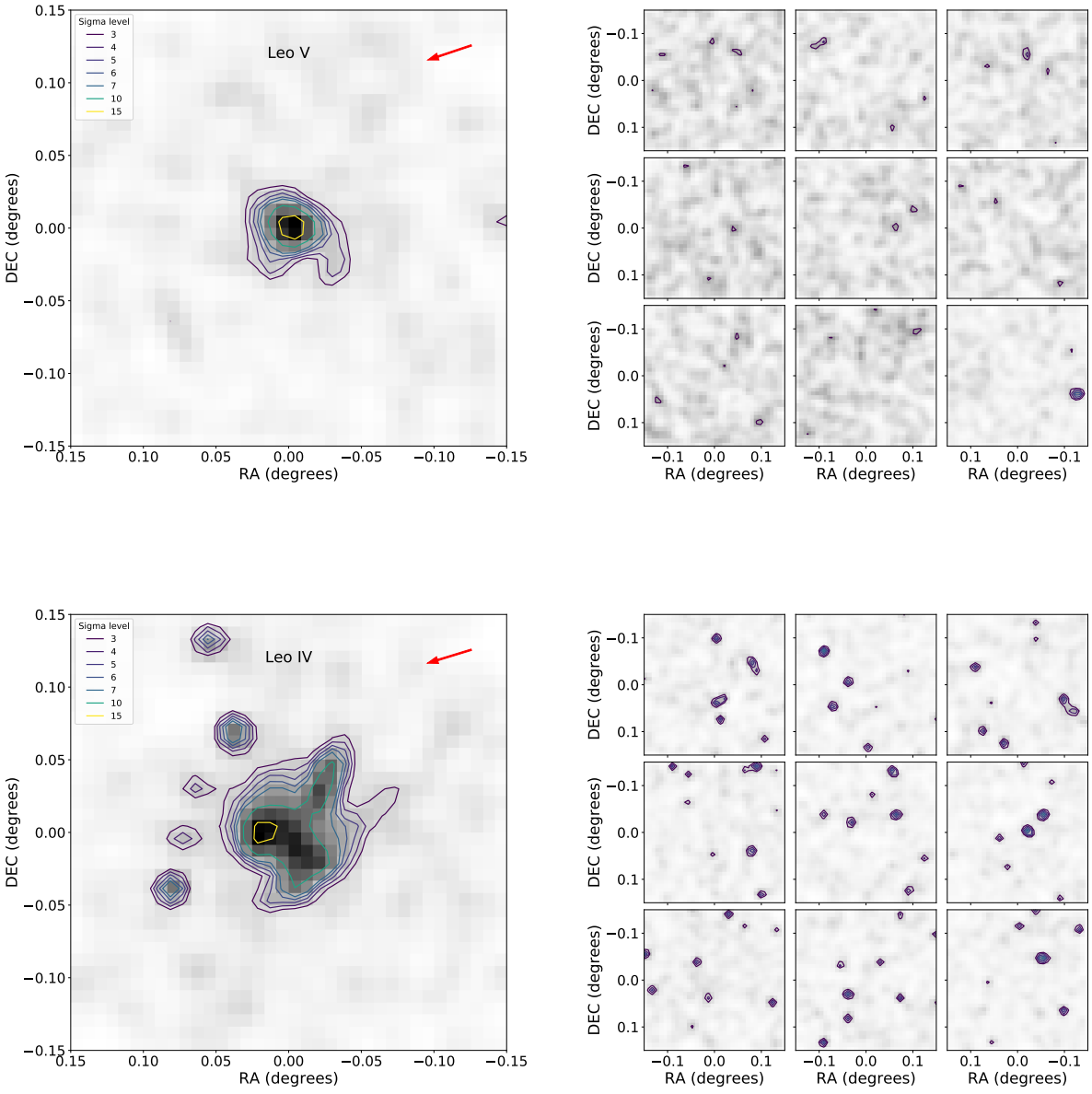

Figure 3.12: Same as Figure 3.9 but for Leo V and Leo IV UFDs.

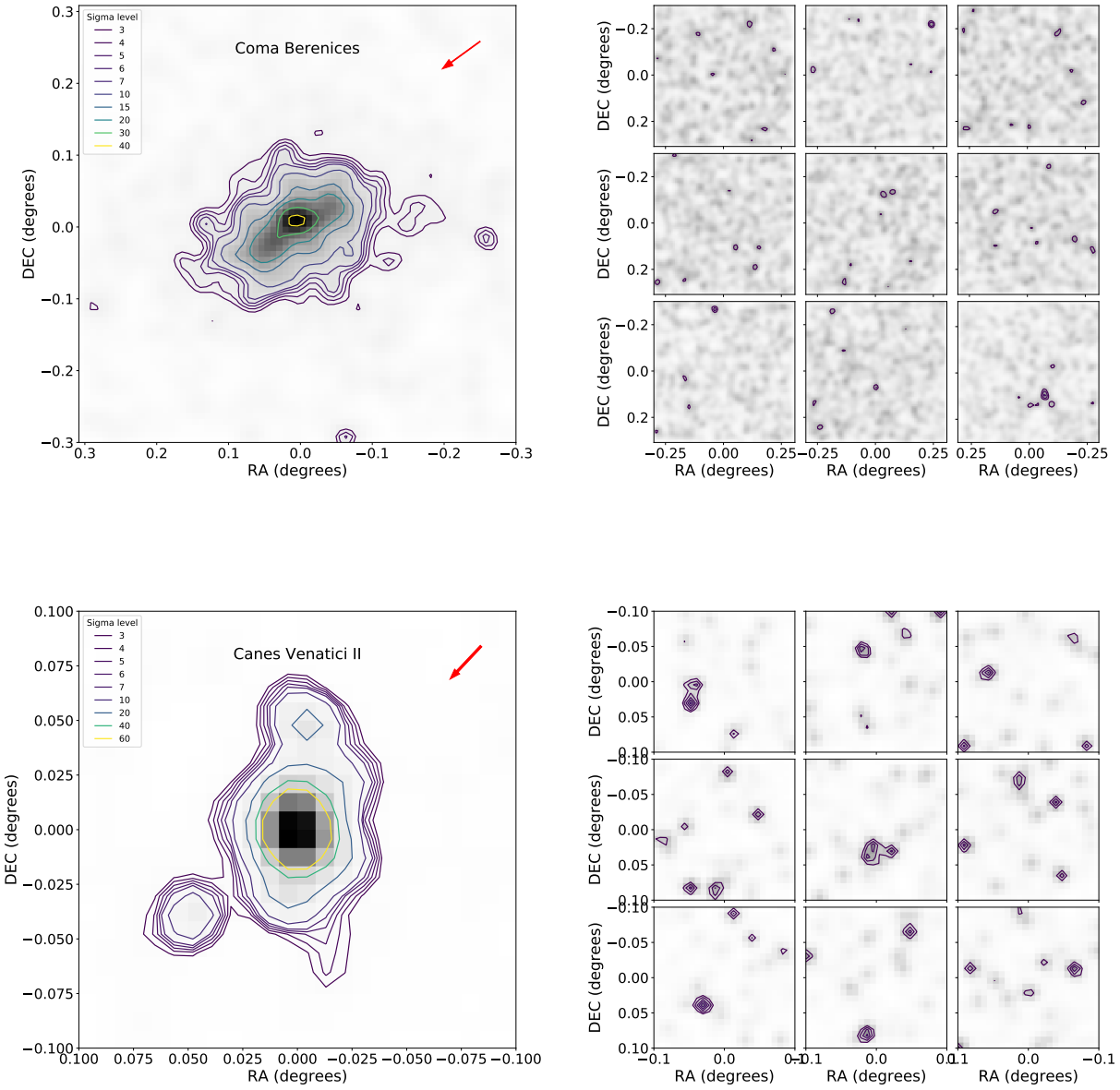

Figure 3.13: Same as Figure 3.9 but for Coma Berenices and Canes Venatici II UFDs.

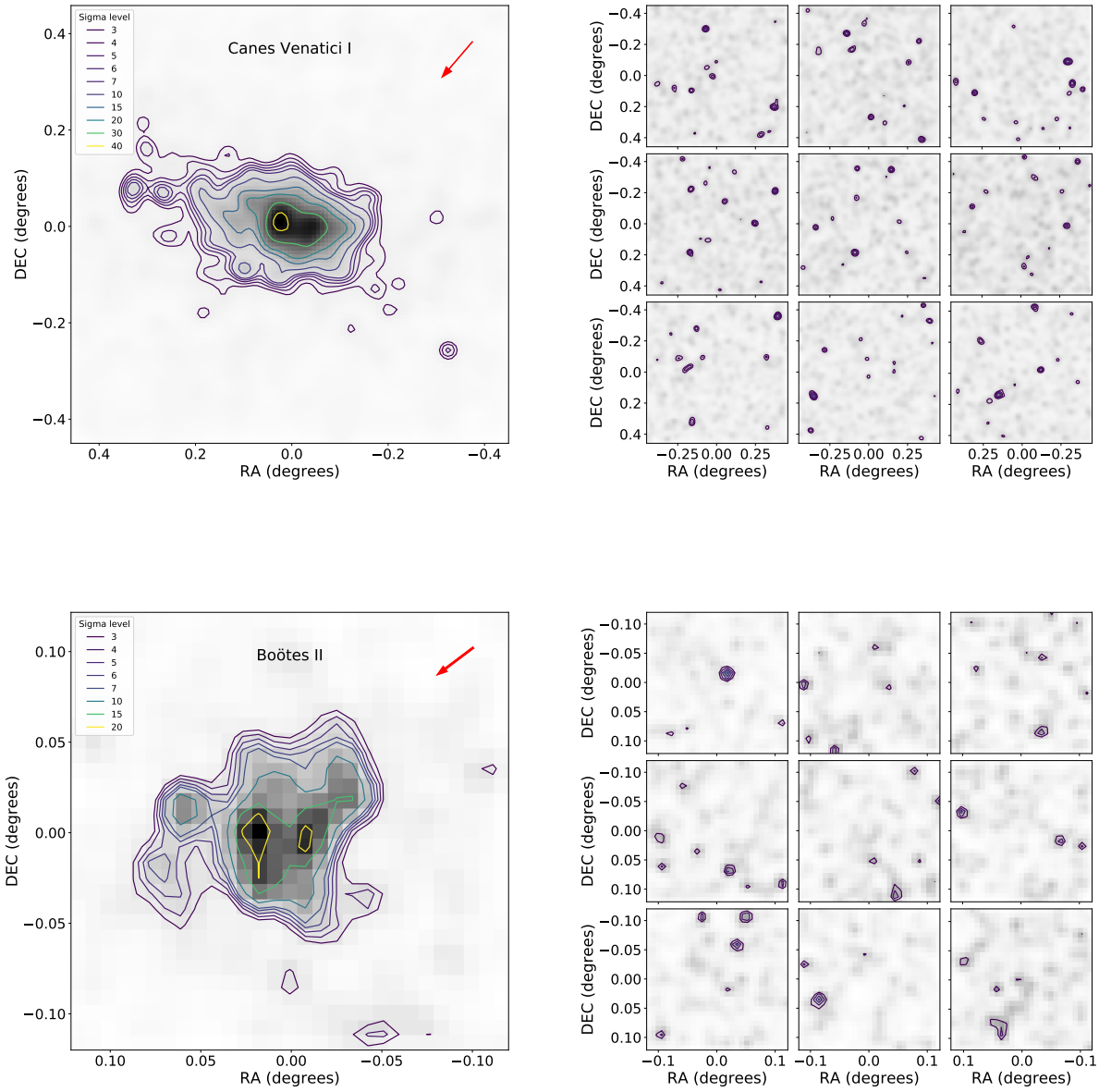

Figure 3.14: Same as Figure 3.9 but for Canes Venatici I and Boötes II UFDs.

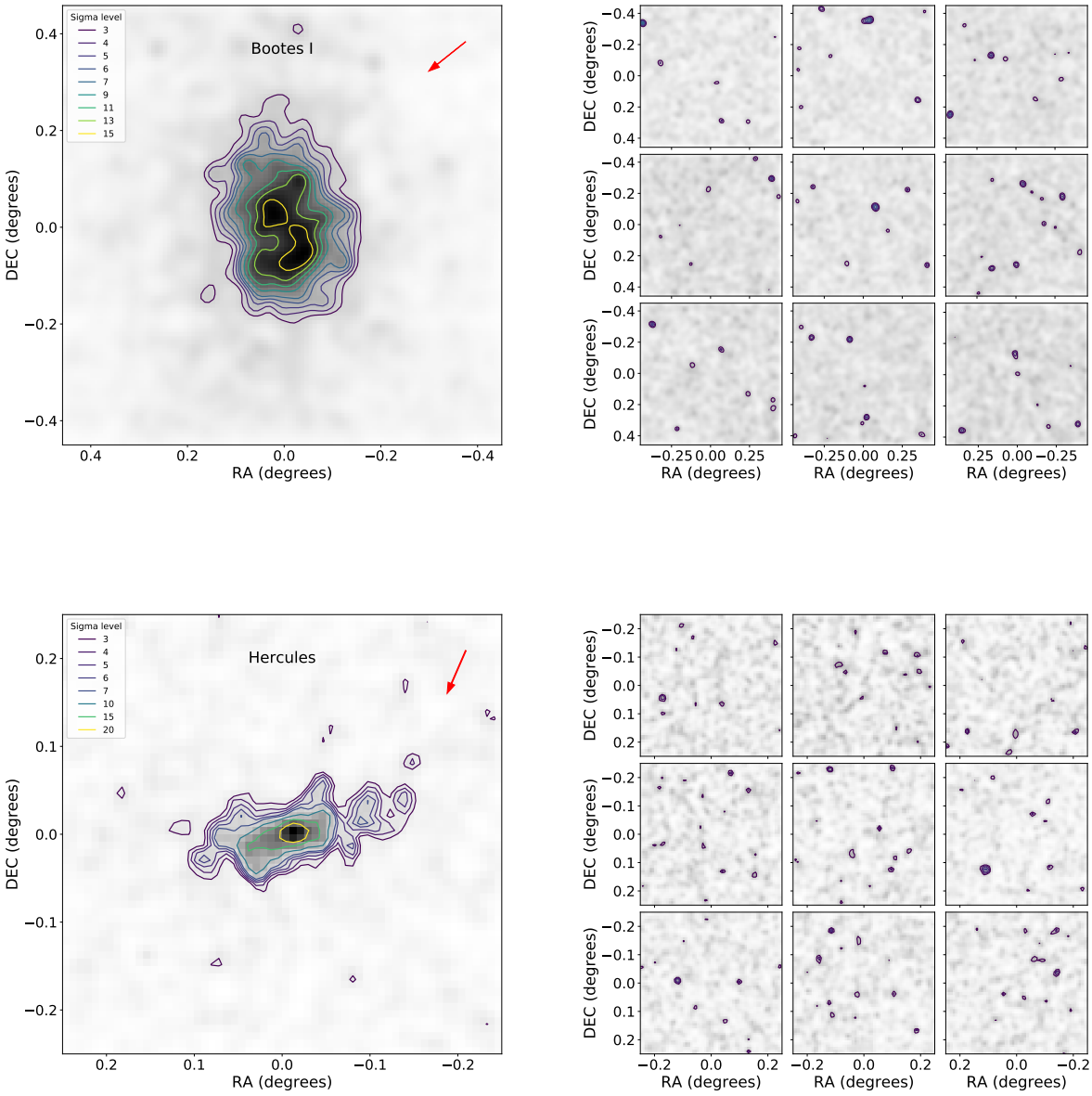

Figure 3.15: Same as Figure 3.9 but for Boötes I Hercules UFDs.

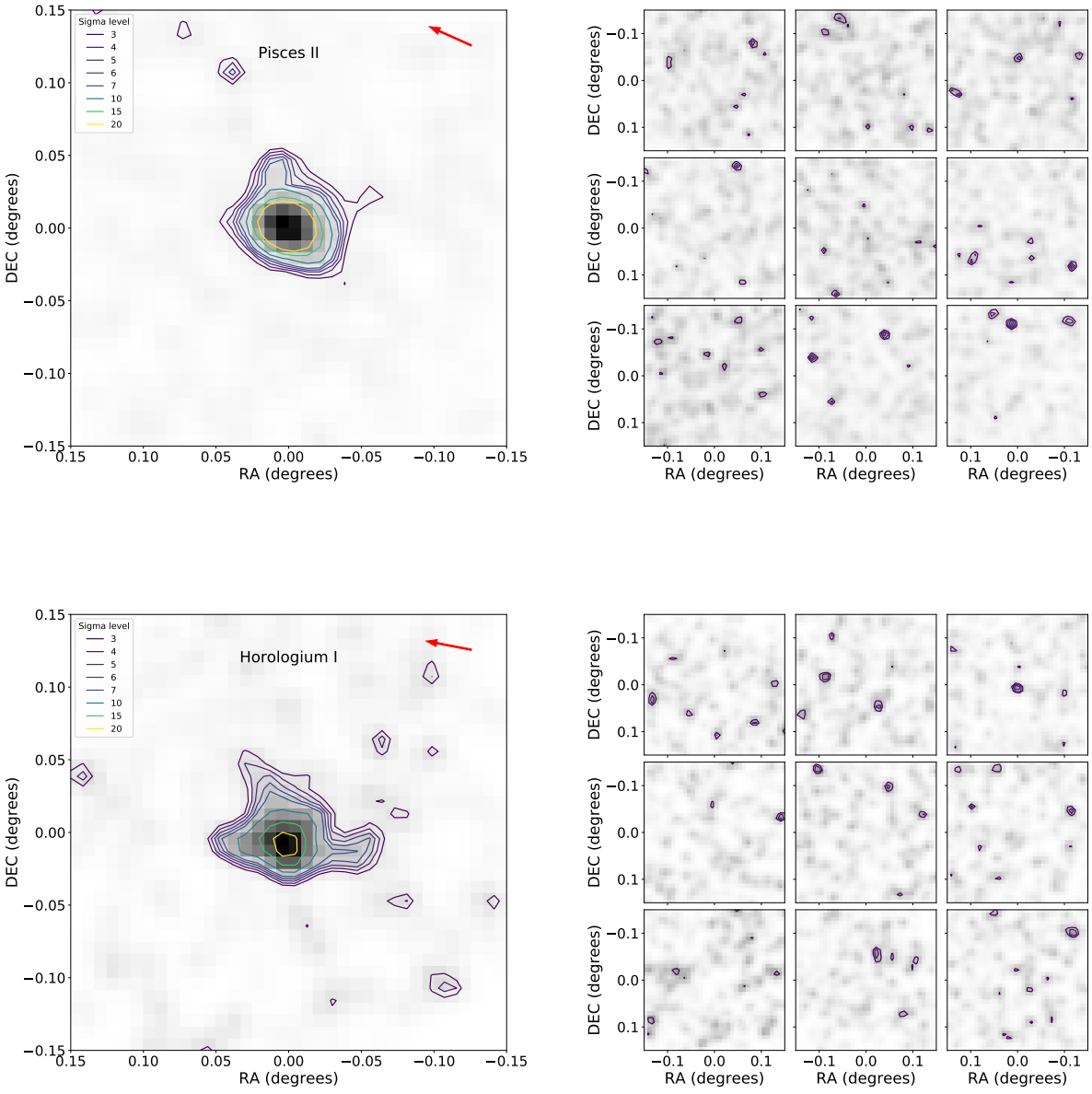

Figure 3.16: Same as Figure 3.9 but for Pisces II and Horologium I UFDs.

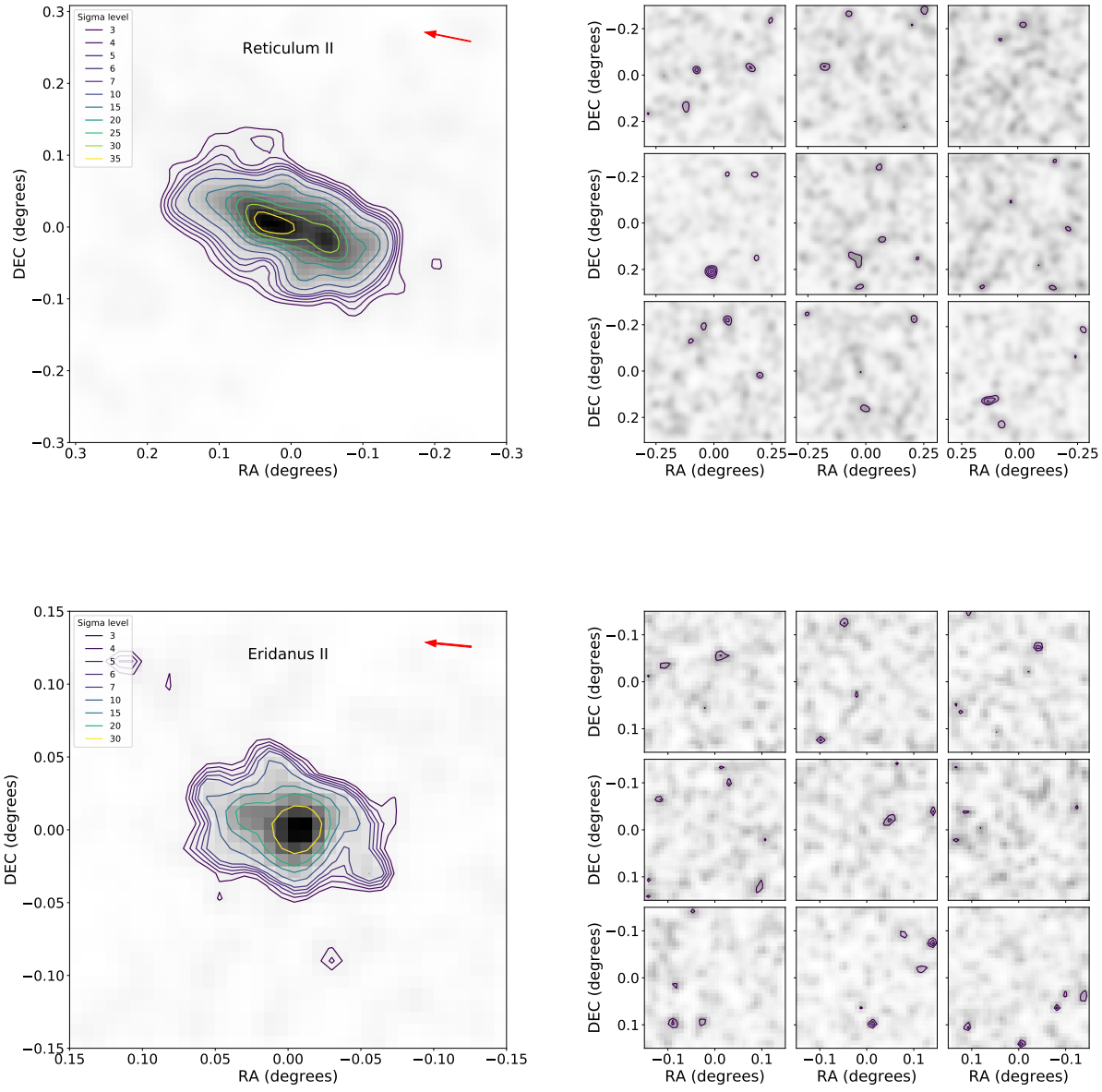

Figure 3.17: Same as Figure 3.9 but for Reticulum II and Eridanus II UFDs.

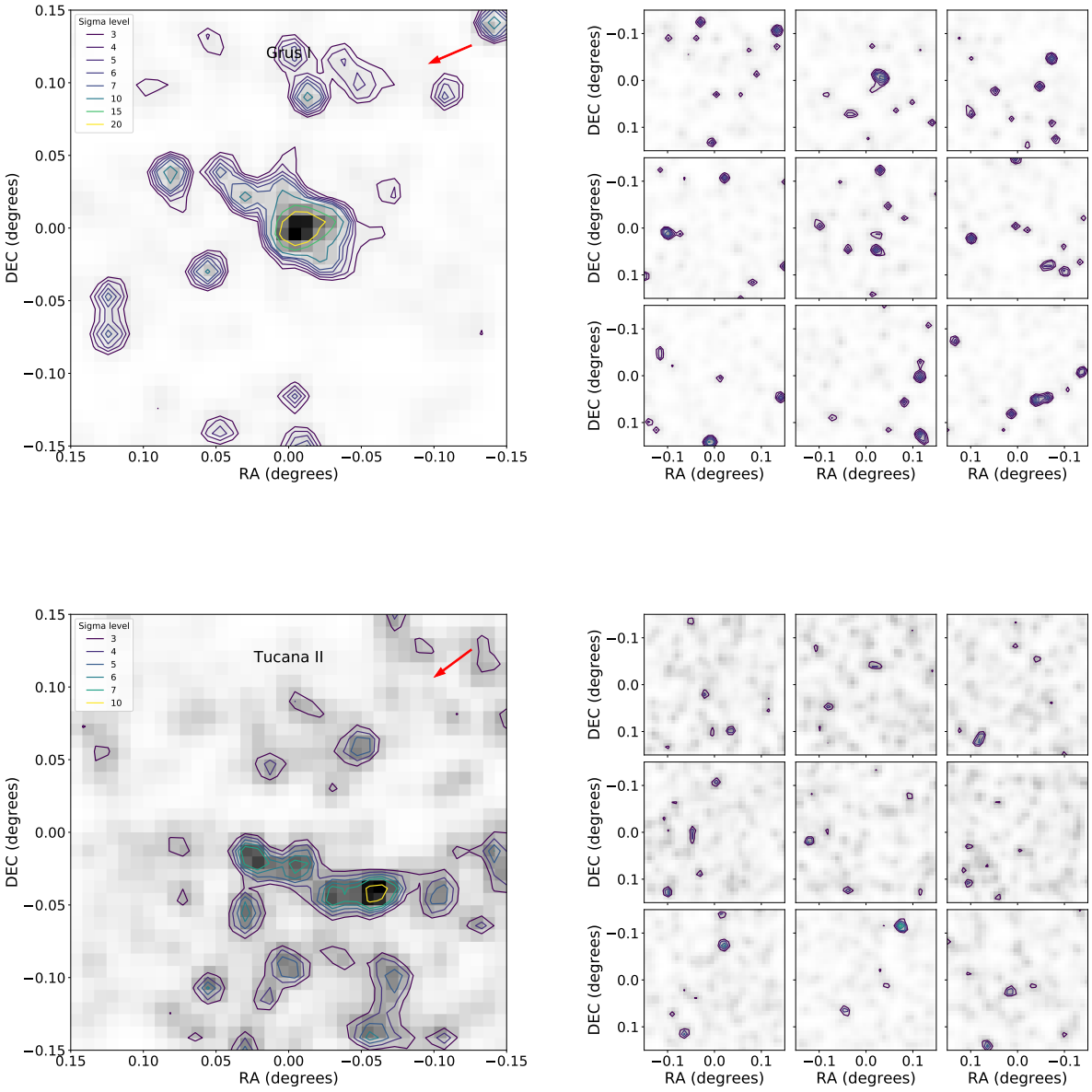

Figure 3.18: Same as Figure 3.9 but for Grus I and Tucana II UFDs.

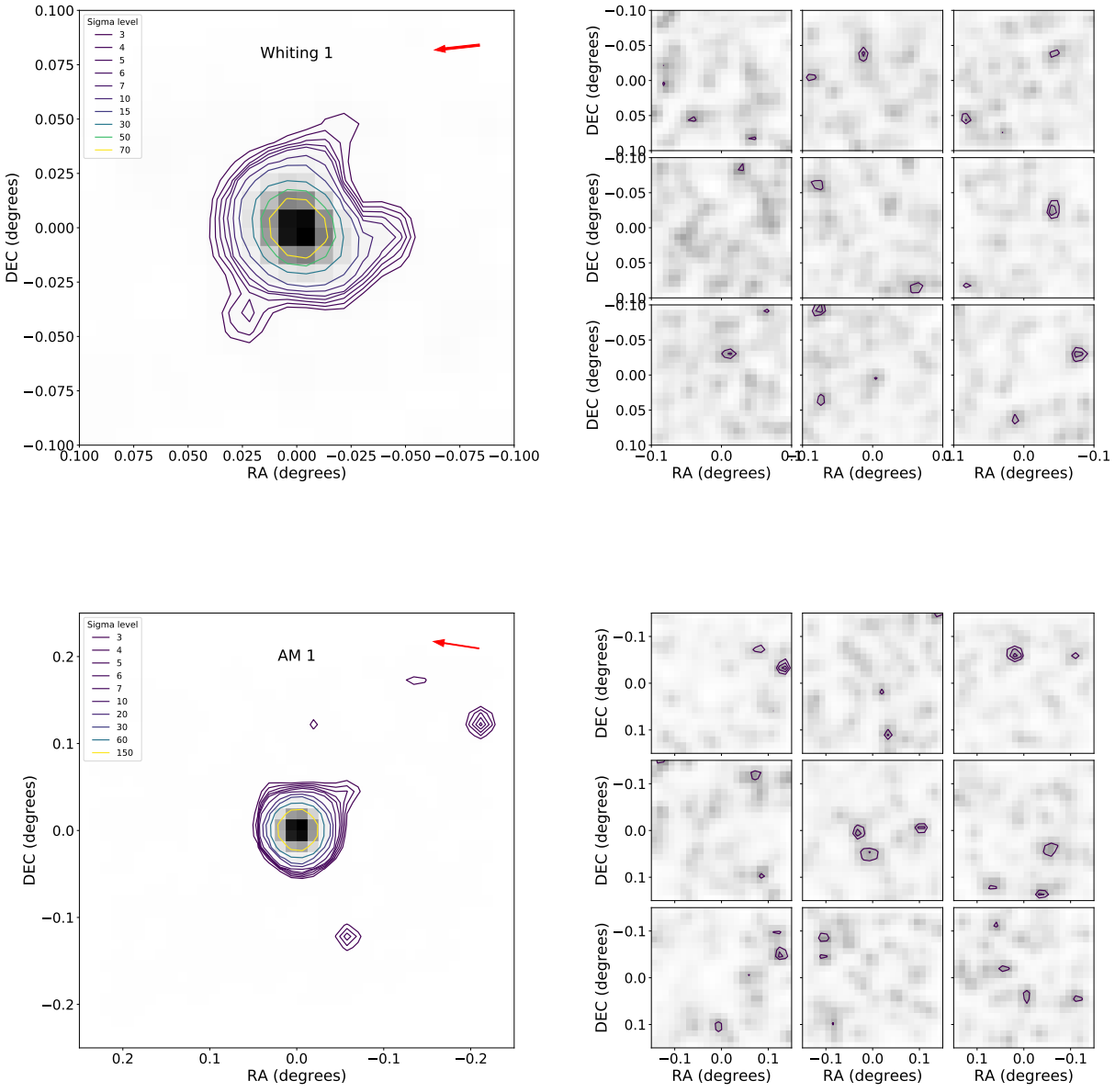

Figure 3.19: Matched-filter results for Whitting 1 and AM 1 outer halo GCs. Left panels: isodensity contours for different levels of above the residual background noise. Right panels: Bootstrap iterations for the determination of isodensity contours, made by uniformly randomizing the position of stars across the field-of-view. The red arrow points to the center of the MW.

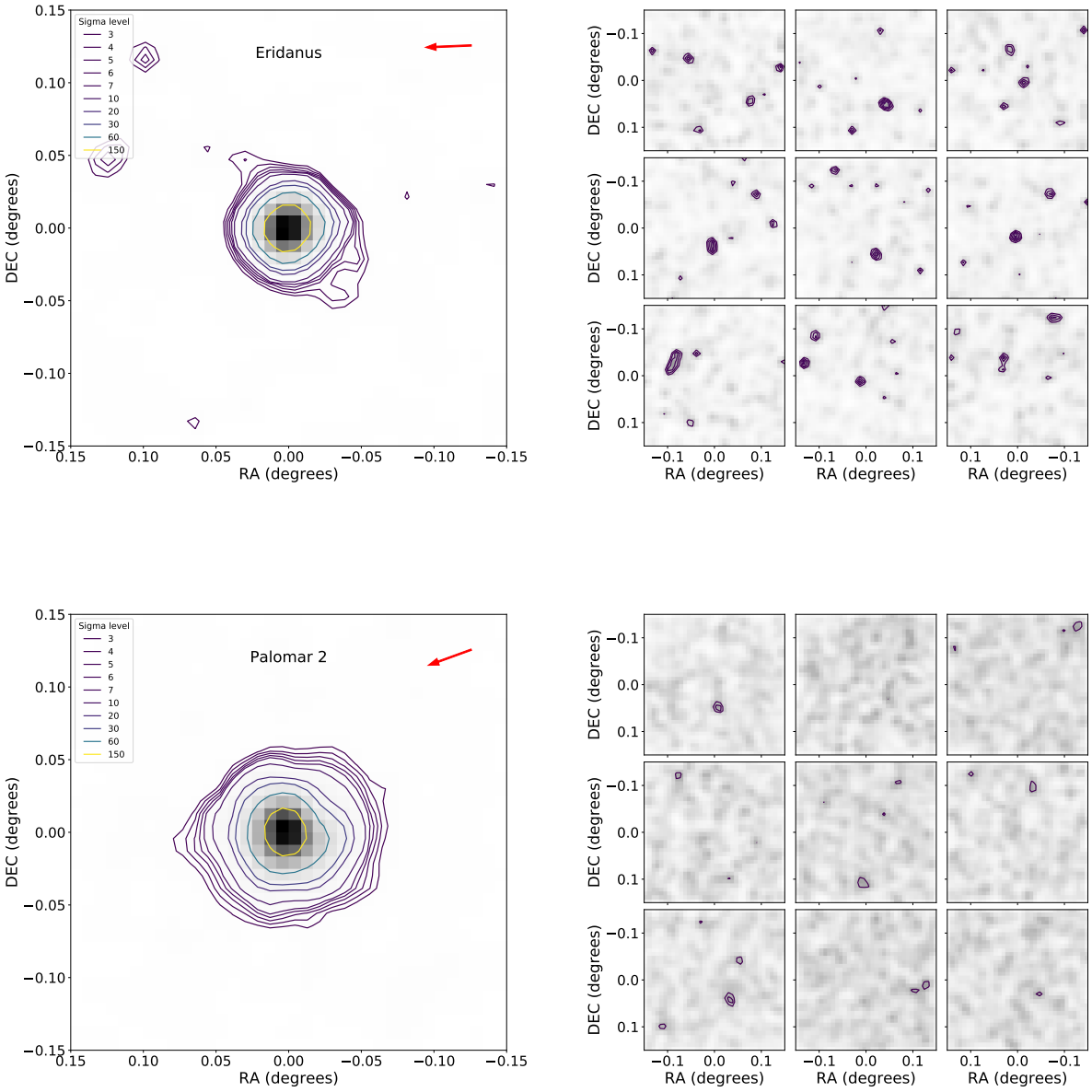

Figure 3.20: Same as 3.19 but for Eridanus and Palomar 2 outer halo GCs.

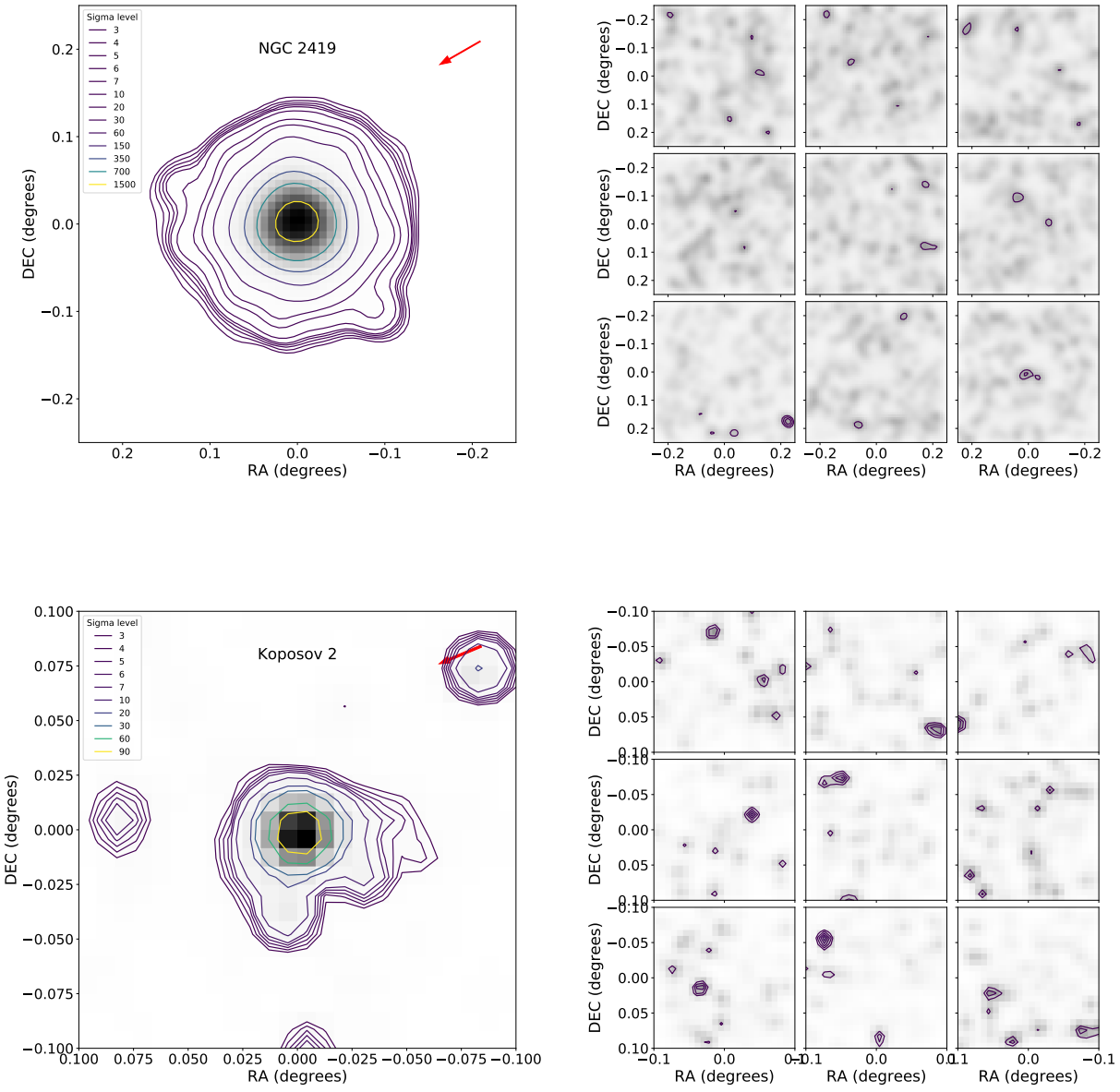

Figure 3.21: Same as 3.19 but for NGC 2419 and Koposov 2 outer halo GCs.

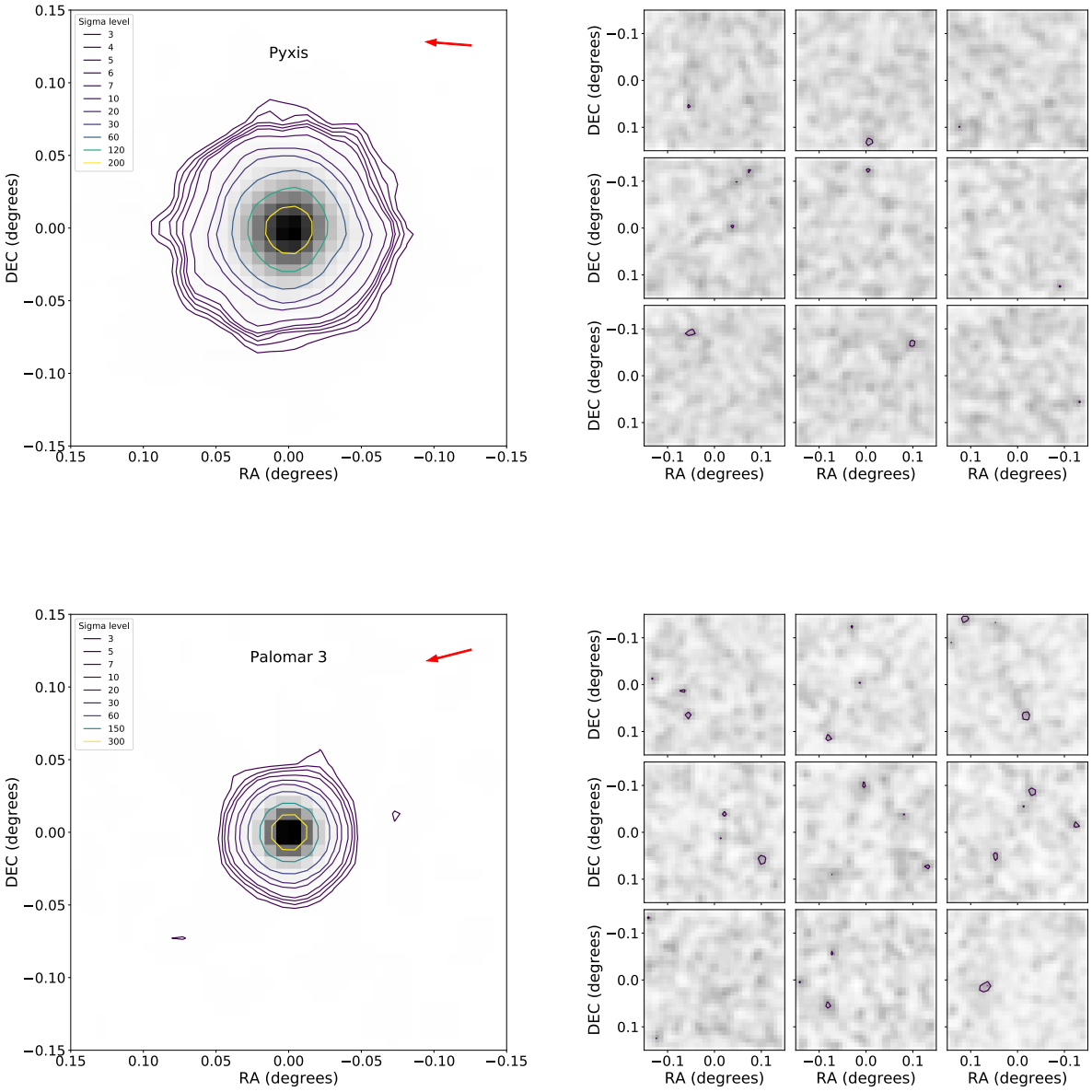

Figure 3.22: Same as 3.19 but for Pyxis and Palomar 3 outer halo GCs.

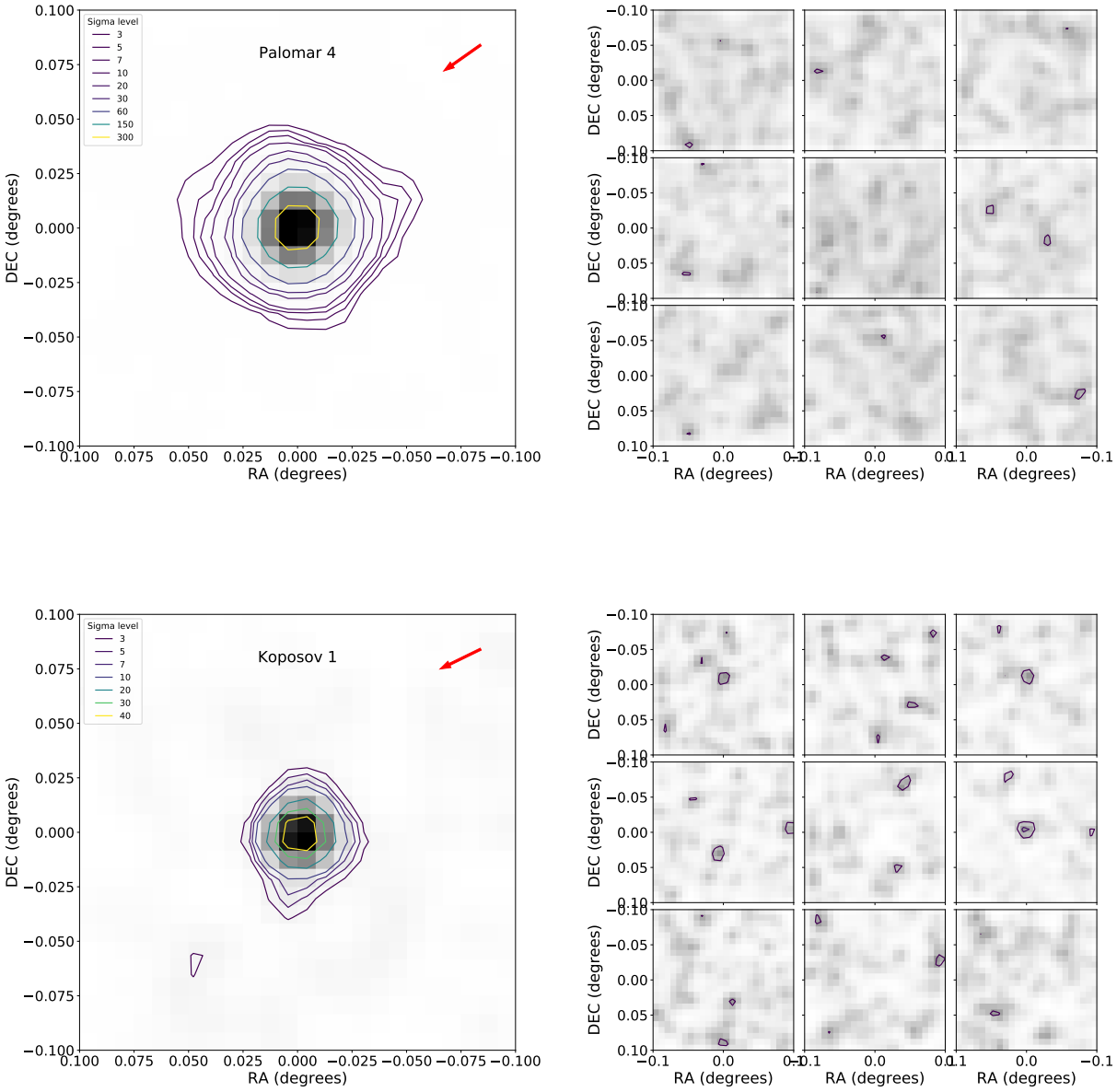

Figure 3.23: Same as 3.19 but for Palomar 4 and Koposov 1 outer halo GCs.

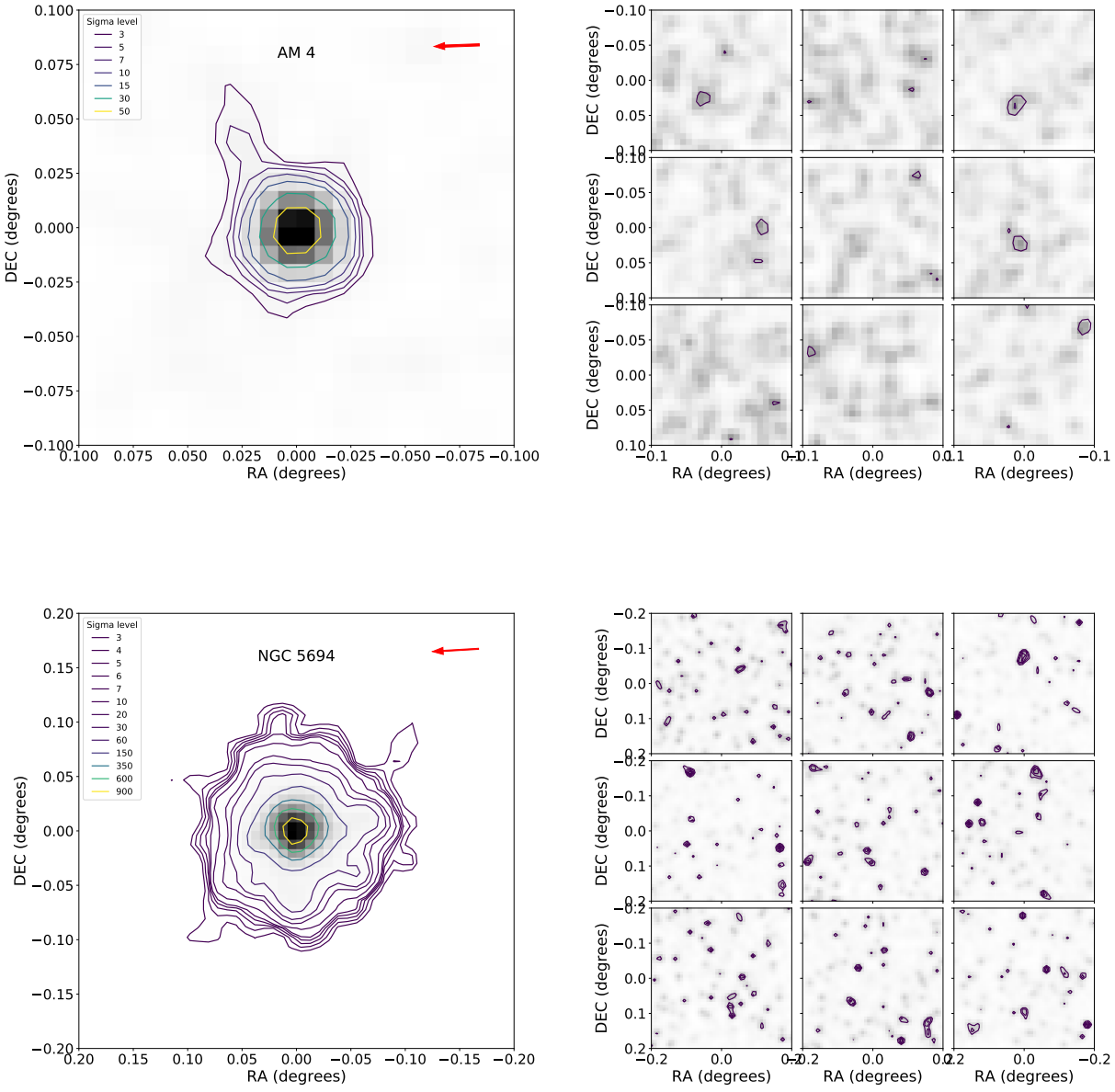

Figure 3.24: Same as 3.19 but for AM 4 and NGC 5694 outer halo GCs.

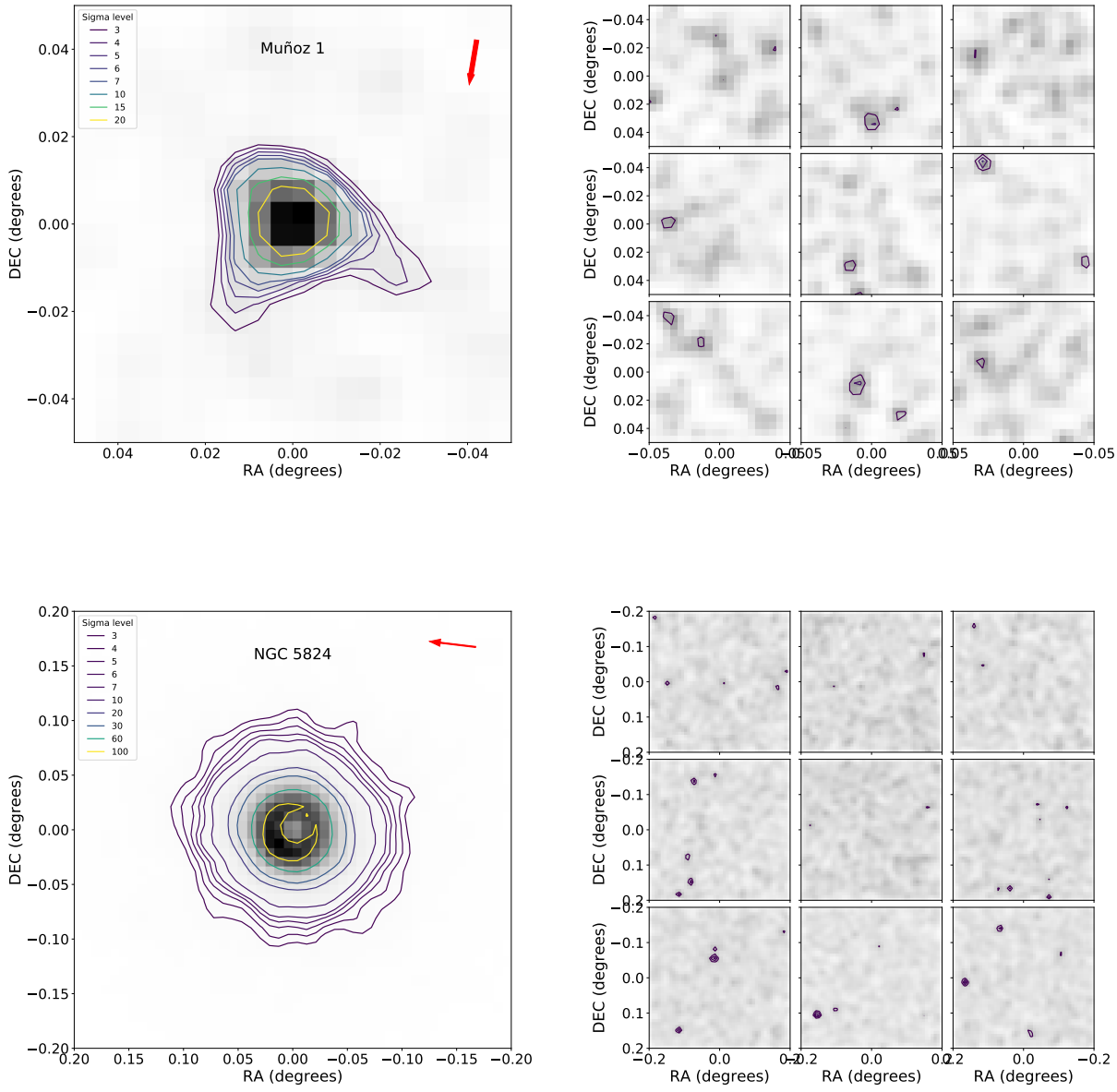

Figure 3.25: Same as 3.19 but for Mñoz 1 and NGC 5824 outer halo GCs.

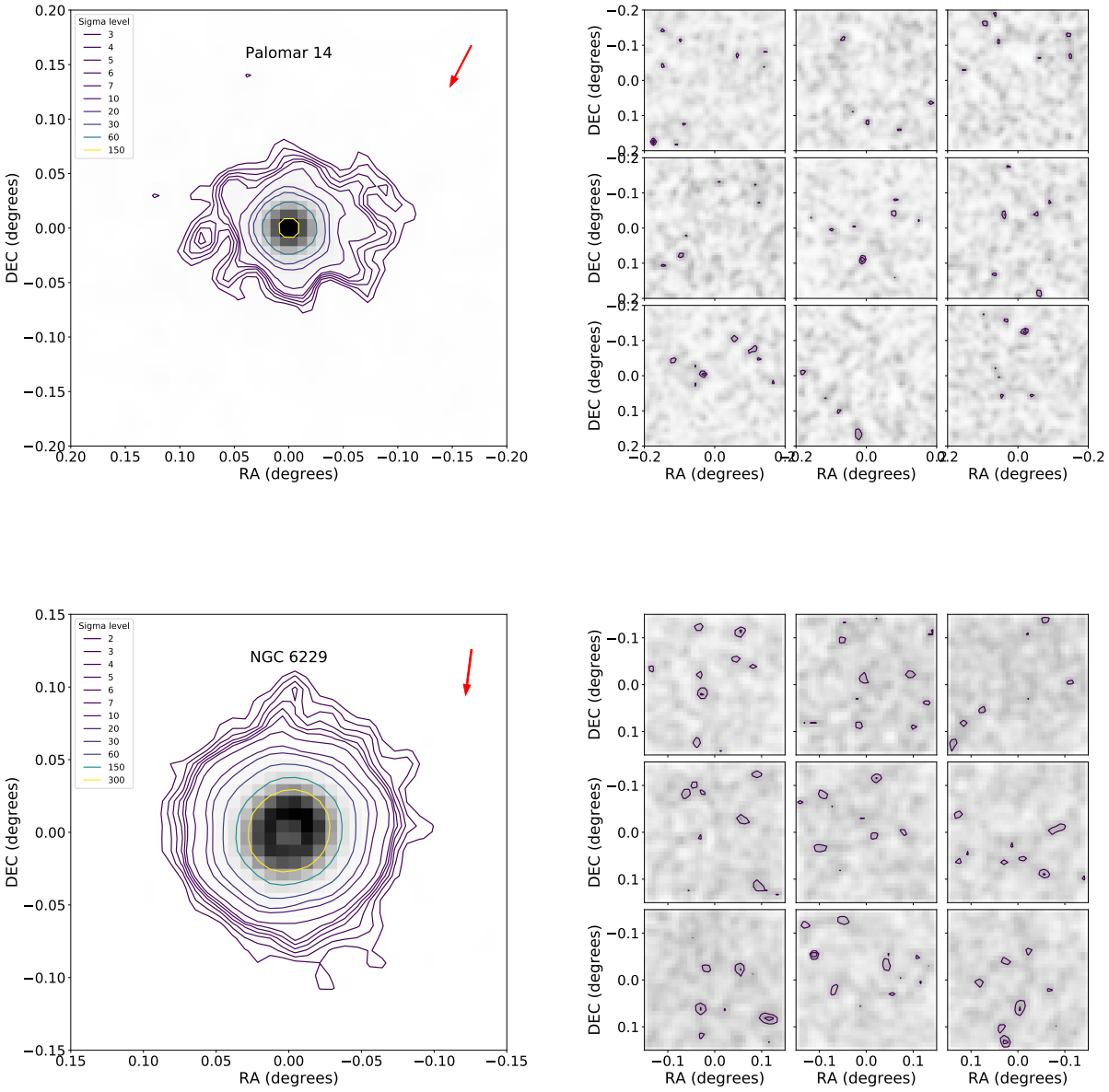

Figure 3.26: Same as 3.19 but for Palomar 14 and NGC 6229 outer halo GCs.

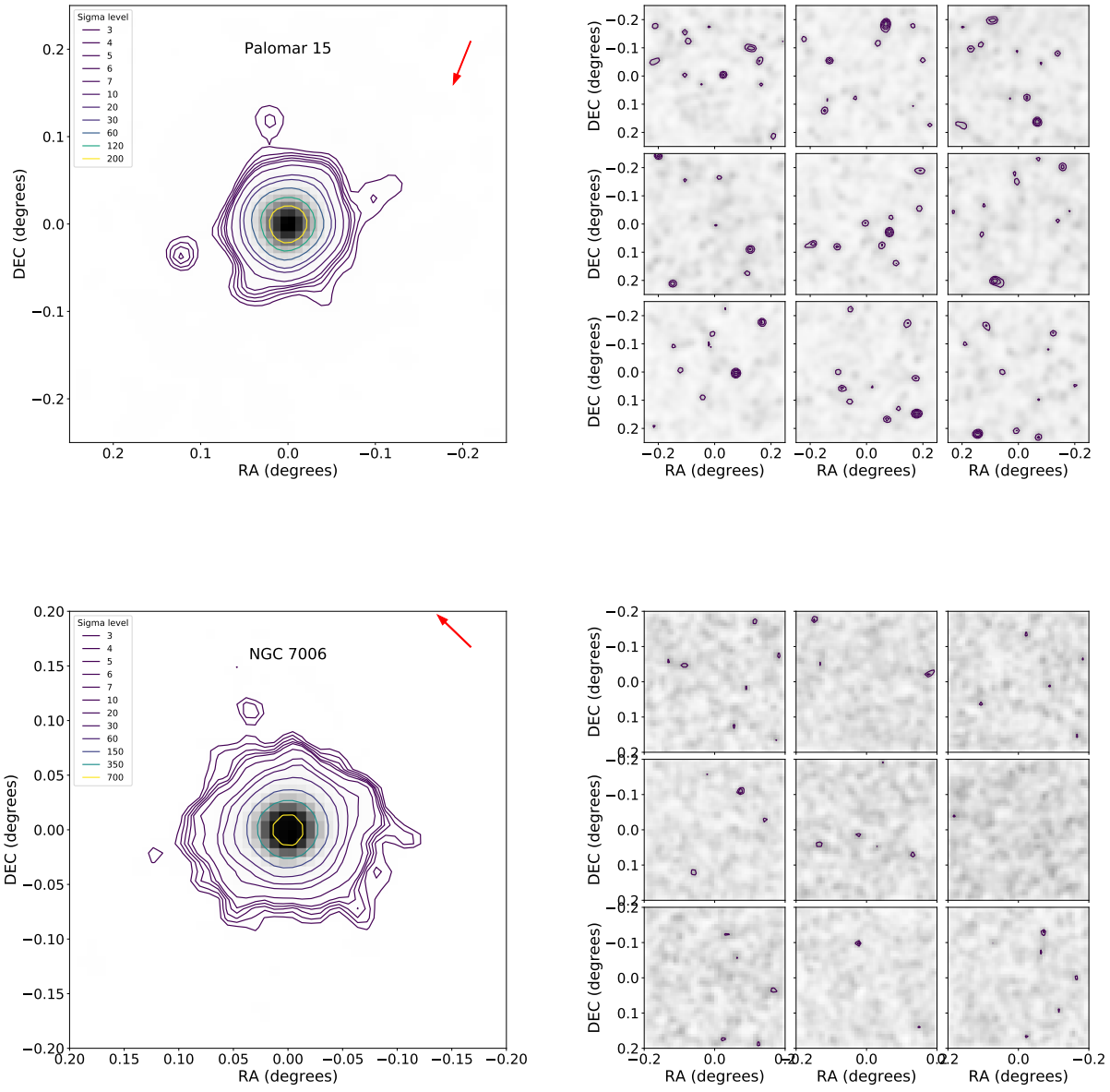

Figure 3.27: Same as 3.19 but for Palomar 15 and NGC 7006 outer halo GCs.

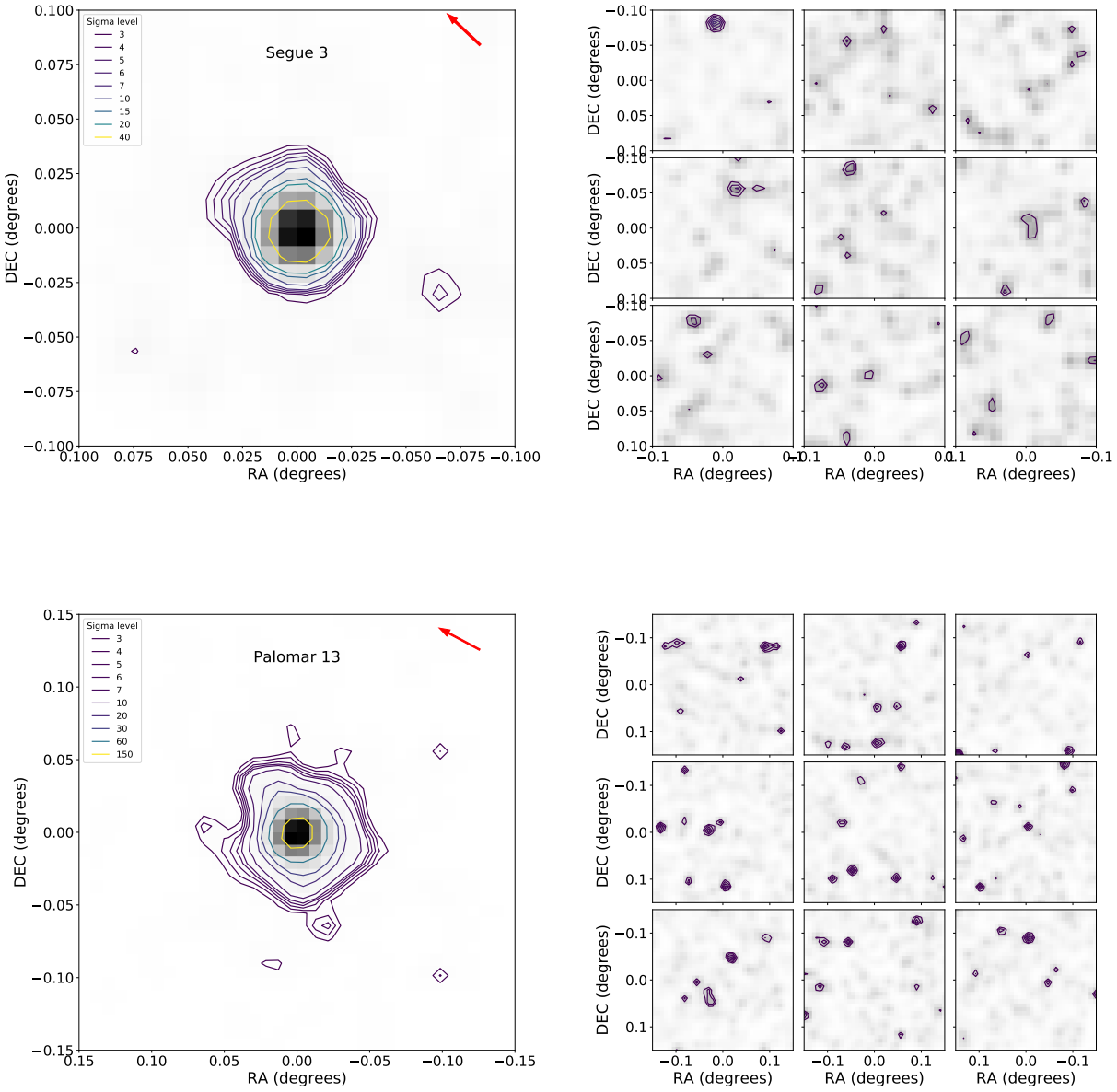

Figure 3.28: Same as 3.19 but for Segue 3 and Palomar 13 outer halo GCs.

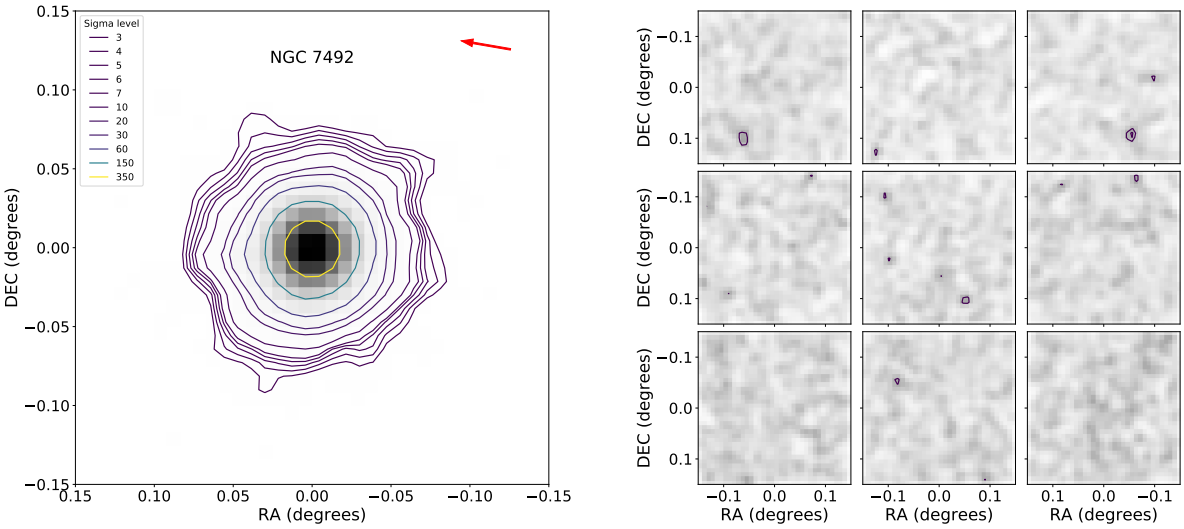

Figure 3.29: Same as 3.19 but for NGC 7492 outer halo GC.

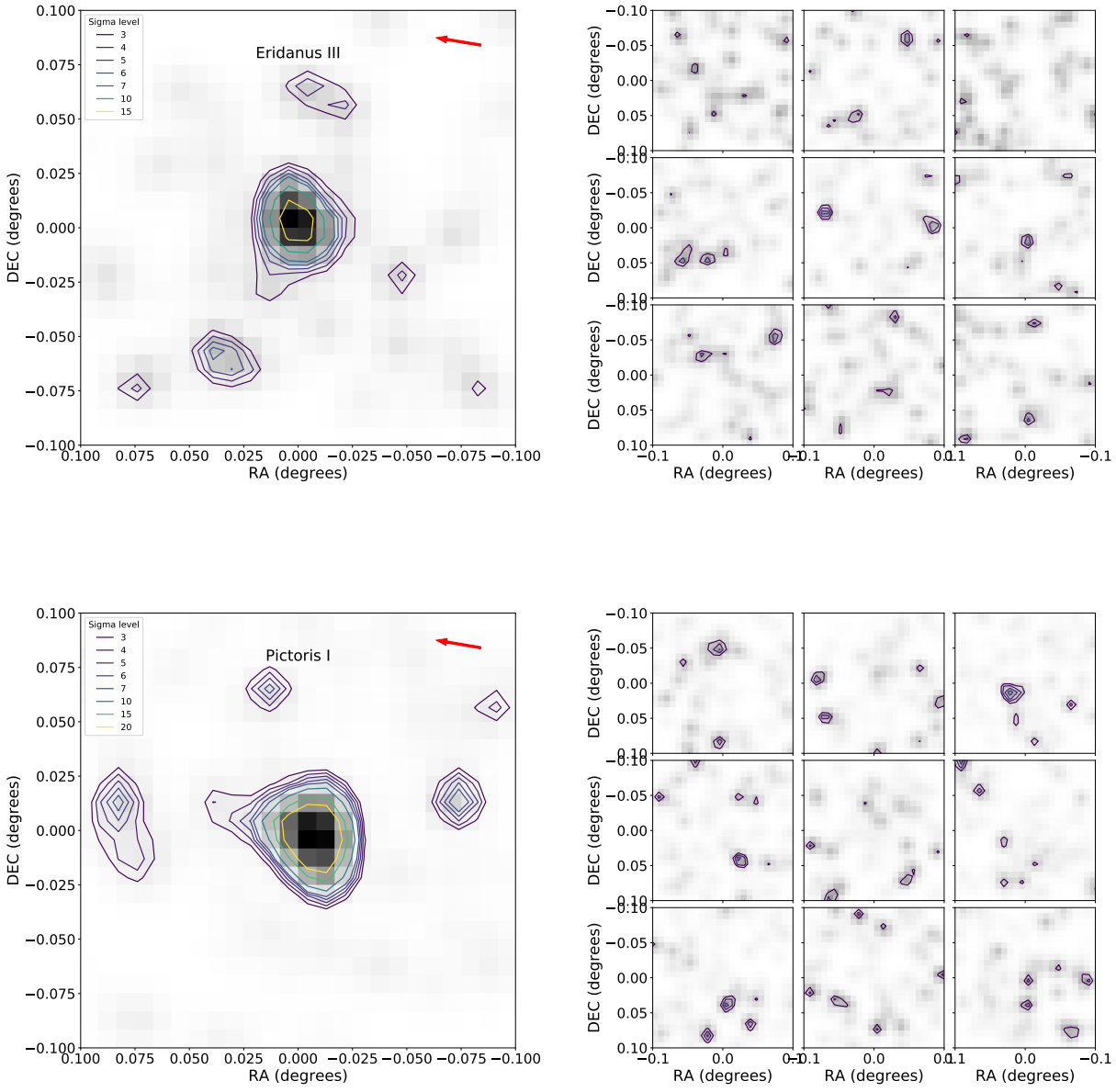

Figure 3.30: Matched-filter results for Eridanus III and Pictoris I outer halo satellites, which fall in the "not classified" category. Left panels: isodensity contours for different levels of above the residual background noise. Right panels: Bootstrap iterations for the determination of isodensity contours, made by uniformly randomizing the position of stars across the field-of-view. The red arrow points to the center of the MW.

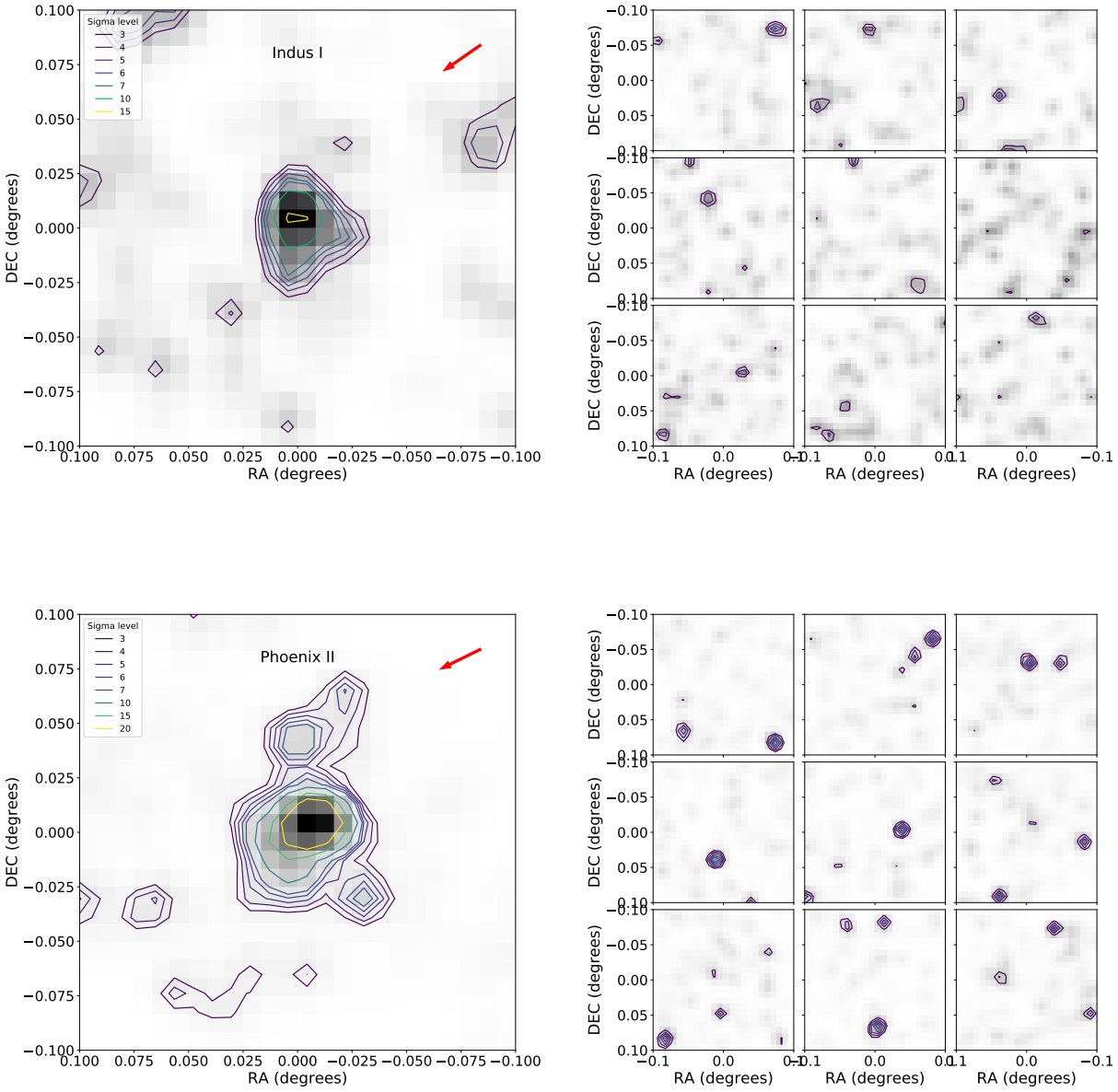

Figure 3.31: Same as 3.30 but for the Indus I and Phoenix II not classified satellites.

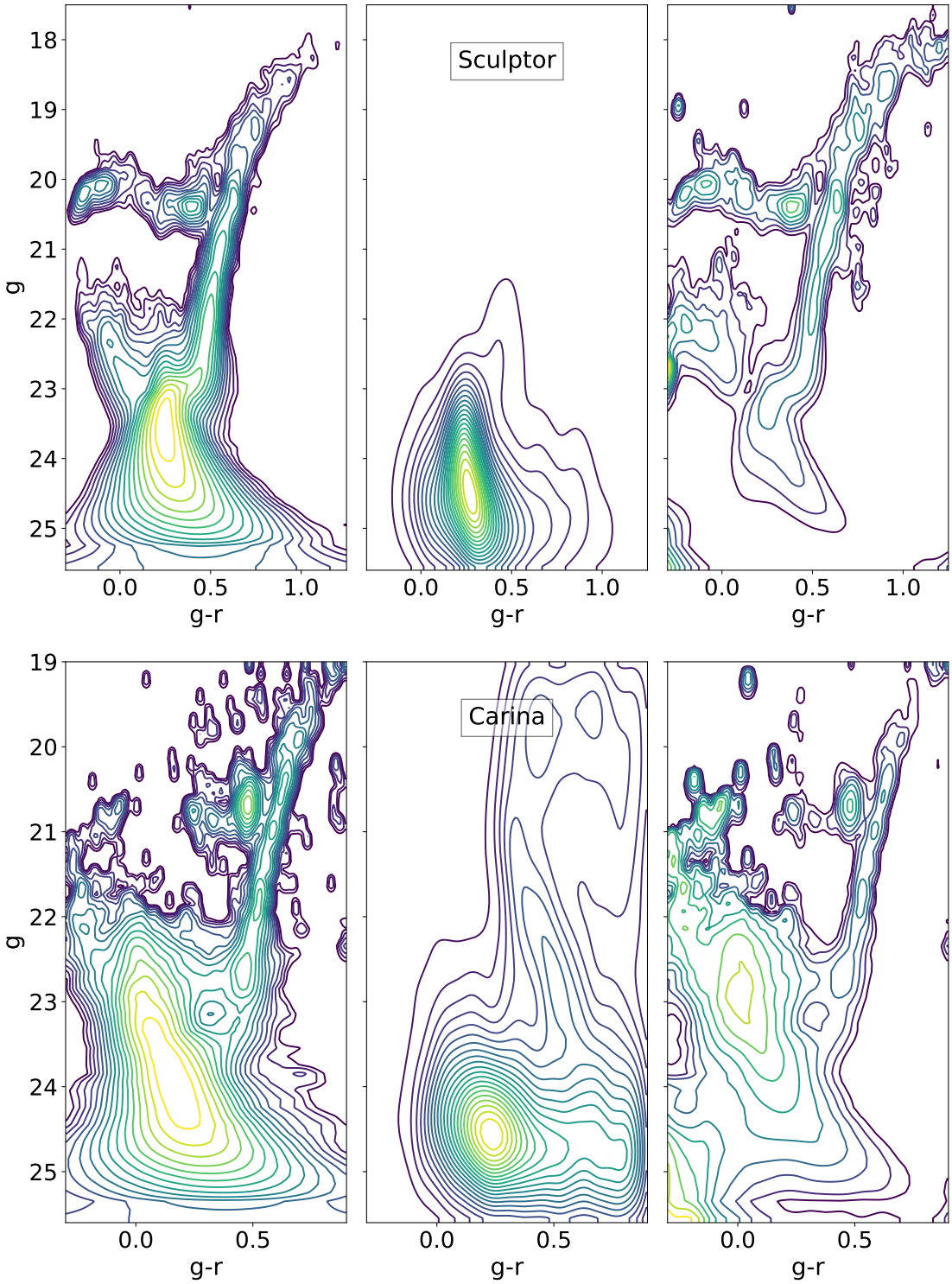

Figure 3.32: Estimated member star distribution (left panel), background star distribution (middle panel), and star weight distribution (right panel) for the Sculptor and Carina classical dSphs. The star weight in each color-magnitude bin is given by the factor $f_{\mathrm{obj,(i,j)}}/n_{\mathrm{bkg,(i,j)}}$. In all panels, yellow represents higher counts than purple.

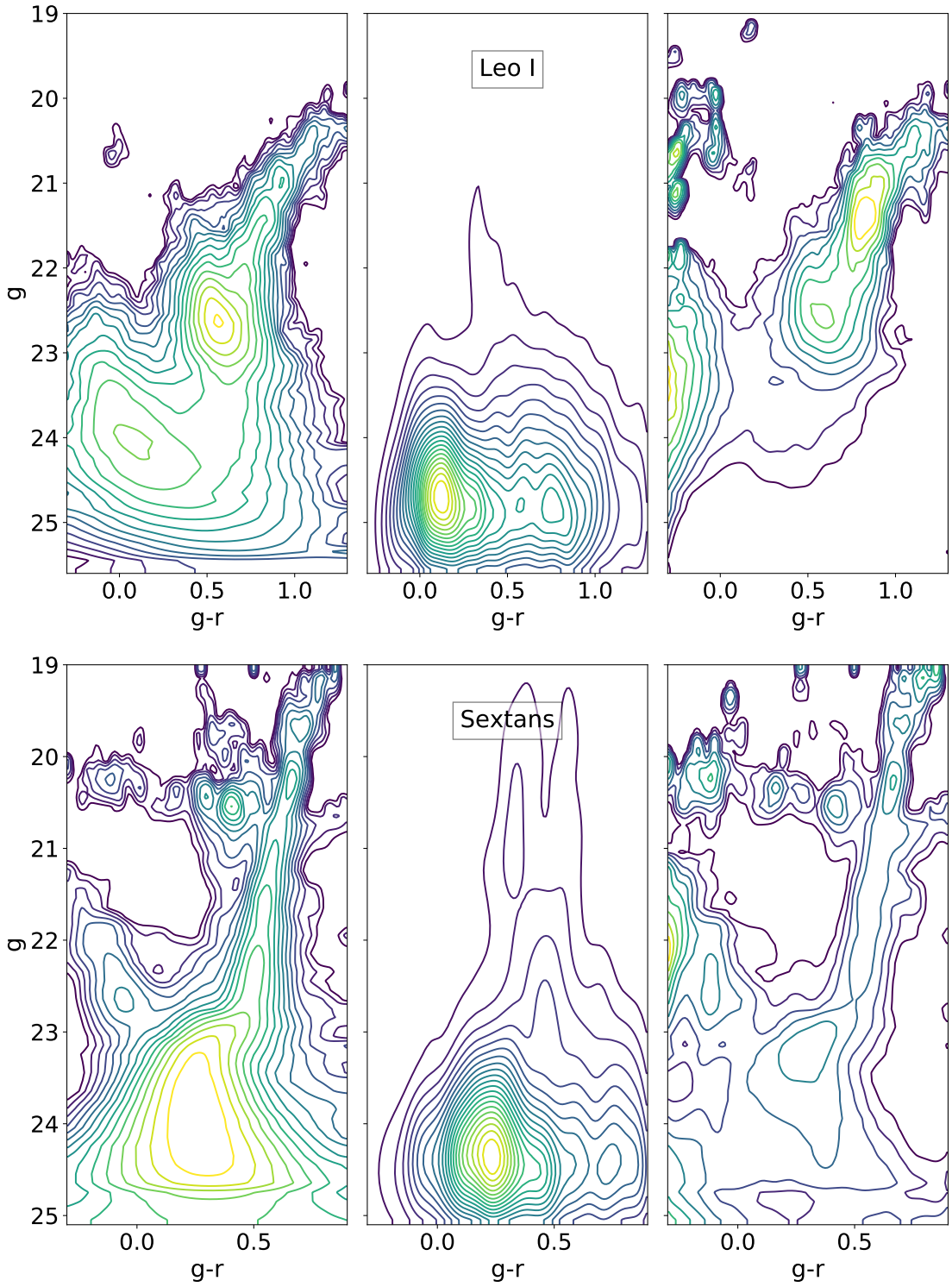

Figure 3.33: Same as 3.32, but for the Leo I and Sextans classical dSphs.

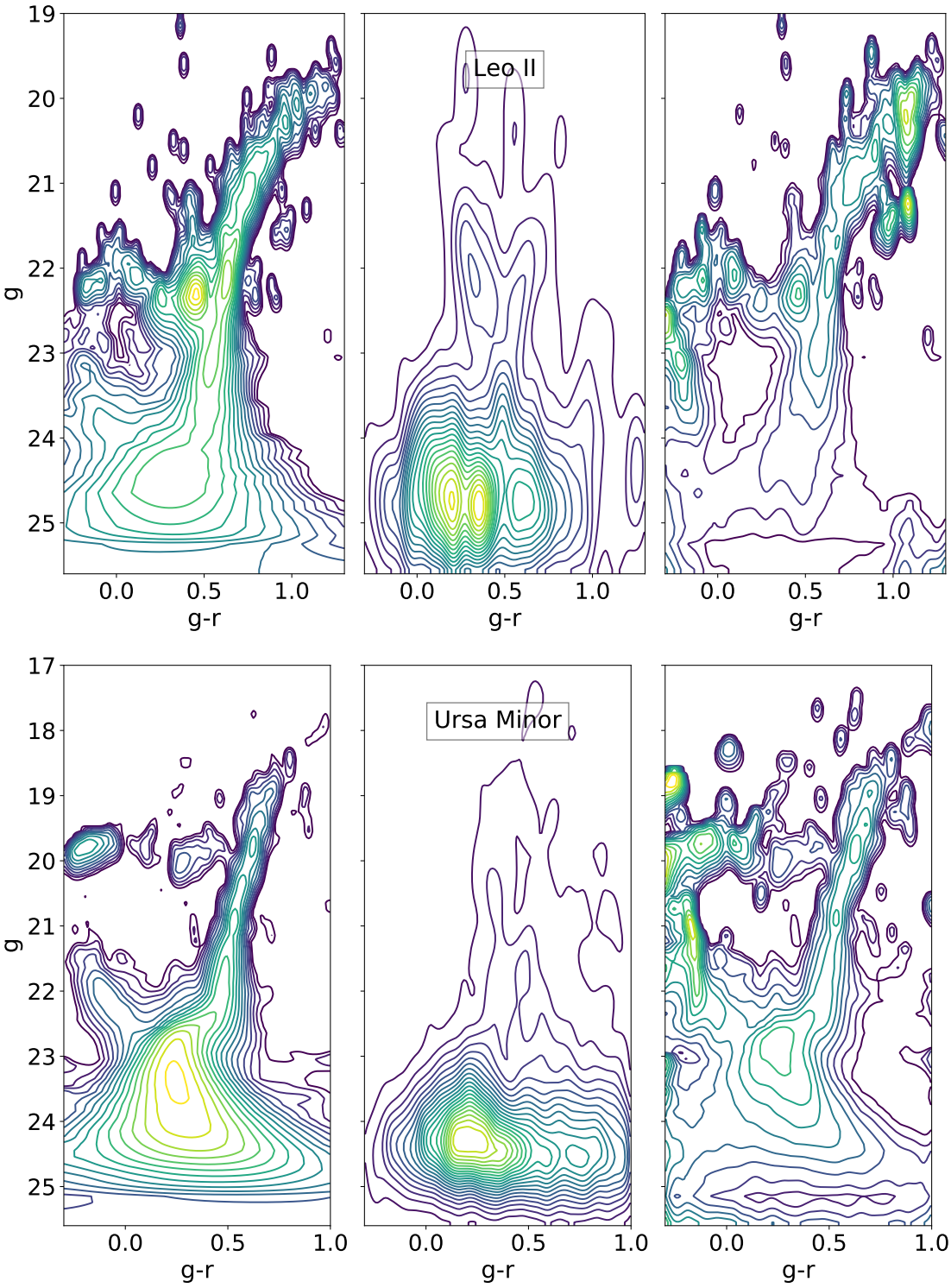

Figure 3.34: Same as 3.32, but for the Leo II and Ursa Minor classical dSphs.

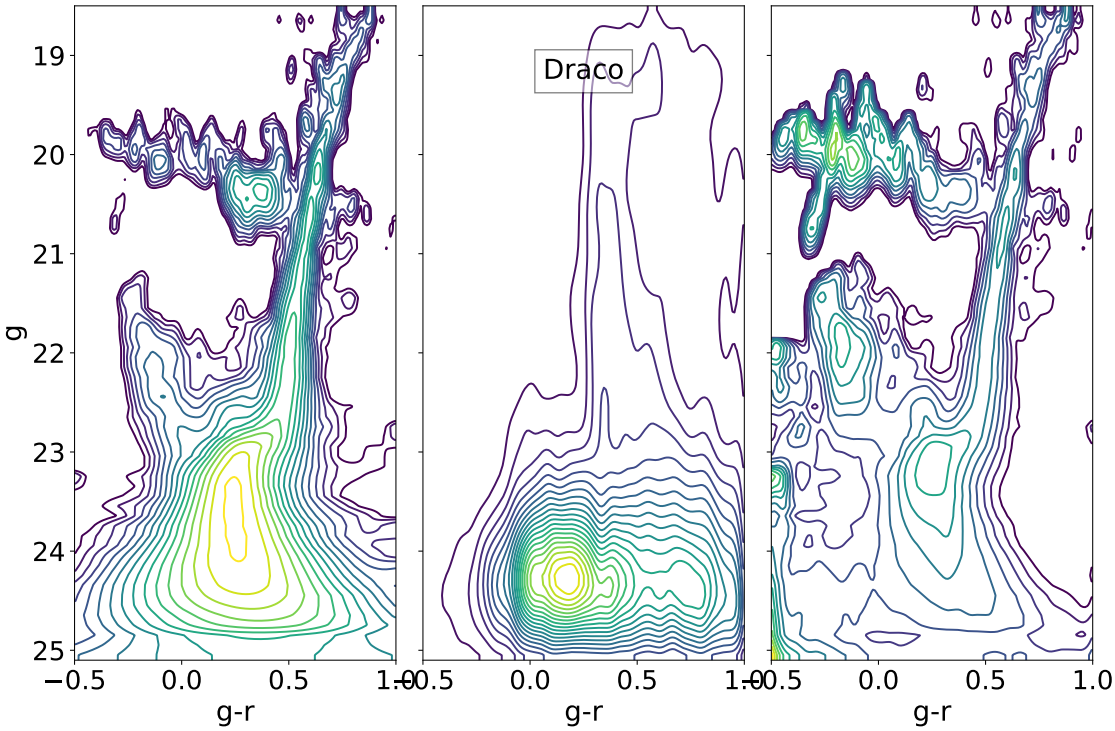

Figure 3.35: Same as 3.32, but for the Draco classical dSph.

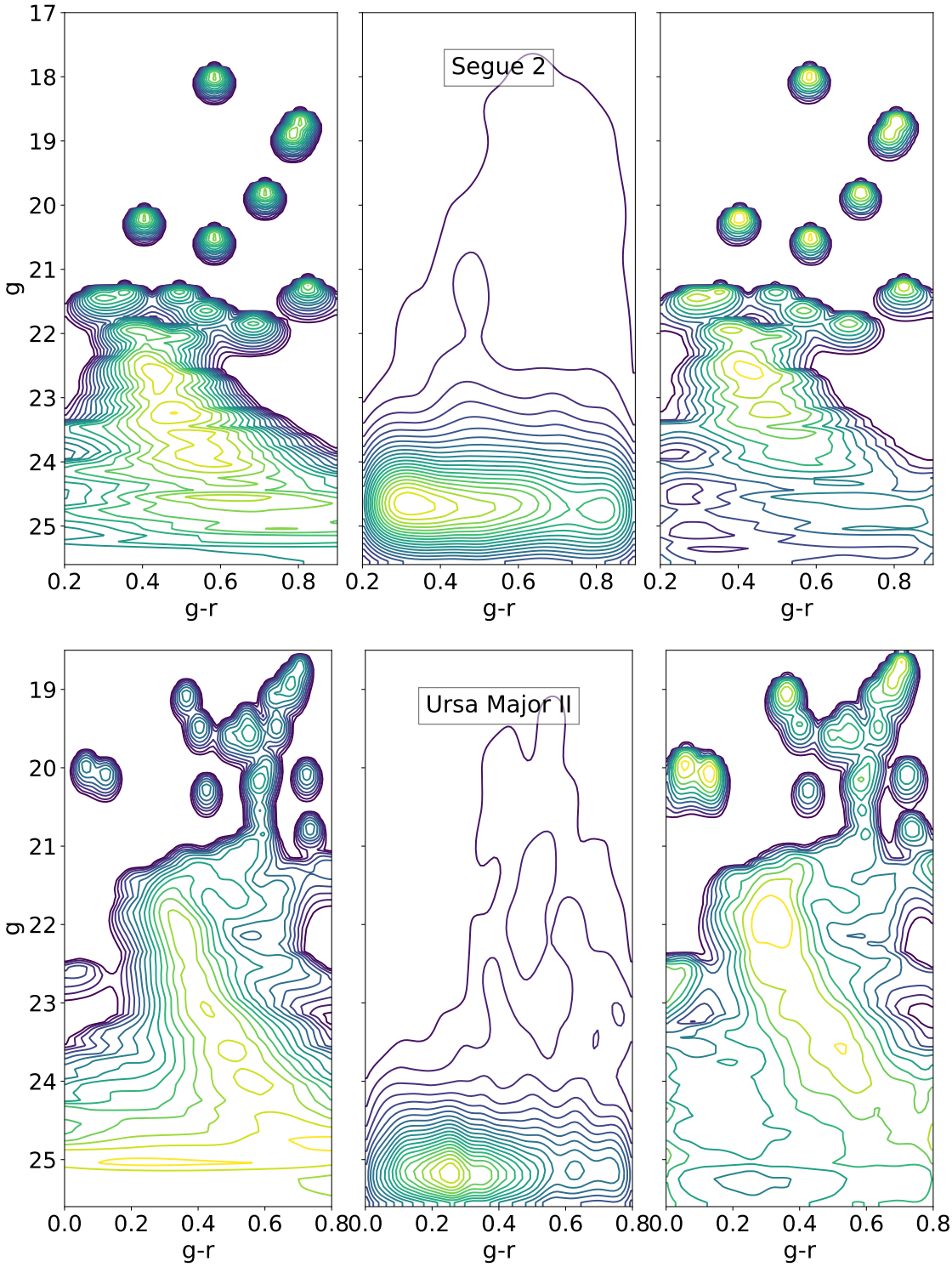

Figure 3.36: Estimated member star distribution (left panel), background star distribution (middle panel), and star weight distribution (right panel) for the Segue 2 and Ursa Major II UFDs. The star weight in each color-magnitude bin is given by the factor $f_{\mathrm{obj,(i,j)}}/n_{\mathrm{bkg,(i,j)}}$. In all panels, yellow represents higher counts than purple.

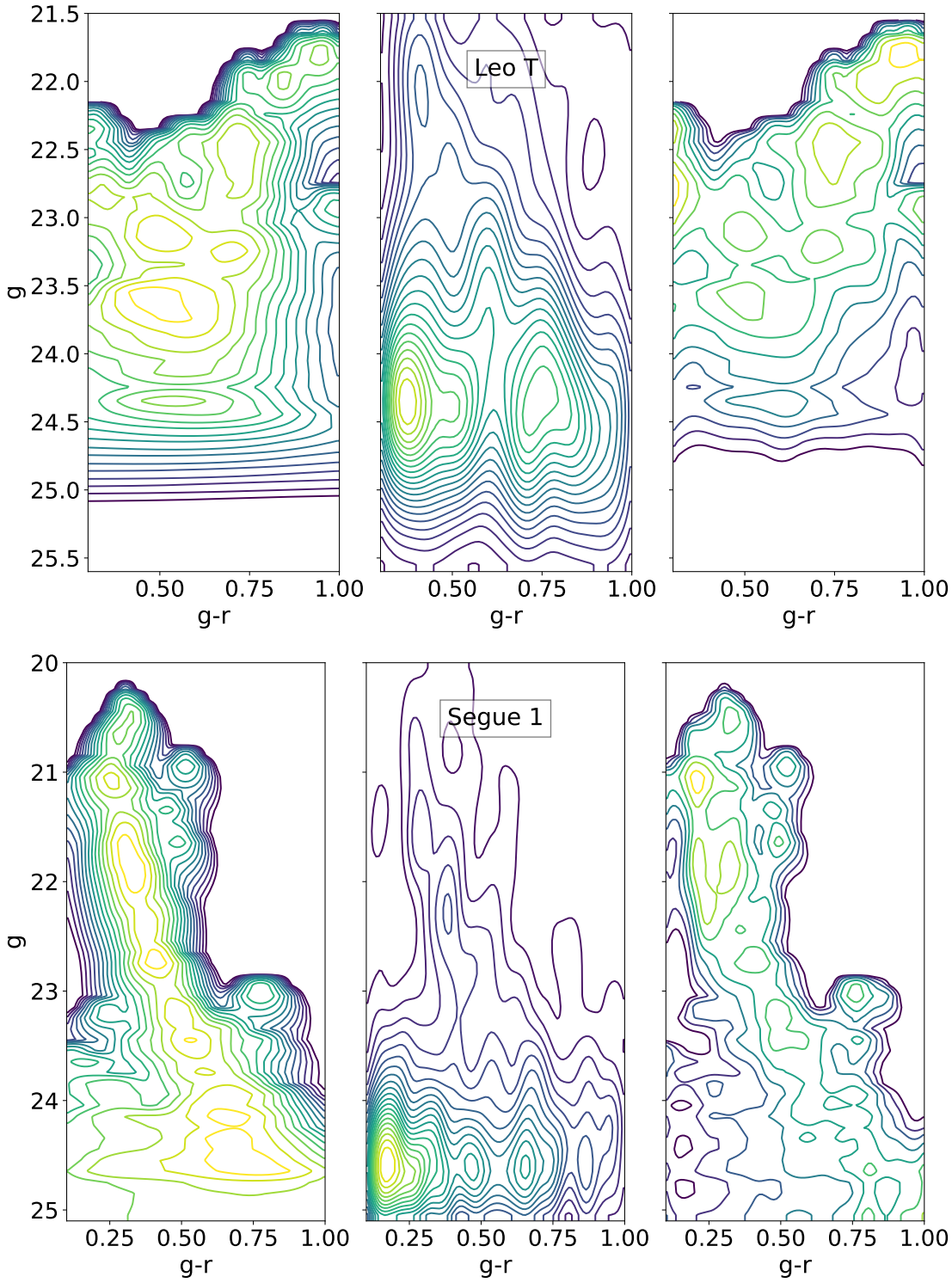

Figure 3.37: Same as 3.36, but for the Leo T and Segue 1 UFDs.

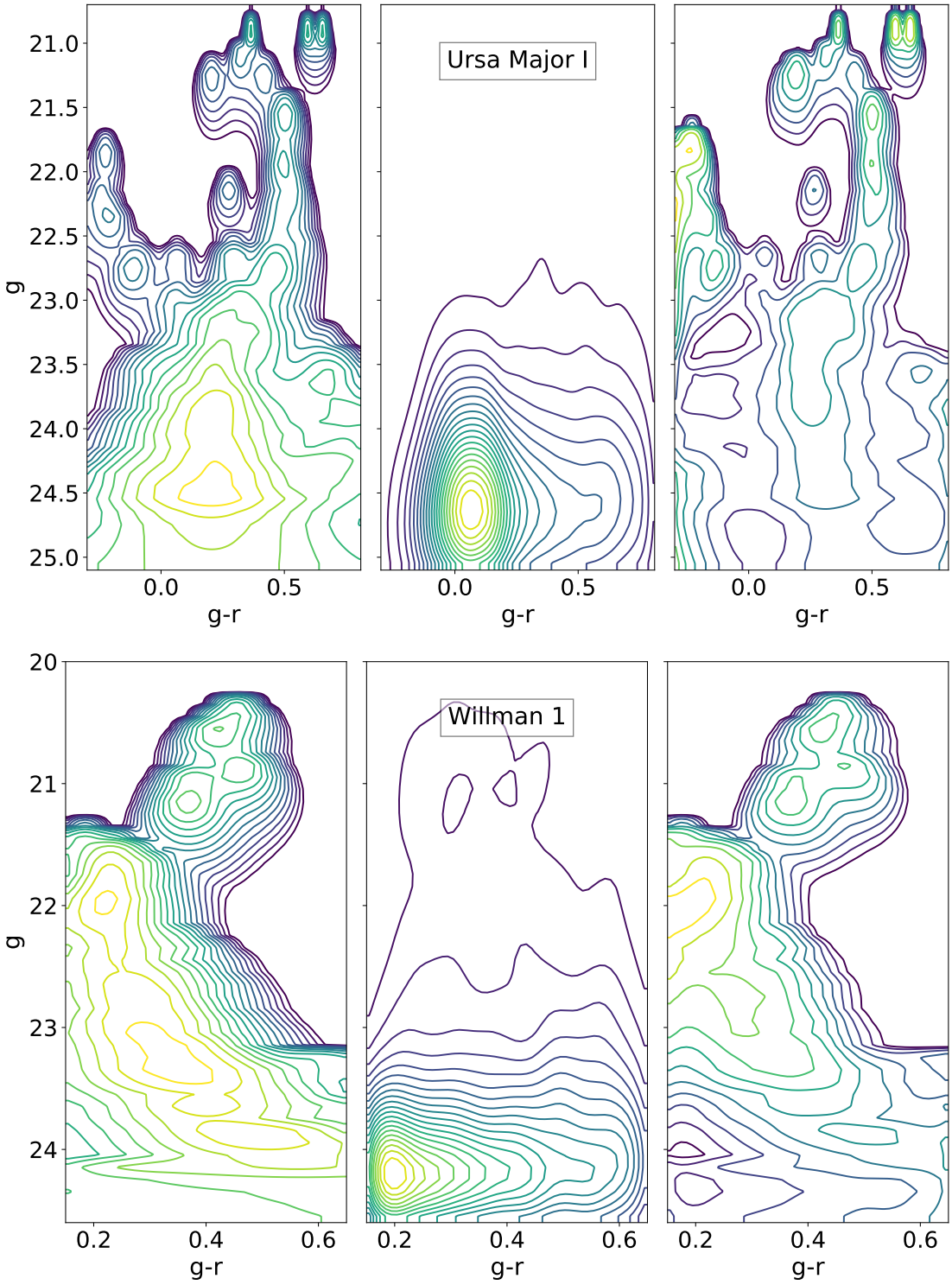

Figure 3.38: Same as 3.36, but for the Ursa Major I and Willman 1 UFDs.

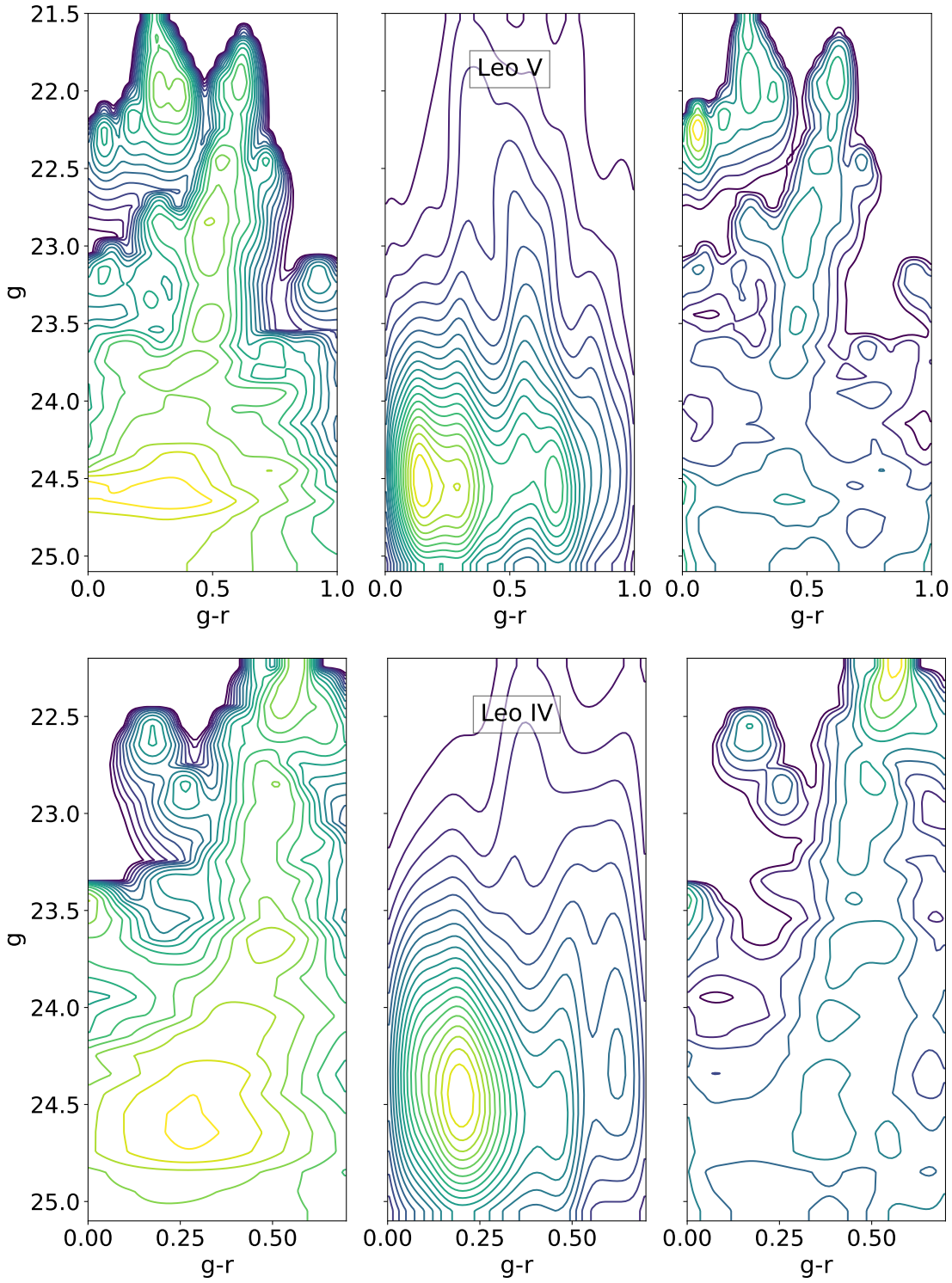

Figure 3.39: Same as 3.36, but for the Leo V and Leo IV UFDs.

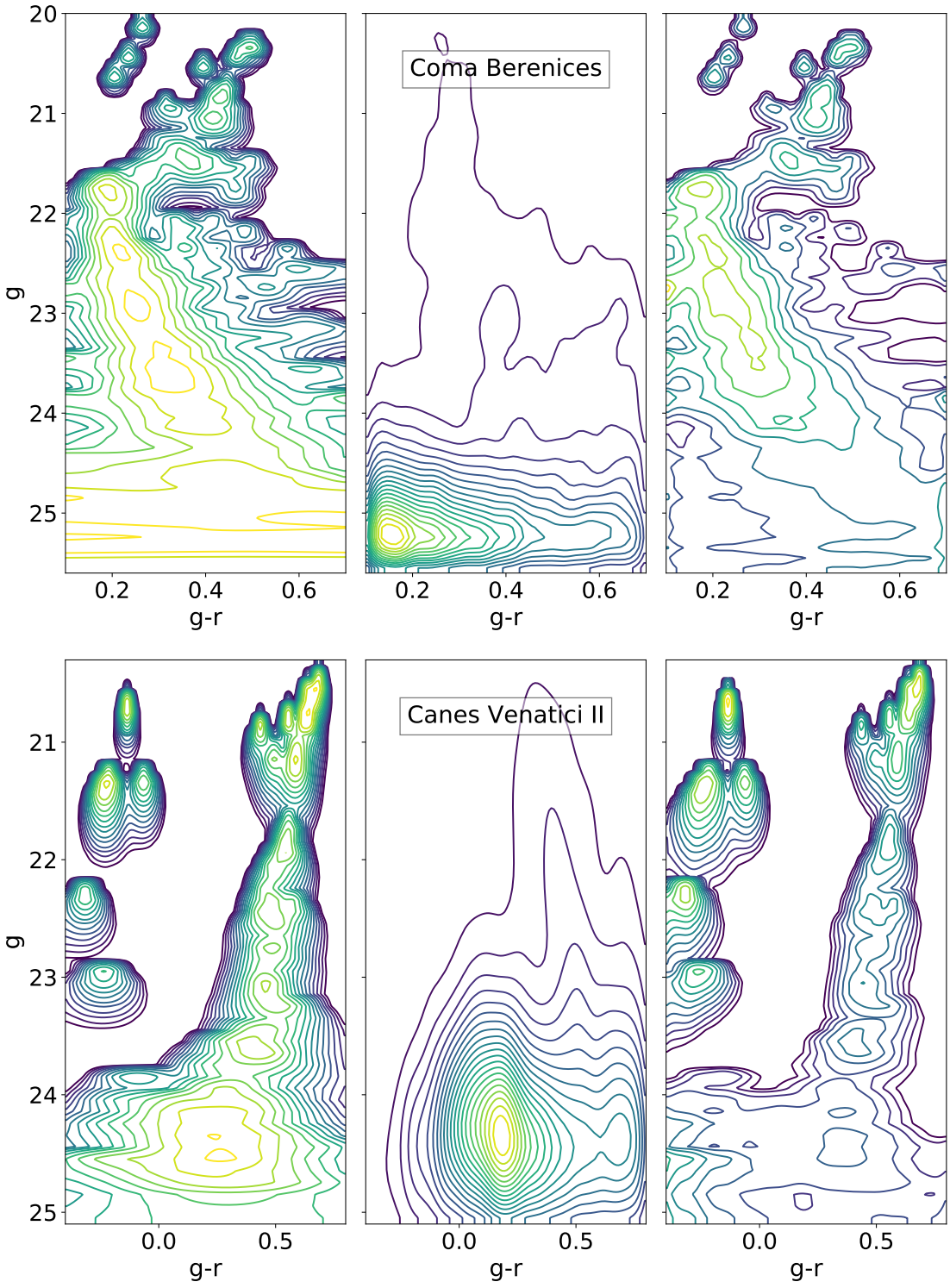

Figure 3.40: Same as 3.36, but for the Coma Berenices and Canes Venatici II UFDs.

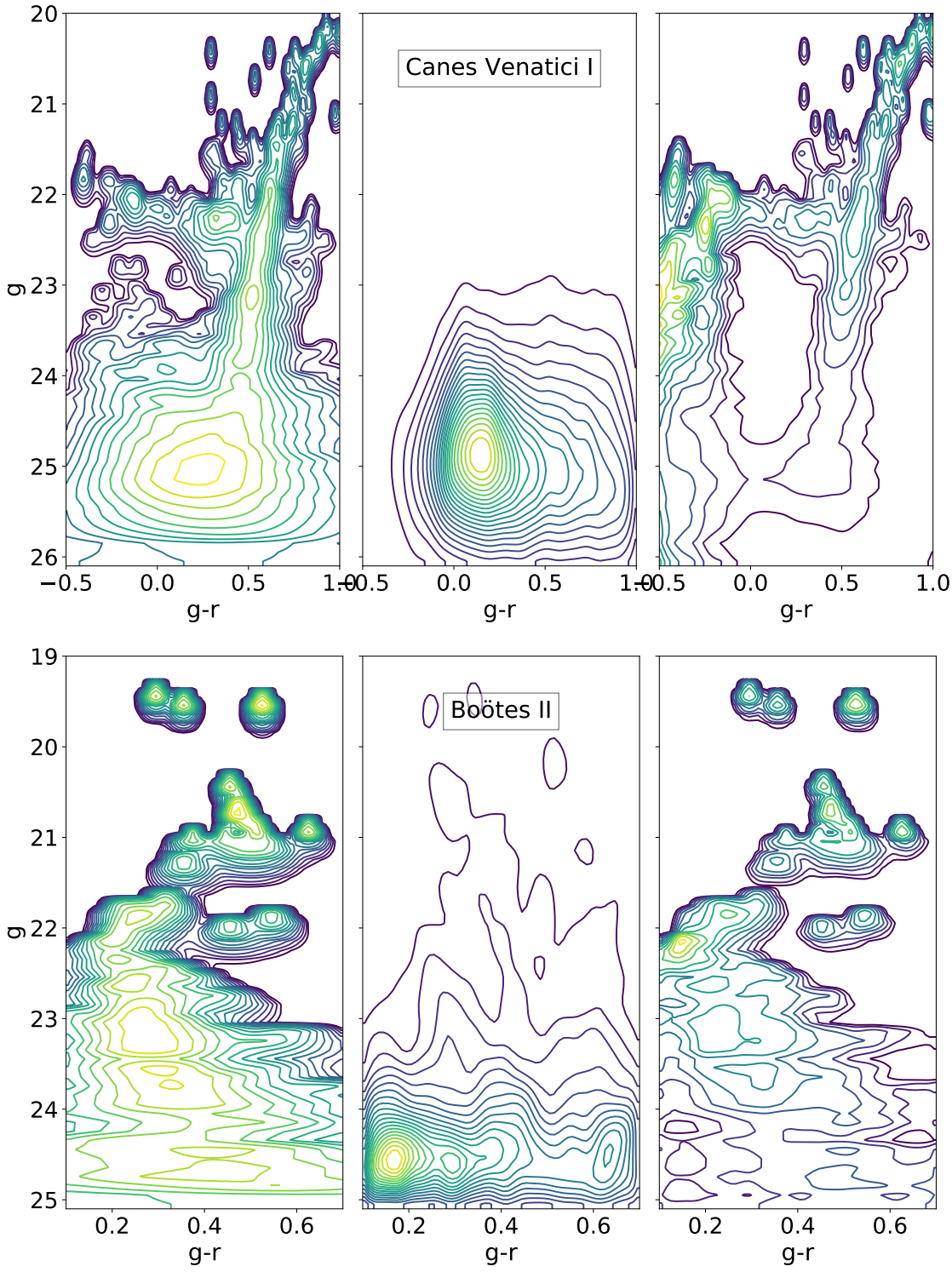

Figure 3.41: Same as 3.36, but for the Canes Venatici I and Boötes II UFDs.

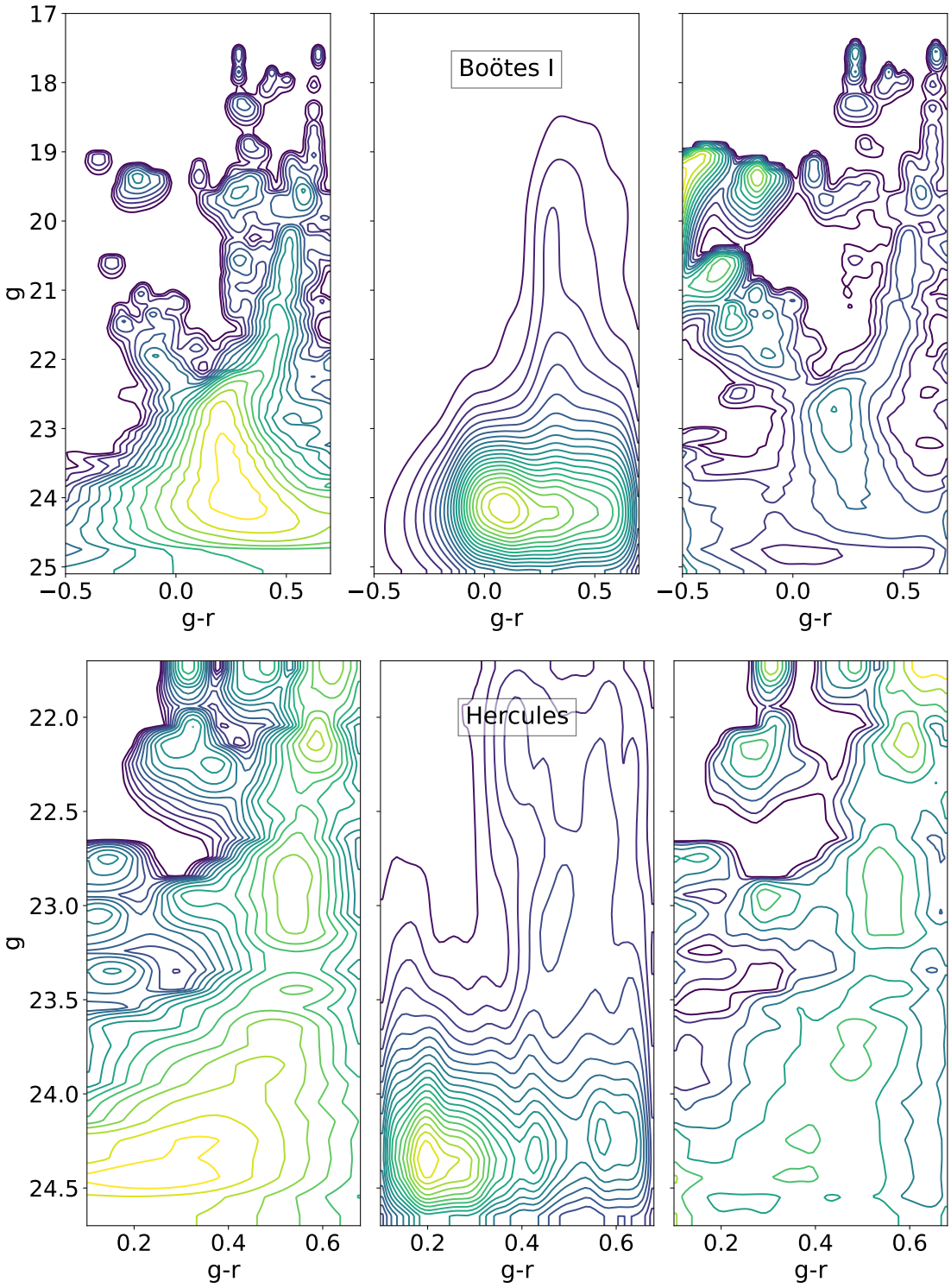

Figure 3.42: Same as 3.36, but for the Boötes I and Hercules UFDs.

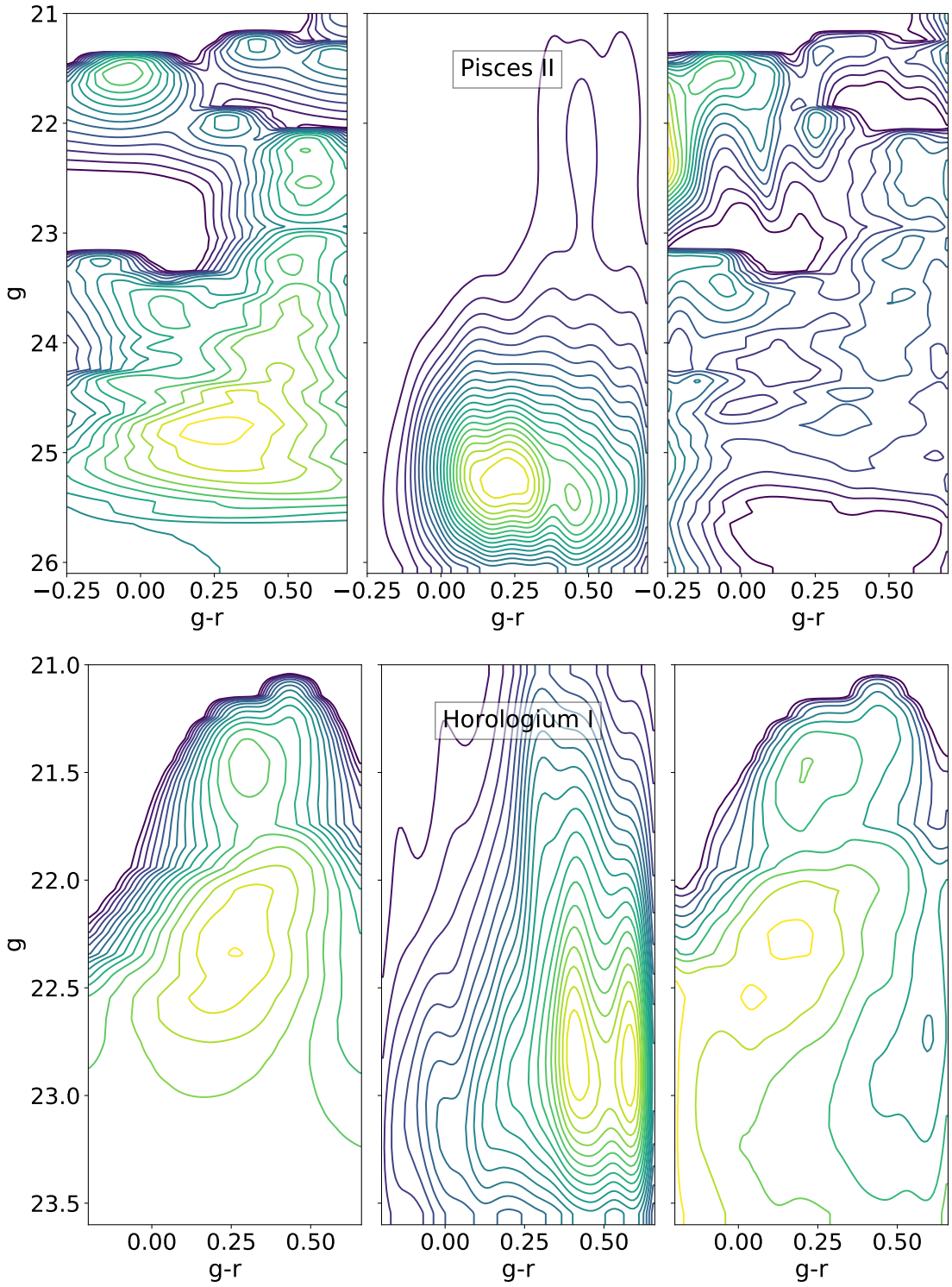

Figure 3.43: Same as 3.36, but for the Pisces II and Horologium I UFDs.

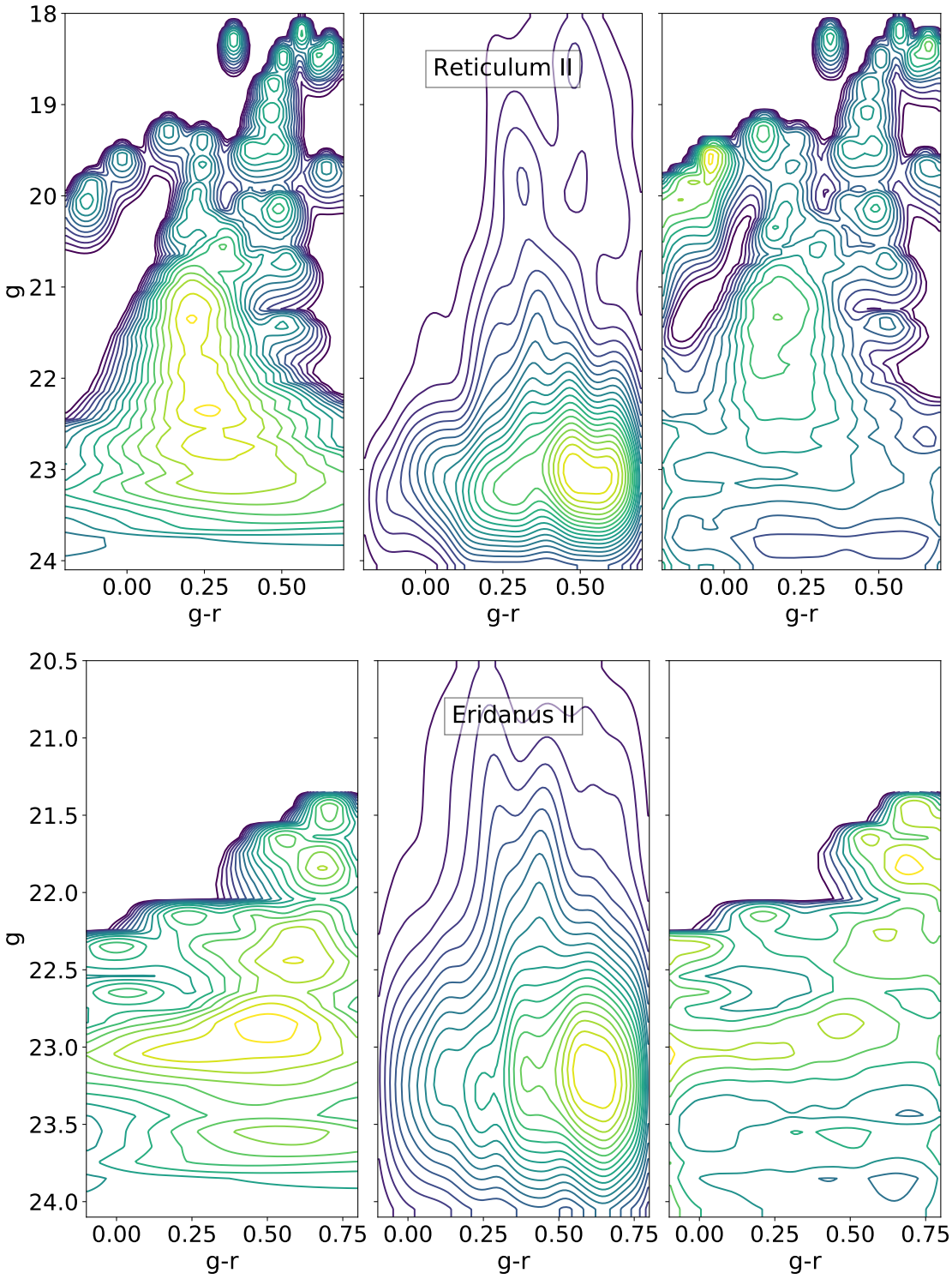

Figure 3.44: Same as 3.36, but for the Reticulum II and Eridanus II UFDs.

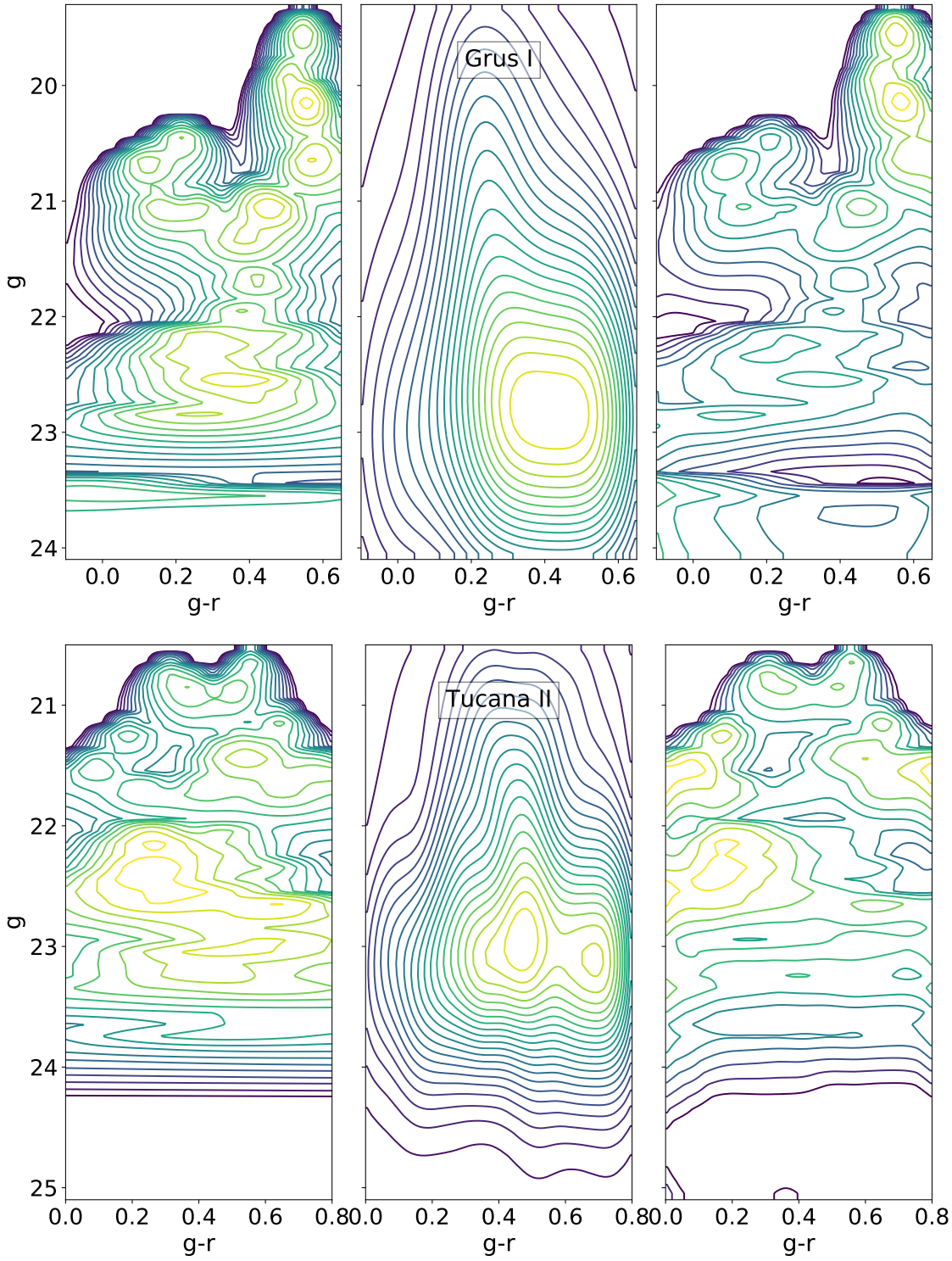

Figure 3.45: Same as 3.36, but for the Grus I and Tucana II UFDs.

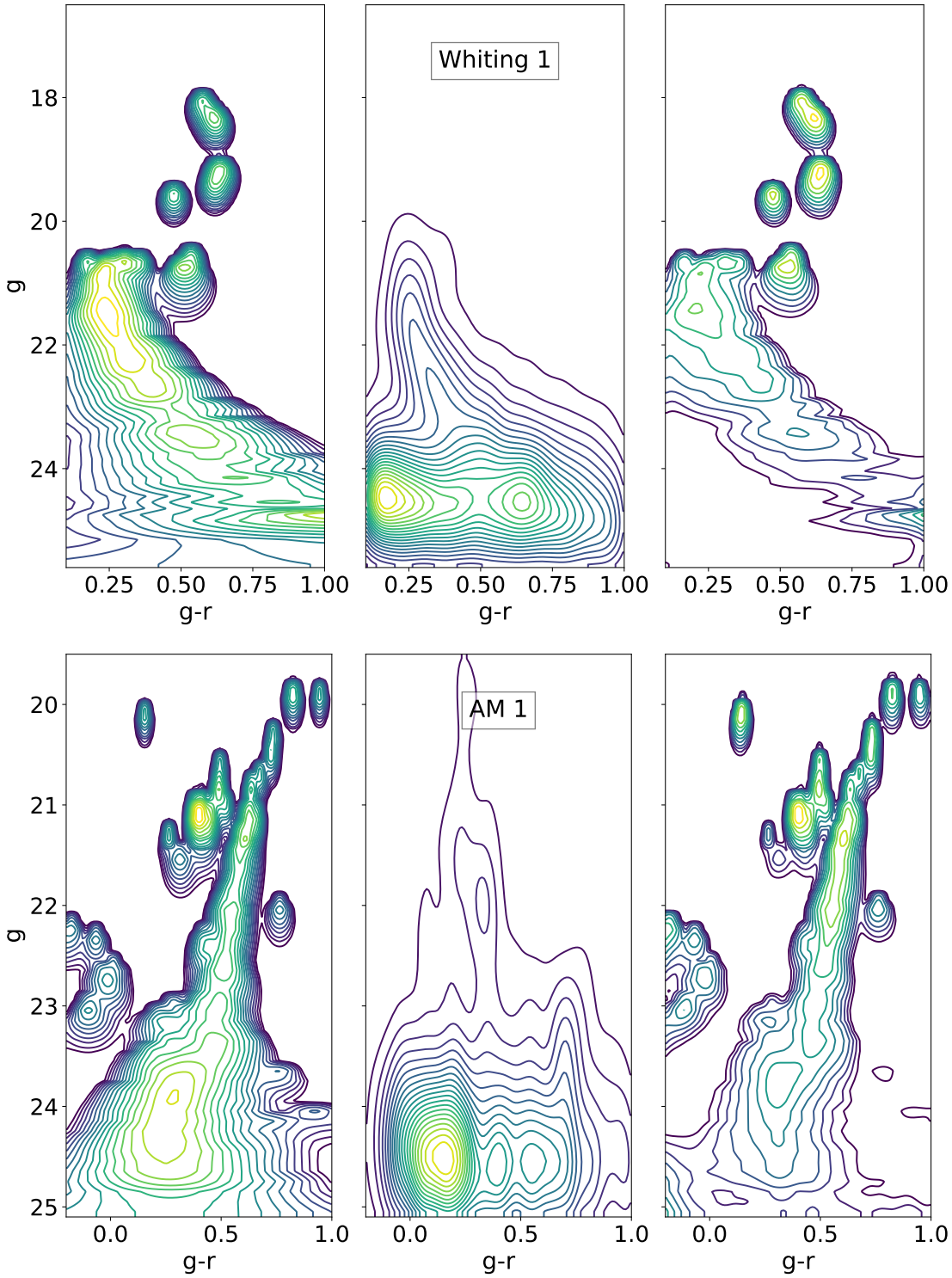

Figure 3.46: Estimated member star distribution (left panel), background star distribution (middle panel), and star weight distribution (right panel) for the Whiting 1 and AM 1 outer halo GCs. The star weight in each color-magnitude bin is given by the factor $f_{\mathrm{obj,(i,j)}}/n_{\mathrm{bkg,(i,j)}}$. In all panels, yellow represents higher counts than purple.

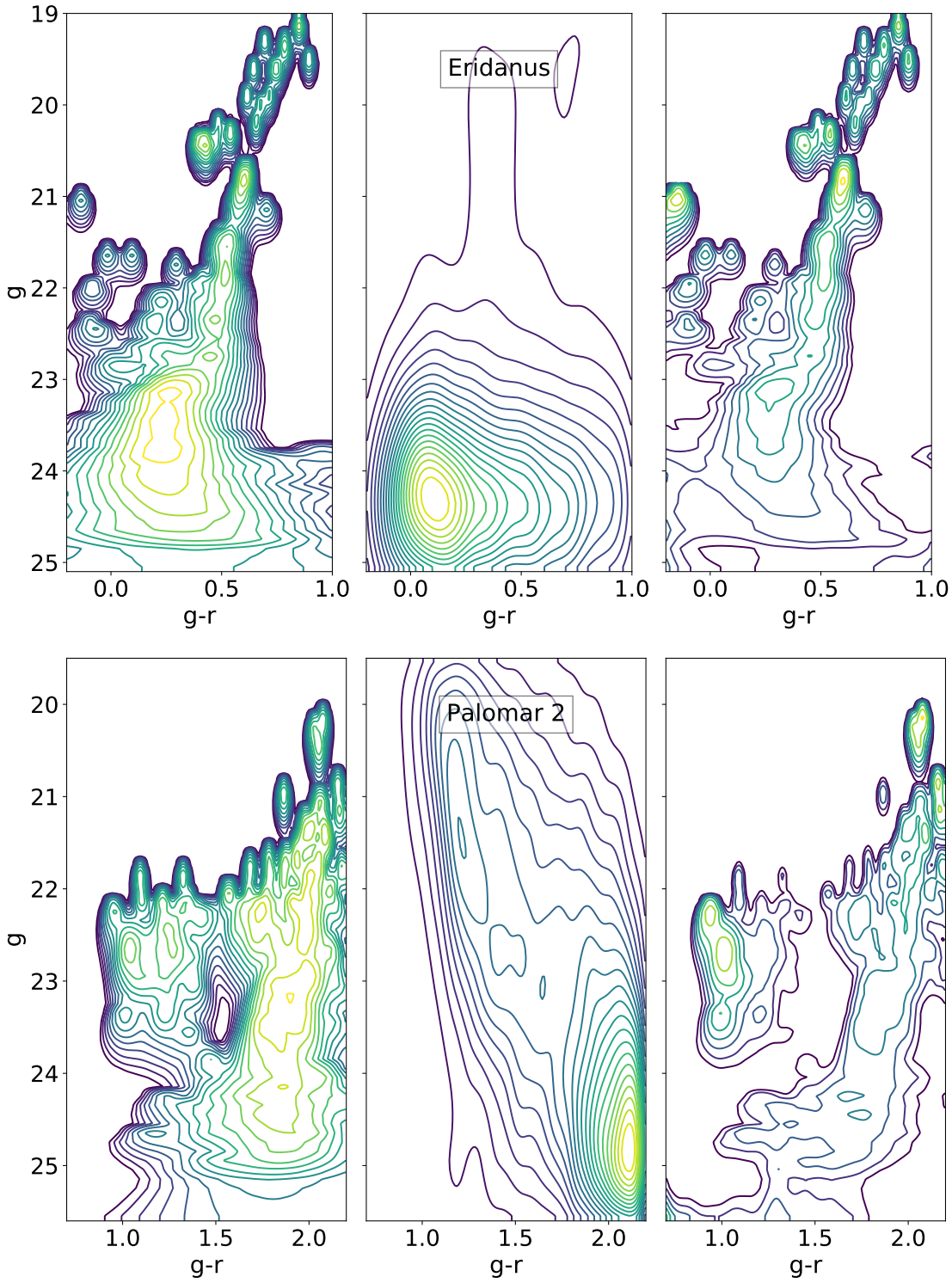

Figure 3.47: Same as Figure 3.46, but for the Eridanus and Palomar 2 outer halo GCs.

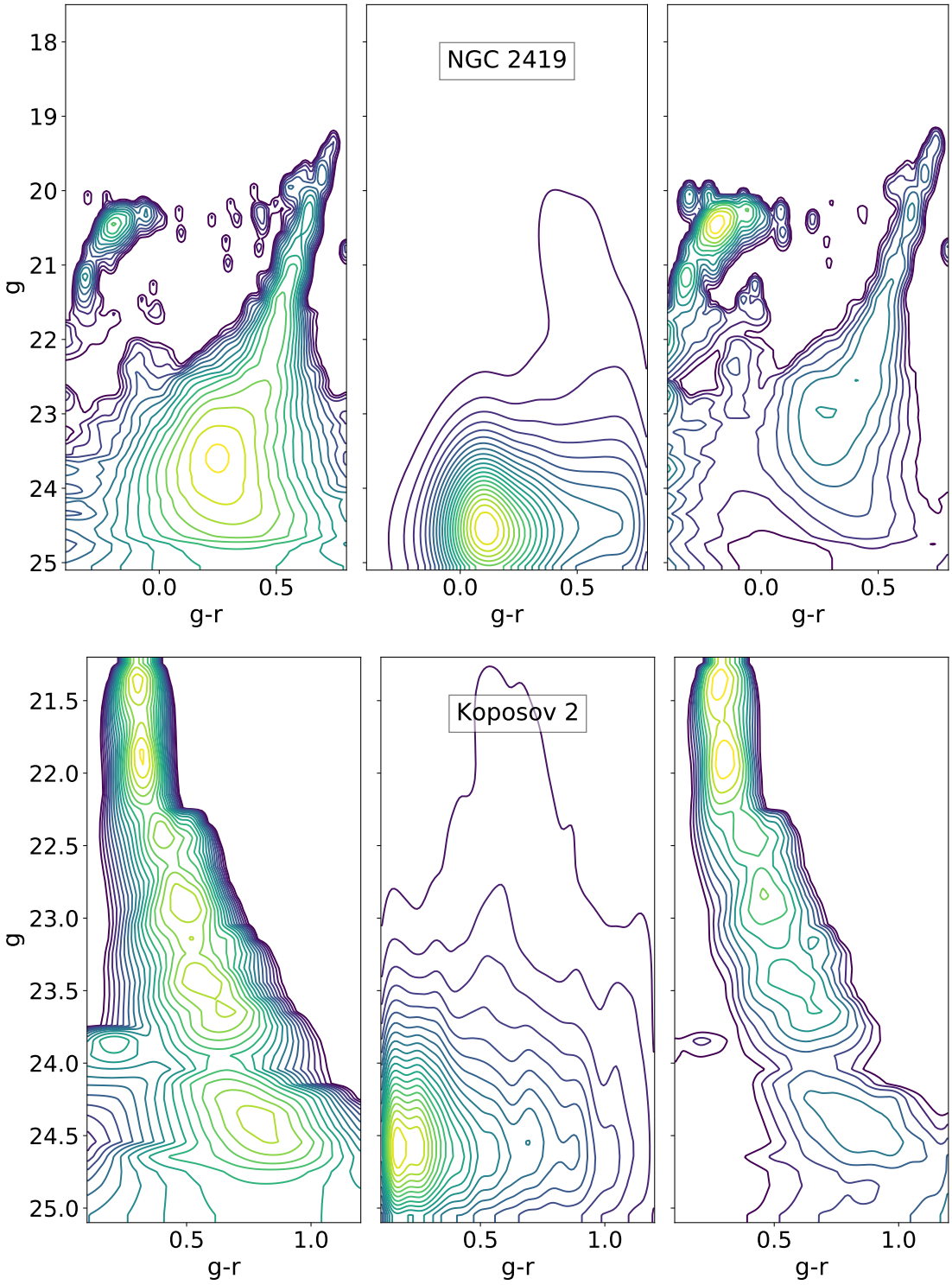

Figure 3.48: Same as Figure 3.46, but for the NGC 2419 and Koposov 2 outer halo GCs.

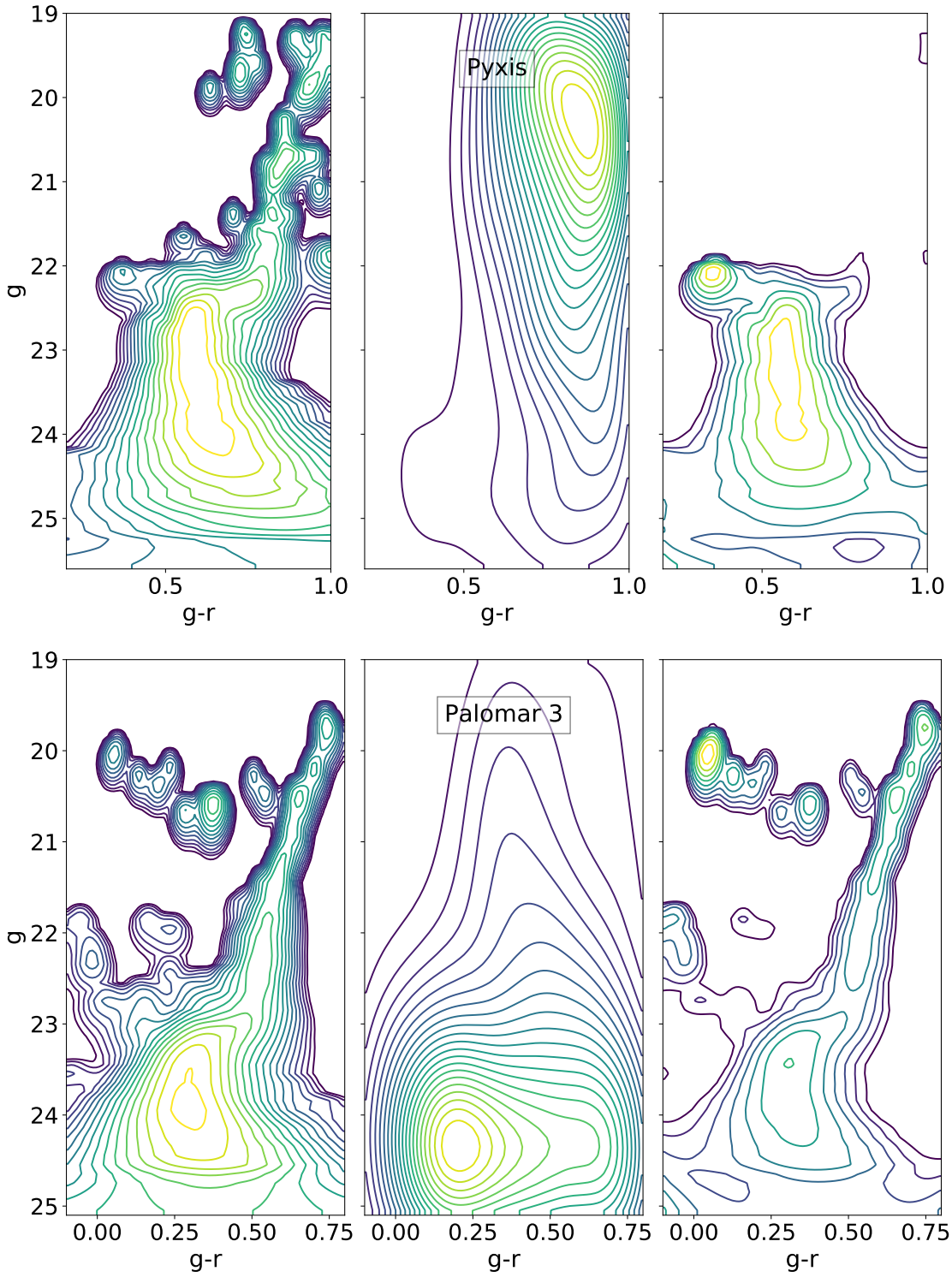

Figure 3.49: Same as Figure 3.46, but for the Pyxis and Palomar 3 outer halo GCs.

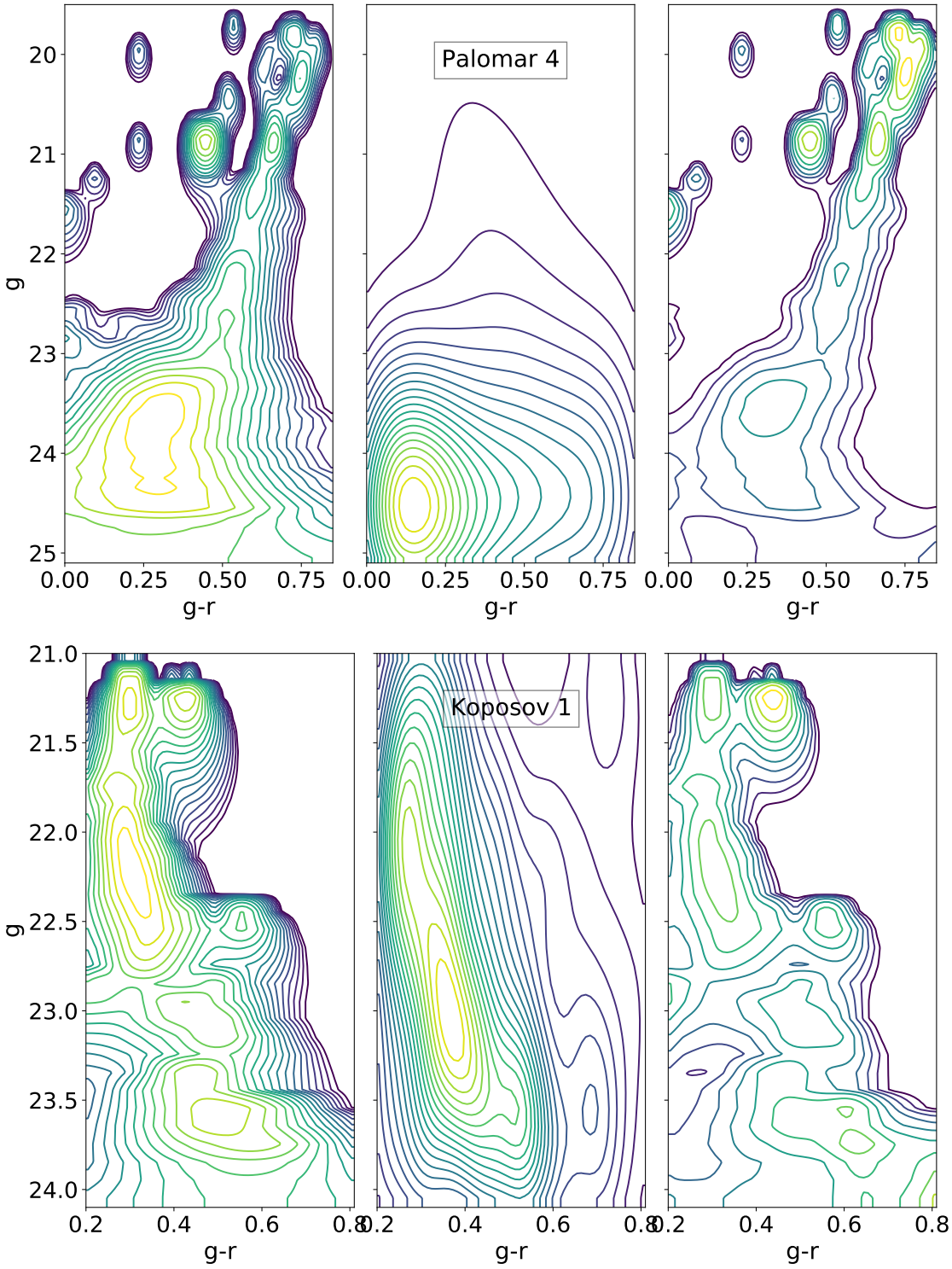

Figure 3.50: Same as Figure 3.46, but for the Palomar 4 and Koposov 1 outer halo GCs.

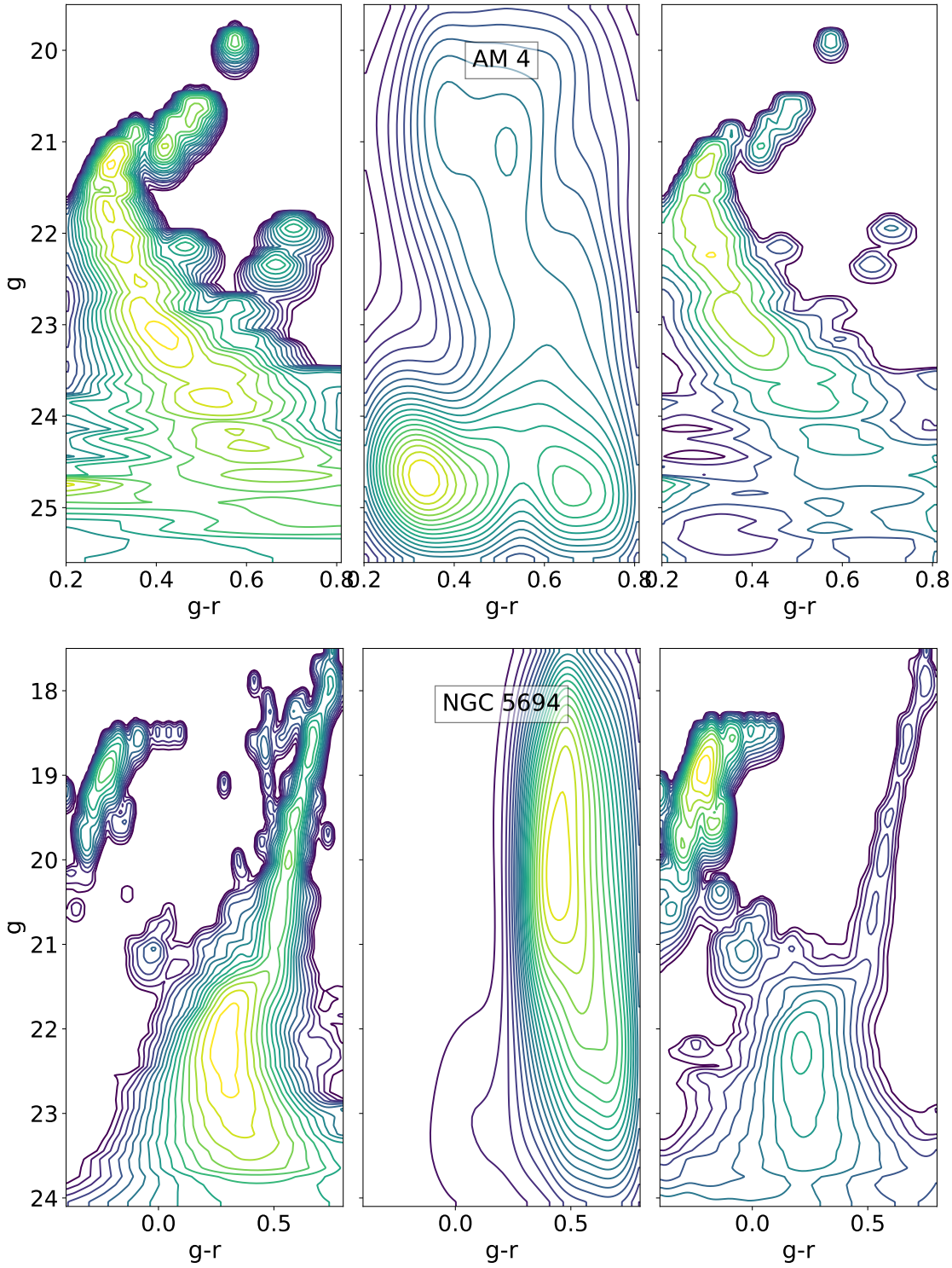

Figure 3.51: Same as Figure 3.46, but for the AM 4 and NGC 5694 outer halo GCs.

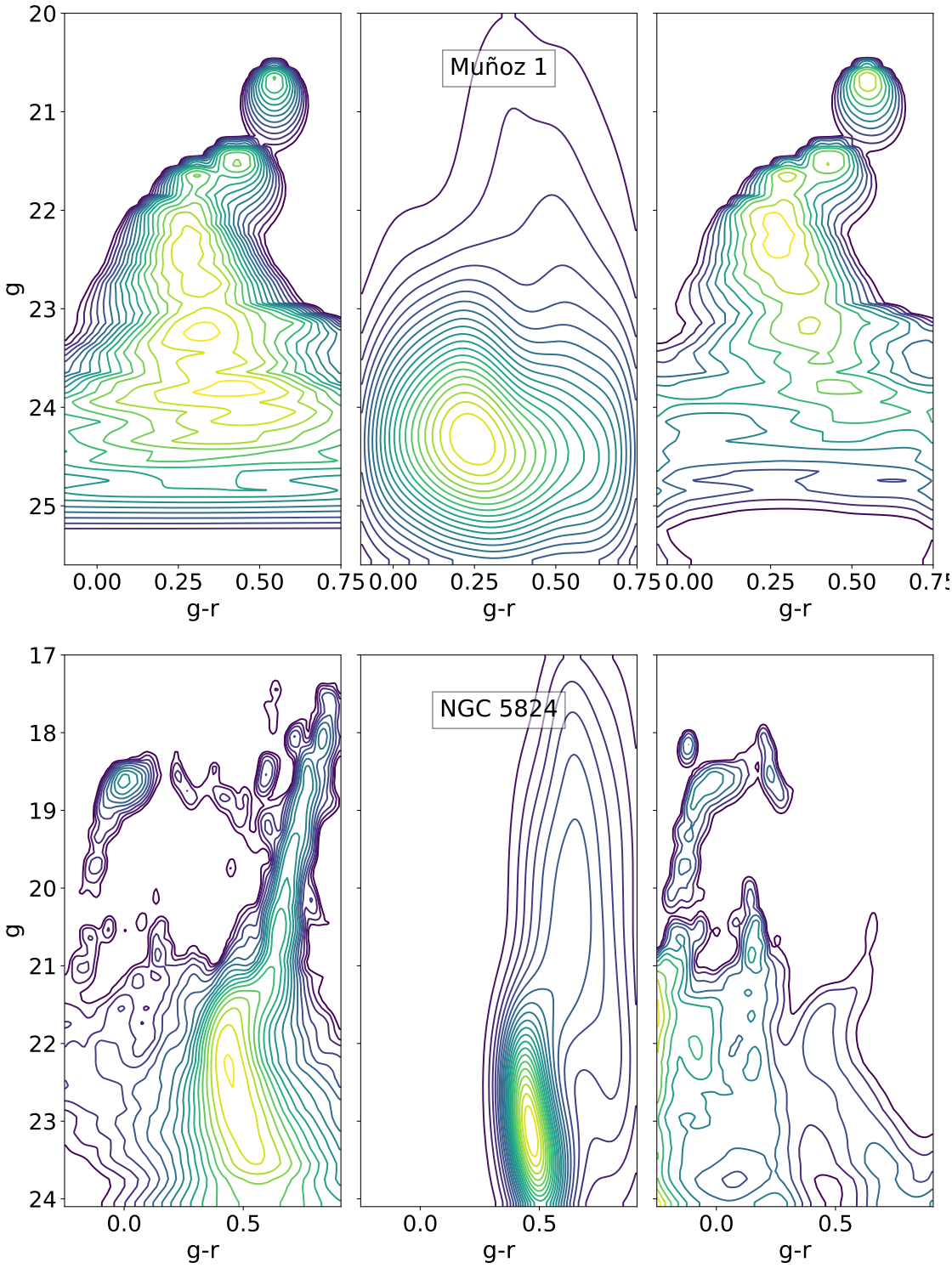

Figure 3.52: Same as Figure 3.46, but for the Muñoz 1 and NGC 5824 outer halo GCs.

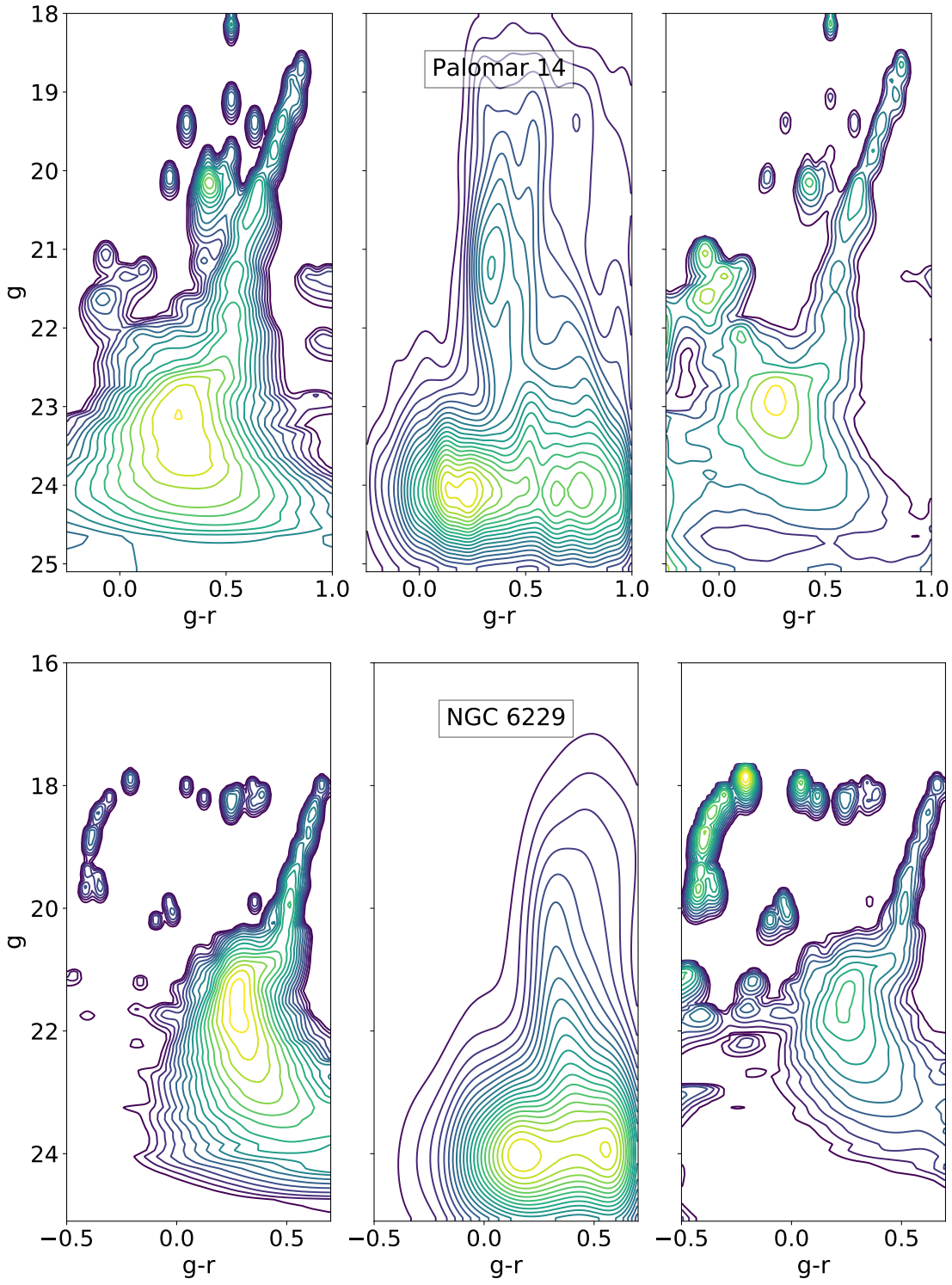

Figure 3.53: Same as Figure 3.46, but for the Palomar 14 and NGC 6229 outer halo GCs.

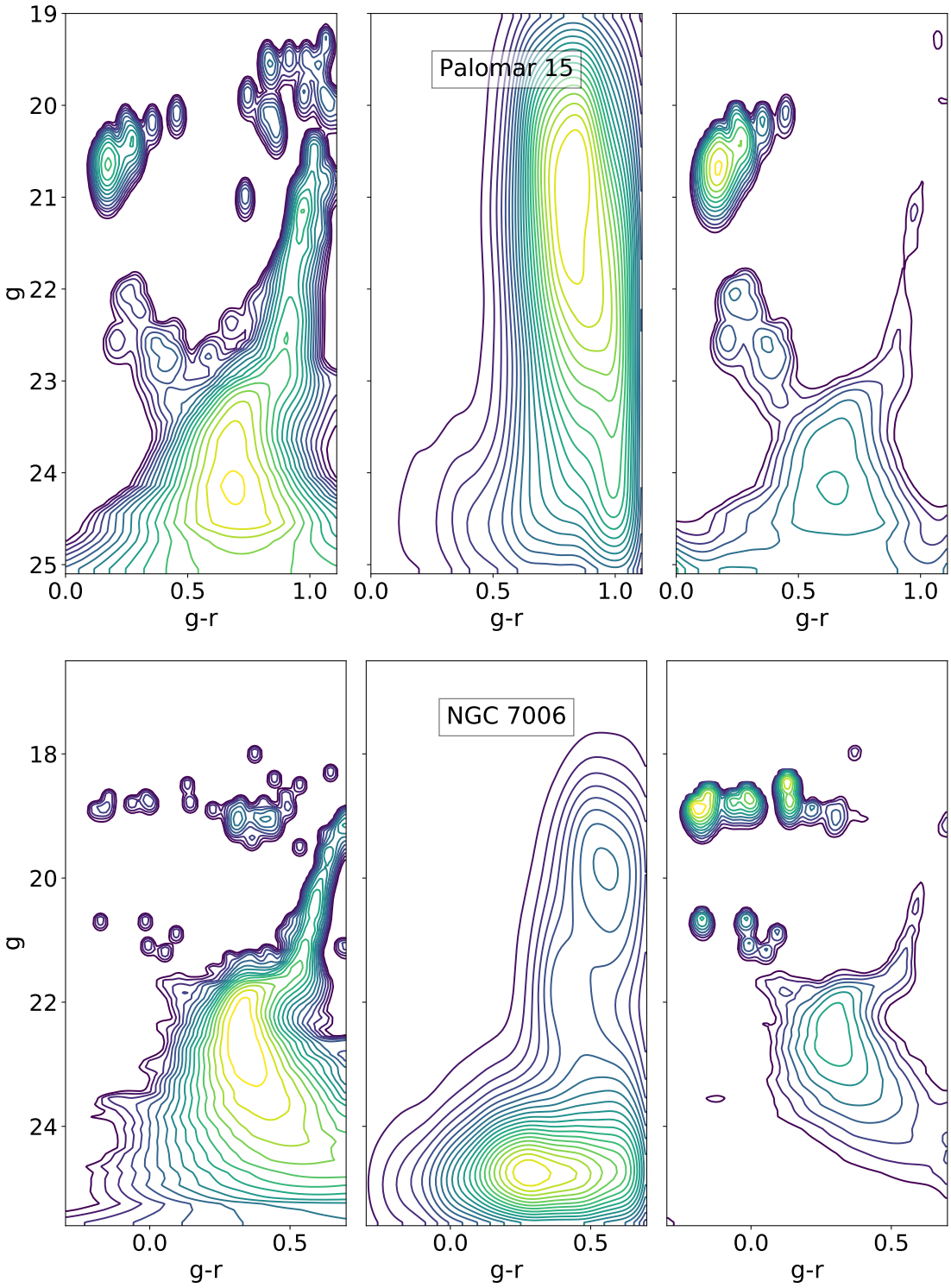

Figure 3.54: Same as Figure 3.46, but for the Palomar 15 and NGC 7006 outer halo GCs.

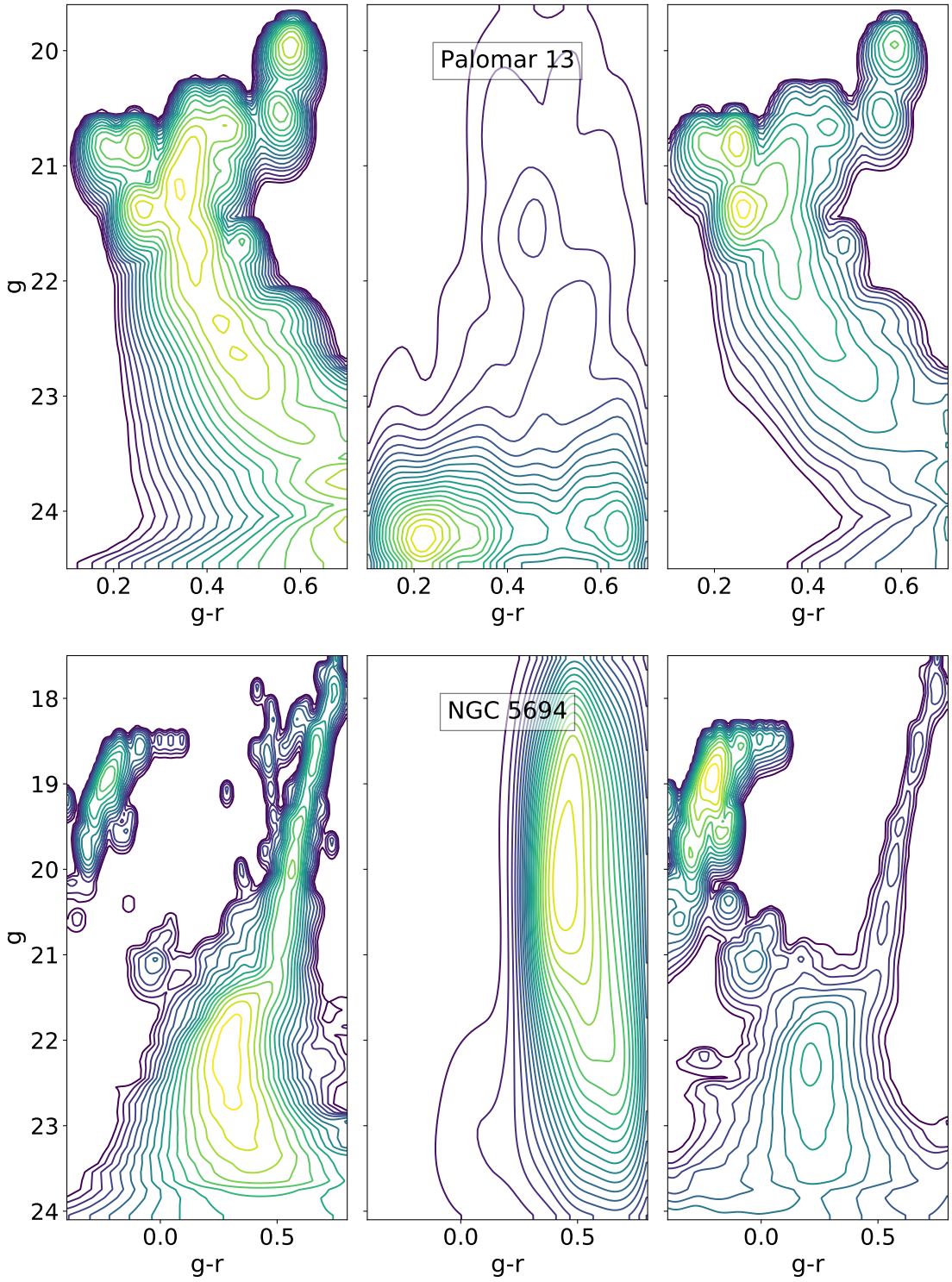

Figure 3.55: Same as Figure 3.46, but for the Palomar 13 and Segue 3 outer halo GCs.

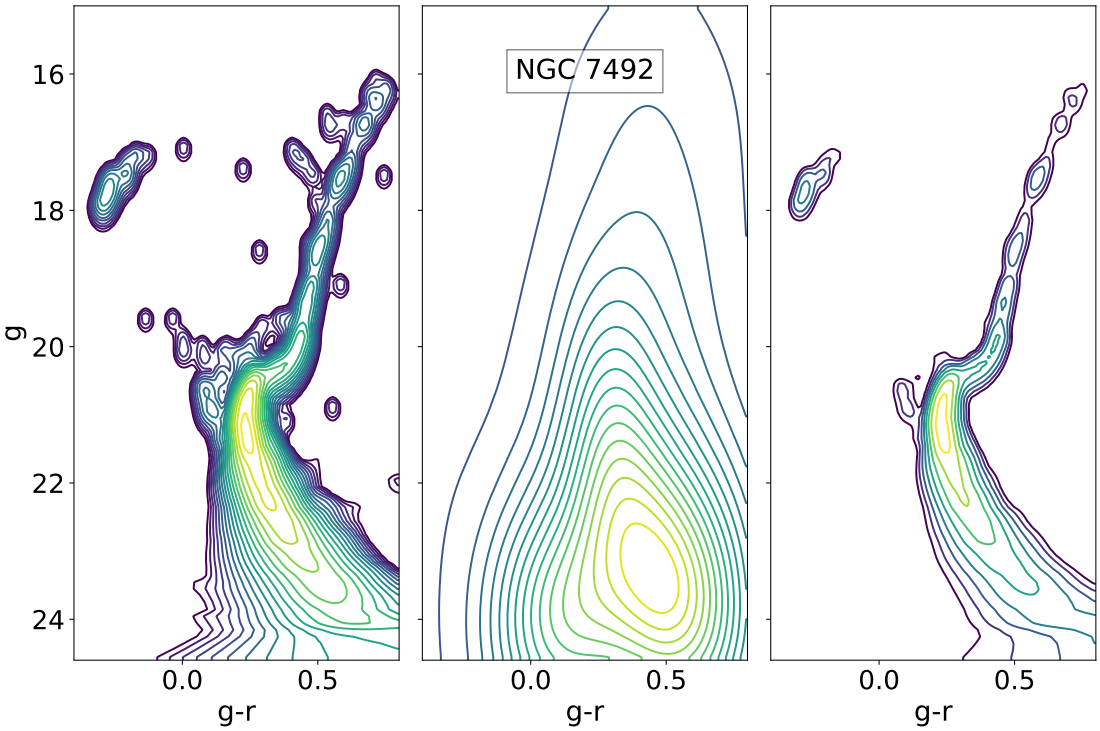

Figure 3.56: Same as Figure 3.46, but for the NGC 7492 outer halo GC.

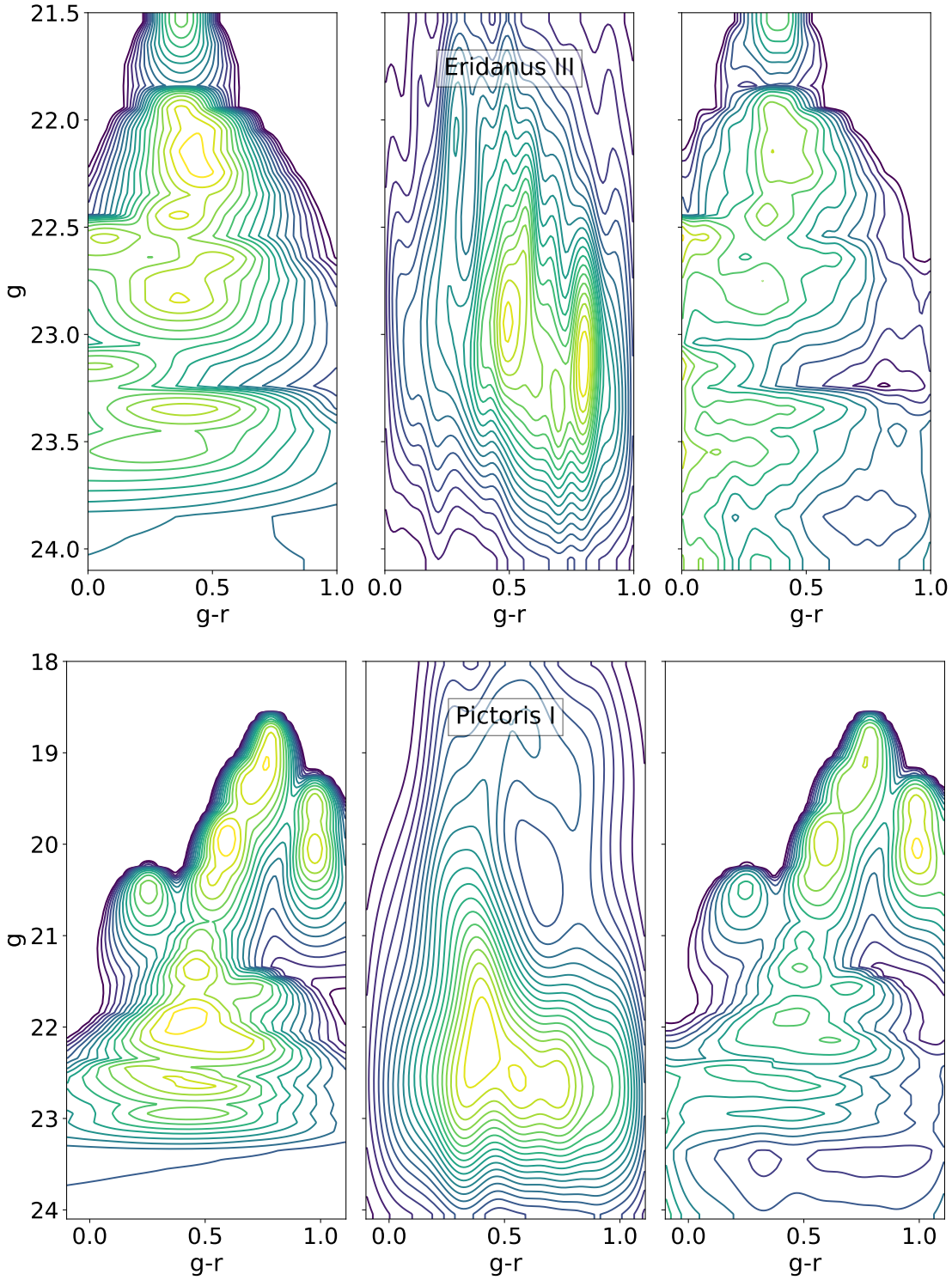

Figure 3.57: Estimated member star distribution (left panel), background star distribution (middle panel), and star weight distribution (right panel) for the Eridanus III and Pictoris I not classified satellites. The star weight in each color-magnitude bin is given by the factor $f_{\mathrm{obj,(i,j)}}/n_{\mathrm{bkg,(i,j)}}$. In all panels, yellow represents higher counts than purple.

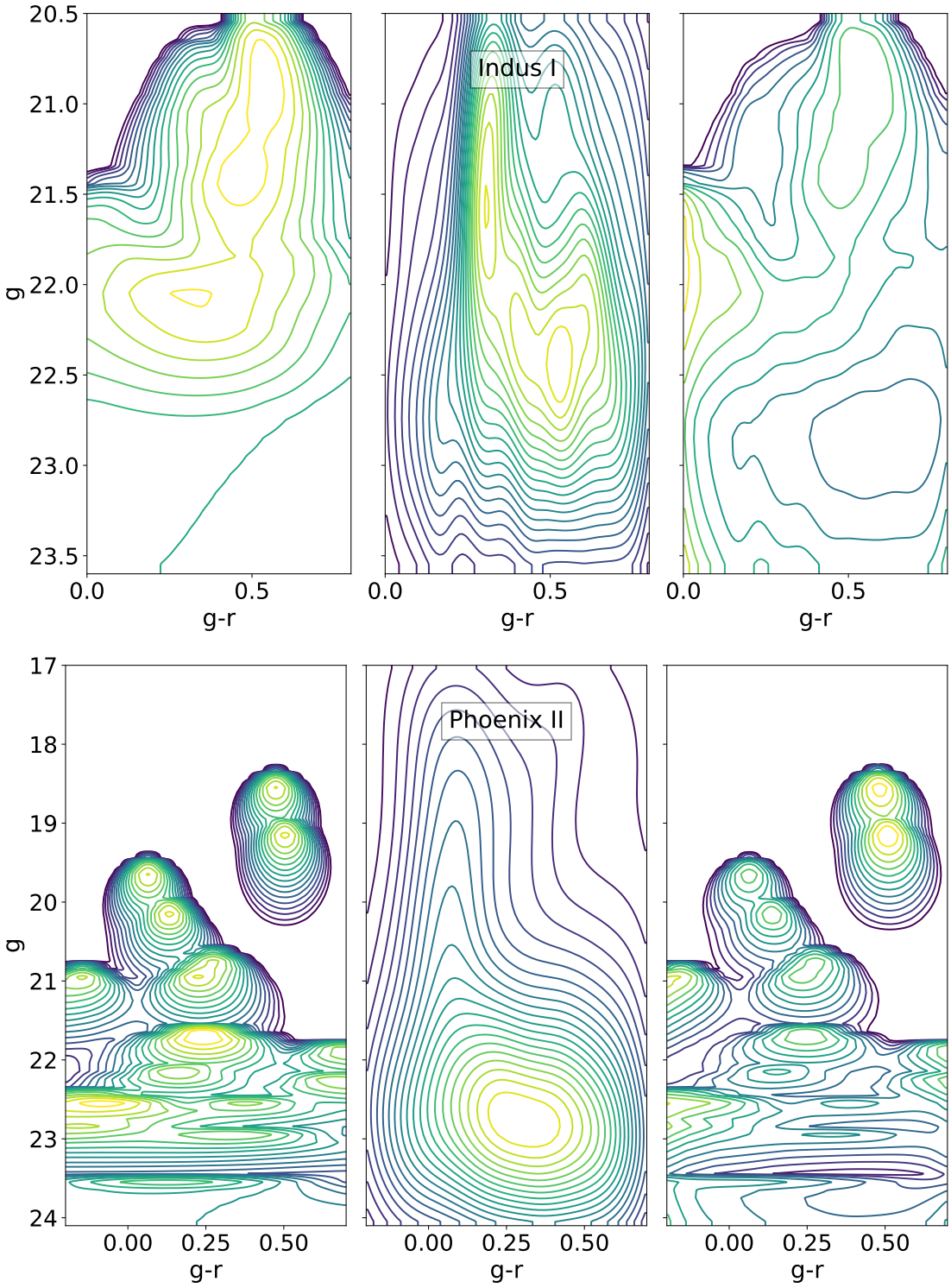

Figure 3.58: Same as Figure 3.57, but for the Indus I and Phoenix II not classified satellites.

Summary

In this thesis, I performed a comprehensive analysis of the photometric and structural properties of the satellites in the outer halo of the Milky Way (MW). The main objective is to shed light on the formation history of the MW and the processes that shape the properties of its structures.

To achieve this, I use a new dataset composed of observations of 57 outer halo satellites of the MW, which includes Globular Clusters (GCs), classical dwarf-spheroidal (dSph) galaxies, Ultra-faint dwarf (UFD) galaxies, and several objects not yet classified. Unlike other datasets in the literature, the one used in this work is at the same time deep, wide-field and highly homogeneous, characteristics that make it ideal to study and compare the properties of satellite structures of different types.

In Chapter 2, I explored in detail a strong correlation between the Sérsic index and half-light radius that is followed by almost all the outer halo satellite objects included in our MegaCam sample (Muñoz et al., 2018a). More importantly, in this trend, a large number of GCs follow the same locus as dwarf galaxies, adding support to the similarities between these two types of objects.

I followed the procedure of Graham & Driver (2005) to see if the correlation in the $n - R_{\rm e}$ plot can be a consequence of empirical linear relations in the $\mu_0 - M_{\rm V}$ and $n - M_{\rm V}$ parameter spaces for objects that follow a Sérsic density profile. I showed that this is possible if we consider two different classes of outer halo GCs: one that is composed of clusters of low surface brightness (LSB), with properties similar to UFD galaxies (the LSB group), and another that is composed of clusters of high surface brightness (HSB), with properties similar to inner halo GCs (the HSB group). From my analysis, we saw that empirical linear relations can be fit to the LSB GC + dwarf galaxy group and for the HSB GC group (including the inner GCs). However, for HSB GCs, the $n - R_{\rm e}$ relation cannot be reproduced, probably because they are not fully described by a pure Sérsic profile.

Given the strong similarities between LSB GCs and dwarf galaxies, and considering that the latter are dominated by dark matter (DM), I proposed that this is consistent with the notion that GCs also formed inside halos of DM, sharing a common formation process. This idea is supported by previous works that show that GCs with properties similar to what is empirically observed today can be originated by a formation process inside a DM halo.

Finally, to explain the existence of HSB and LSB GCs in a scenario where all clusters formed through a common process, I proposed that the tidal effects of the host galaxy play

a major role in the shaping of the cluster's properties. GCs of both types are formed inside MW-like and dwarf galaxies. However, the ones formed inside MW-like galaxies are subjected to stronger tidal forces than the ones inside dwarf galaxies. Thus, LSB GCs inside the MW were quickly disrupted, while HSB GCs, given their higher masses and densities, survived, albeit losing part of their mass; on the other hand, both HSB and LSB GCs survived inside dwarf galaxies. Later, during the process of accretion of dwarf galaxies by the MW, the external HSB and LSB GC populations were incorporated into our Galaxy's cluster system. From this moment, the stronger potential of the MW started its tidal effect over them. The scenario just proposed would explain the observed proportion of external and in-situ origin for both HSB and LSB GCs. In fact, following the classification scheme proposed by Zinn (1993), around half of the HSB GCs are of OH type, while the other half is of YH type, a distribution consistent with a mix of external and in-situ origin. In contrast, for the LSB group, almost all of them are of YH type, suggesting that the majority of them were stripped from accreted dwarf galaxies.

Future high-precision proper motion measurements of satellite galaxies, especially for UFDs and outer halo GCs, will allow us to know the true origin of HSB and LSB clusters. I predict that the majority of LSB clusters should have orbits similar to UFDs and dSphs, while HSB clusters should orbit the Galaxy in a way similar to inner halo GCs.

In Chapter 3, I used a matched-filter technique to study in detail the morphology of 52 outer halo satellite objects of the MW. The dataset is composed of 7 classical dSphs, 20 UFDs, 21 GCs, and 4 not-classified objects and used wide-field and deep photometry from Muñoz et al. (2018b). The matched-filter technique allows assigning a probability of belonging to the satellite to each star in the object's catalog, according to its position on the CMD resulting from the ratio of the member stars' distribution and the background distribution. From the results, I conclude that almost all UFDs show some signs of irregularities, with a few of them showing strong signs of tidal disruption, while classical dSphs and GCs have for the most part regular elliptical or spherical morphologies.

I also calculated the $g_{\rm ratio}$ parameter, which aims at quantifying the relative importance of the tidal pull of the MW against the internal gravity of the satellite object, and the dynamical mass-to-light ratio $(M_{1/2}/L_{1/2})_{\rm dyn}$, for all the objects with available kinematic data. I showed that UFDs, classical dSphs and GCs follow a correlation when comparing these two parameters, where galaxies with higher $g_{\rm ratio}$ also have a higher $(M_{1/2}/L_{1/2})_{\rm dyn}$ (see Figure 3.4). Moreover, I found that satellites with the highest values of $g_{\rm ratio}$ are the ones whose morphologies are more consistent with showing signs of tidal disruption.

I argued that the existence of this correlation does not necessarily imply a problem for the Λ-CDM paradigm. If tidal disruption is removing stellar mass from satellites, and because $M_{1/2}$ should remain unaffected by tidal effects, the loss of stellar mass should be reflected in both higher $(M_{1/2}/L_{1/2})_{\rm dyn}$ and $g_{\rm ratio}$, leading naturally to the correlation of figure 3.4.

Finally, I showed that among the outer halo satellite objects, UFDs are the ones that are currently most likely to be affected by the tidal effects of the MW potential. This suggests that in the "nurture vs nature" paradigm, the "nurture" component plays a major role in shaping the properties of satellite objects.

In this thesis, I showed that both the internal physical processes of satellites ("Nature") and the influence of the MW's gravitational potential ("Nurture") play a major role in shaping the properties of MW's outer halo satellites. The observed differences in properties of outer halo GCs require that they form on different galactic environments and, when accreted by the MW, their properties are affected by the stronger potential. Additionally, the strong signs of tidal disruption in UFDs and the correlation between $(M_{1/2}/L_{1/2})_{\rm dyn}$ and $g_{\rm ratio}$ support the idea that "nurture" from the MW's potential is still affecting the observed properties of satellites.

A more complete census of the satellites surrounding our Galaxy and a better estimation of their photometric, dynamical and structural parameters are necessary to fully understand the extent of the "Nature versus Nurture" scenario. The Large Synoptic Survey Telescope (LSST), with its deep observations and wide coverage, will be able to detect all dwarf galaxies within the MW's virial radius (if the luminosity range of the undetected population is similar to what is currently observed) and a large number of new GCs. This census will provide more objects to study the differences and similarities between the classes of satellites and will also help to better characterize their spatial distribution across the Galactic outer halo. Furthermore, the observations of the same portion of the sky in different epochs by the LSST will provide proper motions of stars in satellites. This, together with radial velocity measurements, will allow us to compute the orbits of the satellites, unlocking information useful to associate them with current orphan stellar streams and to know which satellites have been orbiting the MW for a long time and which have been recently accreted. This knowledge is fundamental to peek deeper into the formation history of the MW and to better understand the role of our Galaxy's gravitational potential in shaping the observed properties of satellites.

Bibliography

Aaronson, M. 1983, ApJ, 266, L11

Adén, D., Feltzing, S., Koch, A., et al. 2009, A&A, 506, 1147

Albert, A., Anderson, B., Bechtol, K., et al. 2017, ApJ, 834, 110

Archambault, S., Archer, A., Benbow, W., et al. 2017, PhRvD, 95, 082001

Armandroff, T. E. 1989, AJ, 97, 375

Armandroff, T. E., & Da Costa, G. S. 1986, AJ, 92, 777

Armandroff, T. E., Olszewski, E. W., & Pryor, C. 1995, AJ, 110, 2131

Baade, W., & Hubble, E. 1939, PASP, 51, 40

Balbinot, E., Santiago, B. X., da Costa, L., et al. 2013, ApJ, 767, 101

Baumgardt, H., Côté, P., Hilker, M., et al. 2009, MNRAS, 396, 2051

Bechtol, K., Drlica-Wagner, A., Balbinot, E., et al. 2015, ApJ, 807, 50

Bellazzini, M., Mucciarelli, A., Sollima, A., et al. 2015, MNRAS, 446, 3130

Belokurov, V., Irwin, M. J., Koposov, S. E., et al. 2014, MNRAS, 441, 2124

Belokurov, V., Zucker, D. B., Evans, N. W., et al. 2006a, ApJ, 647, L111

—. 2006b, ApJ, 642, L137

—. 2007, ApJ, 654, 897

Belokurov, V., Walker, M. G., Evans, N. W., et al. 2008, ApJ, 686, L83

—. 2009, MNRAS, 397, 1748

—. 2010, ApJ, 712, L103

Benson, A. J., Lacey, C. G., Baugh, C. M., Cole, S., & Frenk, C. S. 2002, MNRAS, 333, 156

Blaña, M., Fellhauer, M., Smith, R., et al. 2015, MNRAS, 446, 144

Bovill, M. S., & Ricotti, M. 2009, ApJ, 693, 1859

Bradford, J. D., Geha, M., Muñoz, R. R., et al. 2011, ApJ, 743, 167

Bullock, J. S., & Johnston, K. V. 2005, ApJ, 635, 931

Bullock, J. S., Kravtsov, A. V., & Weinberg, D. H. 2000, ApJ, 539, 517

Cannon, R. D., Hawarden, T. G., & Tritton, S. B. 1977, MNRAS, 180, 81P

Caon, N., Capaccioli, M., & D'Onofrio, M. 1993, MNRAS, 265, 1013

Caon, N., Capaccioli, M., & Rampazzo, R. 1990, A&AS, 86, 429

Capaccioli, M. 1989, in World of Galaxies (Le Monde des Galaxies), ed. J. Corwin, Harold G. & L. Bottinelli, 208–227

Carballo-Bello, J. A., Gieles, M., Sollima, A., et al. 2012, MNRAS, 419, 14

Carballo-Bello, J. A., Martínez-Delgado, D., Navarrete, C., et al. 2018, MNRAS, 474, 683

Carollo, D., Beers, T. C., Lee, Y. S., et al. 2007, Nature, 450, 1020

Carollo, D., Beers, T. C., Chiba, M., et al. 2010, ApJ, 712, 692

Casetti-Dinescu, D. I., Carlin, J. L., Girard, T. M., et al. 2008, AJ, 135, 2013

Chambers, K. C., & Pan-STARRS Team. 2016, in American Astronomical Society Meeting Abstracts, Vol. 227, American Astronomical Society Meeting Abstracts #227, 324.07

Chen, C. W., & Chen, W. P. 2010, ApJ, 721, 1790

Coleman, M. G., de Jong, J. T. A., Martin, N. F., et al. 2007, ApJ, 668, L43

Côté, P., Ferrarese, L., Jordán, A., et al. 2007, ApJ, 671, 1456

Da Costa, G. S., Held, E. V., & Saviane, I. 2014, MNRAS, 438, 3507

Dark Energy Survey Collaboration, Abbott, T., Abdalla, F. B., et al. 2016, MNRAS, 460, 1270

de Vaucouleurs, G. 1948, Annales d'Astrophysique, 11, 247

Deason, A. J., Belokurov, V., Evans, N. W., Watkins, L. L., & Fellhauer, M. 2012, MNRAS, 425, L101

Dehnen, W., McLaughlin, D. E., & Sachania, J. 2006, MNRAS, 369, 1688

Diehl, H. T., & Dark Energy Survey Collaboration. 2014, in American Astronomical Society

Meeting Abstracts, Vol. 223, American Astronomical Society Meeting Abstracts #223, 254.10

Drlica-Wagner, A., Bechtol, K., Rykoff, E. S., et al. 2015, ApJ, 813, 109

Duffau, S., Zinn, R., Vivas, A. K., et al. 2006, ApJ, 636, L97

Efstathiou, G. 1992, MNRAS, 256, 43P

Eggen, O. J., Lynden-Bell, D., & Sandage, A. R. 1962, ApJ, 136, 748

Ellis, R. S. 1997, ARA&A, 35, 389

Eskridge, P. B. 1988, AJ, 96, 1352

Fadely, R., Willman, B., Geha, M., et al. 2011, AJ, 142, 88

Fellhauer, M., Wilkinson, M. I., Evans, N. W., et al. 2008, MNRAS, 385, 1095

Ferrarese, L., Côté, P., Jordán, A., et al. 2006, ApJS, 164, 334

Flaugher, B., Diehl, H. T., Honscheid, K., et al. 2015, AJ, 150, 150

Foreman-Mackey, D., Hogg, D. W., Lang, D., & Goodman, J. 2013, Publications of the Astronomical Society of the Pacific, 125, 306

Frank, M. J., Hilker, M., Baumgardt, H., et al. 2012, MNRAS, 423, 2917

Fritz, T. K., Battaglia, G., Pawlowski, M. S., et al. 2018, A&A, 619, A103

Gaia Collaboration, Helmi, A., van Leeuwen, F., et al. 2018, A&A, 616, A12

Garling, C., Willman, B., Sand, D. J., et al. 2018, ApJ, 852, 44

Geha, M., Willman, B., Simon, J. D., et al. 2009, ApJ, 692, 1464

Goodwin, S. P. 1997, MNRAS, 286, L39

Graham, A. W. 2011, in EAS Publications Series, Vol. 48, EAS Publications Series, ed. M. Koleva, P. Prugniel, & I. Vauglin, 231–236

Graham, A. W., & Driver, S. P. 2005, Publications of the Astronomical Society of Australia, 22, 118

Graham, A. W., Erwin, P., Trujillo, I., & Asensio Ramos, A. 2003, AJ, 125, 2951

Graham, A. W., & Guzmán, R. 2003, AJ, 125, 2936

Grillmair, C. J. 2009, ApJ, 693, 1118

Grillmair, C. J., & Dionatos, O. 2006, ApJ, 641, L37

Grillmair, C. J., & Johnson, R. 2006, ApJ, 639, L17

Gurzadyan, V. G., Kocharyan, A. A., & Petrosian, A. R. 1993, Ap&SS, 201, 243

Hammer, F., Yang, Y., Arenou, F., et al. 2018, ApJ, 860, 76

Hammer, F., Yang, Y., Wang, J., et al. 2019, ApJ, 883, 171

Harrington, R. G., & Wilson, A. G. 1950, PASP, 62, 118

Harris, W. E. 1996, AJ, 112, 1487

Hayashi, E., Navarro, J. F., Taylor, J. E., Stadel, J., & Quinn, T. 2003, ApJ, 584, 541

Helmi, A., White, S. D. M., de Zeeuw, P. T., & Zhao, H. 1999, Nature, 402, 53

Hodge, P. W. 1961a, AJ, 66, 249

—. 1961b, AJ, 66, 384

—. 1971, ARA&A, 9, 35

Homma, D., Chiba, M., Okamoto, S., et al. 2018, Publications of the Astronomical Society of Japan, 70, S18

Hurley, J. R., & Mackey, A. D. 2010, MNRAS, 408, 2353

Hwang, N., Lee, M. G., Lee, J. C., et al. 2011, ApJ, 738, 58

Ibata, R., Nipoti, C., Sollima, A., et al. 2013, MNRAS, 428, 3648

Ibata, R., Sollima, A., Nipoti, C., et al. 2011, ApJ, 738, 186

Ibata, R. A., Gilmore, G., & Irwin, M. J. 1994, Nature, 370, 194

Innanen, K. A., & Papp, K. A. 1979, AJ, 84, 601

Iorio, G., Nipoti, C., Battaglia, G., & Sollima, A. 2019, MNRAS, 1366

Irwin, M., & Hatzidimitriou, D. 1995, MNRAS, 277, 1354

Irwin, M. J., Bunclark, P. S., Bridgeland, M. T., & McMahon, R. G. 1990, MNRAS, 244, 16P

Irwin, M. J., Belokurov, V., Evans, N. W., et al. 2007, ApJ, 656, L13

Ivezić, Ž., Beers, T. C., & Jurić, M. 2012, Annual Review of Astronomy and Astrophysics, 50, 251

Jerjen, H., & Binggeli, B. 1997, Astronomical Society of the Pacific Conference Series, Vol. 116, The Surface-BrightnessLuminosity Relation as Distance Indicator, ed. M. Arnaboldi,

G. S. Da Costa, & P. Saha, 298

Johnston, K. V., Hernquist, L., & Bolte, M. 1996, ApJ, 465, 278

Jordi, K., & Grebel, E. K. 2010, A&A, 522, A71

Jordi, K., Grebel, E. K., Hilker, M., et al. 2009, AJ, 137, 4586

Kallivayalil, N., Sales, L. V., Zivick, P., et al. 2018, ApJ, 867, 19

Karachentsev, I. 1996, A&A, 305, 33

Kauffmann, G., White, S. D. M., & Guiderdoni, B. 1993, MNRAS, 264, 201

Kepner, J., Fan, X., Bahcall, N., et al. 1999, ApJ, 517, 78

Kim, D., & Jerjen, H. 2015, ApJ, 808, L39

Kim, D., Jerjen, H., Mackey, D., Da Costa, G. S., & Milone, A. P. 2015a, ApJ, 804, L44

Kim, D., Jerjen, H., Milone, A. P., Mackey, D., & Da Costa, G. S. 2015b, ApJ, 803, 63

Kim, D., Jerjen, H., Geha, M., et al. 2016, ApJ, 833, 16

King, I. 1962, AJ, 67, 471

King, I. R. 1966, AJ, 71, 64

Kirby, E. N., Boylan-Kolchin, M., Cohen, J. G., et al. 2013, ApJ, 770, 16

Kirby, E. N., Cohen, J. G., Simon, J. D., & Guhathakurta, P. 2015a, ApJ, 814, L7

Kirby, E. N., Simon, J. D., & Cohen, J. G. 2015b, ApJ, 810, 56

Kleyna, J., Geller, M., Kenyon, S., & Kurtz, M. 1999, AJ, 117, 1275

Kleyna, J., Wilkinson, M. I., Evans, N. W., Gilmore, G., & Frayn, C. 2002, MNRAS, 330, 792

Klimentowski, J., Łokas, E. L., Kazantzidis, S., et al. 2007, MNRAS, 378, 353

Klypin, A., Gottlöber, S., Kravtsov, A. V., & Khokhlov, A. M. 1999a, ApJ, 516, 530

Klypin, A., Kravtsov, A. V., Valenzuela, O., & Prada, F. 1999b, ApJ, 522, 82

Klypin, A., Zhao, H., & Somerville, R. S. 2002, ApJ, 573, 597

Koch, A., Kleyna, J. T., Wilkinson, M. I., et al. 2007, AJ, 134, 566

Koch, A., Wilkinson, M. I., Kleyna, J. T., et al. 2009, ApJ, 690, 453

Koposov, S., Belokurov, V., Evans, N. W., et al. 2008, ApJ, 686, 279

Koposov, S. E., Belokurov, V., Torrealba, G., & Evans, N. W. 2015, ApJ, 805, 130

Koposov, S. E., Gilmore, G., Walker, M. G., et al. 2011, ApJ, 736, 146

Kormendy, J. 1985, ApJ, 295, 73

Kravtsov, A. V., & Yepes, G. 2000, MNRAS, 318, 227

Kroupa, P. 1997, New Astronomy, 2, 139

Kuhn, J. R., Smith, H. A., & Hawley, S. L. 1996, ApJ, 469, L93

Laevens, B. P. M., Martin, N. F., Sesar, B., et al. 2014, ApJ, 786, L3

Laevens, B. P. M., Martin, N. F., Ibata, R. A., et al. 2015a, ApJ, 802, L18

Laevens, B. P. M., Martin, N. F., Bernard, E. J., et al. 2015b, ApJ, 813, 44

Law, D. R., Johnston, K. V., & Majewski, S. R. 2005, ApJ, 619, 807

Leaman, R., VandenBerg, D. A., & Mendel, J. T. 2013, MNRAS, 436, 122

Lee, Y.-W., Demarque, P., & Zinn, R. 1994, ApJ, 423, 248

Łokas, E. L., Mamon, G. A., & Prada, F. 2005, MNRAS, 363, 918

Luque, E., Queiroz, A., Santiago, B., et al. 2016, MNRAS, 458, 603

Lynden-Bell, D., & Lynden-Bell, R. M. 1995, MNRAS, 275, 429

Mackey, A. D., & Gilmore, G. F. 2004a, MNRAS, 352, 153

—. 2004b, MNRAS, 355, 504

Mackey, A. D., & van den Bergh, S. 2005, MNRAS, 360, 631

Mackey, A. D., Ferguson, A. M. N., Irwin, M. J., et al. 2010, MNRAS, 401, 533

Majewski, S. 2004, in Astronomical Society of the Pacific Conference Series, Vol. 327, Satellites and Tidal Streams, ed. F. Prada, D. Martinez Delgado, & T. J. Mahoney, 63

Majewski, S. R., Skrutskie, M. F., Weinberg, M. D., & Ostheimer, J. C. 2003, ApJ, 599, 1082

Majewski, S. R., Frinchaboy, P. M., Kunkel, W. E., et al. 2005, AJ, 130, 2677

Marchi-Lasch, S., Muñoz, R. R., Santana, F. A., et al. 2019, ApJ, 874, 29

Martin, N. F., de Jong, J. T. A., & Rix, H.-W. 2008, ApJ, 684, 1075

Martin, N. F., Ibata, R. A., Chapman, S. C., Irwin, M., & Lewis, G. F. 2007, MNRAS, 380, 281

Martin, N. F., & Jin, S. 2010, ApJ, 721, 1333

Martin, N. F., Nidever, D. L., Besla, G., et al. 2015, ApJ, 804, L5

Martínez-Delgado, D., Alonso-García, J., Aparicio, A., & Gómez-Flechoso, M. A. 2001, ApJ, 549, L63

Martínez-Delgado, D., Peñarrubia, J., Jurić, M., Alfaro, E. J., & Ivezić, Z. 2007, ApJ, 660, 1264

Marzke, R. O., & da Costa, L. N. 1997, AJ, 113, 185

Mashchenko, S., Couchman, H. M. P., & Sills, A. 2005, ApJ, 624, 726

Mashchenko, S., & Sills, A. 2005a, ApJ, 619, 243

—. 2005b, ApJ, 619, 258

Massari, D., & Helmi, A. 2018, A&A, 620, A155

Mateo, M., Olszewski, E., Welch, D. L., Fischer, P., & Kunkel, W. 1991, AJ, 102, 914

Mateo, M., Olszewski, E. W., Pryor, C., Welch, D. L., & Fischer, P. 1993, AJ, 105, 510

Mateo, M., Olszewski, E. W., & Walker, M. G. 2008, ApJ, 675, 201

Mateo, M. L. 1998, ARA&A, 36, 435

Mayer, L., Governato, F., Colpi, M., et al. 2001, ApJ, 559, 754

Mayer, L., Moore, B., Quinn, T., Governato, F., & Stadel, J. 2002, MNRAS, 336, 119

McConnachie, A. W. 2012, AJ, 144, 4

McConnachie, A. W., Peñarrubia, J., & Navarro, J. F. 2007, MNRAS, 380, L75

McLaughlin, D. E. 2000, ApJ, 539, 618

Momany, Y., Zaggia, S., Gilmore, G., et al. 2006, A&A, 451, 515

Moore, B. 1996, ApJ, 461, L13

Moore, B., Ghigna, S., Governato, F., et al. 1999, ApJ, 524, L19

Muñoz, R. R., Carlin, J. L., Frinchaboy, P. M., et al. 2006, ApJL, 650, L51

Muñoz, R. R., Côté, P., Santana, F. A., et al. 2018a, ApJ, 860, 65

—. 2018b, ApJ, 860, 66

Muñoz, R. R., Geha, M., Côté, P., et al. 2012a, ApJ, 753, L15

Muñoz, R. R., Majewski, S. R., & Johnston, K. V. 2008, ApJ, 679, 346

Muñoz, R. R., Padmanabhan, N., & Geha, M. 2012b, ApJ, 745, 127

Muñoz, R. R., Frinchaboy, P. M., Majewski, S. R., et al. 2005, ApJ, 631, L137

Myeong, G. C., Jerjen, H., Mackey, D., & Da Costa, G. S. 2017, ApJ, 840, L25

Newberg, H. J., Willett, B. A., Yanny, B., & Xu, Y. 2010, ApJ, 711, 32

Newberg, H. J., Yanny, B., & Willett, B. A. 2009, ApJ, 700, L61

Newberg, H. J., Yanny, B., Rockosi, C., et al. 2002, ApJ, 569, 245

Norris, J. E., Wyse, R. F. G., Gilmore, G., et al. 2010, ApJ, 723, 1632

Odenkirchen, M., Grebel, E. K., Dehnen, W., Rix, H.-W., & Cudworth, K. M. 2002, AJ, 124, 1497

Odenkirchen, M., Grebel, E. K., Kayser, A., Rix, H.-W., & Dehnen, W. 2009, AJ, 137, 3378

Odenkirchen, M., Grebel, E. K., Rockosi, C. M., et al. 2001, ApJ, 548, L165

Odenkirchen, M., Grebel, E. K., Dehnen, W., et al. 2003, AJ, 126, 2385

Okamoto, S., Arimoto, N., Yamada, Y., & Onodera, M. 2008, A&A, 487, 103

Pace, A. B., & Li, T. S. 2019, ApJ, 875, 77

Palma, C., Kunkel, W. E., & Majewski, S. R. 2000, PASP, 112, 1305

Palma, C., Majewski, S. R., Siegel, M. H., et al. 2003, AJ, 125, 1352

Peñarrubia, J., McConnachie, A. W., & Navarro, J. F. 2008a, ApJ, 672, 904

Peñarrubia, J., Navarro, J. F., & McConnachie, A. W. 2008b, ApJ, 673, 226

Peñarrubia, J., Varri, A. L., Breen, P. G., Ferguson, A. M. N., & Sánchez-Janssen, R. 2017, MNRAS, 471, L31

Piatek, S., & Pryor, C. 1995, AJ, 109, 1071

Pietrzyński, G., Gieren, W., Szewczyk, O., et al. 2008, AJ, 135, 1993

Rees, M. J., & Ostriker, J. P. 1977, MNRAS, 179, 541

Rejkuba, M., Dubath, P., Minniti, D., & Meylan, G. 2007, A&A, 469, 147

Renaud, F., Agertz, O., & Gieles, M. 2017, MNRAS, 465, 3622

Ripepi, V., Clementini, G., Di Criscienzo, M., et al. 2007, ApJ, 667, L61

Rockosi, C. M., Odenkirchen, M., Grebel, E. K., et al. 2002, AJ, 124, 349

Rood, H. J., Page, T. L., Kintner, E. C., & King, I. R. 1972, ApJ, 175, 627

Sand, D. J., Olszewski, E. W., Willman, B., et al. 2009, ApJ, 704, 898

Sand, D. J., Seth, A., Olszewski, E. W., et al. 2010, ApJ, 718, 530

Sawala, T., Frenk, C. S., Fattahi, A., et al. 2016, MNRAS, 457, 1931

Searle, L., & Zinn, R. 1978, ApJ, 225, 357

Sersic, J. L. 1968, Atlas de Galaxias Australes

Shapley, H. 1918, PASP, 30, 42

—. 1938, Harvard College Observatory Bulletin, 908, 1

—. 1939, Proceedings of the National Academy of Science, 25, 565

Simon, J. D. 2018, ApJ, 863, 89

Simon, J. D., & Geha, M. 2007, ApJ, 670, 313

Simon, J. D., Geha, M., Minor, Q. E., et al. 2011, ApJ, 733, 46

Simon, J. D., Drlica-Wagner, A., Li, T. S., et al. 2015, ApJ, 808, 95

Sofue, Y. 2012, PASJ, 64, 75

Sohn, S. T., Majewski, S. R., Muñoz, R. R., et al. 2007, ApJ, 663, 960

Sohn, Y.-J., Park, J.-H., Rey, S.-C., et al. 2003, AJ, 126, 803

Sollima, A., Martínez-Delgado, D., Valls-Gabaud, D., & Peñarrubia, J. 2011, ApJ, 726, 47

Stetson, P. B. 1994, PASP, 106, 250

Tollerud, E. J., Bullock, J. S., Strigari, L. E., & Willman, B. 2008, ApJ, 688, 277

Torrealba, G., Koposov, S. E., Belokurov, V., & Irwin, M. 2016a, MNRAS, 459, 2370

Torrealba, G., Koposov, S. E., Belokurov, V., et al. 2016b, MNRAS, 463, 712

Torrealba, G., Belokurov, V., Koposov, S. E., et al. 2018, MNRAS, 475, 5085

Trujillo, I., Graham, A. W., & Caon, N. 2001, MNRAS, 326, 869

van den Bergh, S. 1993, ApJ, 411, 178

van den Bergh, S., & Mackey, A. D. 2004, MNRAS, 354, 713

Vasiliev, E. 2019, MNRAS, 484, 2832

Vickers, J. J., Smith, M. C., Hou, Y., Wang, Y., & Zhang, Y. 2016, ApJ, 816, L2

Vogt, S. S., Mateo, M., Olszewski, E. W., & Keane, M. J. 1995, AJ, 109, 151

Walker, M. G., Mateo, M., & Olszewski, E. W. 2009a, AJ, 137, 3100

—. 2009b, AJ, 137, 3100

Walker, M. G., Mateo, M., Olszewski, E. W., et al. 2006, AJ, 131, 2114

—. 2007, ApJ, 667, L53

—. 2009c, ApJ, 704, 1274

Walker, M. G., Olszewski, E. W., & Mateo, M. 2015, MNRAS, 448, 2717

Walsh, S. M., Jerjen, H., & Willman, B. 2007, ApJ, 662, L83

Walsh, S. M., Willman, B., Sand, D., et al. 2008, ApJ, 688, 245

Watkins, L. L., Evans, N. W., Belokurov, V., et al. 2009, MNRAS, 398, 1757

Westfall, K. B., Majewski, S. R., Ostheimer, J. C., et al. 2006, AJ, 131, 375

Wilkinson, M. I., Kleyna, J. T., Evans, N. W., et al. 2004, ApJ, 611, L21

Willman, B. 2010, Advances in Astronomy, 2010, 285454

Willman, B., Geha, M., Strader, J., et al. 2011, AJ, 142, 128

Willman, B., & Strader, J. 2012, AJ, 144, 76

Willman, B., Dalcanton, J. J., Martinez-Delgado, D., et al. 2005a, ApJ, 626, L85

Willman, B., Blanton, M. R., West, A. A., et al. 2005b, AJ, 129, 2692

Wilson, A. G. 1955, PASP, 67, 27

Wolf, J., Martinez, G. D., Bullock, J. S., et al. 2010, MNRAS, 406, 1220

Xue, X. X., Rix, H. W., Zhao, G., et al. 2008, ApJ, 684, 1143

York, D. G., Adelman, J., Anderson, John E., J., et al. 2000, AJ, 120, 1579

Zaritsky, D., Crnojević, D., & Sand, D. J. 2016, ApJ, 826, L9

Zinn, R. 1985, ApJ, 293, 424

Zinn, R. 1993, in Astronomical Society of the Pacific Conference Series, Vol. 48, The Globular Cluster-Galaxy Connection, ed. G. H. Smith & J. P. Brodie, 38

Zinn, R. 1996, in Astronomical Society of the Pacific Conference Series, Vol. 92, Formation of the Galactic Halo...Inside and Out, ed. H. L. Morrison & A. Sarajedini, 211

Zucker, D. B., Belokurov, V., Evans, N. W., et al. 2006a, ApJ, 643, L103

—. 2006b, ApJ, 650, L41

Appendix

A.1 The MCMC algorithm and the Bayes' theorem

The MCMC (Markov Chain Monte Carlo) algorithm is used to sample from a probability distribution. The objective is to obtain numerical approximations of integrals that are difficult to solve analytically and/or depend on a large number of unknown parameters.

One typical area where the MCMC algorithm is used is in problems where Bayesian inference takes a protagonist role. Bayesian inference is based on the Bayes' theorem, which states that the probability of an event is related to the prior knowledge of certain conditions that directly influence that event. In mathematical form,

$$P(A|B) = \frac{P(B|A)P(A)}{P(B)} \tag{A.1}$$

where $P(A)$ is the probability of observing event A, $P(B)$ is the probability of observing event B, $P(A|B)$ is the conditional probability of observing A given B, and $P(B|A)$ is the conditional probability of observing B given A. In the Bayesian inference context, $P(B|A)$ is called the likelihood function, $P(A|B)$ the posterior distribution, and $P(A)$ the prior distribution.

When having data and a model to fit, the probability distributions in equation A.1 take the form

$$P(M|D) = \frac{P(D|M)P(M)}{P(D)} \tag{A.2}$$

where M is the model one wants to fit to the data D. In equation A.2, the likelihood $P(D|M)$ represents the probability of observing the empirical data given specific parameters that define the model; the posterior distribution $P(M|D)$ defines the distribution of each free parameter on the model, given the observed empirical data; the prior distribution $P(M)$ states the distribution of the possible values of each free parameter on the model, without assuming any observed data; and $P(D)$ represents the probability of observing the data without assuming any particular model. It is common to not consider the probability $P(D)$ because is a constant and it only affects the normalization of the posterior distribution. Then, one typically uses

$$P(M|D) \propto P(D|M)P(M) \tag{A.3}$$

One of the advantages of the Bayesian inference is that instead of getting a single value for each free parameter in the model, a probability distribution is obtained, making it easy to derive further statistics, like standard deviations. Moreover, when having new complementary data, the posterior distribution can be used to update the prior distribution, taking advantage of previous knowledge.

The MCMC algorithm is used to sample the free parameters of the model from the prior distribution $P(M)$ and uses them to fit the model M to data D to obtain the likelihood $P(D|M)$. The "Monte Carlo" part of the MCMC name is because the sampling from the prior distribution is random, i.e. the value for a free parameter is a random variable. The "Markov Chain" part states that the move to sample the next value of a free parameter is only influenced by the current value of that parameter and not by the chosen values in the past. The MCMC algorithm incorporates a method to decide if the new random value for the free parameter goes in the right direction of improving the fit of the model M to the data D. Finally, after several steps for the chain defined by the user, the algorithm reaches a convergence on the values for each free parameter of the model, and a probability distribution for each free parameter can be obtained from the frequency of the values.